



Università degli Studi di Firenze

Scuola di Ingegneria

DIEF - Department of Industrial Engineering of Florence

PhD School: *Energetica e Tecnologie Industriali Innovative*

Scientific Area: ING-IND/08 - *Macchine a Fluido*

MATRIX COOLING SYSTEMS FOR GAS TURBINE
NOZZLES AND BLADES: EXPERIMENTAL
INVESTIGATIONS AND DESIGN CORRELATIONS

PhD Candidate: ING. MARCO PIEVAROLI

Tutor: PROF. ING. BRUNO FACCHINI

Academic Supervisor: DR. ING. CARLO CARCASI

Industrial Supervisor: DR. ING. LORENZO TARCHI

Industrial Supervisor: DR. ING. ALBERTO CECCHERINI

PhD School Coordinator: PROF. ING. MAURIZIO DE LUCIA

XXVII PhD School Cycle - 2012-2014

To my parents and to all those who have supported me...



Regione Toscana



REPUBBLICA ITALIANA



Unione Europea

Le ali alle tue idee

*The research project reported in this PhD Thesis
has received funding from the POR CReO FESR 2007-2013
supported by the European Fund on Regional Development*

*Il progetto di ricerca presentato in questa Tesi di Dottorato
è stato finanziato dal programma POR CReO FESR 2007-2013
e cofinanziato dal fondo Europeo di Sviluppo Regionale*

Acknowledgements

I still remember with pleasure the day I moved my first step in the legendary Lab Colonne. During my first months in Lab I was assigned to the Ferrari F1 Test Rig and I was happy as a child...it was a very lucky event for me.

From those first moments, day after day, I realized that my greatest lucky event was to have met lots of special people...you...the members of the HTC Group...you...my dear friends.

In this special moment for me, at the end of my PhD course, I want to take this opportunity to thank everyone, even though these few lines will not be enough to express my gratitude for you all.

First of all, I would like to thank Prof. Bruno Facchini...thank you very much for your trust in me, for giving me the chance to work in this fantastic team...and thank you for your patience and your great support during these three years and especially during these last days close to deadline for the conclusion of my PhD Thesis.

I wish to express my gratitude to Ing. Luca Innocenti and Ing. Alberto Ceccherini: your great experience, competence and helpfulness have represented for me an inestimable support in the realization of this project. A special thanks goes to Alberto, one of my supervisors: your reviews and suggestions have been of great value for my PhD thesis.

I would also like to thank Nuovo Pignone GE Oil & Gas for giving me the opportunity to collaborate and work in this challenging project during

these three years.

My warmest thanks go to Ing. Carlo Carcasci and Ing. Lorenzo Tarchi, my supervisors and mentors during these years. Thank you very much for all the time you have devoted to me, for your precious and brilliant advices: you have represented an important guide for my work, for my academic and personal formation.

Therefore, I want to remember with great pleasure the opportunity you gave me the Wednesday, August 1st, 2012: the first trip to Ferrari Ges in Maranello and the visit to the engine test room. I realized one of the dreams of my life...thank you very much!!!

Many thanks to my colleagues and friends that have shared with me important working experiences and also funny moments.

Thanks to my experimental ex-colleagues and ex-PhD mates of the Lab Colonne: Francesco (Maio), Alessio (Picchi), Leonardo (Bonannone), Francesco (Fransis), Gianluca (Gianlucuccio). You were the first to welcome me and you gave me important friendly advices about my first experiments in the Lab. I will never forget the funny experiences spent with you.

Thanks to my current experimental colleagues in the Lab Colonne: Daniele and Giulio (the newcomer in Lab). It is a pleasure to work with you every day; we work all together in a very fruitful and enjoyable collaboration. I am indebted to you for sharing with me scary moments during my rotating tests close to 200 rpm !!!

Thanks to the other experimental guys Riccardo B. and Tommaso B., inhabitants of the new THT-Lab in Calenzano.

Thanks to my numerical colleagues: Antonio, Alessio (Bonini), Luca (Andrei), Riccardo (Ferraro), Lorenzo M. (Mazze), Lorenzo W. (Winchler), Alessandro, Tommaso F., Emanuele B., Leopoldo M. and the newcomers Sabri and Stefano.

Thanks to the Ergon guys Cosimo, Mirko and Riccardo D.S.

I also devote my thanks to the visitor PhD mates Ahmed and Mahfoud. I

spent more than a year with Ahmed in the Lab Colonne sharing both good and bad moments at the rotating test rig and...also funny moments listening to his songs. I spent only few months with Mahfoud but I remember with pleasure him for his generosity and cordiality.

*Then I want to thank the people closer to my mind and to my heart.....
Thanks to my family: thank you Mamma, thank you Babbo...you are the best parents in the World !!! In every moment of my life, you have given me the best to support my educational trip, my career, my life; it would have been impossible to reach my goals without you!
A final thanks to my beautiful sweetheart Letizia...your hugs, your kisses, your sweet words of encouragement gave me the force to conclude my PhD work. Thanks my Love !!!*

Abstract

The research project presented in the present PhD thesis is focused on the development of innovative internal cooling systems for both nozzles and blades of current and future industrial gas turbines. This project is a collaboration between the Department of Industrial Engineering of the University of Florence and the industrial partner GE Oil & Gas.

Gas turbines for Oil and Gas applications were historically derived from power generation and aircraft engines with small design effort. More recently, due to a large growth of the business segment, specific products were designed with the objective of maintaining high efficiency while increasing inspection intervals and reducing components maintenance as much as possible.

As a consequence, some specific research paths were developed in order to increase the lifetime of the airfoils while maintaining the high turbine inlet temperatures (TIT) well above the melting point of the airfoils materials directly exposed to hot gases.

One of the most critical part of these components is represented by the trailing edge region; in fact, because of its reduce metal thickness and cross section, this part is easily subject to low cycle fatigue cracking, oxidation and creep and hence to premature failures. For these reasons modern designs of trailing edge regions must guarantee a high structural rigidity and a high and uniform heat transfer enhancement at the same time.

Among the different internal cooling technologies, a very promising solution is represented by the latticework-matrix cooling systems, a widespread

technology in the Eastern european countries not well known among the designers of the Western world.

Starting from these considerations the present work regards an intensive experimental survey on different scaled up models of matrix cooling geometries. Several experimental campaigns have been carried out with the aim of measuring pressure losses and heat transfer coefficient distributions of different geometries reproducing the typical operating conditions of real gas turbines in terms of Reynolds and Biot number. Moreover, further experimental tests have been performed in rotating conditions reproducing the Rotation number similitude with real applications.

In a first stage tests have been carried out on geometries with constant cross section in order to evaluate the effects of the main geometric parameters on both friction and heat transfer performance. In the next stage, both static and rotating tests have been performed on two convergent matrix geometries reproducing realistic trailing edge arrangements. All these geometries have been designed in order to meet the requirements of the industrial partner.

A steady-state technique with heated segments and embedded thermocouples has been employed to determine the regionally averaged heat transfer coefficients for different streamwise and spanwise positions along the test models. Moreover, a specific post-processing procedure has been developed to evaluate the non uniform temperature field on the surface of matrix ribs, fin effectiveness and the additional heat transfer surface area provided by the ribs. This post-processing has allowed to determine the average heat transfer coefficient distributions; average values have been evaluated as effective coefficients between rib surfaces and fluid, but also as equivalent coefficients applicable on the internal endwalls of the airfoil in order to determine the overall heat removed from these surfaces.

In the last part of the present work the experimental data have been used to find heat transfer and friction correlations. These correlations have been applied to a real case in a trailing edge system and the performance of the current cooling scheme have been compared with those achievable by means of the investigated matrix geometries.

Contents

Abstract	ix
Contents	xiii
List of Figures	xxvii
List of Tables	xxx
Nomenclature	xxxix
1 Introduction	1
1.1 Evolution of the Gas Turbine	1
1.2 Objectives of Present Research	13
1.3 Thesis outline	17
2 Overview of Gas Turbine Cooling Systems	19
2.1 Internal Cooling Systems	19
2.1.1 Internal Cooling of Gas Turbine Vanes	23
2.1.1.1 Impingement cooling	24
2.1.1.2 Pin-Fin Cooling	30
2.1.1.3 Dimple Cooling	34
2.1.2 Internal Cooling of Gas Turbine Blades	36
2.1.2.1 Rib Turbulated Cooling	37
2.1.3 Trailing Edge Cooling Systems	45
2.1.4 Rotational Effects on Internal Cooling	55

2.1.4.1	Rotational Effects on Trailing Edge Cooling Systems	64
2.2	Matrix Cooling Systems	68
2.2.1	Basic Principles	68
2.2.2	Literary Overview	73
2.2.2.1	Goreloff et al. (1990)	73
2.2.2.2	Nagoga (1996)	73
2.2.2.3	Gillespie et al. (2000)	79
2.2.2.4	Bunker (2004)	83
2.2.2.5	Acharya et al. (2004)	91
2.2.2.6	Oh et al. (2008-2012)	102
2.2.2.7	Saha et al. (2008-2013)	108
3	Heat Transfer Measurement Techniques	115
3.1	Introduction to HTC Measurement	115
3.1.1	Flow Temperature Measurements Techniques	120
3.1.2	Mass Transfer Measurements Techniques	121
3.1.3	Heat Transfer Measurements Techniques	122
3.2	Steady State Measurement Techniques	123
3.2.1	Heated High Conducting Elements Technique	123
3.2.2	Heated Thin Foil Technique	126
3.3	Transient Measurement Techniques	127
3.3.1	Thin Wall Lumped Capacitance Method	128
3.3.2	Semi-infinite Wall Method	131
3.4	Critical Aspects on Matrix Cooling Measurements	134
4	Experimental Apparatus and Data Reduction	137
4.1	Test Rig Layout for Static Tests	137
4.1.1	Test models	139
4.1.2	Matrix geometries with constant cross section	144
4.1.3	Matrix geometries with convergent cross section	147
4.2	Test Rig Layout for Rotating Tests	150
4.2.1	Matrix geometries for rotating tests	153
4.3	Measuring devices	158

4.3.1	Mass flow rate measurements	158
4.3.2	Static pressure measurements	159
4.3.3	Temperature measurements	160
4.4	Heat Transfer Coefficient measurement	163
4.4.1	Heated segments with thermocouples	163
4.4.2	Data reduction and post-processing procedure	164
4.4.3	Heat losses determination	174
4.5	Friction factor measurement	179
4.6	Measurement uncertainty	182
5	Experimental Results: Friction and Pressure Losses	191
5.1	Friction results of static tests for matrix geometries with constant cross section	192
5.2	Friction results of static tests for matrix geometries with convergent cross section	204
5.3	Friction results of rotating tests	214
5.4	Comparison of friction results and critical evaluation	222
6	Experimental Results: Heat Transfer	227
6.1	Heat transfer results of static tests for matrix geometries with constant cross section	228
6.2	Heat transfer results of static tests for matrix geometries with convergent cross section	243
6.3	Heat transfer results of rotating tests	253
6.4	Comparison of Heat Transfer Results and Critical Evaluation	267
7	Experimental Correlations for Blade Cooling Design	273
7.1	Heat Transfer Correlations	274
7.2	Friction Correlations	283
7.3	Application of Correlations to a Real Case	287
	Conclusions	293
	Bibliography	312

List of Figures

1.1	Drawing of first patent for a gas turbine (John Barber, 1791)	2
1.2	The world's first industrial gas turbine-generator realized by Brown Boveri and installed in Neuchatel, Switzerland (1939)	3
1.3	Layout of gas turbine-generator realized by Brown Boveri and installed in Neuchatel, Switzerland (1939)	3
1.4	The first turbojet engine designed by Frank Whittle (1930)	4
1.5	The turbojet Heinkel HeS 3B designed by Hans von Ohain and Max Hann (1939)	4
1.6	Improvement of power output with the increasing of turbine inlet temperature (TIT) [2]	6
1.7	Schematic view of typical cooling and sealing airflows in a gas turbine [3]	7
1.8	Example of a nozzle guide vane and turbine blade cooling arrangement [3]	8
1.9	Trend of turbine inlet temperature (TIT) over recent years [2]	8
1.10	Cooling effectiveness as a function of the heat load parameter for different cooling technologies [5]	10
1.11	Schematic of a cross-section through a prepared mould showing the pinned ceramic cores within the wax preform and the ceramic shell mould	12

2.1	Complex flow phenomena in a turbine rotor hot-gas passage (Gladden and Simoneau, 1988; collected in Sokolowski, 1988) [2]	20
2.2	Heat flux distribution around an inlet guide vane and a rotor blade	21
2.3	Effect of a non uniform temperature inlet profile on dimensionless adiabatic wall temperature distribution (Bonini [8])	22
2.4	Schematic of a turbine vane cross-section with different cooling systems	24
2.5	Comparison of flow regions in an impinging jet with flow regions of a free jet (Viskanta, 1993) [2]	26
2.6	Typical test model for studies on multiple impingement jets	28
2.7	Schematic of the impingement cooling at the airfoil's leading edge (Chupp et al., 1968) [2]	29
2.8	Leading edge impingement with film cooling extraction (Metzger et al., 1990) [2]	30
2.9	Cross-sectional view of a pin-fin cooling system at the trailing edge	31
2.10	Typical test model and schematic of secondary flows for Pin-Fin cooling	32
2.11	Typical test model for Dimple cooling studies and schematic view of dimple induced secondary flows [39]	36
2.12	Schematic of common internal cooling techniques in modern gas turbine blades [40]	37
2.13	Example of ribbed channel with ribs on two opposite walls [7]	38
2.14	Schematic of flow separation and rib orientations in heat-transfer coefficient enhancement (Han and Dutta, 1995) [2]	40
2.15	Typical test models for turbulated cooling studies with rib induced secondary flows	41
2.16	High performance rib turbulators for turbine blade internal cooling	42

2.17 Radial and multipass configurations of ribbed channels [3]	44
2.18 Examples of cooled blades with different trailing edge configurations	46
2.19 Example of trailing edge cooling schemes in a rotor blade	47
2.20 Two wedge-shaped with different outlet flow orientations [54]	49
2.21 Heat transfer and pressure loss results for different configurations of wedge-shaped ducts: straight/lateral flow orientation and staggered/in-line pin-fin arrays [54]	50
2.22 Comparison of heat transfer and pressure loss results between pin-less wedge duct and rectangular pin-less duct [54]	50
2.23 Schematic of long ribs (pedestals) and pin fins geometry in the convergent wedge-shaped channel [56]	51
2.24 Scheme of a trailing edge cooling section with pin fins and enlarged pedestals [62]	53
2.25 Typical high-pressure turbine blade showing trailing-edge cooling openings and pressure-side ejection slots [61] . . .	53
2.26 View of the shaped holes on the pressure side of the gas turbine airfoil [63]	54
2.27 Different openings of the holes at the exit section [63] . .	54
2.28 Stable and unstable regions in a rotating flow (Lezius and Johnston,1976) [2]	56
2.29 Conceptual view of the rotation effects on the coolant flow through a two-pass rotating channel [65]	57
2.30 Typical cooling passage size and orientation with conceptual views of the rotation induced secondary flows	60
2.31 Schematic of the leading-edge impingement configuration used by Mattern and Hennecke (1996) [2]	63
2.32 Schematic of the trailing edge wedge-shaped channel investigated by Liu et al. [60]	66
2.33 Schematic of the trailing edge model investigated by Bonanni [59]	67

2.34	Example of a matrix geometry and a schematic view of the flow [86]	69
2.35	Main geometric parameters of a matrix channel and detailed view of the flow turn at the sidewall [86]	70
2.36	Scheme of an open matrix geometry [7]	71
2.37	Experimental lattice cooled blade (Goreloff et al. 1990) [89]	74
2.38	Example of experimental matrix model used by Nagoga [7]	75
2.39	Photographs of the test model used by Gillespie et al. [89]	80
2.40	Reduction of coolant temperature potential ($T_{gas} - T_w$)[89]	81
2.41	Heat transfer coefficients based on the inlet and local mixed bulk temperature [89]	82
2.42	Maps of heat transfer coefficients h_{mb} based on the local mixed bulk temperature for two different Reynolds number [89]	83
2.43	Test apparatus for heat transfer tests on acrylic test models [86]	86
2.44	HTC map and laterally averaged distributions of heat transfer coefficients for primary surfaces of geometry with narrow sub-channels [86]	87
2.45	Heat transfer enhancement evaluated on the primary surfaces of the two acrylic models [86]	88
2.46	Test apparatus for transient heat transfer tests on metallic models using an IR camera [86]	89
2.47	HTC maps from transient infrared method for two Reynolds numbers (Model #3) [86]	92
2.48	Overall heat transfer enhancement of the two investigated geometries as a function of Reynolds number [86]	92
2.49	Rotating test rig used by Acharya et al. [92]	93
2.50	Test model (leading side) installed on the rotating test rig [92]	94
2.51	Sub-channel averaged Nusselt numbers as a function of Reynolds number Re_s [92]	97

2.52	Sub-channel averaged Nusselt numbers as a function of Rotation number Ro_s [92]	98
2.53	Nusselt number distributions on individual rows for stationary experiments [92]	99
2.54	Rotation effects on the leading outer row at $Re_s = 20000$ [92]	100
2.55	Rotation effects at $Re_s = 5000$ [92]	101
2.56	Friction factors at different Reynolds and Rotation numbers [92]	101
2.57	Geometry and nomenclature of geometric parameters for the test model used by Oh et al. [97]	102
2.58	Schematic view of the rotating test rig adopted by Oh et al. [97]	103
2.59	Contour plots of Sh/Sh_0 in the stationary case ($Ro = 0$) for the trailing surface and line averaged Sh_L/Sh_0 distributions for the trailing surface [97]	105
2.60	Contour plots of Sh/Sh_0 in the stationary case ($Ro = 0$) for the leading surface and line averaged Sh_L/Sh_0 distributions for the leading surface [97]	105
2.61	Friction factor ratios for various Rotation and Reynolds numbers [97]	106
2.62	Comparison of Thermal Performance Factors TPF for various cooling methods [97]	107
2.63	Acrylic test section with converging matrix core and convergent structure with dimensions used for calculation of the sub-channel hydraulic diameter at inlet [6]	110
2.64	Examples of Nu/Nu_0 maps for 4 and 2 inlet channel configurations [6]	110
2.65	Comparison of the average heat transfer enhancement Nu/Nu_0 as a function of Reynolds number between the investigated matrix geometries and a pin fin configuration [6]	111
2.66	TPF comparison between the investigated matrix geometries and a pin fin configuration [6]	113

3.1	Energy balance for a heated element to calculate the bulk fluid temperature along the streamwise direction	119
3.2	Classification of the heat transfer measurement techniques	123
3.3	Scheme of the heated high conducting elements technique	125
3.4	Scheme of the heating foil technique	127
3.5	Diagram for the lumped capacitance method to determine the averaged heat transfer coefficient on a rib	130
4.1	Test facility for static tests	139
4.2	Picture of the test facility for static tests instrumented with thermocouples, heaters and pressure taps	139
4.3	Top section view of the lower half of a test model	143
4.4	Detailed view of four matrix blocks instrumented with thermocouples and foil heaters	143
4.5	Geometric parameters of tested matrix geometries	146
4.6	Geometric parameters of tested matrix geometries with convergent cross section	148
4.7	Test facility for rotating tests	150
4.8	Details of rotary joint and electric motor [62]	151
4.9	Schematic of the two investigated test model orientations: <i>0deg</i> and <i>30deg</i>	153
4.10	Details of the test section installed on the rotating chassis	154
4.11	Top section view of a test model employed during rotating experiments	156
4.12	Orifice plate for mass flow measurement	159
4.13	Example of a FEM simulation to evaluate the correct depth to locate thermocouples	161
4.14	Difference between effective and equivalent Heat Transfer Coefficients HTC	165
4.15	Nomenclature of the indices used in the data reduction procedure to identify the position of the blocks	166
4.16	Heat fluxes and wall temperature distribution through a single matrix block	168

4.17	Conduction and convection in a rectangular fin of uniform cross section	169
4.18	Overall length rib and sub-channel width for a single matrix block	172
4.19	Definition of sub-channel hydraulic diameter of the whole matrix model and single i -th matrix block	175
4.20	Example of Q_{loss} polynomial trends as a function of block temperature $T_{w,i}$ respect to ambient temperature T_{amb}	177
4.21	Schematic of the thermal circuit used to evaluate heat losses in rotating conditions	178
4.22	Difference between the length of a matrix model L and the effective overall distance of the flow along a track L_{tot}	181
4.23	Schematic of a generic measurement chain	183
4.24	Systematic errors vs random errors	185
5.1	Geom 01 - pressure taps location along different sub-channel tracks	196
5.2	Geom 02, Geom 03, Geom 04 - pressure taps location along different sub-channel tracks	196
5.3	Geom 01 - pressure ratio distributions along different sub-channel tracks	197
5.4	Geom 01 - pressure ratio distributions along track #1	197
5.5	Geom 01 vs Geom 02 - Comparison of pressure ratio distributions along track #1	198
5.6	Geom 03 vs Geom 04 - Comparison of pressure ratio distributions along track #1	199
5.7	Comparison between friction factor distributions for Geom 01,02,03,04 and Karman-Nikuradse correlation for smooth ducts (Equation 4.31	200
5.8	Comparison between friction factor distributions for Geom 01,02,03,04 and Nagoga correlation for matrix geometries (Equation 2.13)	200

5.9	Geom 01 - Non dimensional mass flow as a function of total to static pressure ratio	201
5.10	Geom 02 - Non dimensional mass flow as a function of total to static pressure ratio	201
5.11	Geom 03 - Non dimensional mass flow as a function of total to static pressure ratio	202
5.12	Geom 04 - Non dimensional mass flow as a function of total to static pressure ratio	202
5.13	Comparison of non dimensional mass flow as a function of total to static pressure ratio for Geom 01,02,03,04	203
5.14	Geom 05, Geom 06 - pressure taps location along different sub-channel tracks	207
5.15	Geom 06 - pressure ratio distributions along different sub-channel tracks	207
5.16	Geom 05 vs Geom 06 - Comparison of pressure ratio distributions along track #1	208
5.17	Geom 01 vs Geom 03 vs Geom 06 - Comparison of pressure ratio distributions along track #1	209
5.18	Geom 02 vs Geom 04 vs Geom 05 - Comparison of pressure ratio distributions along track #1	210
5.19	Comparison between friction factor distributions for Geom 05,06 and Karman-Nikuradse correlation for smooth ducts (Equation 4.31)	211
5.20	Comparison between friction factor distributions for Geom 05,06 and Nagoga correlation for matrix geometries (Equation 2.13)	211
5.21	Geom 05 - Non dimensional mass flow as a function of total to static pressure ratio	212
5.22	Geom 06 - Non dimensional mass flow as a function of total to static pressure ratio	212
5.23	Comparison of non dimensional mass flow as a function of total to static pressure ratio for Geom 05,06	213

5.24	Geom 07, Geom 08 - pressure taps location along different sub-channel tracks	215
5.25	Schematic of the pressure connection pipe between the pressure scanner and the pressure taps	216
5.26	Geom 07 vs Geom 08 - Comparison of pressure ratio distributions along track #1	218
5.27	Geom 08 - pressure ratio distributions along track #1 for different Rotation numbers	219
5.28	Comparison between friction factor distributions for Geom 07,08 and Karman-Nikuradse correlation for smooth ducts (Equation 4.31)	219
5.29	Comparison between friction factor distributions for Geom 07,08 and Nagoga correlation for matrix geometries (Equation 2.13)	220
5.30	Geom 07 + Geom 05 - Non dimensional mass flow as a function of total to static pressure ratio	220
5.31	Geom 08 + Geom 06 - Non dimensional mass flow as a function of total to static pressure ratio	221
5.32	Friction factor distributions for different Reynolds numbers - Comparison between all investigated geometries	224
5.33	Normalized friction factor (f/f_0) distributions for different Reynolds numbers - Comparison between all investigated geometries	224
5.34	Non dimensional mass flow as a function of total to static pressure ratio - Comparison between all investigated geometries	225
6.1	Geom 01 - Distributions of the normalized effective heat transfer coefficient htc_r/htc_{ref} for the different rows of matrix blocks	232
6.2	Geom 02 - Distributions of the normalized effective heat transfer coefficient htc_r/htc_{ref} for the different rows of matrix blocks	233

6.3	Geom 03 - Distributions of the normalized effective heat transfer coefficient htc_r/htc_{ref} for the different rows of matrix blocks	234
6.4	Geom 04 - Distributions of the normalized effective heat transfer coefficient htc_r/htc_{ref} for the different rows of matrix blocks	235
6.5	Geom 01 vs Geom 02 - Distributions of the normalized effective Nusselt number $Nu_{r,s,in}/Nu_{ref}$ for the two couple of rows	236
6.6	Geom 03 vs Geom 04 - Distributions of the normalized effective Nusselt number $Nu_{r,s,in}/Nu_{ref}$ for the two couple of rows	237
6.7	Distributions of the normalized equivalent heat transfer coefficients htc_{eqT}/htc_{ref} and htc_{eqB}/htc_{ref} as a function of mass flow rate \dot{m}_{air} and Reynolds number $Re_{s,in}$. . .	238
6.8	Distributions of the normalized effective heat transfer coefficients htc_r/htc_{ref} as a function of mass flow rate \dot{m}_{air} and Reynolds number $Re_{s,in}$	239
6.9	Distributions of the normalized equivalent and effective average Nusselt number as a function of Reynolds number $Re_{s,in}$	240
6.10	Geom 01 vs Geom 02 - Distributions of the normalized effective Nusselt number $Nu_{r,s,in}/Nu_{ref}$ for different stream-wise positions and Reynolds numbers	241
6.11	Geom 03 vs Geom 04 - Distributions of the normalized effective Nusselt number $Nu_{r,s,in}/Nu_{ref}$ for different stream-wise positions and Reynolds numbers	242
6.12	Geom 05 - Distributions of the normalized effective heat transfer coefficient htc_r/htc_{ref} for the different rows of matrix blocks	245
6.13	Geom 06 - Distributions of the normalized effective heat transfer coefficient htc_r/htc_{ref} for the different rows of matrix blocks	246

6.14	Geom 01 vs Geom 03 vs Geom 06 - Comparison between distributions of the normalized effective heat transfer coefficient htc_r/htc_{ref} for the different rows of matrix blocks at the same mass flow rate	247
6.15	Geom 05 vs Geom 06 - Distributions of the normalized effective Nusselt number $Nu_{r,s,ave}/Nu_{ref}$ for the two couple of rows	248
6.16	Geom 05 vs Geom 06 - Distributions of the normalized equivalent heat transfer coefficients htc_{eqT}/htc_{ref} and htc_{eqB}/htc_{ref} as a function of mass flow rate \dot{m}_{air} and Reynolds number $Re_{s,ave}$	249
6.17	Geom 05 vs Geom 06 - Distributions of the normalized effective heat transfer coefficients htc_r/htc_{ref} as a function of mass flow rate \dot{m}_{air} and Reynolds number $Re_{s,ave}$	250
6.18	Geom 05 vs Geom 06 - Distributions of the normalized equivalent and effective average Nusselt number as a function of Reynolds number $Re_{s,ave}$	251
6.19	Geom 05 vs Geom 06 - Distributions of the normalized effective Nusselt number $Nu_{r,s,ave}/Nu_{ref}$ for different stream-wise positions and Reynolds numbers	252
6.20	Test matrices for rotating tests on Geom 07 and Geom 08	257
6.21	Geom 07 - Distributions of the normalized effective heat transfer coefficient htc_r/htc_{ref} for the different rows of matrix blocks at different rotating conditions	258
6.22	Geom 08 - Distributions of the normalized effective heat transfer coefficient htc_r/htc_{ref} for the different rows of matrix blocks at different rotating conditions	259
6.23	Geom 07 vs Geom 08 - Distributions of the normalized equivalent and effective heat transfer coefficients htc_{eqT}/htc_{ref} , htc_{eqB}/htc_{ref} and htc_r/htc_{ref} as a function of Reynolds numbers at different rotating conditions	260

6.24	Geom 07 vs Geom 08 - Distributions of the normalized equivalent and effective Nusselt numbers Nu_{eqT}/Nu_{ref} , Nu_{eqB}/Nu_{ref} , Nu_r/Nu_{ref} as a function of Reynolds numbers at different rotating conditions	261
6.25	Geom 07 - Streamwise distributions of the normalized effective Nusselt number Nu_r/Nu_{ref} for pressure and suction sides of the matrix model at different rotating conditions .	262
6.26	Geom 08 - Streamwise distributions of the normalized effective Nusselt number Nu_r/Nu_{stat} for pressure and suction sides of the matrix model at different rotating conditions .	263
6.27	Geom 07 vs Geom 08 - overall rotation effects at different Reynolds numbers: distributions of the rotation-to-stationary ratio Nusselt number $Nu_{r,s}/Nu_{stat}$	264
6.28	Geom 07 - $0deg$ vs $30deg$ - Distributions of the normalized effective heat transfer coefficient $Nu_{r,s}/Nu_{stat}$ for the different rows of matrix blocks at different rotating conditions	265
6.29	Geom 08 - $0deg$ vs $30deg$ - Distributions of the normalized effective heat transfer coefficient $Nu_{r,s}/Nu_{stat}$ for the different rows of matrix blocks at different rotating conditions	266
6.30	Normalized equivalent Nusselt number distributions for different Reynolds numbers - Comparison between all investigated geometries	270
6.31	Normalized effective Nusselt number distributions for different Reynolds numbers - Comparison between all investigated geometries	270
6.32	Heat transfer enhancement $Nu_{r,s}/Nu_0$ vs Reynolds number - Comparison between experimental and literature data	271
6.33	Thermal Performance Factor TPF vs Reynolds number - Comparison between experimental and literature data . .	272
7.1	Examples of schematic division for a matrix model in 5 streamwise positions and corresponding averaged Nusselt number distribution for each streamwise block	278

7.2	Example of the averaged effective Nusselt number distribution for each streamwise block for a convergent model (Geom 05)	279
7.3	Schematic of the reference middle section for the geometric parameters used in the correlations	280
7.4	Comparison between experimental and calculated effective Nusselt number by correlation	280
7.5	Comparison between effective Nusselt experimental trends and relative correlation	281
7.6	Equivalent Nusselt number correlations for the investigated geometries	281
7.7	Comparison between experimental and calculated friction factor values by correlation	284
7.8	Comparison between experimental trends of friction factor and relative correlation	285
7.9	Comparison between experimental and calculated non dimensional mass flow values by correlation	286
7.10	Schematic representation of the $HTC_{ave_{eq}}$ applied to the internal endwall surface of the airfoil	288
7.11	Performance comparison between the experimental matrix geometries and current serpentine solutions from GE Oil & Gas experience	291

List of Tables

2.1	Ranges for Nagosa’s correlations [7]	79
2.2	Acrylic model dimensions for the two geometries tested by Bunker [86]	85
2.3	Metallic model dimensions for the two geometries tested during transient heat transfer tests [86]	90
2.4	Dimensions of aluminum test model for rotating tests [97]	102
4.1	Dimensions of matrix geometries with constant cross section	145
4.2	Complete set of geometric dimensions of matrix geometries with constant cross section	146
4.3	Dimensions of matrix geometries with convergent cross section	148
4.4	Complete set of geometric dimensions of matrix geometries with convergent cross section	149
4.5	Dimensions of matrix geometries for rotating tests	156
4.6	Complete set of geometric dimensions of matrix geometries for rotating tests	157
4.7	Comparison of heat losses Q_{loss} between static and rotating experiments	179
4.8	Uncertainty analysis on mass flow rate	189
4.9	Uncertainty analysis on Reynolds number	189
4.10	Uncertainty analysis on Friction Factor	189
4.11	Uncertainty analysis on Heat Transfer Coefficient HTC for Static Tests	190

4.12	Uncertainty analysis on Heat Transfer Coefficient HTC for Rotating Tests	190
6.1	Geom 07 vs Geom 08 - Overall heat transfer enhancement due to rotation	264
7.1	Exponents and coefficients of the heat transfer correlation	276
7.2	Ranges for heat transfer correlation	277
7.3	Geom 05 - Example of Reynolds number variation for different streamwise blocks	279
7.4	Exponents and coefficients of equivalent Nusselt number correlations	282
7.5	Exponents and coefficients of the friction factor correlation	284
7.6	Exponents and coefficients of the \dot{m}_{rid} vs. β_{TS} correlation	286
7.7	Coolant supply conditions of the real case at the design point	288
7.8	Heat transfer and pressure loss performance of the convergent matrix geometry with 4 entry channels evaluated in design and off-design points of a real case	290
7.9	Heat transfer and pressure loss performance of the convergent matrix geometry with 6 entry channels evaluated in design and off-design points of a real case	290

Nomenclature

Acronyms

<i>AR</i>	Aspect Ratio of a cooling channel
<i>BC</i>	Boundary Condition
<i>DS</i>	Directional Solidification
<i>DX</i>	Right rows of matrix models
<i>FEM</i>	Finite Element Method
<i>HTC</i>	Heat Transfer Coefficient
<i>IR</i>	Infrared Thermography
<i>INF</i>	Lower matrix module
<i>LDA</i>	Laser Doppler Anemometry
<i>LCF</i>	Low Cycle Fatigue
<i>PIV</i>	Particle Image Velocimetry
<i>PMMA</i>	PolyMethyl Methacrylate
<i>PS</i>	Pressure Side
<i>SC</i>	Single Crystal
<i>SF</i>	Scale Factor
<i>SS</i>	Suction Side
<i>SX</i>	Left rows of matrix models
<i>SAS</i>	Secondary Air System
<i>SUP</i>	Upper matrix module
<i>TBC</i>	Thermal Barrier Coating
<i>TIT</i>	Turbine Inlet Temperature
<i>TLC</i>	Thermochromic Liquid Crystals

<i>TPF</i>	Thermal Performance Factor
<i>TSP</i>	Temperature Sensitive Paints

Greeks

α	Converging angle of a matrix module	[deg]
α_s	Thermal diffusivity	[$m^2 s^{-1}$]
β	Heat load parameter	[–]
β	Sub-channel inclination angle	[deg]
β_{TS}	Total to static pressure ratio	[–]
γ	Heat capacity ratio	[–]
ε_f	Fin effectiveness	[–]
φ	Cooling effectiveness	[–]
η	Rib efficiency	[–]
μ	Dynamic viscosity	[Pa s]
ρ	Density	[$kg m^{-3}$]
τ	Dimensionless measurement time	[–]
ω	Rotational speed	[$rad s^{-1}$]

Letters

<i>A</i>	Cross-sectional area	[mm^2]
<i>A_b</i>	Base area of single matrix block	[mm^2]
<i>A_c</i>	Cross-sectional area of a rib/fin	[mm^2]
<i>A_{can}</i>	Cross-sectional area of a single sub-channel	[mm^2]
<i>A_{lat}</i>	Lateral contact area between adjacent matrix elements	[mm^2]
<i>Bi</i>	Biot number	[–]
<i>c_p</i>	Specific heat	[$J kg^{-1} K^{-1}$]
<i>d</i>	Hydraulic diameter	[mm]
<i>d_{h,s}</i>	Hydraulic diameter of the matrix sub-channel	[mm]
<i>D_h</i>	Hydraulic diameter of the whole matrix cross section	[mm]

f	Friction factor	$[-]$
f_0	Friction factor in a smooth duct	$[-]$
f_s	Friction factor based on the sub-channel hydraulic diameter	$[-]$
f_x	Friction factor at the local axial coordinate (Nagoga correlation)	$[-]$
h	Local heat transfer coefficient	$[W\ m^{-2}\ K^{-1}]$
h_b	Thickness of the matrix module without ribs	$[mm]$
h_{rib}	Rib height in a matrix module	$[mm]$
h_{TC}	Distance base of matrix block-thermocouple hole	$[mm]$
htc_{eqT}	Equivalent heat transfer coefficient	$[W\ m^{-2}\ K^{-1}]$
htc_{eqB}	Equivalent heat transfer coefficient in Biot number similitude with real application	$[W\ m^{-2}\ K^{-1}]$
htc_r	Effective heat transfer coefficient between fluid and rib surface	$[W\ m^{-2}\ K^{-1}]$
H	Overall cross section height of a matrix model	$[mm]$
HTC_{aveeq}	Equivalent heat transfer coefficient evaluated in the real case	$[W\ m^{-2}\ K^{-1}]$
I	Electrical current	$[A]$
k	Thermal conductivity	$[W\ m^{-1}\ K^{-1}]$
l	Development length between matrix turning regions	$[mm]$
L	Matrix module length	$[mm]$
L_c	Development length between matrix turning regions	$[mm]$
L_{rib}	Overall length of rib for each matrix block	$[mm]$
L_{tot}	Overall length of a sub-channel in a matrix module	$[mm]$

m	Fin parameter $(htc_r \cdot A_c / k_{met} \cdot P)^{0.5}$	[-]
\dot{m}	Mass flow rate	[kg s ⁻¹]
\dot{m}_{rid}	Non dimensional mass flow rate	[-]
M	Mach number	[-]
n_{can}	Number of sub-channels in a matrix module	[-]
Nu	Nusselt number	[-]
Nu_0	Nusselt number in a smooth duct	[-]
Nu_{eqB}	Nusselt number evaluated from htc_{eqB} values	[-]
Nu_{eqT}	Nusselt number evaluated from htc_{eqT} values	[-]
Nu_r	Nusselt number evaluated from htc_r values	[-]
Nu_d	Nusselt number based on the sub-channel hydraulic diameter (Nagoga correlation)	[-]
Nu_l	Nusselt number averaged on the length of the matrix sub-channel (Nagoga correlation)	[-]
Nu_x	Nusselt number at the local axial coordinate (Nagoga correlation)	[-]
Nu_s	Nusselt number based on the sub-channel hydraulic diameter	[-]
Nu_{st}	Nusselt number evaluated in static conditions	[-]
Nu_{stat}	Nusselt number evaluated in static conditions	[-]
Nu_L	Nusselt number evaluated for a flat plate	[-]
p	Pressure	[Pa]
p	Rib pitch	[mm]
P	Perimeter	[mm]

P_{el}	Heater power	[W]
Pr	Prandtl number	[-]
q	Heat flux	[W m ⁻²]
q_{conv}	Convective heat flux	[W m ⁻²]
q_f	Heat flux transferred from the base of the fin/rib	[W m ⁻²]
q_{max}	Maximum heat flux transferred from the base of the fin/rib	[W m ⁻²]
q_{net}	Net heat flux	[W m ⁻²]
Q_{cond}	Heat transferred by conduction	[W]
Q_{input}	Power supplied by etched foil heaters	[W]
Q_{loss}	Heat loss	[W]
Q_{net}	Net heat	[W]
r	Radial position of the pressure tap	[mm]
R	Electrical resistance	[ohm]
R	Radius of surface curvature	[mm]
R_{vp}	Open area ratio	[-]
Re	Reynolds number	[-]
Re_s	Reynolds number based on the sub-channel hydraulic diameter	[-]
Re_d	Reynolds number based on the sub-channel hydraulic diameter (Nagoga correlation)	[-]
Re_l	Reynolds number based on the length of the matrix sub-channel (Nagoga correlation)	[-]
Re_x	Reynolds number at the local axial coordinate (Nagoga correlation)	[-]
Re_L	Reynolds number based on the length of a flat plate	[-]
Ro	Rotation number	[-]

Ro_s	Rotation number based on the sub-channel hydraulic diameter	$[-]$
Sh	Sherwood number	$[-]$
Sh_0	Sherwood number in a smooth duct	$[-]$
s	Thickness	$[mm]$
t	Time	$[s]$
t_{rib}	Rib thickness	$[mm]$
T	Temperature	$[K]$
U	Air velocity	$[ms^{-1}]$
U_{eq}	Overall heat transfer coefficient	$[W m^{-2} K^{-1}]$
v	Air velocity in a matrix sub-channel	$[m s^{-1}]$
v_{rel}	Bulk velocity of the flow in a sub-channel	$[m s^{-1}]$
V	Air velocity	$[m s^{-1}]$
W	Overall cross section width of a matrix model	$[mm]$
W_b	Width of a single matrix block	$[mm]$
W_c	Width of a sub-channel	$[mm]$
W_i	Width of a sub-channel at the inlet	$[mm]$
Z/d	Jet-to-target surface distance	$[-]$
x/D	Axial coordinate along a cooling channel	$[-]$
x/D	Pin fin array spacing	$[-]$
x/L	Streamwise distance from the inlet section	$[-]$
W/H	Aspect Ratio of internal cooling channels	$[-]$

Subscripts

amb	Room or ambient conditions
air	Air conditions
ave	Average section
aw	Adiabatic wall

<i>b</i>	Bulk temperature
<i>b</i>	Base of matrix blocks
<i>c</i>	Coolant
<i>cool</i>	Coolant supply conditions
<i>corr</i>	Correlation data
<i>can</i>	Matrix sub-channel
<i>exp</i>	Experimental data
<i>ext</i>	External
<i>f</i>	Coolant or fluid
<i>g</i>	Gas
<i>i</i>	<i>i</i> – <i>th</i> block
<i>i</i>	Initial
<i>in</i>	Inlet section
<i>in</i>	Inlet conditions
<i>inf</i>	Lower
<i>init</i>	Initial time
<i>inlet</i>	Inlet conditions
<i>is</i>	Insulator
<i>lat</i>	Lateral
<i>loss</i>	Heat losses
<i>m</i>	Metal
<i>met</i>	Metal
<i>mb</i>	Mixed bulk temperature
<i>mod</i>	Single matrix module
<i>out</i>	Outlet section
<i>out</i>	Outlet conditions
<i>outlet</i>	Outlet conditions
<i>ref</i>	Reference
<i>sup</i>	Upper
<i>tot</i>	Total or stagnation values
<i>w</i>	Wall
<i>wall</i>	Wall

Chapter 1

Introduction

1.1 Evolution of the Gas Turbine

The first patent for a basic gas turbine was given to John Barber (United Kingdom - UK) in 1791 (figure 1.1). In this turbine gas was produced from heated coal, mixed with air, compressed and then burnt; this produced a high speed jet that impinged on radial blades on a turbine wheel rim. Barber's invention included practically all main components of a modern gas turbine: a compressor, a combustion chamber and a turbine [1].

In the next years other ideas abounded but all these attempts were not able to produce a working hardware. For example in 1872 Franze Stolze designed the first true gas turbine where a multi-stage axial compressor was driven by a multi-stage axial turbine; this engine also included a regenerator utilizing exhaust gases to heat the compressor discharge air but unfortunately this engine never ran successfully [1].

At the beginning of the 20th century the previous ideas were finally transformed into working engines. In 1899 Charles Gordon Curtis patented the first gas turbine engine in the USA and some years later this became an efficient machine commercially available. Slowly, year by year, the development and the performance of gas turbines for stationary applications increased especially due to the installation of heat exchangers and

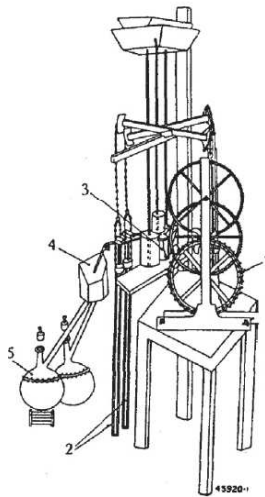


Figure 1.1: Drawing of first patent for a gas turbine (John Barber, 1791)

water or steam injection systems. These systems also allowed to reduce the temperature of hot gases to a limit allowable by materials of which main critical components were made (combustors, blades, nozzles...). In 1905 Brown Boveri built the first gas turbine for a refinery of the Sun Oil Company near Philadelphia (USA) and in 1939 realized the first gas turbine in simple cycle for a power station in Neuchatel (Switzerland) (figure 1.2). This unit provided a power output of 4MW and an efficiency of 17.4% at 3000rpm. As it is shown in figure 1.3 this consisted of an axial flow compressor, a single combustion chamber and a multi-stage reaction turbine; the excess air was used to cool the exterior of combustor and to heat the air at the inlet of turbine.

At the same time the development of gas turbine for aircraft propulsion was obstructed by some relevant factors: very high values of weight-to-power ratio and fuel consumption. These difficulties were finally overcome by Sir Frank Whittle, who designed and patented the first turbo

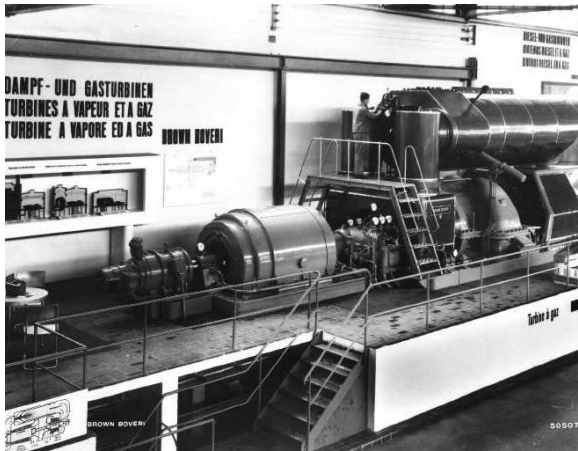


Figure 1.2: The world's first industrial gas turbine-generator realized by Brown Boveri and installed in Neuchatel, Switzerland (1939) [1]

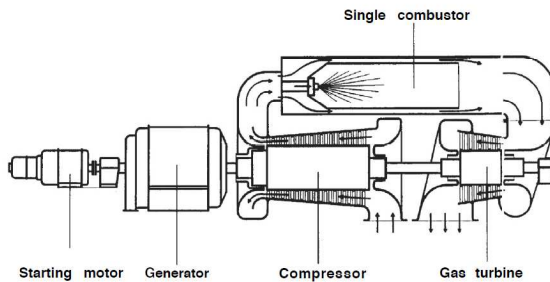


Figure 1.3: Layout of gas turbine-generator realized by Brown Boveri and installed in Neuchatel, Switzerland (1939)

jet engine in 1930. After some technical improvements the Whittle's engine, also designated as Whittle Unit (WU), was successfully tested in 1937. This engine consisted of a double entry centrifugal compressor and a single stage axial turbine (figure 1.4).

As Frank Whittle was working in Great Britain, the German engineers Hans von Ohain and Max Hann developed their own turbojet engine (Heinkel HeS 3B), which flew for the first time in the August of 1939 for the aircraft company Ernst Heinkel (figure 1.5).

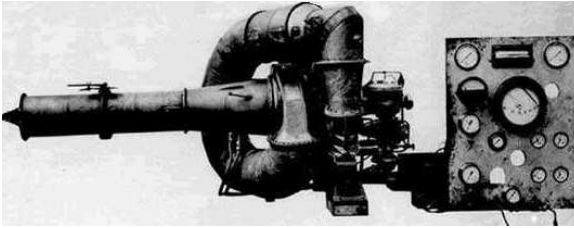


Figure 1.4: The first turbojet engine designed by Frank Whittle Unit (1930)

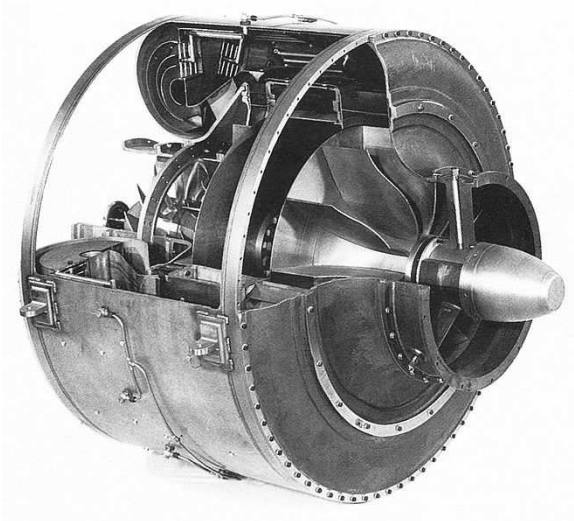


Figure 1.5: The turbojet Heinkel HeS 3B designed by Hans von Ohain and Max Hann (1939)

During the years of the Second World War the development in the design of gas turbines led to several changes among the main components (radial and axial turbines, combustion chambers and axial compressors); for this reason turbojet became the most popular engine of powering air-planes. In the next years various technical improvements obtained in the aircraft propulsion were transferred to the stationary gas turbine applications. For example in 1959 the world's first aeroderivative industrial gas turbine was installed in a compressor drive application at Clementsville (USA) [1].

Since the 1960s the gas turbine has made a progressive evolution in an increasing variety of applications: aircraft propulsion, land-based power generation and industrial applications. Throughout the following years the development of gas turbines has been related to three main factors:

1. metallurgical advances led to an increase of temperatures in the combustor and turbine components
2. cumulative knowledge of aerodynamic and thermodynamic
3. development of numerical tools and software for the design and simulation of turbine airfoils, combustors and blade cooling configurations

The synergy of these factors has led to the following improvements:

1. compressor design: increase of pressure ratio
2. combustor design: installation of regenerators and reduction of NO_x emissions
3. turbine design: employment of single crystal superalloys and development of cooling systems

In these last decades the progressive growth of gas turbines performance, especially thermal efficiency and power output, has led to a growing trend of the overall pressure ratio of the thermodynamic cycle and, consequently, a progressive upward trend of the gas temperature value

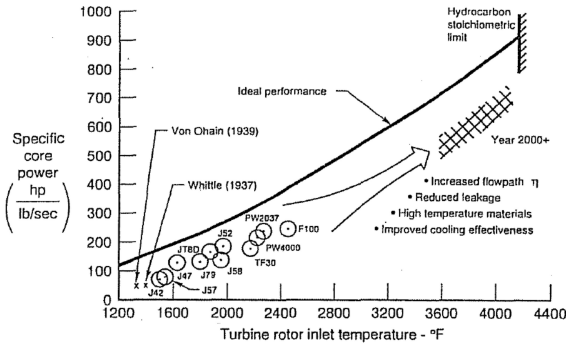


Figure 1.6: Improvement of power output with the increasing of turbine inlet temperature (TIT) [2]

entering the turbine, well known as turbine rotor inlet temperature (TIT). This is well illustrated in Figure 1.6, where the specific power output is plotted as a function of TIT; it is clearly depicted that real engines tend to approach the ideal performance line, which represents a cycle power output with 100% gas turbine efficiency with no leakage or cooling flows.

For this reason gas turbine blades and vanes of advanced gas turbines are required to withstand high temperatures in a hot, corrosive and unsteady environment. Since these operating temperatures are far higher than the melting point of materials, these components need to be cooled in order to guarantee a safe and reliable operation of the engine. Blades and vanes are cooled by specific amounts of air extracted from different axial locations (i.e. different pressure levels) of the compressor; then a complex feeding system, also known as Secondary Air System (SAS) provides to distribute this cooling air inside the most critical parts of turbine such as blades and vanes. A schematic view of typical cooling and sealing airflows circulating through the Secondary Air System is given in Figure 1.7.

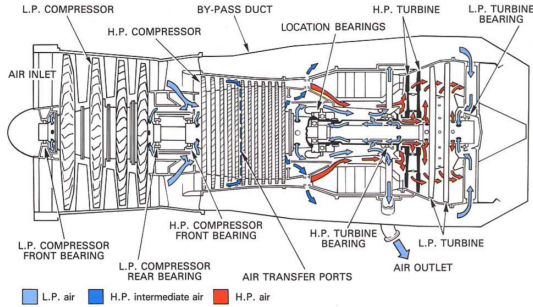


Figure 1.7: Schematic view of typical cooling and sealing airflows in a gas turbine [3]

Once the cooling air has reached turbine vanes and blades, it flows through internal passages within these components and realize an internal cooling; in some cases the internal coolant air is ejected out through discrete holes or slots and provide a coolant film to protect the outside surface from hot gases (Figure 1.8). In this latter case an external cooling of the components is obtained; this is more properly known in literature as film cooling.

Over the years several arrangements of internal and external cooling systems have been employed to ensure that the maximum surface temperatures and temperature gradients during operation are compatible with the maximum thermal stress in order to obtain the maximum lifetime of the engine [2]. Figure 1.9 depicts the increasing of TIT with the development of cooling technologies over the recent years; moving from the simple cooling configurations of the past (i.e smooth radial ducts) to the modern sophisticated combinations of impingement with turbulated serpentes and film cooling, TIT is raised from 1500 K to 2000 K .

In the cooling technology area the fundamental aim is to obtain the

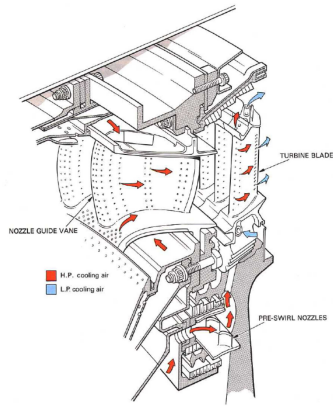


Figure 1.8: Example of a nozzle guide vane and turbine blade cooling arrangement [3]

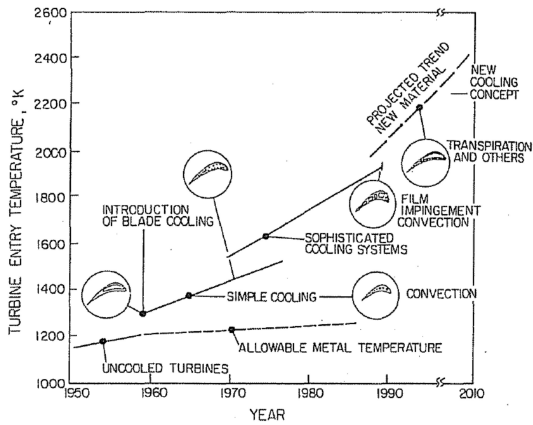


Figure 1.9: Trend of turbine inlet temperature (TIT) over recent years [2]

highest overall cooling effectiveness with the lowest possible penalty on the thermodynamic cycle performance. Figure 1.10 gives an overview about the gross *cooling effectiveness* with the increasing of *heat load parameter* for the different cooling technologies developed over the years. These are two of the most important parameters to evaluate cooling performance of turbine airfoils. The first is the *cooling effectiveness* φ and is defined as a dimensionless temperature ratio of gas-to-metal temperature difference over the gas-to-coolant temperature difference:

$$\varphi = \frac{T_g - T_m}{T_g - T_c} \quad (1.1)$$

where T_g , T_m and T_c represent the temperature of inlet hot gases, blade metal surface and inlet coolant respectively. To understand the meaning of this parameter two extreme cases should be considered: the first $\varphi = 0$ means that there is no cooling effect, the second $\varphi = 1$ indicates that the metal surface and coolant have the same temperature. In general φ lies within these two limits.

The other parameter is the so-called *heat load parameter* and is defined as the ratio of internal heat to the external heat fluxes as follows:

$$\beta = \frac{W_c \cdot C_p}{U \cdot A_g} \quad (1.2)$$

Figure 1.10 shows the *cooling effectiveness* as a function of the *heat load parameter* for typical cooling configurations. It should be noted that the *cooling effectiveness* is a function of coolant configuration, coolant ejection requirements and it is also a strong function of the amount of coolant used that is usually measured as percentage of the mainstream gas. For example, as regards the state-of-the-art engines, turbine cooling air and leakage may be as high as 25 – 30% of engine mainstream flow; in terms of efficiency a very approximate rule-of-thumb of 1% cooling air may represent a loss of fraction of that percentage in specific fuel consumption. This leads to the obvious conclusion that turbine cooling needs to be minimized. Clearly, this is not the only loss mechanism in the engine. Other losses may include mixing and aerodynamic losses, such

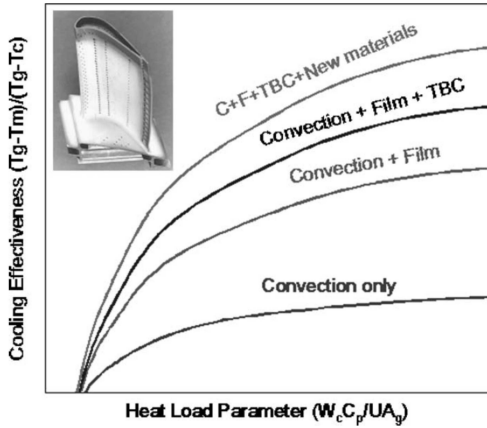


Figure 1.10: Cooling effectiveness as a function of the heat load parameter for different cooling technologies [5]

as profile drag, skin-friction, gas diffusion, secondary flows, tip clearance, boundary-layer separation, shocks, losses due to off-design airfoil incidence angles, trailing edge vortex shedding, and blockage losses [4].

Figure 1.10 also shows that for small amounts of coolant the *cooling effectiveness* increases rapidly, while for higher quantities (higher values of heat load parameter) φ rises with a lower rate. This means that, when large amounts of coolant are required in case of higher thermal loads, an increase of coolant consumption does not allow to reach higher effectiveness. For this reason, since cooling air is directly drawn from the compressor, it is necessary to minimize this quantity with the aim of avoiding excessive losses of efficiency. However, as well represented in the same Figure 1.10, one way of raising the *cooling effectiveness* without increasing coolant consumption is the employment of more complex and hence more efficient cooling arrangements such as multipass serpentine or impingement systems combined with film cooling.

In these last years further improvements of TIT have been obtained by means of the development of new materials and modern manufacturing

techniques such as directionally-solidification castings and single-crystal castings. In addition to this, the development of thermal barrier coatings (TBC) has brought other important advantages such as: a better insulation of the airfoil surface from hot gases, a stronger protection of the base airfoil material from corrosion and oxidation attack and the capability of damping thermal gradients during transient events. Moreover the addition of these coatings onto single-crystal nickel based superalloys has allowed to further increase TIT of about 100-150 K and hence the gas turbine efficiency [2].

Further improvements in cooling performance could result from the optimization of existing cooling schemes, from the compounding effects of more conventional systems and from the development of alternative or innovative systems (i.e. dimple and matrix cooling).

Even the manufacturing process of gas turbine airfoils has determined an important contribution to the development of gas turbines performance. In fact as the turbine blades have assumed more complex internal geometries it has become more important to improve the precision of the casting process.

This process is also known as “lost wax process”; the different stages of this process can be summarized as follows.

First of all, the ceramic cores for the cooling channels are positioned within a master mould pattern. Then, the wax is injected into the mould cavity to produce a preform of the turbine blade.

Some pinning wires are then pressed through the wax to butt against the ceramic cores within the preform.

In a next step, the preform is coated with multiple layers of ceramic, ultimately forming a thick casing around the preform with the pinning wires embedded in it. Finally, the assembly is heated to melt out the wax and then fired to strengthen the ceramic. The result is a ceramic shell mould containing a complex ceramic core pattern which is held in position by pinning wires anchored in the ceramic shell (Figure 1.11).

In addition to this, the manufacturing process requires the nucleation and growth of precisely controlled microstructures. The grain structure

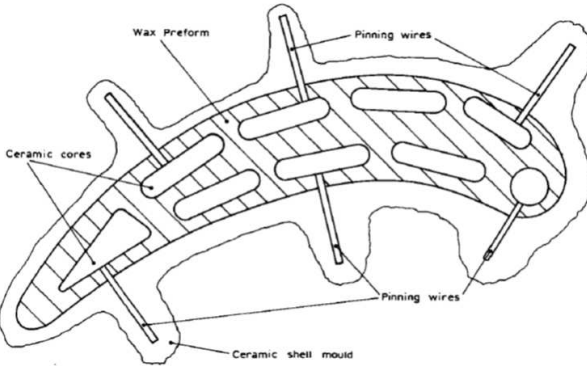


Figure 1.11: Schematic of a cross-section through a prepared mould showing the pinned ceramic cores within the wax preform and the ceramic shell mould

within the turbine-blade superalloy material is frequently described by terms such as: “equi-axed”, “directionally solidified” (DS) and “single crystal” (SC). These characterize the grain boundary length and thus affect the performance of the turbine blades.

“Equi-axed” blades contain many small grains of similar size without any preferential orientation. These types of blades are widely used in the cooler parts of an engine. However “equi-axed” castings have many grain boundaries surrounding the crystals of the superalloy forming failure initiation points in fatigue, creep and oxidation.

On the other hand the “directionally solidified” blades offer significant advantages in terms of mechanical performance over “equi-axed” blades because of their preferred crystallographic orientation of the grains and

the absence of transverse grain boundaries. This solidification process eliminates the weaker grain boundaries in the tensile direction providing an improved resistance to thermal fatigue and creep. Such blades are used in the hottest parts of the engine where service conditions are the most arduous.

A further evolution is given by the “single crystal” casting process that completely eliminates all weaker grain boundaries and provides further improvements in resistance to creep, fatigue and oxidation. This technology also guarantees the possibility to cast a complete turbine airfoil, dovetail and platform in a single superalloy crystal.

In addition to this the introduction of directional solidification (DS) and single crystal (SC) castings has led to higher metal temperature capability; in fact these techniques produced a breakthrough providing a 200 °F increase in metal temperature capability over conventional multigrain equi-axed cast materials.

1.2 Objectives of Present Research

As already discussed in the previous section, the design of more efficient cooling systems is necessary to improve the overall performance of the turbine. Moreover an accurate design followed by a correct prediction of local heat transfer coefficient and local airfoil metal temperature distributions is extremely important in order to avoid local hot spots and hence premature failures of the components. In fact it is widely accepted that the life of a turbine blade can be reduced by half if the temperature prediction of the metal blade is off by only 30°C[2].

Therefore designers have to take into account all these aspects with the aim of maintaining acceptable lifetime and reliability requirements during the operation of the engine under such extreme heat load conditions. In addition to this it must be considered that some parts of the airfoil are more critical than others because of the higher thermal loads and the mechanical strength requirements. The airfoil leading and trailing edge regions represent two critical parts even if the trailing edge may be more

sensitive to premature failures because of the very small cross section and thickness. The blade cooling design of this part has to fulfill many requirements at the same time: in fact the profile thickness must be thin to reduce weight and improve airfoil aerodynamic efficiency, but it must also ensure a high structural rigidity and a high heat transfer enhancement.

In this context industrial companies or gas turbine manufacturers have developed a great interest on the design and optimization of blade cooling systems with the following aims:

- improving cooling performance of current cooling systems
- replacing current schemes with innovative solutions

Both aims are addressed to obtain the best tradeoff between the enhancement of cooling performance and the extension of reliability and lifetime ranges of the components.

The project reported in this thesis is part of a collaboration between the Department of Industrial Engineering of the University of Florence and GE Oil & Gas and has the fundamental aim of developing innovative cooling solutions for both nozzles and blades of current and future gas turbines. Several objectives are related to this work such as:

- Increase gas turbine performance by means of: reduction of coolant need and reduction of bleed air from the compressor
- Increase life of components by means of: increased mechanical strength due to a different architecture of the inner cooling geometry and reduction of thermal stresses due to a more uniform internal cooling
- Reduction of costs: for example an innovative convective scheme with a higher cooling effectiveness could lead to remove other expensive solutions from the airfoil (i.e. film cooling or TBC). A further reduction of costs also derives from an improved manufacturing process aimed to the realization of the complex internal structures within the airfoils.

Based on these considerations the present research has been addressed to investigate the cooling performance of latticework-matrix cooling systems. In fact the available information reported in the technical literature describe matrix structures as a very good alternative to current conventional cooling solutions such as pin fins and multipass serpentine with turbulators. Compared to these conventional technologies, lattice-matrix systems would provide a higher heat transfer enhancement with similar pressure losses and a greater robustness of the ceramic core for the investment casting. However, it must be said that, in addition to the conventional manufacturing process (e.g. investment casting), the innovative additive manufacturing technologies may be advantageous for the realization of such complex matrix cooling geometries.

Moreover, in addition to the higher heat transfer performance, a lattice-matrix structure give promising results when applied to the trailing edges because of its higher mechanical strength and higher uniformity of cooling [6]. According to practical tests a matrix structure would also increase the blade life in high pressure turbines which is 3 to 4 times more than the ability of pin fin configurations at the trailing edge [7].

For these motivations the present work aims at deepening the knowledge of matrix cooling systems by means of three experimental campaigns focused on the measurement of heat transfer and friction performance under representative operating conditions as close as possible to that of a real application.

The first experimental campaign has been addressed to understand the effects of the main geometric parameters on the heat transfer and friction performance such as: rib height, rib thickness and number of sub-channels. In this part of the work several static tests have been performed on four different matrix geometries under conditions of Reynolds and Biot number similitude with a real case. These geometries have a constant cross section from the inlet to the outlet and are characterized by two rib heights that are representative of extreme cases: two are suitable for an application in the mid-chord region and two have the same dimensions of the minimum cross section available at the trailing edge region. For

each of these two rib heights two different configurations with extreme different passage areas have been studied: one having four entry channels and a lower rib thickness and one having six entry channels with a higher rib thickness.

The second experimental campaign has been focused on two convergent geometries that result from the combination of the previous test articles with constant cross section and reproduce realistic trailing edges. The objective of this campaign is to illustrate the effects of the flow area variation along the streamwise direction.

In the third and last campaign the same convergent geometries have been tested under rotation conditions reproducing the Rotation number similitude of a real blade. The objective of these experiments is to find the possible effects of Coriolis and centrifugal forces even in case of a different channel orientation with respect to the rotating plane. For this reason the inclination of the matrix model was varied from 0deg to 30deg in order to reproduce the exit angle of a real gas turbine blade.

Results obtained from the above mentioned experimental campaigns on both constant and convergent geometries have been post-processed in a proper way with the aim of developing heat transfer and friction correlations. These correlations allow to establish a relationship between the desired performance parameters (i.e. Nusselt number or friction factor) with the main geometric parameters of a matrix system and the Reynolds number for each streamwise position. The development of these correlations has been performed in view of a future implementation within an in-house developed procedure to predict cooling performance and metal temperatures of gas turbine blades and nozzles.

1.3 Thesis outline

The present thesis is structured as follows:

Chapter 1 has presented the evolution of gas turbines focusing on the technological problems related to the increasing trend of gas temperatures entering the turbine. In addition to this the objectives of the present work are reported.

Chapter 2 reports a literary overview about the main internal cooling systems for both vanes and blades of gas turbines with a particular attention to the cooling of the trailing edge region. In the second part this chapter presents a full description of matrix cooling systems together with a complete review of the experimental works found in literature.

Chapter 3 focuses on the description of the main experimental approaches to measure the local heat transfer coefficient distributions on geometries for internal blade cooling applications. Moreover it provides the motivations that have driven to the choice of the experimental approach adopted for the evaluation of the heat transfer coefficient distributions in the present experiments.

Chapter 4 provides the description of the test rig layouts, matrix test models and measurement devices adopted for the experimental campaigns in static and rotating conditions. A part of this chapter is also dedicated to the description of the data reduction procedure developed for the evaluation of the heat transfer coefficients.

Chapter 5 reports the experimental results of the investigated matrix geometries in terms of friction factors, pressure losses and total to static pressure ratios as a function of Reynolds number and non dimensional mass flow rate for both static and rotating tests.

Chapter 6 includes all the experimental results about the heat transfer performance of all the investigated matrix geometries. The results are reported as distributions of the average heat transfer coefficients and average Nusselt numbers as a function of both streamwise position and Reynolds number. As regards rotating tests, the distributions also show the effect of Rotation number with the varying of flow condition and streamwise position for both pressure and suction side of the test models.

The last part of this chapter reports a summary and a comparison between the investigated geometries not only in terms of the heat transfer performance but also considering the behaviour in terms of friction factor and pressure losses; for this reason the comparison is made evaluating the Thermal Performance Factor over the investigated Reynolds range. Comparisons have been also performed between the experimental data and literary works.

Chapter 7 is dedicated to the presentation of the heat transfer and friction correlations. These correlations express a relationship between the average Nusselt number and friction factor with Reynolds number and some specific dimensionless geometric parameters.

This chapter also reports the application of these correlations to a real case and the comparison between the performance obtained applying a matrix structure and those for the current cooling solution of the considered real blade.

Chapter 2

Overview of Gas Turbine Cooling Systems

As mentioned in section 1.2 the theme of the present work is an internal cooling system for gas turbine airfoils, that could represent a promising alternative solution to current conventional schemes: the matrix cooling. Before starting to describe the main features of this cooling technology together with the main results found in the technical literature, it is necessary to give an overview about the state-of-the-art of current internal cooling systems for both vanes and blades of gas turbines.

To better understand how the adoption of a matrix cooling geometry could be advantageous compared to traditional solutions, this chapter has been divided in two main parts: section 2.1 reports an overview about the main current cooling solutions, while all the details about latticework-matrix cooling systems will be presented in section 2.2.

2.1 Internal Cooling Systems

Over the years the main gas turbine manufacturers have invested many resources in the technological research with the aim of optimizing the design of internal cooling systems within gas turbine airfoils. Their

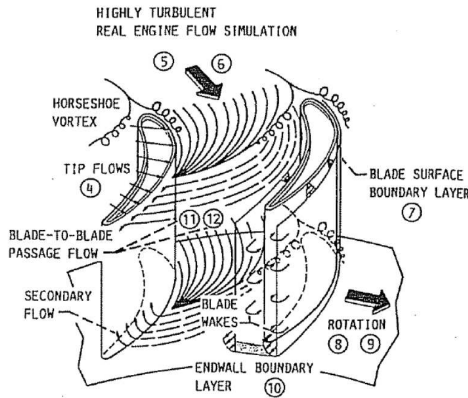


Figure 2.1: Complex flow phenomena in a turbine rotor hot-gas passage (Gladden and Simoneau, 1988; collected in Sokolowski, 1988) [2]

programs of research and development have been focused to accurately predict the heat transfer coefficient and metal temperature distributions under turbomachinery flow conditions. In fact an accurate prediction of these distributions around the airfoils allows to use the correct amounts of cooling air avoiding to penalize the cycle performance in terms of power and specific fuel consumption.

To reach this target, it is necessary to carry out several numerical simulations and experimental investigations because of the high complexity of the flow field over the airfoils; in fact, as depicted in Figure 2.1, several flow phenomena can occur around an airfoil such as secondary flows, tip flows, wakes and rotation flows.

Moreover, as depicted in Figure 2.2, the hot gases generate a not uniform heat flux distribution around vanes or nozzles and rotor blades.

Usually at the leading edge of the vane the heat transfer coefficients are very high and, as the flow splits and travels along the vane, the heat flux decreases. Along the suction side the flow experiences a transition from laminar to turbulent and the heat transfer coefficients increase. On the

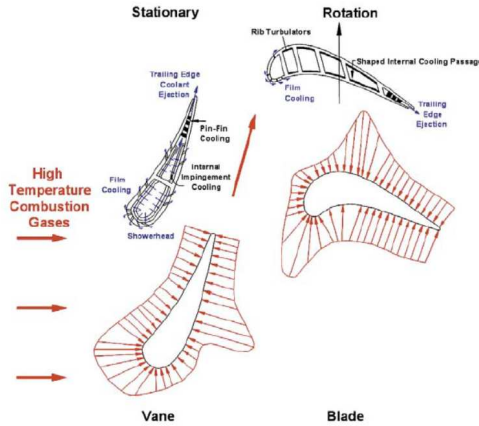


Figure 2.2: Heat flux distribution around an inlet guide vane and a rotor blade

pressure surface heat flux distribution may be more uniform; the flow accelerates along the pressure surface and the heat transfer coefficients also increase.

The trends are similar for the turbine rotor blade: the heat flux at the leading edge is very high and decreases along the profile. Even in this case on the suction surface there is the flow transition from laminar to turbulent, and the heat flux sharply increases; on the pressure surface the heat transfer increases as the flow accelerates around the blade.

Other factors affect the heat transfer distributions of the hot gas path around the vanes such as: non uniform temperature inlet profile, combustor-generated high turbulence, film cooling flows, platform secondary flows and surface roughness. As regards rotating blades additional factors to be considered are: rotational force, centrifugal force, blade tip clearance and leakages.

Designers must take into account all these aspects in order to accurately identify the position of the potential hot spots on the airfoil surface. For

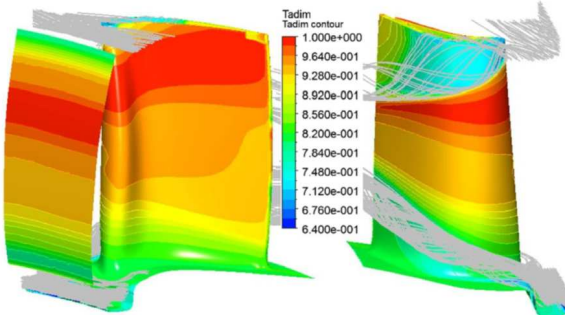


Figure 2.3: Effect of temperature inlet profile on dimensionless adiabatic wall temperature distribution (Bonini [8])

these reasons gas turbine airfoils usually employ a combination of external and internal cooling arrangements. The external cooling configurations (i.e. film cooling) are based on the ejection of coolant through holes in the airfoil body that results in a protective layer between the outside surface and the hot gas path flow. On the other hand in the internal cooling configurations the coolant flows through internal passages that are usually turbulated in order to enhance the heat transfer by increasing both heat transfer surface area and flow turbulence. Starting from the previous considerations it is obvious that different external and internal cooling solutions must be used depending on specific region of the airfoil and therefore of the corresponding thermal load and mechanical strength requirements.

To have an idea about the effects of the complex flow field, especially due to secondary flows, on the temperature distributions around an airfoil, Figure 2.3 reports the contours of the normalized adiabatic wall temperature distributions. These distributions are determined by the

non uniform temperature inlet profile that is affected by the various secondary flows. It is clear that the temperature variation from the hub to the tip of the blade is very high and the distribution on the pressure side is different from that on the suction side. For example, on the pressure side a hot streak is pushed towards the upper half of the passage, thus producing a significant adiabatic wall temperature gradient in the radial direction. The situation is very different at the suction side, where a significant reduction of temperature occurs at the hub and tip of the profile, thus delimiting the hot region at the midspan of the blade.

Since the cooling arrangements applied on a stator vane may be different from those suitable for a rotor blade (e.g. Figure 2.2), in the following sections the attention is focused first on the internal cooling solutions for stator vanes (Section 2.1.1) and then on the typical arrangements for rotor blades (Section 2.1.2).

2.1.1 Internal Cooling of Gas Turbine Vanes

As shown in Figure 2.4 different internal cooling solutions may be applied within a typical stator vane of gas turbine. At the leading edge and mid-chord regions a system of jet impingement is applied; since this arrangement weakens the structural strength of the airfoil it is most suitable for the leading edge of both stator and rotor airfoils where the thermal load is highest and where there is a thicker cross section. Since the structural strength required in a stator vane is less than that required in a rotor blade, the impingement cooling may be also used in the mid-chord region of stator airfoils. However this technique is not suitable for an application in the narrow trailing edge.

The middle portion of the airfoil is usually cooled by means of multipass serpentes with rib-roughened coolant passages, while the vane trailing edges are usually cooled using arrays of short cylinders well known as pin fins. After impinging on the walls of the airfoil, the coolant exits the vane and provides a protective film on the outer surfaces. At the same time the coolant travelling through the pin-fin arrays is ejected from the trailing edge of the airfoil.

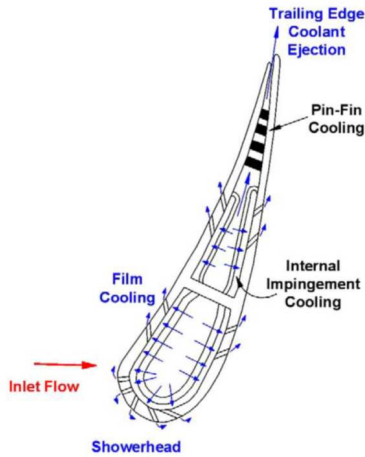


Figure 2.4: Schematic of a turbine vane cross-section with different cooling systems

In the following paragraphs a short description of the typical internal cooling systems within stator vanes is given.

2.1.1.1 Impingement cooling

Jet impingement cooling consists in a high velocity coolant mass flow ejected from a hole or slot and directed to the heat transfer target surface.

As mentioned above impingement cooling is usually applied at the leading edge of the airfoils and can also be used near the mid-chord of stator vanes (Figure 2.4).

In the design of an efficient impingement cooling scheme several aspects must be considered because of their influence on heat transfer coefficient distribution: effect of jet-hole size and distribution, cooling channel cross-section, and target surface shape. As regards this latter aspect the jet impingement near the mid-chord is very similar to impingement on a flat plate; while the sharp curvature at the leading edge of the vane must be

considered for the application of jet impingement at the leading edge. Considering a single round jet impingement (Figures 2.5) the typical flow field can be divided into three characteristic regions: free jet region, stagnation flow and the wall jet regions (Figure 2.5a). Before striking the target plate, the impingement jet acts as a free jet. The flow of a free jet is divided into the potential core zone, the developing zone and the fully developed zone (Figure 2.5b). When the jet exits from the impingement hole, the outer part of the jet starts to mix with the surrounding air; this process increases the jet diameter and the turbulence of the flow. The inner part of the jet, that is not involved in the mixing, is called potential core. As the distance between jet and hole increases the interaction between jet and surrounding air increases and finally the potential core vanishes (typically at 6-7 jet diameters from the nozzle. Then, in the developing zone, the axial velocity profile changes towards the fully developed profile that can be approximated by a Gaussian distribution (fully developed zone).

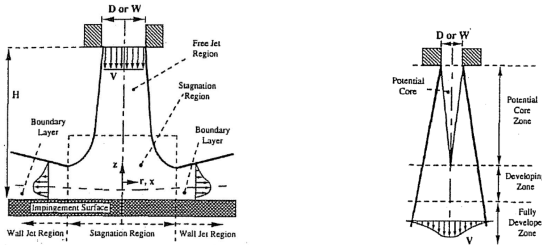
As regards the flow regions of an impinging jet (Figure 2.5a), in the free jet region the jet begins to broaden due to an intensive shear interaction with the surrounding air; this results in an entrainment of mass, momentum and energy.

The free jet region is followed by the stagnation region, which is located where the jet impinges on the target plate. It is surrounded by developing boundary layers. After impingement, the spent jet causes a highly turbulent flow which increases the heat transfer. In theory, no heat transfer can occur in the stagnation point as the velocity is zero, but in reality the stagnation point is very unstable and moves all the time, so the heat transfer coefficient in the stagnation region is very high due to the thin laminar boundary layer [7]. The heat transfer coefficient decreases with increased distance from the stagnation point. However, when the wall jet changes from laminar to turbulent flow, a second heat transfer peak can occur for certain Reynolds number and for certain jet-to-impingement target distances.

Finally in the wall jet region, the flow is parallel to the impingement

plate and is directed radially outwards. Its velocity profile is described in Figure 2.5a; the initially laminar boundary layer undergoes a turbulent transition that is induced by the impingement of large eddies created in the jet shear layer. This turbulent transition is believed to increase locally, and the heat transfer rate diminishes progressively.

For a single impingement jet the point of maximum heat transfer is typically the stagnation point, from which heat transfer rates decrease monotonically in radial directions. In absence of a cross-flow, the stagnation point coincides with the geometrical center of the jets. The heat transfer coefficient in the stagnation point increases with the jet Reynolds number. On the contrary, for low jet-to-target surface distances ($Z/d < 1$) or high jet Reynolds numbers, an offset between the maximum heat transfer and the center of the jet can occur.



(a) Flow regions in an impinging jet (b) Flow regions in a free jet

Figure 2.5: Comparison of flow regions in an impinging jet with flow regions of a free jet (Viskanta, 1993) [2]

In a gas turbine application multiple impingement jets are used instead of an isolated single jet, either as a row of jets or as arrays of jets. Many jets are useful to increase the heat transfer from the vane wall; however this complicates the flow structure and velocity profiles in multiple jets are difficult to obtain.

Moreover, as shown in Figure 2.6, in an array of multiple jets the upstream jet creates a cross flow, which flows perpendicular to the adjacent jet flow along the target plate. As the coolant travels along the test sur-

face, the spent air from the upstream jets could affect the heat transfer coefficient distributions of the downstream jets, and this effect increases as more spent air accumulates on the target surface.

For multiple jets Metzger et al. [9] proved that the Nusselt number is strongly dependent on the Reynolds number, while there is no significant dependence on the jet-to-target plate spacing. However, the most significant differences are due to the jet cross-flow from the spent jets. Studies by Florschuetz et al. [10] and Koopman et al. [11] showed that the mass from one jet moves in the cross-jet flow direction, and this flow can alter the performance of adjacent jets. In particular the cross-flow jet may deflect a jet away from its impinging location on the target plate; in case of a strong cross-flow and sufficiently large jet-to-target plate spacing Z/d , the cross-flow can completely deflect the jet away from the impingement surface and, as reported by Florschuetz et al. [12], this can lead to a strong decay of the overall heat transfer from the impingement surface. Starting from these experimental results correlations were developed by Kercher et al. [13] and Florschuetz et al. [14] to estimate the heat transfer enhancement from an array of impinging jets. All these correlations demonstrate the dependence of the heat transfer enhancement on the amount of cross-flow. Florschuetz et al. [14] also showed the cross-flow effect is much stronger in staggered arrays of jets than in inline arrays. Bailey et al. [15] extended the correlation developed by Florschuetz et al. to include the effect of jet spacing and hence dense impingement arrays. Later Ekkad et al. [16] studied the effect of the cross-flow traveling in two opposite directions together with the effect of coolant extraction for film cooling; results showed that the heat transfer enhancement on the target plate decreases near the edges due to the decreased coolant flow. Also the presence of initial cross-flow affects the heat transfer enhancement from the target plate. In fact the cross-flow described in the previous cases is created by the spent flow from the jets; therefore, the first row of jets is not affected by the cross-flow. However, in many situations the cross-flow may develop upstream of the first row and this flow can significantly alter the flow near the jets, and thus alter the heat transfer

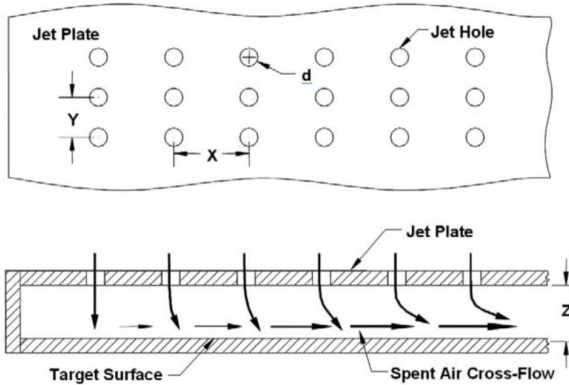


Figure 2.6: Typical test model for studies on multiple impingement jets

coefficients on the target surface. The results obtained by Florschuetz et al. [17] about the effect of initial cross-flow show that the heat transfer enhancement on the target plate decreases when initial cross-flow is present.

The above studies investigated the heat transfer on flat target plates. The results obtained for flat plates are representative of an impingement application near the mid-chord of the vane. However, the effect of target surface curvature must be considered when the designer has to apply jet impingement near the leading edge of the airfoil; in fact the curvature of the airfoil creates a different cross-flow behavior, and therefore, the heat transfer coefficients on the curved surface are different than those on the flat surface.

In the open literature the first studies were performed considering the jet impingement cooling over concave surfaces that are comparable to a leading edge cooling scheme. In 1969 Chupp et al. [18] studied the effects of a single row of impinging jets on a curved surface (Figure 2.7) and concluded that the average Nusselt number ratio increases as the curvature of the target plate increases. Interesting experimental results about the

effect of target surface shape were also given by Bunker et al. [19] and Metzger et al. [20] using the test rig in Figure 2.8. They performed detailed heat transfer measurements using temperature sensitive coatings, varying impingement jet holes spacing, jet-to-target spacing, leading edge radius of curvature and jet Reynolds number. Moreover they studied the effects of film cooling mass flow extraction on the leading edge target surface. They concluded that a sharper nose radius yields a more uniform Nusselt number distribution compared to a smooth-nosed chamber. They also found an increase of heat transfer coefficient with aligned jet holes and extraction holes arrangement, while staggered configurations led to a decrease of the HTC's. Finally, as regards the mass flow extraction for film cooling, they found that this does not affect the HTC distribution.

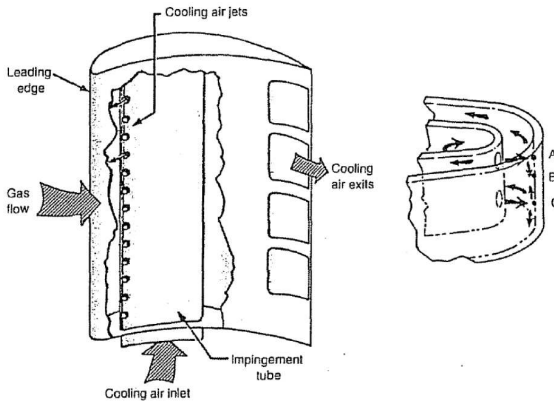


Figure 2.7: Schematic of the impingement cooling at the airfoil's leading edge (Chupp et al., 1969) [2]

Since 2001 Taslim et al. [21] performed experimental and numerical analyses on more complex leading edge cooling configurations including the effect of the mass flow extraction from film cooling holes. In recent years Maiuolo et al. [22] [23] investigated the effects of different geometries of impingement holes and the influence of both shower-head

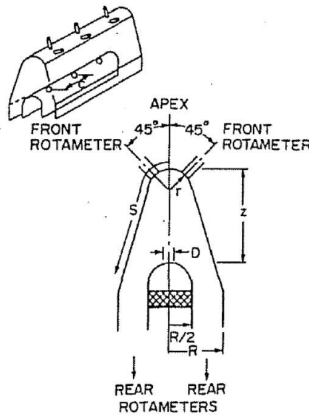


Figure 2.8: Leading edge impingement with film cooling extraction
(Metzger et al., 1990) [2]

and film cooling extraction on the heat transfer performance of more realistic leading edge cavities.

2.1.1.2 Pin-Fin Cooling

Pin fins are projections protruding from the heat transfer surface to the coolant flowpath. Generally they have a circular cross-section and are placed perpendicular to the flow direction to maximize the forced convected fin cooling. Flow around a pin is comparable to the flow around a single cylinder. As the coolant flows around the pin, the flow separates and a vortex shedding occurs downstream the pin; this increases the free-stream turbulence and alters the boundary layer development over the pin-mounted surface. The wakes from upstream pins also affect both the flow and heat transfer performance of downstream pins.

In addition to this wake formation, a horseshoe vortex forms just upstream of the pin; this creates an additional mixing and hence increases the heat transfer.

The heat transfer enhancement is also due to the fin effect and the in-

creased heat transfer surface area provided by the pins. In fact pins conduct thermal energy away from the heat-transfer surface; in case of long pins a high increase of the effective wet heat transfer area can occur.

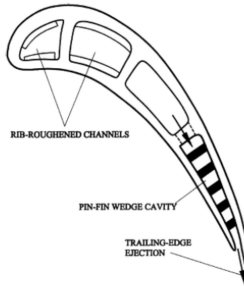


Figure 2.9: Cross-sectional view of a pin-fin cooling system at the trailing edge

Pin fins are typically applied in the narrow trailing edge of the airfoils (Figure 2.9), where other cooling schemes (i.e. impingement jets or ribbed channels) cannot be accommodated due to the very thin thickness required to obtain the highest airfoil aerodynamic efficiency. In this type of application the pins have a height-to-diameter ratio between $1/2$ and 4 and are grouped in several arrays with the aim of cover a large area. In a pin-fin array the heat is transferred from both the smooth channel endwall and the numerous pins. Moreover the heat transfer in a pin-fin array combines the cylinder heat transfer and endwall heat transfer; due to the turbulence enhancement caused by pins, heat transfer from endwalls is higher than the smooth-wall condition.

In the technical literature many factors have been investigated about pin-fin cooling such as: type of pin-fin array, spacing between pins, pin size, pin shape and the effect of coolant extraction to reproduce the trailing edge ejection.

Two array configurations are commonly used: one is the in-line array and the other is the staggered array; this latter has usually higher heat transfer coefficients compared to the in-line array for different shapes of pin fins. Figure 2.10 show a typical experimental test model with a staggered array of pin-fins.

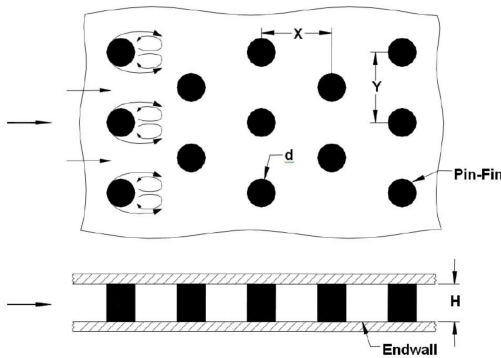


Figure 2.10: Typical test model and schematic of secondary flows for Pin-Fin cooling

Metzger et al. [24] used staggered arrays of circular pins with 1.5 to 5 pin diameter spacing in a rectangular channel; results proved that a closer spaced array (smaller x/D) allows to reach higher heat transfer coefficient. Moreover they observed that the addition of pin-fins significantly enhances the heat transfer coefficient but also increases the pressure drop in the flow channel. These experimental results have been correlated by Metzger and Van Fossen [25] to predict the Nusselt number in channels with pin-fin arrays. It was found that the average Nusselt number in a

channel with short pin-fins is primarily dependent on the Reynolds number of the flow and a weaker dependence is present for the pin spacing. Some years later Metzger et al. [26] studied the effects of pin shape and array orientations; in particular they reported the effect of flow incident angle on oblong pins. It was found that all incident angles, except the $90deg$, yield higher Nusselt numbers than circular pins; the $90deg$ array yields significantly lower Nusselt numbers especially for low Reynolds numbers, while the $\pm 30deg$ array has the highest Nusselt numbers, about 20% higher than the circular pin array on the average. As regards pressure drop, all the array configurations of oblong pins, except the $90deg$, have higher pressure losses than circular pins; this is mainly due to the increase in the friction factor associated with the flow turning.

Other important effects on cooling performance of pin fins were carried out by Chyu et al.; in a first work [27] it was investigated the effects of a fillet at the base of cylindrical pins, while in a second work [28] the effects of cube and diamond pins were analyzed for both in-line and staggered configurations. As regards the effects of the fillet it was found that the straight cylinders (i.e. without fillet) in staggered array formation have the highest heat transfer followed by the filleted cylinders in the staggered configuration. On the other hand for in-line configurations the fillet cylinder in-line formation has a better heat transfer than the straight cylinders. Moreover these results confirmed that the staggered arrays of cylindrical pins have higher heat transfer coefficients than in-line arrays, but the addition of the fillets implies a sharp decrease of performance.

As regards the comparison between cube and diamond pins, it was found that the cube-shaped pins have the highest heat transfer coefficients among the shapes considered and round pins have the lowest ones. On the other hand the corresponding pressure loss coefficients are higher for both cube and diamond shaped pins than the circular pins.

In recent years other important effects have been investigated on pin fins configurations for the application at the trailing edge such as: the effects of flow convergence and turning, and the effect of ejection holes. Shepard et al. [29] demonstrated the effects of flow acceleration on heat transfer

performance within a convergent channel; the results, presented as row averaged, show an increase in the heat transfer coefficient with the reduction of cross-section and hence the increase of flow velocity.

Then the effect of a perpendicular flow turning or entry in a realistic trailing edge cavity was studied by Chyu et al.[30] on both in-line and staggered arrays; results show that the turning inlet configuration always produce a reduction of heat transfer coefficients with respect to the straight entry: this reduction is about 40 – 50% for the in-line array and 20 – 30% for the staggered array.

Finally since a trailing edge channel has normally ejection holes through which the spent coolant exhausts to the main stream flow, some interesting effects must be considered. First of all Kumaran et al. [31] investigated the effects of the length of coolant ejection holes on the heat transfer coefficient; these results indicate that the length of the ejection hole can significantly alter the discharge rate of coolant. In addition to this it has been found that a higher coolant ejection reduces the Nusselt number with respect to the case with no ejection. This decrease in the heat transfer coefficient can be explained by the fact that coolant mass is extracted from the coolant channel before its cooling capacity is fully utilized. Moreover the results indicate that the correlation based on the local Reynolds number can predict the heat transfer coefficient distribution for lower coolant ejection but does not adequately predict the same HTC's distributions at higher ejection rates.

Some year later Hwang et al. [32] investigating a converging channel with ejection holes found that an increase of coolant ejection degrades the heat transfer at the endwall near the tall wall opposite of the ejection, while the heat transfer on the channel endwall surface near the ejection holes is increased. Moreover in case of large ejection flows no significative differences were found among square, diamond and circular pin-fin arrays.

2.1.1.3 Dimple Cooling

In contrast to the pin fins, the dimples are concavities and are considered an interesting alternative solution to ribbed ducts and pin fins

because of their low pressure penalty (compared with pin fins) and moderate heat transfer enhancement.

It should be said that this kind of application was largely unknown in the Western world until the dissolution of the Soviet Union in the 1980's.

The flow behaviour over concavities of spherical or cylindrical shape is well described in the study of Afanas'yev et al. [33]; as the flow encounters a concavity it experiences a separated region on the entry side. Then the spherical shape creates a pressure field within the concavity acting to collapse or concentrate the flow in the downstream portion of the recess and this generates a vortex structure. A schematic view of the flow behaviour over a dimple is shown in Figure 2.11.

Numerical results found by Isaev et al. [34] show that a pair of symmetric and counter-rotating vortices is formed but in most real cases only one vortex appears; starting from this condition the vortex is expelled from the concavity and it starts to interact with the mainstream flow. This interaction allows to continuously bring fresh core fluid to the surface and generates a flow reattachment on the flat surface immediately downstream of the dimple; these phenomena lead to a heat transfer enhancement. In addition to this, since this vortex motion is organized, rather than the more dissipative effect of shearing layers, the pressure loss is less than that observed with projecting obstructions such as turbulators; in some cases dimpled surfaces have friction nearly the same as smooth surfaces.

Globally the heat transfer in the dimpled channels is from 2 to 2.5 times greater than the heat transfer in a smooth channel with a pressure loss penalty of 2 to 4 times that of a smooth channel. These values have a little dependence on Reynolds number and channel aspect ratio. Moreover, recent studies [35] [36] have been focused in evaluating the effects of dimple size, dimple depth-to-diameter ratio, dimple shape (cylindrical, hemispheric, teardrop) on the heat transfer distribution in rectangular channels. Dimples have been also investigated by Bunker [37] in a circular channel; measured levels of heat transfer enhancement and friction loss are similar to the above mentioned cases.

Finally Syred et al. [38] demonstrated the effects of surface curvature comparing the heat transfer enhancement due to a single dimple on both flat and curved surfaces. From this study it was found that the heat transfer performance on an endwall surface that is concavely shaped is higher with respect to the flat endwall; on the other hand a convexly curved surface decreases the level of heat transfer enhancement.

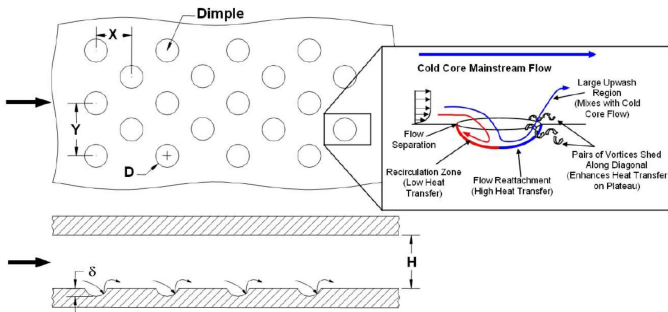


Figure 2.11: Typical test model for Dimple cooling studies and schematic view of dimple induced secondary flows [39]

2.1.2 Internal Cooling of Gas Turbine Blades

Also for modern gas turbine blades a combination of different internal cooling techniques is usually applied within the same rotor blade (Figure 2.12): for example serpentine cooling passages with rib turbulators in the middle portion, jet impingement at the leading edge and pin-fin cooling with ejection near the trailing edge. Although some of these techniques are similar to those used to cool the vanes (§ 2.1.1), the heat transfer

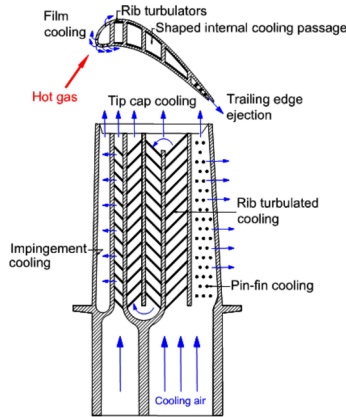


Figure 2.12: Schematic of a turbine vane cross-section with different cooling systems [40]

trends in the vanes and blades are very different; for example, because the blades are rotating, the flow of the coolant in the passages is altered. Therefore, the effect of rotation on the internal heat transfer enhancement must be considered in these cases.

In the following paragraphs only a description of the typical internal cooling techniques suitable for rotor blades will be given, while for the similar cooling systems (i.e. jet impingement and pin-fin cooling) it will be necessary to refer to the previous paragraphs.

2.1.2.1 Rib Turbulated Cooling

In turbine vanes but mostly on turbine blades, a very common solution applied in the middle portion of the airfoil consists in internal channels with turbulence promoters, better known as rib turbulators or ribs.

Many works found in literature are focused on internal channels modeled as short rectangular or square channels with different aspect ratios and

only few works have been performed on circular ribbed ducts. As shown in Figure 2.12 the aspect ratio W/H of the channels changes from the leading to the trailing edge of the blade; near the leading edge the ribbed channel may have an aspect ratio around $1/4$, while near the trailing edge much broader channels are present with aspect ratios around 4.

The ribs, that are repeated along these internal cooling channels, are typically cast on walls as projections from the internal surface into the flow. Usually they are located on two opposite walls of the channel (Figure 2.13), almost always towards the pressure side and suction side; sometimes only one side has ribs, because the internal cooling has to match the external load, which can be different on pressure and suction side.

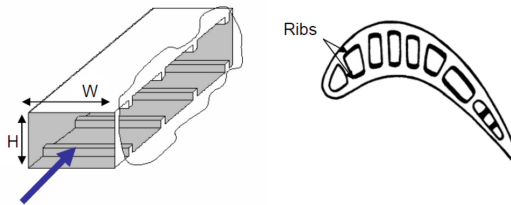


Figure 2.13: Example of ribbed channel with ribs on two opposite walls
[7]

It is well known that ribs cause separation from the flow at the rib tops and reattachment to the flow between the ribs; the reattachment of the boundary layer between two adjacent ribs results in increased heat transfer coefficients. This flow behaviour of separation, recirculation and reattachment continues throughout the channel along with the pattern

of repeated ribs (Figure 2.14).

All these mechanisms increase fluid turbulence and mixing among the fluid elements near the wall with the cooler ones in the middle of the flowpath. Therefore ribbed ducts provide two favourable contributions to enhance internal heat transfer: increase of turbulence level and increase of heat exchange area. On the other hand the presence of ribs induce a pressure drop along the channels. Consequently, designers have to find out the best rib geometry in order to obtain the highest heat transfer coefficients with the minimum friction penalty across the internal cooling passages [41].

Moreover, as shown in Figure 2.15, these ribs induce different patterns of secondary flows depending on the different shape and distribution of ribs. For example, if the rib turbulators are skewed to the mainstream flow direction then counter-rotating vortices are created. In case of angled ribs two counter-rotating vortices are formed in the cross-section of the cooling passage, while if V-shaped rib turbulators are used then four vortices are generated. The additional set of counter-rotating vortices associated with the V-shaped ribs results in more heat transfer enhancement in a channel with V-shaped ribs than angled ribs.

Over the years several studies have been performed on ribbed channels to investigate the effects of both Reynolds number and many geometrical parameters on the heat transfer enhancement and pressure losses such as: channel hydraulic diameter D_h , channel aspect ratio W/H , rib height e , rib pitch p , rib angle of attack α , different rib configurations (i.e. V-shaped, Wedge and Delta-shaped ribs) and different cross-section of the channel (i.e. rectangular, square, triangular).

In 1988 Han et al. [42] found that the heat transfer enhancement slightly decreases with the increasing of Reynolds number. The reason is that flow reattaches faster for higher Reynolds; for example the flow reattaches approximately 2 rib heights downstream for $Re=60000$ and 6 rib heights downstream for $Re=10000$.

The effects of rib angle were investigated by Han et al. [43] [44] [45]; from these studies comes out that using ribs with an attack angle be-

tween $30deg$ and $60deg$ results in increased heat transfer and reduces the pressure penalty. Moreover, for each test case, periodic distributions of Nusselt number were found because of the continuous separation and reattachment of the flow with some differences depending on the channel aspect ratio and cross-section. For square ducts with transverse ribs ($\alpha = 90deg$) Nusselt number Nu decreases along the streamwise direction until $x/D_h > 3$ where the periodic distribution reaches a constant value. For square ducts with angled ribs, Nu also decreases after the inlet, but it increases again for $x/D_h > 3$ because of the secondary flows induced by the rib angle.

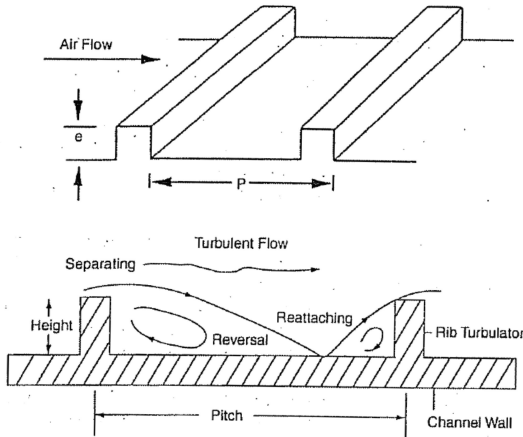


Figure 2.14: Schematic of flow separation and rib orientations in heat-transfer coefficient enhancement (Han and Dutta, 1995) [2]

For ducts with larger aspect ratio ($W/H > 1$) this effect is gradually decreased; while as regards ducts with $W/H < 1$ for $\alpha = 90deg$ or $30deg$ the Nusselt number neither increase nor decrease between the ribs after $x/D_h > 3$, while for $\alpha = 60deg$ or $45deg$ Nu increases along the channel due to the secondary flow described above.

Moreover Han et al. [44] found that for a duct with square cross-section

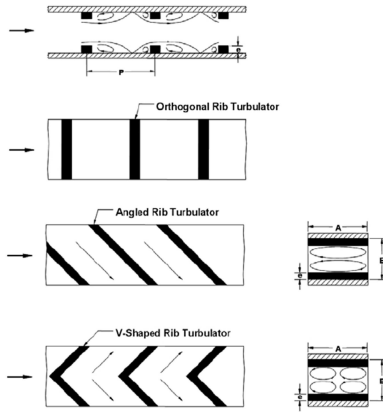


Figure 2.15: Typical test models for turbulated cooling studies with rib induced secondary flows

($W/H = 1$) the highest Nusselt number and friction factor f were obtained for $\alpha = 60deg$, while for a duct with $W/H = 4$, suitable for an application near the trailing edge, the highest Nu and f values were obtained for $\alpha = 90deg$.

Final results of these studies indicate that the best performance in terms of both Nusselt number and friction factor is obtained for $\alpha = 30deg$ or $45deg$; in addition to this the ribs with $60deg$ and $45deg$ angle of inclination to the flow have from 25 to 30% higher heat transfer performance than transverse ribs.

Also the effects of rib height and rib pitch were investigated. It was found that a small increase of rib height produces only a small increase in Nusselt number but a higher increase of pressure. On the other hand for pitch-to-rib height ratio no less than 10 the Nusselt increases with a reduction of p/e and the maximum heat transfer is obtained for $p/e = 10$;

in fact for smaller rib spacings the reattachment of flow between ribs cannot occur and hence the heat transfer enhancement due to this effect is not present.

Several works were dedicated to the investigations about the effects of different rib configurations in order to find out the geometry with the highest performance; examples of some high performance rib turbulators are reported in Figure 2.16. Among these works Han et al. [46] showed that V-shaped ribs allow to achieve better results than the angled ribs; in fact, for a given pressure drop, the V-shaped ribs give more heat transfer enhancement. Some years later these results were confirmed by other studies in a variety of channels and flow conditions.

To further improve heat transfer performance discrete rib configurations were analyzed by Cho et al. [47]. Discrete ribs are similar to the traditional rib but they are broken in one or more locations. Results proved that these configurations perform better than the previous continuous angled or V-shaped ribs.

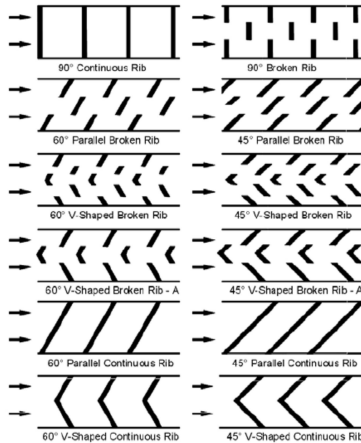


Figure 2.16: High performance rib turbulators for turbine blade internal cooling

Additional investigations were also performed on various profiled ribs without the conventional square cross-section; this is the case of the so-called wedge-shaped and delta-shaped ribs where the heat transfer enhancement mechanisms combine the benefits of ribbed channels and pin-fins. About these configurations Han et al. [48] demonstrated that delta-shaped ribs guarantee higher heat transfer enhancement than the traditional angled ribs. Higher heat transfer performance were also found by Bunker et al. [37] concerning particular profiled ribs leaning into or away from the flow.

Other studies were also focused on ribbed channels with more blockage than all above mentioned configurations; for example about 10% blockage of the channel by ribs [49]. These results showed that an increasing in the effective blockage leads to an increase of the heat transfer coefficients, but this improvement comes at the cost of a significant increase in the pressure loss. As regards a potential application it can be concluded that the use of these ribs is beneficial when the heat loads are extremely high and the high frictional losses can be tolerated.

Moreover, since modern turbine airfoils have ribs in the internal ribbed channel and film cooling for the outside surface, some of the cooling air is bled through a periodic distribution of film cooling holes along the channel. This periodic bleed of coolant along the channel determines axial and spanwise variations in the heat transfer distributions. The effect of this coolant extraction on the heat transfer enhancement has been investigated by Shen et al. [50] and Thurman et al.[51]. These studies reported that the heat transfer coefficients increase only in the near-hole regions; this effect could become higher when the ribs are placed near the bleed holes. Since the variations in the other regions of the channel are negligible it results that the regional-averaged Nusselt number ratios for different rib orientations are almost identical with and without bleed hole extraction. For this reason it could be concluded that the performance of the ribbed channel is affected only when the mass flow extraction for film cooling is about 20 to 25%

To conclude this section it should be noted that ribbed channels are ap-

plied inside the turbine blades according to both radial and multipass configurations (Figure 2.17). In the first case the ribbed channels are located in different streamwise positions along the airfoil; the coolant flow enters in each channel from the hub to the blade or from the tip to the hub in case of stator vanes but in each case it develops along the only radial direction. These configurations are usually known as single-pass with radial inward and outward flow.

In the second case the coolant flows through serpentine passages realized inside the blades; these are well known as multipass configurations with both radial outward and radial inward flow. Unlike the radial ducts, in case of multipass serpentine the additional effects of the sharp turns should be included in the evaluation of the overall performance. A detailed overview about the effects and correlations developed for multipass serpentine is given by Sundberg [7].

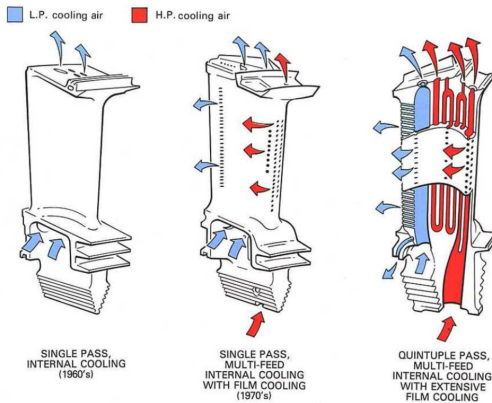


Figure 2.17: Radial and multipass configurations of ribbed channels [3]

2.1.3 **Trailing Edge Cooling Systems**

Since a wide part of the present work has been dedicated to investigate the performance of innovative or alternative cooling schemes for airfoil trailing edges, this section gives an overview about the state-of-the-art of trailing edge systems for gas turbine.

As already mentioned in section 1.2 the trailing edge region is a very critical part in the modern airfoils because it is more sensitive to premature failures compared to other regions due to the very small cross section and thickness. For this reason the blade cooling design of this part has to fulfill many requirements at the same time: the profile thickness must be thin to reduce weight and improve airfoil aerodynamic efficiency, but it must also ensure a high structural rigidity and a high heat transfer enhancement.

Because of the reduced metal thickness of this region its thermal inertia is low with respect to the other parts of the airfoil; this means that the metal of the trailing region takes shorter times to heat up or cool down than the other adjacent regions. This situation leads to a continuous and cyclic status of differential thermal expansions between the different parts and hence to thermally induced stresses that affect the Low Cycle Fatigue (LCF) cracking of the component.

In combination with the cyclic operation due to the Low Cycle Fatigue, the oxidation can determine a considerable loss of wall thickness and a certain cracking at the internal cooling holes. The oxidation may be also facilitated by the combination of high external heat transfer coefficients together with a low internal cooling.

Moreover, the small thickness of the profile at this region in combination with the higher temperatures can lead to creep problems from long exposure to the strain.

All these phenomena should be considered by the designers in order to avoid premature failures of the components.

As regards the internal cooling design, the most typical solutions provide that the trailing edge is internally cooled by means of ribbed serpentine or pin-fin arrays, while externally it is protected by a film cooling

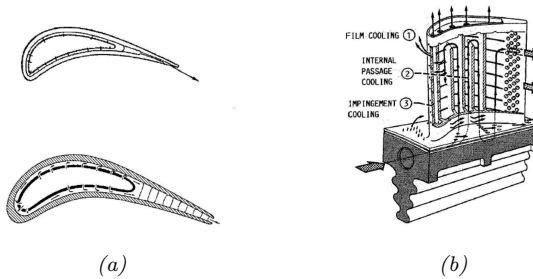


Figure 2.18: Examples of cooled blades with different trailing edge configurations

system. For example, in Figure 2.18a, two different cooling configurations for vanes are represented: in the first case, the axial duct with a constant diameter along the radii ensures the coolant flows through the vane; in the second example pin fins are inserted in a wedge duct. A similar solution is applied for the rotor blade in Figure 2.18b, in this case a serpentine ribbed duct with turbulence promoters is present upstream the pin fin array in the wedge duct.

Another kind of rotor blade is illustrated in Figure 2.19; in this case the trailing edge includes a wedge duct with a system of enlarged pedestals that allow to redirect in axial flow the coolant flow at the discharge exit. From this point the coolant flow exiting from the axial slots provides a protective film above the external final part of the pressure side; this latter solution is better known as *cutback film cooling*.

Because of these above reported constraints it results clear that pin fins and pedestals are the most typically used techniques to enhance the overall heat transfer coefficient in the trailing edge region. The pedestals have a lengthened shape of the base section and guarantee a higher structural strength with lower pressure losses but also with a lower heat transfer increase compared to circular pin fins.

Over the years in the technical literature some works were dedicated to study different configurations and different shapes of pin fins and

pedestals, while other works were addressed to investigate the effects of other important features in order to reproduce the flow conditions in realistic trailing edge schemes such as: converging channel, blowing tip condition, 90deg turning of the flow from radial inlet to axial discharge exit. Some of the works have been already cited in the previous section 2.1.1 about pin-fin cooling.

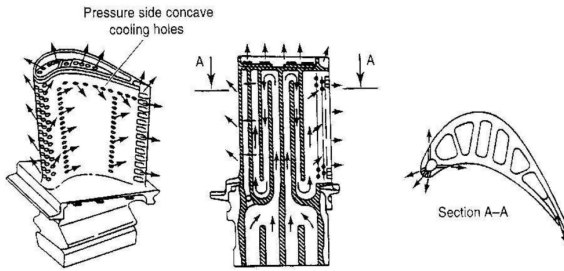


Figure 2.19: Example of trailing edge cooling schemes in a rotor blade

First of all, Metzger et al. [24] and Shepard et al. [29] investigated several staggered arrays of circular pin fins with 1.5 to 5 pin diameter spacing. Results show that heat transfer coefficients are higher for closer spacings, but a higher number of pins also increases the pressure drop through the channel; it was also found that the heat transfer enhancement Nu/Nu_0 was between 1.8 and 2.3 for the investigated range of Reynolds number.

Moreover Metzger et al. [26] studied the effects of pin shape and array orientations reporting a comparison between oblong and circular pins for several flow incidence angles. These results show that oblong pins have higher heat transfer coefficients but also higher pressure losses than cir-

cular pins for all incident angles with the exception of $90deg$.

Some years later Chyu et al. [28] [52] performed comparisons between staggered arrays and in-line arrays of pins for cube and diamond-shaped pins. Results conclude that the staggered arrays have higher heat transfer coefficients compared to in-line configurations and the cube-shaped pins have the highest heat transfer enhancement; on the other hand pressure loss coefficients are higher for both cube and diamond-shaped pins than the circular pins.

In more recent years Hwang et al. [53] [54], Facchini et al. [55] and Innocenti et al.[56] investigated the effects of the accelerating flow in wedge-shaped trailing edges with different arrangements of circular pin fins and enlarged pedestals both on heat transfer and pressure losses.

Hwang et al. [54] performed endwall heat transfer and pressure drop measurements in a wedge-shaped ducts containing an array of circular pin fins. Measurements were performed for two outlet flow orientations (straight and turned) (Figure 2.20) and for two pin fins formations (in-line and staggered). As shown by Figure 2.21, results indicate that the straight wedge duct with a staggered pin array is the most recommended configuration since it produces the highest endwall heat transfer enhancement with a moderate pressure drop penalty. On the other hand the same staggered pin array in a turned wedge duct represents the least recommended solution because it has high pressure losses and presents a non uniform heat transfer distribution with severe hot spots.

In addition to this, other experimental tests were performed for a smooth or pin-less wedge duct and a smooth rectangular duct to evaluate the isolated effect of the flow acceleration; further comparisons were performed with heat transfer and friction correlations for fully developed turbulent flow in circular ducts. As shown by the results reported in Figure 2.22, the increase of heat transfer due to the flow acceleration effect is about $10 \div 20\%$.

Some years later Facchini et al. [55] and Innocenti et al.[56] evaluated heat transfer and pressure drop in thin wedge-shaped trailing edge with two different turbulators arrangement: long ribs or pedestals and stag-

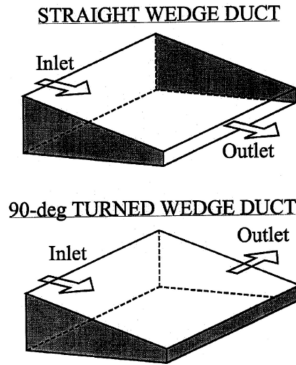
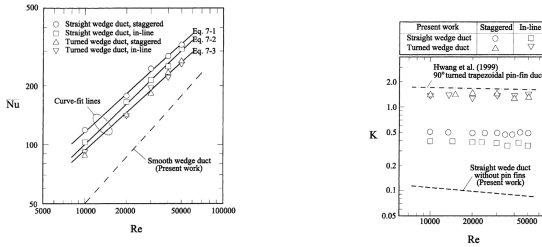


Figure 2.20: Two wedge-shaped with different outlet flow orientations [54]

gered pin fins (Figure 2.23). In the present work a new approach was proposed to evaluate the separate contribution to heat transfer of endwalls and inserts surfaces; a TLC transient technique is used to measure a very detailed and accurate heat transfer coefficient distribution on the endwall surface, while a FEM analysis is used to evaluate an average heat transfer coefficient over inserts surface. This technique requires that inserts are made of high conductive material but also a comparison with inserts in low conductive material is necessary to understand the isolated effect of pin fins and pedestals.

Results showed that the contribution of inserts to heat transfer of the whole cooling system is significant; in fact heat transfer values around pedestals are about 2.7 times greater than for the endwall surface, while for the pin fin are about 2.3 times [56].

In recent years Bianchini et al. [57] [58] analyzed the performances of innovative distributions of pin fins and pedestals in a wedge-shaped converging duct and investigated the effects of different blowing tip conditions. Moreover, to reproduce the mixed axial-radial flow inside a realistic trailing edge the combined effect of a $90deg$ turning flow and channel



(a) Area-averaged endwall Nusselt number as a function of duct Reynolds number (b) Pressure drop coefficient as a function of duct Reynolds number

Figure 2.21: Heat transfer and pressure loss results for different configurations of wedge-shaped ducts: straight/lateral flow orientation and staggered/in-line pin-fin arrays [54]

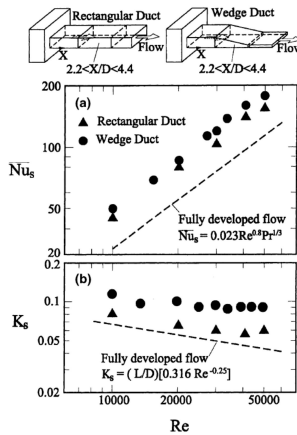


Figure 2.22: Comparison of heat transfer and pressure loss results between pin-less wedge duct and rectangular pin-less duct [54]

shape was considered.

Later Bonanni et al. [59] extended the previous study of Bianchini et al. [58] and experimentally investigated the effects of rotation on the same

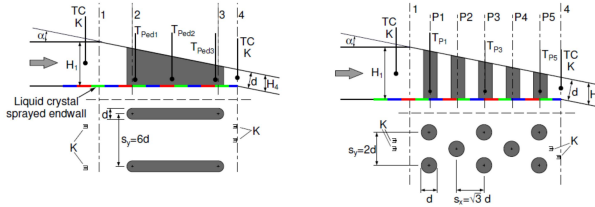


Figure 2.23: Schematic of long rib (pedestal) and pin fin geometry in the convergent wedge-shaped channel [56]

configurations. Another important contribution was also given by Liu et al. [60] who estimated rotation effects on wedge-shaped channels with slot ejection under high Rotation numbers.

More details about rotational effects on trailing edge channels will be given in the next section.

In the last years the gas turbine manufacturers continue to dedicate a high degree of attention to the design of this section in order to improve the performance and the durability targets. Some examples of the most recent solutions of trailing edge schemes are shown in the following figures.

One trailing edge scheme that includes some of the above reported solutions is shown in Figure 2.24; first, the coolant flow meets some rows of pin fins, then it is discharged at the exit passing through a row of enlarged pedestals. Moreover the internal flow path is axial-radial with a $90deg$ turn.

Another example is illustrated in Figure 2.25 ([61]); this configuration

is designed for a typical high-pressure turbine blade. In this case the trailing-edge scheme is made up of two cooling arrangements: first, the pressure-side cutback with slots located in the upper portion of the blade, second, the centerline discharge with round openings located in the lower portion of the blade. The combination of slots and round openings at the trailing edge provides a performance improvement caused by the thin trailing edge in the upper portion of the airfoil. The use of centerline discharge with cooling holes in the lower portion of the blade is practical, as the gas-path temperatures can be considerably reduced at the lower radial portion of the airfoil [61].

Among the most recent solutions of trailing edges, a high attention is focused to improve the scheme for film cooling at the cut-back region. For example the patent reported in Figure 2.26, represents a particular solution of shaped holes with a surfacial exit opening located at the pressure side of the trailing edge. In addition to this, the cross-section of the holes at the point of exit, that can be in a step or on the pressure side of the blade/vane, can be circular, oval, elliptical or racetrack (Figure 2.27).

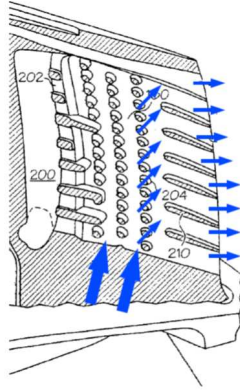


Figure 2.24: Scheme of a trailing edge cooling section with pin fins and enlarged pedestals [62]

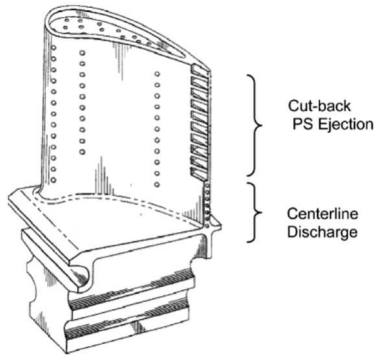


Figure 2.25: Typical high-pressure turbine blade showing trailing-edge cooling openings and pressure-side ejection slots [61]

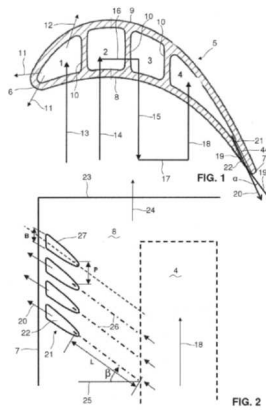


Figure 2.26: View of the shaped holes on the pressure side of the gas turbine airfoil [63]

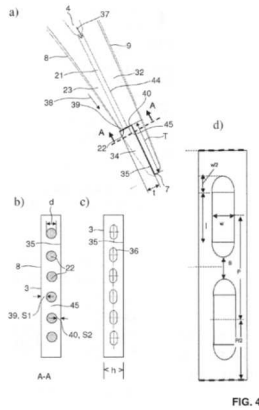


Figure 2.27: Different openings of the holes at the exit section [63]

2.1.4 Rotational Effects on Internal Cooling

Unlike the stator vanes, the predictions on heat transfer and friction performance of rotor blades must also consider the rotational forces such as: Coriolis force and Centrifugal buoyancy force. These two forces combined generate secondary flows inside the cooling channels and the core flow gets redistributed asymmetrically; these phenomena could alter the flow and temperature profiles in the rotor coolant passages and, as a consequence, distributions of heat transfer coefficients could be very different from those in stationary passages.

From the studies of Anderson [64] it is well known that the Coriolis force affects the stability of turbulent boundary layer and alter the distribution of radial velocity and temperature in the channel, while the buoyancy force promote the velocity profile distribution.

Moreover, in rotating conditions the induced secondary flow redistributes velocity and also alters the random velocity fluctuations in turbulent flows. This behaviour is proved by the experimental tests of Lezius and Johnston in 1976 [2]. Using water as working fluid in a rotating high-aspect-ratio rectangular channel they observed a stable and an unstable region; the stable side shows a decay of turbulence, while in the unstable side a turbulence enhancement occurs (Figure 2.28). It should be noted that stable and unstable regions are also known in literature as leading side and trailing side respectively.

Since the flow field affects the heat transfer coefficient distribution inside a coolant channel, it is necessary to understand the flow field under the effects of rotation starting from the example shown in Figure 2.29. In this case the secondary flows and the axial flow distribution in a two-pass channel are depicted for both radial outflow and radial inflow passes [65]; flow is radial outward in the first pass and radial inward in the second pass. Since the Coriolis force is the cross product of the angular velocity of rotation and the streamwise coolant fluid velocity, its direction changes passing from radial inflow to radial outflow pass. For this reason the Coriolis force is opposite in these two channels, and, as a consequence, the resultant secondary flows are different.

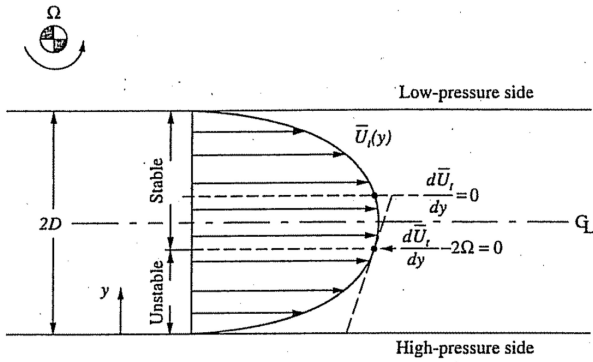


Figure 2.28: Stable and unstable regions in a rotating flow (Lezius and Johnston, 1976) [2]

In the first pass, where the direction of coolant velocity is radially outward, the Coriolis force acts towards the trailing surface and shifts the core flow towards this wall. On the other hand, in the second pass, where the coolant flow is radial inward, the Coriolis force acts in the opposite direction and hence shifts the core flow towards the leading surface.

If both the trailing and leading surfaces are symmetrically heated, then the faster moving coolant near the trailing wall of the first pass would be cooler and hence the heat transfer would be higher than the slower moving coolant near the leading wall.

In addition to the Coriolis force the rotational buoyancy, induced by a centrifugal force, pushes the cooler and heavier fluid away from the center of rotation. In the first pass this force acts in the same direction of the Coriolis force and causes a further increase in flow and heat transfer near the trailing wall; in the second pass the rotational buoyancy combines with the Coriolis force and make the velocity profile more uniform. The effects of Coriolis and centrifugal buoyancy forces in rotating channels

have been confirmed by many velocity measurements with PIV (Particle Image Velocimetry) or LDA (Laser Doppler Anemometry) systems.

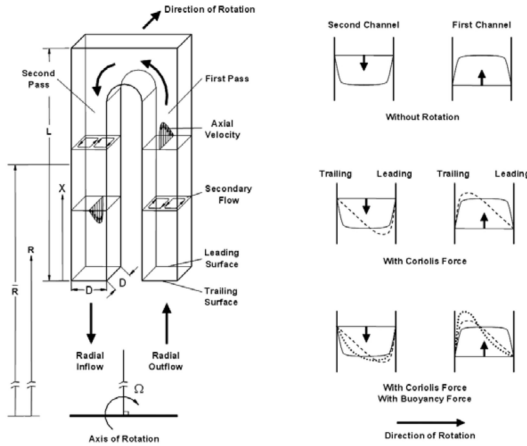


Figure 2.29: Conceptual view of the rotation effects on the coolant flow through a two-pass rotating channel [65]

It should be noted that the rotational buoyancy induced by the centrifugal force is due to the temperature difference between the coolant and the channel walls under rotating conditions. Since this temperature difference varies along the coolant passages, also the rotational buoyancy varies; for this reason it is possible that the wall heating condition would affect the heat transfer along the rotor passage. The channel heating conditions imply that the channel walls may be at the same temperature (or heat flux) in both streamwise and circumferential directions, or the trailing wall temperature may be higher than the leading wall temperature in real turbine blade cooling applications. Han et al. [65] studied the uneven wall temperature effect on the rotating two-pass square channels with smooth walls reported in Figure 2.29; results concluded that in the first pass the local uneven wall temperature interacts with the Coriolis force-driven secondary flow and enhances the heat transfer coefficients

in both leading and trailing surfaces, with a noticeable increase in the leading side, as compared with the uniform wall temperature case. However, the uneven wall temperature significantly enhances heat transfer coefficients on both leading and trailing surfaces. Parsons et al. [66] and Zhang et al. [67] studied the influence of wall heating condition on the local heat transfer coefficient in rotating two-pass square channels with $90deg$ ribs and $60deg$ ribs on the leading and trailing walls, respectively. They concluded that the uneven wall temperature significantly enhances heat transfer coefficients on the first-pass leading and second-pass trailing surfaces as compared with the uniform wall temperature condition.

Some years later other studies were addressed to investigate the effects of rotation in cooling channels with different shape of ribs with respect to the usual square ribs of the above mentioned works. For example Acharya et al. [68] investigated the heat/mass transfer in a square, two-pass rotating channel with various profiled ribs placed on the leading and trailing surfaces and showed that certain profiled ribs provide better heat transfer enhancement than the conventional square ribs. Also the smooth sidewalls of the channel have a higher heat transfer enhancement with respect to the smooth walls with square ribs.

In further experimental studies on rotating channels Wagner et al. [69] reported that the heat transfer coefficients on the trailing surface of the first pass with radial outflow can be enhanced 2-3 times that of a non-rotating channel, while the leading surface experiences a declination of up to 50%; opposite trends were found in the second pass with radial inflow. By a comparison with previous tests on smooth rotating channels it was found that the maximum values of the heat transfer coefficients obtained in ribbed channels under high rotation speed were only slightly above the highest levels obtained with the smooth channels. Moreover, with respect to the corresponding results on stationary experiments, it was found that there is less of an effect of rotation in a ribbed channel than a smooth channel. Since the heat transfer enhancement of the ribbed channel is already 3.5 times greater than that of a smooth channel, the rotation does not provide the same percentage of enhancement in the

cooling channel with ribs. Other experiments confirmed that the overall heat transfer in a rotating channel with ribbed surfaces is not affected by the Coriolis force as much as that in a rotating channel with smooth surfaces [70].

In addition to the several effects of rotation on ribbed surfaces, also the effects of model orientation on heat-transfer distribution in rotating channels must be considered for an accurate design of rotor blades. In fact, since the turbine blade is curved, the rotor blade cooling passage changes its orientation with respect to the rotating plane as it moves away from the middle of the blade; this aspect together with the distribution of secondary vortices for the different model orientations are well represented in Figure 2.30.

As regards the effects of this different inclination, Johnson et al. [71] compared heat transfer distributions in serpentine channels for smooth and $45deg$ angled ribs and for two different channel orientations of $0deg$ and $45deg$ with respect to the axis of rotation. By this comparison they found that the differences between the heat transfer coefficient distributions on the leading and trailing surfaces due to rotation become smaller as the model inclination varies from $0deg$ to $45deg$. In the next years other studies confirmed that these differences are reduced with the increasing of inclination angle.

Moreover, moving from the leading to the trailing edge of the airfoil, the cooling passage may change not only its orientation with respect to the rotating plane but also its cross section and aspect ratio. For example, as already explained in previous section 2.1.2, the aspect ratio of the channels may vary from 1:4 to 4 with different channel orientations to fit the turbine blade profile from the leading to the trailing edge; this range covers the majority of channels that could be applied in actual blades.

The effects of different aspect ratios in rotating ribbed channels have been reported by an interesting work of Dutta et al. [72]; they numerically analyzed 5 different aspect ratios (AR=1:4, 1:2, 1:1, 2:1, 4:1) for a radially outward channel. In case of higher AR (i.e. close to the trailing edge) the effect of Coriolis force is low because of the small height of the channel,

while the centrifugal buoyancy is stronger.

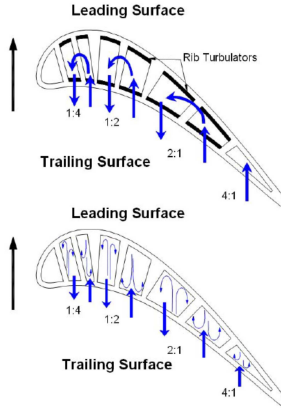


Figure 2.30: Typical cooling passage size and orientation with conceptual views of the rotation induced secondary flows

On the other hand, in case of lower AR, the results show wider differences about Nusselt ratio distributions between trailing and leading surface; among these distributions, for the channel with $AR=1:4$ lower values of heat transfer coefficients were found on the leading wall probably due to the formation of a stagnation zone close to this wall. Then, as the rotation increases, a back flow starts and this increases again the Nusselt ratio. The same back flow given by the centrifugal buoyancy is present for all the aspect ratios and the corresponding increase of Nusselt ratio occurs around a Rotation number equal to 0.12, whereas, on the trailing wall, the Nu ratio starts to decrease for Rotation numbers higher than 0.12.

Other interesting results were found for the extreme aspect ratios; the case for $AR=1:4$ (i.e. close to the leading edge) shows the highest differences of heat transfer distributions between trailing and leading surface and also the highest pressure drop that increases with the increasing of

Rotation number. On the other hand, the case for $AR=4:1$ (i.e. close to the trailing edge) shows the least differences between trailing and leading wall heat transfer and the pressure drop has intermediate values with respect the other aspect ratios.

Also Fu et al. [73] carried out a complete investigation on heat transfer and friction performance in rotating channels with different values of aspect ratios in the same range of the previous study. The effects of channel aspect ratio were investigated in rotating two-pass channels with smooth walls and $45deg$ angled ribbed walls. Moreover, tests were replicated for three channel orientations with respect to the rotating plane: normal or $90deg$, $45deg$ and $135deg$.

The results obtained from this work can be listed as follows:

- The $45deg$ angled ribs configuration gives a heat transfer enhancement approximately 2.5 to 4 times greater than the smooth circular pipe in the fully developed region for the non-rotating channels, while it decreases with the increasing of Reynolds number. This heat transfer enhancement is due to the blockage effect and to the development of vortices induced by ribs.
- The rotation generates differences of heat transfer distributions between trailing and leading surface for both smooth and ribbed channels. These differences depend on the channel aspect ratio: the $AR=1:4$ channel has larger variations than the $AR=4:1$ channel, the $AR=1:2$ channel has larger variations than the $AR=2:1$ channel, and the square channel $AR=1:1$ has the smallest heat transfer variations for both smooth and ribbed channels. It should be noted that a low aspect ratio reduces the rotation induced vortices and this reduces the heat transfer in rotating condition.
- The heat transfer enhancement due to the rotation is generally reduced in the second pass for both smooth and ribbed channels because of the $180deg$ sharp turn effect.
- The variation of channel orientation from $90deg$ to $45deg$ or from

90deg to 135deg reduces the heat transfer differences between leading and trailing surfaces for both smooth and ribbed channels.

- The Nusselt number ratio decreases with increasing Reynolds number in both non-rotating and rotating channels with smooth and ribbed walls.
- The overall heat transfer enhancement is comparable for all the ribbed channels, but important differences arise with the pressure losses through the channels. The lowest pressure penalty was found for the AR=1:4 case; for this reason the thermal performance of the AR=1:4 channel is superior to AR=1:2, AR=1:1, and AR=2:1 channels, respectively.

All the research works above mentioned concern the study of the rotation effects on different configurations of ribbed and smooth channels from the leading to the trailing edge; however, it should be noted that few studies consider the effect of rotation also on impingement cooling. Epstein et al. [74] studied the effects of rotation on impingement cooling in the leading edge of a blade. They reported that the rotation decreases the impingement heat transfer, but the effective heat transfer is higher than a smooth rotating channel. Two configurations were analyzed: one with zero stagger of cooling jets (i.e. jet direction is perpendicular to rotation direction) and one with $-30deg$ stagger. It was concluded that the zero staggered cooling jets have lower heat transfer coefficients compared to those with a staggered angle.

Some years later Mattern et al. [75] investigated the effect of rotation on the leading edge impingement cooling by means of the naphthalene sublimation technique without including the rotating buoyancy effect. As depicted by the test model in Figure 2.31, the jet direction has an offset angle with respect to the rotation direction. In general it was found that the rotation decreases the impingement heat transfer for all staggered angles and the maximum reduction of about 40% is obtained when jet direction is perpendicular to the rotation direction. This is mainly due to the Coriolis force that creates a swirl action on the spent flow and

deflects the jets.

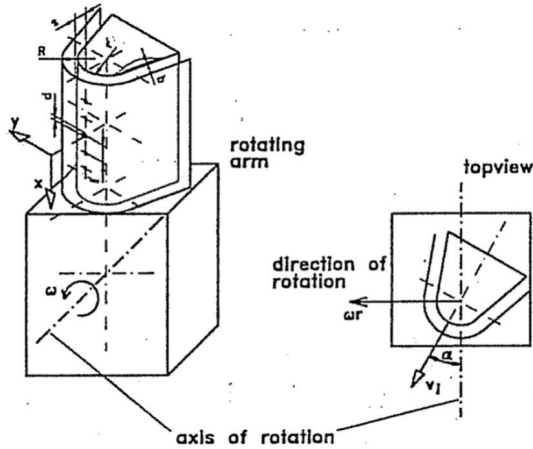


Figure 2.31: Schematic of the leading-edge impingement configuration used by Mattern and Hennecke (1996) [2]

Glezer et al. [76] studied the effect of rotation on swirling impingement cooling in the leading edge of a blade. They found that a screw-shaped swirl cooling can significantly improve the heat-transfer coefficient over a smooth channel and the improvement is not significantly dependent on the temperature ratio and rotational forces. Several tests were performed to find the optimal location and size of the tangential slots in order to get the best performance in the leading edge cooling.

Other studies can be found in literature about the investigation of the rotation effect on impingement cooling in the mid-chord region of the blade [77] [78].

The rotational effects were also investigated on dimple cooling systems for rotor blades. For example Zhou et al [79] analyzed the heat/mass transfer in a rotating square channel with a typical dimple array; they found that the heat transfer enhancement for the stationary dimple channel is around two times that of the smooth wall case, while in rotating

conditions the heat transfer is increased on the trailing dimple surface and is decreased on the leading dimple surface in a similar manner as the rotational effect on the trailing and leading surfaces of the square channel with ribs.

Later Griffith et al. [80] studied the heat transfer performance in rotating rectangular channels ($AR = 4:1$) with typical dimple array on both leading and trailing walls, including the effect of channel orientation with respect to the plane of rotation. The results show that rotation enhances heat transfer on both trailing and leading surfaces of the narrow dimpled channel in a similar trend as the rotational effect on the trailing and leading surfaces of the narrow rectangular channel with ribs or pins; however, the heat transfer enhancement of the ribbed or pinned channel exceeds that of the dimpled channel. Also, the dimpled channel oriented at $135deg$ with respect to the plane of rotation provides greater overall heat transfer enhancement than the orthogonal dimpled channel.

Finally, as regards rotational effects in pin-fin cooling systems, all the details are given in the next paragraph.

2.1.4.1 Rotational Effects on Trailing Edge Cooling Systems

This paragraph is located at the end of this literary overview on internal cooling systems and concerns the rotational effects on trailing edge cooling systems. In this paragraph the most important results coming from experimental works on rotating trailing edges are collected; since a part of the present research is dedicated to two matrix cooling geometries for trailing edges in rotating conditions, these results may be considered as an important basis of comparison for the cooling performance of different solutions.

As already explained in section 2.1.3 the pin-fins represent one of the most typically used techniques to enhance the overall heat transfer in the trailing edge region; pin-fin cooling systems have been investigated for many years, but only recently the effects of rotation have been considered.

For example Willett et al. [81] [82] studied the effects of rotation on

heat transfer in narrow rectangular channels with aspect ratio $AR=10:1$ using both smooth surfaces and typical pin-fin arrays; they also investigated the channel orientation effect with respect to the plane of rotation. These results prove that the heat transfer enhancement in the pin-fin channel due to rotation and buoyancy was less than the enhancement in the smooth channel at the same rotating conditions. In fact it was demonstrated that the heat transfer enhancement is mainly due to the flow disturbances induced by pin fins, but in rotating conditions the same pin fins reduce this enhancement but they do not completely eliminate it.

In addition to this work, Wright et al. [83] studied the effects of rotation on heat transfer in narrow rectangular channels ($AR=4:1$ and $8:1$) with typical pin-fin arrays used in turbine blade trailing edge design and oriented at $150deg$ with respect to the plane of rotation. Results show that turbulent heat transfer in a stationary pin-fin channel can be enhanced up to 3.8 times that of a smooth channel; moreover, the rotation enhances the heat transferred from the pin-fin channels up to 1.5 times that of the stationary pin-fin channels. Overall the heat transfer enhancement due to the rotation occurs on both the leading and trailing surfaces and increases with the increasing of Rotation number.

In more recent years Chang et al. [84], Rallabandi et al.[85] and Liu et al. [60] carried out experimental thermal analyses concerning rotating cooling schemes with axial flow discharge, which are thus comparable to modern trailing edge cavities. In fact these investigations were carried out inside rotating channels of trapezoidal cross section with flow ejection at the trailing side through holes or slots.

For example in the study of Liu et al. [60] the heat transfer has been experimentally investigated inside a wedge-shaped channel to simulate the trailing edge of a gas turbine blade, where the coolant has been discharged through six ejection slots (Figure 2.32). Smooth surface as well as the $45deg$ ribbed surface were tested to evaluate the heat transfer enhancement. In stationary conditions it was found that the Nusselt number is the highest near the narrow region due to slot ejection for both smooth

and ribbed cases, while it decreases towards the wide region of the channel due to reduced slot ejection effect. On the other hand, in rotating conditions, the effect of rotation is stronger near the wider region (inner side) than the narrow region (outer side). In addition to this, the slot ejection dominates over rotation and the heat transfer enhancement due to the rotation is higher near the narrow region.

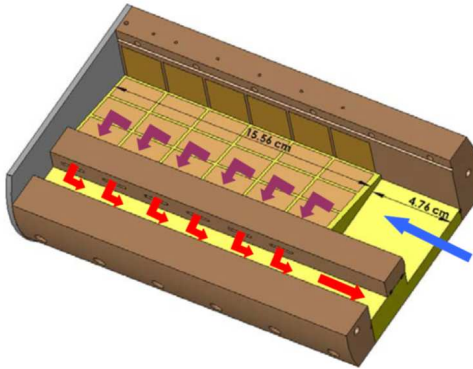


Figure 2.32: Schematic of the trailing edge wedge-shaped channel investigated by Liu et al. [60]

Another interesting study on a realistic trailing edge cavity was performed by Bonanni [59]; in this case they investigated the combined effects of different orientations of angled ribs and rotation inside a trailing edge channel with axial flow discharge through a row of enlarged pedestals (Figure 2.33). In the same study the additional effect of a different blowing tip condition on the heat transfer performance was included. From this study it was found that the increase of rotational speed promotes the heat transfer near the hub and the tip in the region upstream the pedestals. At the same time in the pedestals region the increase of Rotation number for both blowing tip conditions induces a decrease of heat

transfer coefficient peak on the pedestal leading edges due to the variation of the incidence angle on the pedestals. In each case the presence of ribs in the region upstream the pedestals allows to increase the overall heat transfer performance.

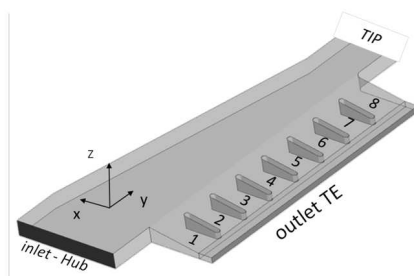


Figure 2.33: Schematic of the trailing edge model investigated by Bonanni [59]

2.2 Matrix Cooling Systems

This section is fully dedicated to the description of latticework or matrix cooling systems, which are the main subject of the present work.

Section 2.2.1 gives a general characterization of these systems starting from a description of the main geometric parameters and of the flow behaviour inside the cooling channels.

Section 2.2.2 provides a literary overview about the most significant contributions in the open technical literature.

2.2.1 Basic Principles

Latticework or matrix cooling systems are relatively unknown among gas turbine manufacturers of the Western world. This is because the application of the matrix structures as cooling systems in gas turbine airfoils originates from former Soviet design engineering system and were largely unknown until the recent dissolution of the Soviet Union in the 1980's, at which time Russian research works began to appear in the international literature.

Despite this fact it is known that many research works concern investigations on matrix systems, but unfortunately only few of these are reported in the open literature.

As depicted in Figure 2.34, a matrix system is mainly composed by two layers of longitudinal ribs with an opposite angle of inclination β forming a system of crossing sub-channels. These two layers are representative of pressure and suction sides of a gas turbine airfoil.

When the cooling air enters the matrix, such as at a blade root section, essentially half flows in the lower layer and half flows in the higher layer of the structure; the air that reaches the dead-end of each sub-channel at the side wall flows through the bend and into the sub-channel on the opposite layer with little or no mixing with the air from the other layer. Each time the flow hits the side wall it has to turn by the angle 2β switching from a pressure side sub-channel to a suction side sub-channel or vice versa. When the flow passes from one sub-channel to another, a

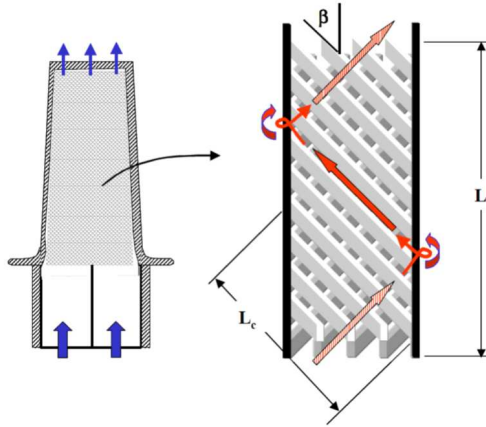


Figure 2.34: Example of a matrix geometry and a schematic view of the flow [86]

swirl motion is created and the turbulence of the flow is increased; this is well shown in the detailed view of Figure 2.35. As a result of this flow path, the overall motion of the flow in the matrix network forms complicated spirals or vortices.

As indicated in Figure 2.35 the most significant geometric parameters are those related to the single sub-channel; the sub-channel is described by the rib height H and the channel width W_c that define the characteristic hydraulic diameter of a matrix geometry. Moreover, the rib thickness t together with the number of sub-channels allow to define the open area available for the flow passage; in fact, keeping constant the overall width of the matrix channel, an increase of rib thickness or an increase of number of sub-channels implies a reduction of the open area.

In addition to this, an increasing of the overall width allows a longer flow development length L_c between the turn regions; this could contribute to increase the overall pressure loss through the matrix channel.

Also an increase of overall length L or an increase of the rib inclination

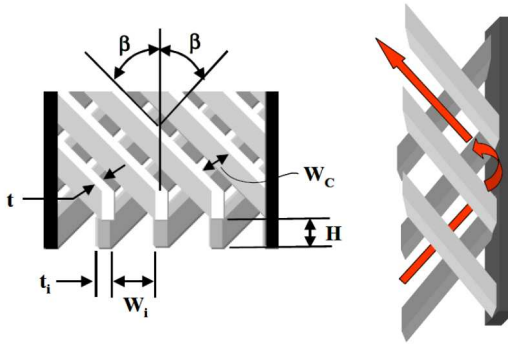


Figure 2.35: Main geometric parameters of a matrix channel and detailed view of the flow turn at the sidewall [86]

angle β contribute to increase the overall pressure loss. Moreover, it should be noted that, even if the overall length does not change, an increase of β is associated with a higher number of flow turns at the side walls along the whole channel; also this results in an increase of pressure losses.

The matrix structure in Figures 2.34–2.35 is a so-called closed matrix, where the several sub-channels reach the side wall and the flow at the side wall is forced to flow on the opposite sub-channel without mixing with the flow coming from the other sub-channels.

An alternative design is called open matrix, where a clearance is located between the end of the sub-channels and the side wall; these clearances are indicated in Figure 2.36 as $\Delta 1$ and $\Delta 2$. In an open matrix the flow that reaches the end of a sub-channel mixes with the flow in the clearances $\Delta 1$ and $\Delta 2$; the air that flows into new sub-channels starting at the clearances, is taken from the flow in the clearance channel.

It is known that internal cooling systems based on open matrix structures

are adopted in some gas turbines produced by Siemens probably at the trailing edge of vanes and blades [7]. Unfortunately no more information is available about open matrix systems; all the other works reported in literature are about closed matrix systems.

From the description of the flow path through a matrix geometry it is clear that a high and uniform level of turbulence is present for the whole length of the matrix channels.

Several factors contribute to raise this turbulence level:

1. At the turning regions the air flows from one sub-channel to another one creating a strong swirl motion
2. Interactions are present between the flow in crossing sub-channels
3. Interactions are generated between the flow in a sub-channel and the crossing ribs on the opposite side

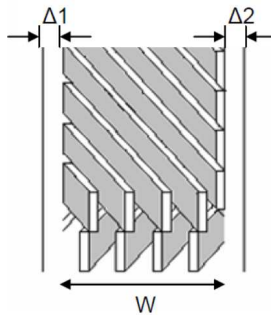


Figure 2.36: Scheme of an open matrix geometry [7]

This high and uniform level of turbulence results in an increase of the heat transfer coefficient through the matrix sub-channels.

Moreover, the heat transfer enhancement is given not only by the high flow turbulence but also by the high heat transfer surface area provided by the longitudinal ribs of the whole lattice-matrix structure. In addition to this, the ribs act as fins and determine a high heat removal from the endwall surfaces depending on their fin effectiveness. The heat transfer contributions given by the additional heat transfer surface and the fin effectiveness represent the so-called *fin effect* of the longitudinal ribs.

Recalling the theory of finned surfaces it must be considered that a fin represents a finite conduction resistance to heat transfer from the end-wall surface and a temperature gradient must exist along the fin; in fact, depending on its thermal conductivity, the fin is not of uniform temperature but is cooler at the tip than the hot base surface. So the effective temperature difference is lower compared to an ideal fin where the whole fin is at wall temperature. This effect is well described by the rib efficiency η defined as the ratio between the actual heat transfer rate and the maximum heat transfer rate at which a fin could dissipate heat if the entire fin surface were at the base temperature. A common definition of η is:

$$\eta = \frac{q_f}{q_{max}} = \frac{\tanh(m \cdot L)}{(m \cdot L)} \quad (2.1)$$

where m is the so-called fin parameter [87] and L is the fin height.

The equation for the rib efficiency may change depending on the heat transfer condition on the fin top: isolated or convective. More details about this definition are given in [87].

In addition to this, it should be considered that the fins are used to increase the heat transfer by increasing the effective surface area. For this reason, to evaluate the heat transfer enhancement due to the adoption of fins it is possible to use the so-called fin effectiveness ε_f defined as the ratio of the fin heat transfer with fin to the heat transfer that would exist without fin:

$$\varepsilon_f = \frac{A_{rib}}{A_b} \cdot \eta \quad (2.2)$$

The longitudinal ribs forming a matrix structure offer several benefits not only in terms of heat transfer; in fact the presence of distributed internal ribs of full or partial extent allows also to improve the structural strength of the ceramic core for the investment casting resulting in an increase of the component lifetime.

It should be noted that the development of the casting technology for the manufacturing of robust ceramic cores for matrix structures in current former Soviet states (i.e. Russia and Ukraine) has been parallel to that for the realization of ribbed serpentines in the Western countries.

2.2.2 Literary Overview

2.2.2.1 Goreloff et al. (1990)

The first investigations on matrix cooling systems reported in the open literature are referred to Goreloff et al. [88], even if only few information are available about this work.

They measured heat transfer coefficients on leading and trailing matrix passages with different inclinations of ribs from $30deg$ to $120deg$. Compared to a smooth passage, these results proved that the greatest heat transfer enhancement occurs at $35deg$ over a range of Reynolds number from 5000 to 20000. Heat transfer coefficients were measured on the blades using the zinc solidification process; according to this technique, the overall heat transfer is evaluated from the mass of zinc crust resulting from the solidification process of molten zinc by means of the coolant blowing. More details about this technique are given by Sundberg [7].

An example of the experimental blade used by Goreloff et al. is shown in Figure 2.37.

2.2.2.2 Nagoga (1996)

A more complete and detailed work about latticework or matrix geometries was carried out by Nagoga [90]; this is the only work that contains heat transfer and friction correlations for these structures. These correlations together with their ranges are reported in the work of Sund-

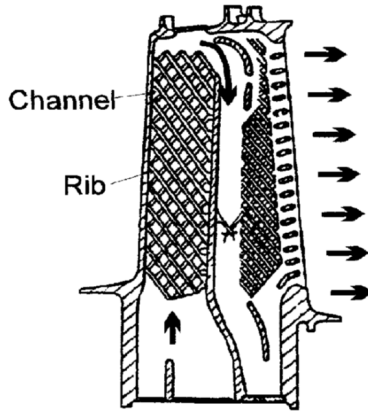


Figure 2.37: Experimental lattice cooled blade (Goreloff et al. 1990) [89]

berg [7].

First of all, Nagoga compared the investigated matrix geometries to a matrix with straight channels (i.e. $\beta = 0deg$) and found a heat transfer enhancement; this approach was considered more reliable with respect to compare the matrix with the flow in a long smooth duct.

Nagoga performed measurements on test models of closed matrix geometries similar to that shown in Figure 2.38.

In his experiments he distinguished between the heat transfer results obtained on the base shells from those obtained on the side bounds; the base shells correspond to the suction and pressure sides of a turbine airfoil and in other works they are called endwalls or primary surfaces, while the side bounds are the side walls and correspond to the turning regions of the flow.

Moreover, according to the nomenclature used by Nagoga, the matrix can be divided into two parts: the initial and the basic section. The initial section consists of the channels that begin at the inlet of the matrix and end at the side bound, while the basic section consists of the channels

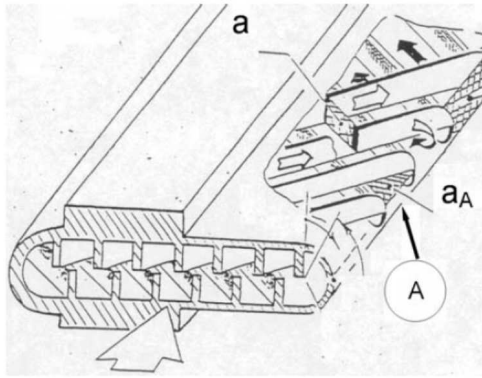


Figure 2.38: Example of experimental matrix model used by Nagoga [7]

beginning at a side bound and ending either at a side bound or at the outlet of the matrix.

For the channels in the initial section Nagoga found the same heat transfer and flow behaviour of a smooth duct.

On the other hand, for the basic section, he found that the heat transfer was higher than that in a straight duct; in particular the local enhancement factor varied from 1.28 to 2.

Moreover he found that this heat transfer enhancement decreases with the increasing of Reynolds number and with the increasing of the axial coordinate x/d along the streamwise direction; for example, local values of Nusselt number Nu_x are close to those in a smooth duct when $x/d > 30$. It was also found that the local Nusselt number reaches a maximum right after each turn and then reduces its value along the channel.

As regards the influence of the rib inclination angle β , Nagoga found that both the local Nusselt number Nu_x and the Nusselt number averaged on the length of the sub-channel Nu_l increase with the increasing of β and reach the maximum heat transfer enhancement for $\beta = 45deg$.

Nagoga also concluded that the rib pitch, the relative sub-channel depth, the cross section of the sub-channel and the type of side bound (i.e. concave or flat) have negligible effects on the local and average heat transfer. As regards the heat transfer results on the side bounds he performed experiments in order to understand the heat transfer on the internal surface on the semi-cylindrical side bounds, which corresponds to the leading edge on a turbine blade. From these investigations he concluded that the heat transfer on the side bounds were higher than for a duct with straight sub-channels and that the heat transfer in this region depends on the rib inclination angle β . By measuring the local and average Nusselt numbers along lines on the internal concave surface of the side bounds Nagoga also developed correlations for this region. These correlations are reported in the work of Sundberg [7].

On the same matrix geometries Nagoga measured the pressure losses and developed friction factor correlations.

He found that the friction in the initial section is similar to that in a smooth, straight duct with $\beta = 0deg$, while in the basic section the friction exceeded that in a duct with straight sub-channels. Moreover, he found that the enhancement of friction factor is always higher than the heat transfer enhancement.

Comparing the heat transfer and friction results, Nagoga concluded that the intensification of heat transfer and friction in matrix channels is caused by the flow rotation induced by the turn of the flow at the side bound of the matrix. At the side bound, the cooling air overflows from one channel to the opposite in a spatial turn. The intensity of friction, heat transfer and rotation is maximal right after the spatial turn, and then decreases with the increasing of distance from the side bound. All these three factors depend on the rib inclination angle β and reach a maximum for $\beta = 45deg$. Moreover, friction, heat transfer and rotation in a sub-channel are not affected by the coplanar crossing flow of the opposite sub-channel [7].

As regards the overall performance of matrix geometries compared to smooth passages, Nagoga concluded that the heat transfer enhancement

is in the range $2.0 \div 3.1$ for several inclination angles between ribs, while the friction factor enhancement is about $1.8 \div 2.1$. However the best performance is obtained at $45deg$ to the flow direction; this is better than other known cooling methods such as serpentine ribbed serpentine and pin fin arrays, but it is less than an impingement cooling on a concave surface.

Other comparisons were made in terms of cooling effectiveness (calculated according to the equation 1.1) as a function of relative mass flow of coolant; even in this case the matrices have better performance than any other cooling methods.

Nagoga also investigated the effects on life of turbine blades and vanes; for this reason he compared matrix geometries to: pin fin turbulators, rectangular ducts with two opposite ribbed walls and dimpled channels. Numerical and practical tests showed that the matrix increased the blade life in high pressure turbines in 40 times, which was 3 to 4 times more than pin fins and ribbed ducts [7].

Heat Transfer and Friction Correlations - Nagoga(1996)

This paragraph reports the heat transfer and friction correlations together with their ranges extracted from the work of Nagoga [90]; these correlations are also reported by Sundberg [7].

First of all, it should be noted that correlations are given for both the initial and basic section of the matrix geometry according to the above mentioned nomenclature given by Nagoga.

The heat transfer correlations for the initial section are as follows:

$$Nu_x = 0.0289 \cdot Re_x^{0.8} \cdot Pr^{0.4} \cdot \left(\frac{T_w}{T_f} \right)^{-0.55} \quad (2.3)$$

$$Nu_t = 0.0361 \cdot Re_t^{0.8} \cdot Pr^{0.4} \cdot \left(\frac{T_w}{T_f} \right)^{-0.55} \quad (2.4)$$

$$Nu_d = 0.023 \cdot Re_d^{0.8} \cdot Pr^{0.4} \cdot \left(\frac{T_w}{T_f} \right)^{-0.55} \cdot K \quad (2.5)$$

where Nu_x is the local Nusselt number, Nu_l is the Nusselt number averaged on the development length of the channel between the turning regions l (or L_c in Figure 2.34) and Nu_d is the Nusselt number based on the sub-channel hydraulic diameter.

The parameter T_w/T_f in Equations 2.3, 2.4 and 2.5 is the ratio of the wall temperature T_w to the coolant temperature T_f , while K is defined as:

$$K = 1 + 0.63 \cdot \left(\frac{l}{d}\right)^{-0.45} \cdot (Re_d \cdot 10^{-4})^{-0.36} \quad (2.6)$$

Depending on the different Nusselt correlation to use the following definitions of Reynolds number must be applied:

$$Re_x = Re_d \cdot \left(\frac{x}{d}\right) \quad (2.7)$$

$$Re_l = Re_d \cdot \left(\frac{l}{d}\right) \quad (2.8)$$

where Re_d is the Reynolds number based on the sub-channel hydraulic diameter d .

As regards the friction, the correlation that gives the local friction factor in the initial section is:

$$f_x = 0.43 \cdot Re_x^{-0.2} \quad (2.9)$$

On the other hand the heat transfer correlations for the basic section are:

$$Nu_x = 0.0361 \cdot n \cdot [1 + 12.77 \cdot \sin^2(2\beta)] \cdot Re_x^n \cdot Pr^{0.4} \cdot \left(\frac{T_w}{T_f}\right)^{-0.55} \quad (2.10)$$

$$Nu_l = 0.0361 \cdot [1 + 12.77 \cdot \sin^2(2\beta)] \cdot Re_l^n \cdot Pr^{0.4} \cdot \left(\frac{T_w}{T_f}\right)^{-0.55} \quad (2.11)$$

where n depends only on the rib inclination angle as follows:

$$n = 0.8 \cdot \left\{ 1 + 0.2 \cdot \left[\left(\frac{4\beta}{\pi} - 1 \right)^2 - 1 \right] \right\} \quad (2.12)$$

As regards the friction in the basic section, the correlation gives the value of friction factor based on the development length of the channel l as follows:

$$f = 0.43 \cdot [1 + 28 \cdot \sin^3(2\beta)] Re_i^{n-1} \quad (2.13)$$

The ranges, for which the above reported correlations of Nagosa are valid, are shown in the following table.

Table 2.1: Ranges for Nagosa's correlations [7]

Parameter	Range
Re_d	3000 ÷ 60000
T_w/T_f	1.4 ÷ 2.2
β	0 ÷ 70deg
d	1.5 ÷ 3.0mm
L/W	0.96 ÷ 5.2
W/d	6 ÷ 34.0
l/d	12 ÷ 67.0

2.2.2.3 Gillespie et al. (2000)

Some years later the work of Nagosa, Gillespie et al. [89] performed flow and heat transfer measurements on a scaled up model reproducing a cooling cavity in the trailing edge region; the model has also a flow ejection through a set of film cooling holes situated along one side of the passage.

This test model was manufactured using perspex in order to perform heat

transfer measurements using a transient liquid crystal technique. It has a trapezoidal cavity cross-section with two layers of 45deg angled ribs; these ribs have height such that the top of each rib lies on the centreline of the cavity. Then the ribs from the two opposite layers, which touch along the centreline, are almost perpendicular to one another. In the engine these ribs would be formed in a single integral casting. Figure 2.39 reports two photographs of the test model used in these experiments.

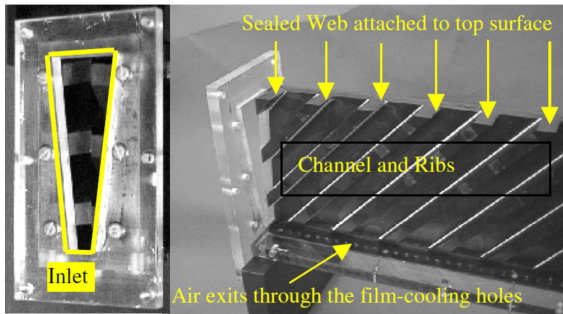


Figure 2.39: Photographs of the test model used by Gillespie et al. [89]

Local heat transfer coefficient distributions on the model surfaces were measured using a transient liquid crystal technique based on a double thermochromic liquid crystal coating displaying colour at 25.2°C and 30.6°C . This coating was applied to all surfaces of the lattice and to the web (i.e. the leading side of the geometry opposite to the surface with film cooling holes).

Since transient tests were performed in according to a method developed by Gillespie in a previous work [91], the local HTC values were found from the surface temperature rise through the solution of the one-dimensional Fourier equation:

$$\left\{ \begin{array}{l} \frac{T_w - T_{init}}{T_{aw} - T_{init}} = 1 - e^{\beta^2} \cdot \operatorname{erfc}(\beta) \\ \beta = \frac{h\sqrt{t}}{\sqrt{\rho c_p k}} \end{array} \right.$$

where t is the time instant at which the heat transfer coefficient h is evaluated, while ρ , c_p and k are density, heat capacity and thermal conductivity of perspex. The term erfc is a complementary error function; more details about this function are given by Gillespie [91].

In the present work the authors derived the distributions of heat transfer coefficients h according to two approaches: one based on the local mixed bulk temperature, one based on the inlet temperature.

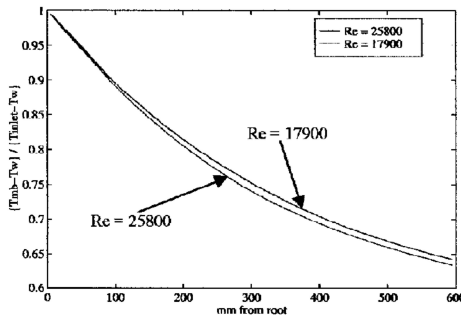


Figure 2.40: Reduction of coolant temperature potential $(T_{gas} - T_w)$ [89]

Then an energy balance approach was used to obtain the local heat transfer driving gas temperature and the local heat transfer coefficient distribution based on this temperature distribution. This approach takes into account two important and independent features of the flow field:

1. The local flow velocity through the system must reduce from root to tip as coolant is bled off to the film-cooling holes.

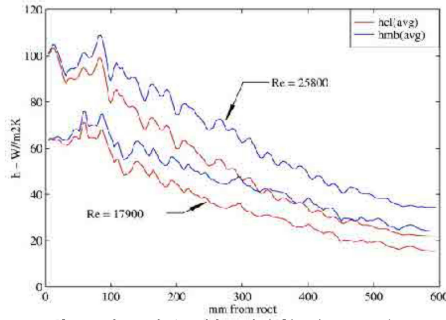


Figure 2.41: Heat transfer coefficients based on the inlet and local mixed bulk temperature [89]

2. Heat pick up through the system reduces the cooling potential of the flow.

Considering that the local heat flux at any point can be described in terms of a temperature difference and a suitably defined heat transfer coefficient, hence it is possible to establish the following relationship:

$$\frac{T_{mb} - T_w}{T_{inlet} - T_w} = \frac{h_{inlet}}{h_{mb}} \quad (2.14)$$

where h_{inlet} and h_{mb} are the heat transfer coefficients based on the inlet temperature and on the mixed bulk temperature respectively.

Then an energy balance, based on the following equation, was applied to calculate the spanwise average of h_{mb} across the surface:

$$\frac{h_{mb}}{h_{inlet}} = \frac{1}{1 - \int_A \frac{h_{local,inlet} dA}{\dot{m} \cdot c_p}} \quad (2.15)$$

Applying the energy balance approach (Equation 2.15) the reduction of coolant temperature potential has been derived as reported in Figure 2.40 and the heat transfer coefficients distributions along the streamwise

direction have been calculated; an example of h_{mb} and h_{inlet} distributions for two different Reynolds numbers are shown in Figure 2.41. The heat transfer coefficient h_{mb} maps inferred from the previous distributions for the two different Reynolds number are reported in Figures 2.42a and 2.42b. The same figures also report the HTC maps for the leading side or web of the geometry. Similar distributions were obtained for the other flow conditions.

From this detailed study Gillespie et al. concluded that all the measurements have high level of heat transfer enhancement, even though a good uniformity is not reached for this configuration with film cooling holes. For the same reason a reduction of the cooling potential through the lattice system was found; both flow field and heat transfer measurements demonstrated that this reduction is due to a combination of the flow velocity reduction (due to the film cooling bleed) and of the heat pick up.

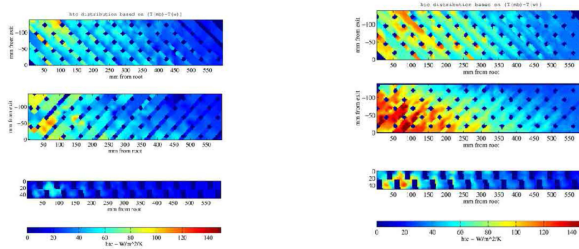
(a) h_{mb} map at $Re = 17900$ (b) h_{mb} map at $Re = 25800$

Figure 2.42: Maps of heat transfer coefficients h_{mb} based on the local mixed bulk temperature for two different Reynolds number [89]

2.2.2.4 Bunker (2004)

A detailed investigation on heat transfer coefficients and pressure losses in lattice-matrix channels was performed by Bunker in 2004. In the same year he presented the results of experiments in both stationary conditions (Bunker [86]) and rotating conditions (Acharya et al. [92]).

The results of the investigations on stationary experiments are reported in this section, while all the details of the rotating experiments will be given in the next section.

Unlike the study of Gillespie et al. [89] reported in the previous section about the convergent model for a trailing edge, Bunker performed experiments on test models with a constant channel and rib height.

In this investigation he used two methods to determine the local and overall heat transfer coefficients for two matrix models. Both thermochromic liquid crystals (TLCs) and infrared thermographic (IR) methods were applied on acrylic and metallic models respectively; in this way it was possible to discern the heat transfer coefficients without and with the effects of internal rib/fin effectiveness.

In the first case heat transfer tests with TLCs were performed in steady state conditions on acrylic test models with insulating ribs in order to determine heat transfer on the primary or endwall surfaces representing the pressure and suction side walls of an airfoil. In the second case heat transfer tests with an infrared camera were performed in transient conditions on metallic models with metal ribs in order to evaluate the additional impact of fin effectiveness provided by ribs.

Tests were executed varying the Reynolds number based on the sub-channel hydraulic diameter from 20000 to 100000 on two geometries with a rib angle of $45deg$. The two geometries have the same geometric parameters with the exception of the overall width W resulting in a different number of sub-channels: 4 for the geometry with the lower width W and 6 for that with the higher W . Moreover, it should be noted that the geometry with a higher overall width allows a longer flow development length L_c . Moreover, in all test cases the sub-channel aspect ratio is close to 1, while the average number of turns experienced by the flow in any sub-channel is 3.

All the geometric parameters for the two test models are indicated in Table 2.2. These parameters are related to the Figure 2.35 shown in the previous section 2.2.1.

The acrylic test models were installed in a test facility (Figure 2.43) com-

posed by a plenum vessel, a smooth developing flow section and a Liquid Crystal Thermography system with a RGB camera. Thermochromic liquid crystals (40C5W) with a wide band response in the range between 40°C and 45°C were applied on two layers representing the two primary surfaces to be investigated, while a thin foil heater made of Inconel was attached to these surfaces in order to set a uniform heat flux during each test.

Table 2.2: Acrylic model dimensions for the two geometries tested by Bunker [86]

Parameter	Model #1	Model #2	
β	45	45	deg
H	1.035	1.035	cm
W	6.096	9.144	cm
W_i	1.143	1.143	cm
W_c	0.808	0.808	cm
t_i	0.381	0.381	cm
t	0.269	0.269	cm
H/W_c	1.28	1.28	-
D_h	0.90748	0.90748	cm
L	18.288	27.432	cm
L_c	8.621	12.932	cm
L_c/D_h	9.500	14.250	-
# Average turns	3	3	-
# Sub-channels	4	6	-

The surface temperature measurements were made using the steady state liquid crystal hue detection method of Farina et al. [93].

Then the local heat transfer coefficient h was derived from the following definition:

$$h = \frac{(Q_{total} - Q_{loss})}{[A_{surface} \cdot (T_{wall} - T_{surface})]} \quad (2.16)$$

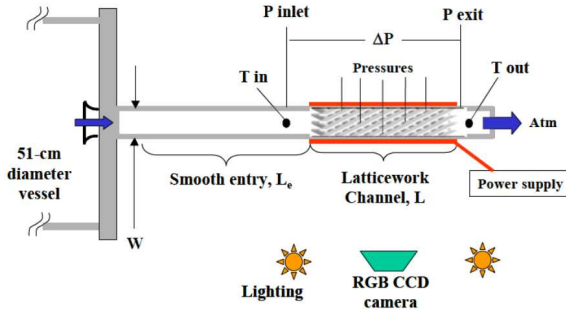
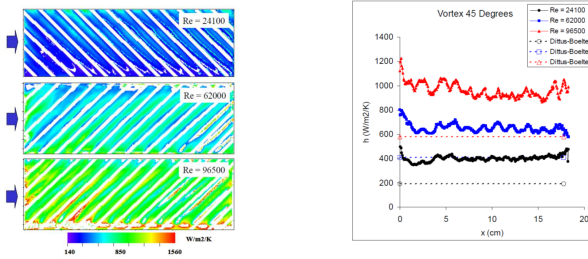


Figure 2.43: Test apparatus for heat transfer tests on acrylic test models [86]

where $(Q_{total} - Q_{loss})$ is the input heater power per unit area after the evaluation of heat losses Q_{loss} , T_{wall} is the local interior wall temperature derived from the local liquid crystal and T_{air} is the bulk air temperature. In all tests the minimum temperature potential between the heated surface and the bulk air was maintained at 20°C.

An example of the heat transfer coefficient maps for the geometry with 4 sub-channels and hence lower overall width (i.e. Model #1) is shown in Figure 2.44a, while the corresponding HTC distributions laterally averaged for the same Reynolds numbers are reported in Figure 2.44b.

Maps in Figure 2.44a show that the heat transfer coefficient only increase after the flow has encountered the first side wall turn region. Then higher HTCs are obtained in the regions where the flow comes out of the turn; in fact the heat transfer coefficient immediately after a turn region is essentially doubled from that on the opposite side of the channel where the flow is entering a turn.



(a) HTC map for primary surface (b) Laterally averaged HTC distributions for primary surface

Figure 2.44: HTC map and laterally averaged distributions of heat transfer coefficients for primary surfaces of geometry with narrow sub-channels [86]

Moreover, both the HTC maps and HTC distributions show that a high and uniform level of heat transfer is maintained both axially and laterally for each Reynolds number.

From these results obtained only on the primary or endwall surfaces of the matrix models, Bunker concluded that the global average heat transfer enhancement lies in the range of 1.5 to 1.75; the model with 4 sub-channels and narrow passages provides the highest levels especially at the lower Reynolds number (Figure 2.45).

A second experimental campaign was carried out to evaluate the additional heat transfer contribution of fin effectiveness provided by ribs and hence the overall heat transfer enhancement with fin effects.

In this case Bunker applied a method developed by Nirmalan et al. [94]; this method consists in a transient infrared thermography technique and it was adopted to provide a direct quantitative measurement of the internal heat transfer distribution within a cooled turbine airfoil.

Moreover this method uses measured flow rates and part geometry in conjunction with transient infrared data and inverse conduction analysis to determine the internal full-surface HTC distribution. For this study Bunker simplified this method through the elimination of the detailed finite element model of the channel structure. Instead, the channel outer

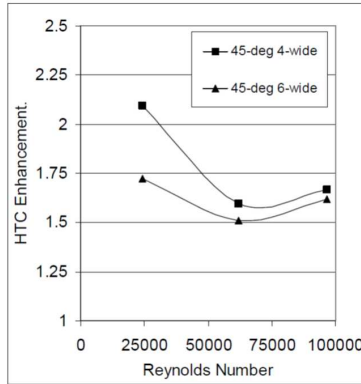


Figure 2.45: Heat transfer enhancement evaluated on the primary surfaces of the two acrylic models [86]

wall is considered to be a uniform sheet of metal with constant thickness. The thermal transient response of the external surface temperature includes the effects of the internally conductive ribs of the several sub-channels.

As regards the heat transfer coefficient on the rib surfaces, this contribution is lumped into the wall response as a fin effectiveness. Since this term may be approximated by a simple one dimensional wall of finite thickness, neglecting conduction laterally within the wall, then a lumped thermal capacity model is used to determine the internal heat transfer coefficient. This thermal capacity model is expressed as:

$$\left\{ \begin{array}{l} \frac{T_s(t) - T_{initial}}{T_{coolant} - T_{initial}} = e^{-at} \\ a = \frac{h}{\rho l c_p} \end{array} \right.$$

where l is the constant thickness of the channel outer wall.

To determine more accurately the heat transfer coefficient on the rib surfaces, this lumped parameter also takes into account: a one-dimensional

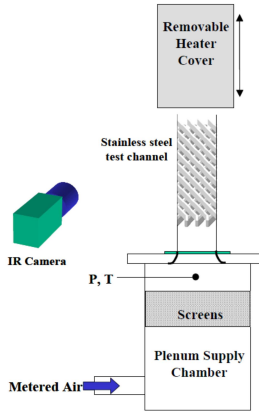


Figure 2.46: Test apparatus for transient heat transfer tests on metallic models using an IR camera [86]

temperature difference across the finite wall thickness and a simple heat balance between the adjacent elements to include the lateral heat conduction.

Figure 2.46 depicts the test section for the transient heat transfer tests on these metallic models. It mainly consists of a plenum chamber with a lattice-matrix test model affixed on the top; the plenum is supplied by a compressor air.

During a heat transfer test a removable heater jacket covers and preheats the test model to about 150°C . At a certain time the heater jacket is quickly lifted and the infrared camera starts to acquire images of the external surface temperature as a function of time.

For these experiments two metallic test models were employed, both with a rib inclination angle of 40^{deg} instead of the 45^{deg} angled ribs adopted for the acrylic models; one has 4 sub-channels, as one of the previous acrylic models, and one has 8 sub-channels. Data for these geometries are reported in Table 2.3. It should be noted that in the

Table 2.3: Metallic model dimensions for the two geometries tested during transient heat transfer tests [86]

Parameter	Model #3	Model #4	
β	40	40	deg
H	0.635	0.635	cm
W	5.080	10.160	cm
W_i	1.016	1.016	cm
W_c	0.778	0.778	cm
t_i	0.254	0.254	cm
t	0.195	0.195	cm
H/W_c	0.816	0.816	-
D_h	0.699	0.699	cm
L	25.4	25.4	cm
L_c	7.903	15.806	cm
L_c/D_h	11.302	22.604	-
# Average turns	4	2	-
# Sub-channels	2	8	-

geometry with a higher overall width W (Model #4) the flow experiences a lower average number of turns (2 instead of 4) because of the longer flow development length L_c between the sidewalls.

The results derived from the infrared images provide the overall heat transfer distributions; unlike the previous results on primary surfaces, these maps also include HTC values on rib surfaces as the effective total heat transfer coefficient experienced by an airfoil pressure or suction surface.

As in the previous HTC maps on the primary surfaces (Figure 2.44a) the distributions of heat transfer coefficient is quite periodic with the repeating ribs and HTC values are higher in the turning regions over the most length of the model.

An example of these maps is shown in Figure 2.47, while the overall heat transfer enhancement derived from these results is given in Figure 2.48.

In this case both narrow and wide geometries have enhancement factors of 2.5 to 3.

Comparing the total or overall HTC enhancement of Figure 2.48 to those of Figure 2.45, it is clear that the difference is due to rib/fin effectiveness. Moreover, these total enhancements correspond very well with those estimated using a simple fin effectiveness method based on the fin effectiveness theory and reported by Bunker in this same work.

Therefore, it can be concluded that the heat transfer coefficients measured on the primary surfaces are also applicable on the rib surfaces in terms of average results; as a consequence, the HTC's distributions on the primary surfaces can be also extended to the rib surfaces. This means that the treatment of the matrix ribs as simple fins is appropriate and each rib surface has about the same HTC value on average as that of the primary surface.

In addition to this, it can be concluded that the range of overall heat transfer enhancements $2.5 \div 3$ rivals with the commonly used turbulated channels; these values are little higher for geometry with narrow sub-channels. According to these results, matrix cooling geometries have a significant potential compared to other more conventional cooling methods.

2.2.2.5 Acharya et al. (2004)

This section describes the work performed by Bunker together with Acharya et al. [92] about the effects of rotation on heat transfer coefficients and friction factor distributions on matrix geometries. They analyzed the performance of a matrix geometry in a rotating test rig varying Reynolds number from 5000 to 50000, Rotation number from 0 to about 0.086 and the inlet density ratio from 0.075 to 0.18.

A matrix geometry was installed on the arm assembly of the rotating test rig shown in Figure 2.49. An electrical motor drives the entire rotating assembly varying the rotational speed from 0 to a maximum of 1500 rpm. The air is provided by a compressor-dryer-reservoir system, is circulated

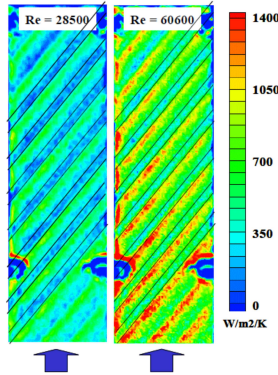


Figure 2.47: HTC maps from transient infrared method for two Reynolds numbers (Model #3) [86]

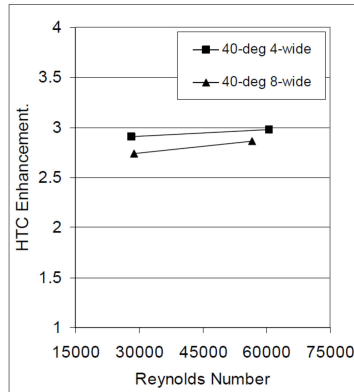


Figure 2.48: Overall heat transfer enhancement of the two investigated geometries as a function of Reynolds number [86]

through a refrigerant cooling loop to achieve the desired density ratio and flows radially into the test model.

Tests were executed on one test model with ribs inclined at 45deg to

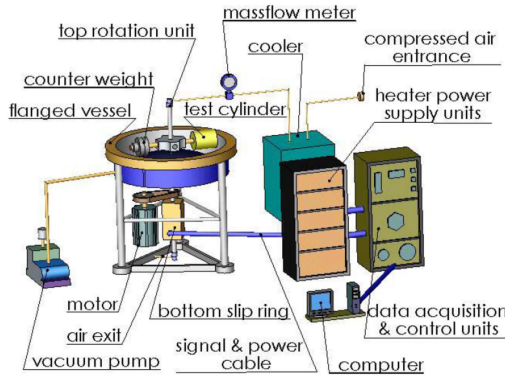


Figure 2.49: Rotating test rig used by Acharya et al. [92]

the radial direction and with 6 sub-channels. The model is formed by two layers: leading and trailing side. A top section view of the leading side is represented in Figure 2.50.

Each layer is composed by a frame and a matrix geometry. The frame is made of a laminated glass fabric (G-10 Garolite) with a thermal conductivity of 0.1 W/mK , while the internal matrix geometry is formed by 17-copper elements, with the adjacent elements separated from each other by insulation spacers of G-10 Garolite.

The passage cross-section has an aspect ratio of 4:1 with dimensions of 2.54 cm by 0.635 cm . The trailing half of the model is a mirror image of the leading side except that the latticework ribs on the copper elements are orthogonal to the ones in the leading side.

Each copper plate is equipped with a Minco Kapton etched foil heater, and a K-type thermocouple; in this way it is possible to individually regulate the heat flux of each copper plate to get an isothermal wall condition as measured by the thermocouple.

The isothermal wall condition was achieved by varying the power

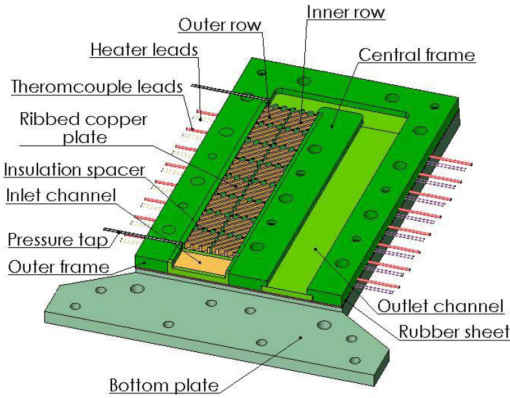


Figure 2.50: Test model (leading side) installed on the rotating test rig [92]

input to each heater attached to the individual copper plates. In addition to this, the temperatures of each copper plate was maintained within $\pm 0.5^\circ\text{C}$ of the average wall temperature T_w . Different density ratios were obtained by varying T_w and inlet flow temperature T_{in} . The local heat transfer coefficient h_i is calculated for the i -th copper plate from the net heat flux $q_{net,i}$, the wall temperature of the plate T_w and the local bulk mean air temperature $T_{b,i}$ as follows:

$$h_i = \frac{q_{net}}{(T_{wall} - T_{b,i})} \quad (2.17)$$

where $q_{net} = (Q_i - Q_{loss,i})/A_i$, while $Q_i = I_i^2 \cdot R_i$ is the power input for each copper element.

The term $Q_{loss,i}$ represents the heat loss from the i -th element considering A_i as the total area (including the area of rib surfaces) and is determined by a series of stationary tests without flow; when the stationary condition is reached it means that the power input is balanced by the

heat loss.

As regards the local bulk mean air temperature $T_{b,i}$, this is calculated at the mid point of each copper plate and is given by an energy balance equation as follows:

$$T_{b,i} = T_{in} + \frac{[\sum_{j=1}^{i-1} (Q_j - Q_{loss,j})_{leading} + \frac{1}{2}(Q_i - Q_{loss,i})_{leading}]}{\dot{m} \cdot c_p} + \frac{[\sum_{j=1}^{i-1} (Q_j - Q_{loss,j})_{trailing} + \frac{1}{2}(Q_i - Q_{loss,i})_{trailing}]}{\dot{m} \cdot c_p} \quad (2.18)$$

where \dot{m} is the mass flow rate and c_p is the specific heat capacity for the air.

Once calculated the heat transfer coefficients h_i , Nusselt numbers Nu_i , based on the sub-channel hydraulic diameter D_h are calculated as:

$$Nu_i = \frac{h_i \cdot D_h}{k} \quad (2.19)$$

Nusselt numbers Nu_i may be normalized by the Dittus-Boelter correlation ($Nu_0 = 0.023 \cdot Re^{0.8} \cdot Pr^{0.4}$) valid for fully turbulent developed flow in smooth ducts in order to obtain the heat transfer enhancement. The performance of this test model were also evaluated in terms of friction factor. Starting from the measurement of the overall pressure drop Δp through the model, the average friction factor f is calculated as:

$$f = \frac{\Delta p \cdot D_h}{4 \cdot L \cdot 1/2 \cdot \rho \cdot V^2} \quad (2.20)$$

where L is the distance between the two pressure taps, while V is the mean velocity of the flow.

To obtain the friction enhancement with respect to the flow condition in a smooth duct, the friction factor f is normalized by f_0 derived from the Karman-Nikuradse correlation ($f_0 = 0.046 \cdot Re^{-0.2}$).

As regards the heat transfer results Acharya et al. evaluated the Nusselt number averaged along both leading and trailing surfaces as a function of

the Reynolds number based on the sub-channel hydraulic diameter Re_s . By the comparison of the present data with the stationary data of Bunker [92] with $45deg$ angled ribs made of insulating material and 6 sub-channels a good agreement was found; in fact, as shown in Figure 2.51, present data with metal ribs is only about 20% higher than the data of Bunker with insulating ribs due to fin-effects.

Higher differences were found from the comparison with the data of Bunker for metallic models. This could be the result of several different factors such as: different boundary conditions (i.e constant wall temperature in the present experiments versus constant heat flux in Bunker's work [92]), differences in the transient technique [92] versus the present steady state technique, variations in rib angle ($45deg$ in the present case to $40deg$ in [92]), and differences in the number of sub-channels (6 in the present study to either 4 or 8 in [92]).

Moreover, the same Figure 2.51 indicates that the overall averaged and normalized Nusselt numbers are relatively independent of the Reynolds number and show only a small decrease at higher Re_s .

The same results reported as a function of Rotation number Ro_s allow to better highlight the rotational effects (Figure 2.52); it is clear that the rotation does not produce a significant effect on the channel-averaged Nusselt number for the whole range of Reynolds number, with the exception of the lowest $Re_s = 5000$, where a reduction of nearly 25% is present at $Ro_s = 0.086$.

The section view of the test model in Figure 2.50 shows two rows of copper elements (inner and outer) for the leading side, but other two rows are present for the trailing side. For this reason, since at each streamwise location, two spanwise copper elements are used, Nusselt number information is obtained at two spanwise locations (inner and outer).

Figure 2.53 shows the averaged normalized Nusselt numbers as Nu_s/Nu_{s0} distributions along the inner and outer locations at $Re_s = 20000$ for stationary conditions. These distributions are quite uniform along the streamwise direction from the inlet to the outlet with heat transfer enhancement levels in the range of $2 \div 2.5$.

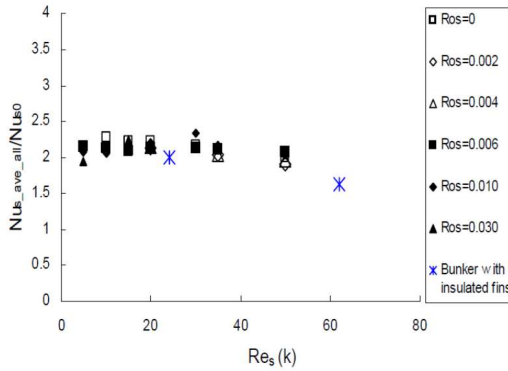


Figure 2.51: Sub-channel averaged Nusselt numbers as a function of Reynolds number Re_s [92]

From these distributions an interesting result should be noted: in fact the heat transfer along the outer row of the leading side (suction-side of the airfoil) is about 20% higher than that along the inner row, while on the trailing side (pressure-side of the airfoil) the heat transfer along the inner row is comparably higher than that along the outer row. The average Nu_s/Nu_{s0} along the leading inner row and the trailing outer row is 2.0, while the average Nu_s/Nu_{s0} along the leading outer row and the trailing inner row is about 2.4 for the same Reynolds number ($Re_s = 20000$). This interesting result is related to the coolant flow path through the matrix sub-channels; in fact the higher heat transfer values along the leading-outer and trailing inner are associated with the flow turning into the sub-channels from the opposite walls at these locations. In these regions the flow turns and impinges on the opposite walls; this impingement effect contributes to raise the heat transfer coefficient. Similar results were found by Bunker [86] and also by Wagner et al. [69] and

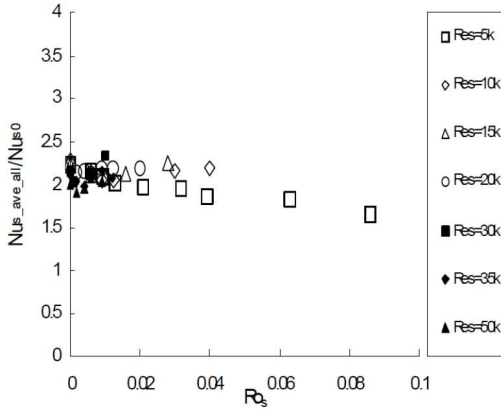


Figure 2.52: Sub-channel averaged Nusselt numbers as a function of Rotation number Ro_s [92]

Zhou et al. [95] in their studies of flow past bends in serpentine cooling passages.

In view of the differences reported in Figure 2.53 for the stationary experiments along the inner and outer sides of the leading and trailing surfaces, the rotation effects were examined along the four individual rows in terms of Nu_s/Nu_{st} distributions for different Rotation numbers, where Nu_{st} is the corresponding Nusselt number for the stationary condition (0 rpm).

As regards the rotating results, the Nu_s/Nu_{st} streamwise distributions along each of the four rows for different values of the Rotation number indicate that the heat transfer is insensitive to the rotational effects till $X/D_{h,s} = 40$ (i.e the initial $2/3rds$ of the coolant passage). An example of these distributions for the leading outer row is reported in Figure 2.54; the results for the other rows can be seen in Acharya et al. [92].

The differences found for $X/D_{h,s} > 40$ do not conform to the rotation effects observed in smooth or normal/angled-ribbed coolant passages; in

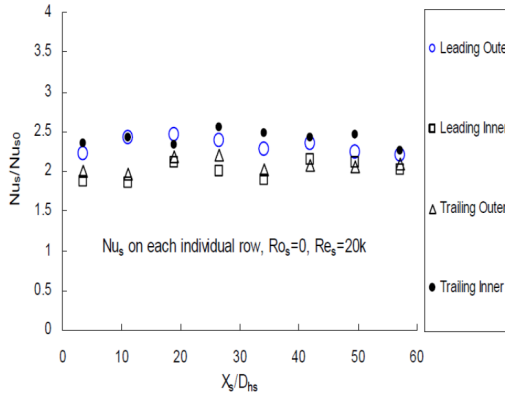


Figure 2.53: Nusselt number distributions on individual rows for stationary experiments [92]

fact it is well known that in the smooth and ribbed passages with radial outflow, rotation-induced secondary flow enhances the heat transfer on the pressure side or trailing wall, but reduces the heat transfer on the suction-side or leading wall. In the present case the rotation effects are reduced by two factors: first, the increased area due to the presence of ribs leads to significant viscous or frictional effects, second, the repeated turning of the flow through the bends makes it much more difficult to maintain sustained secondary patterns, compared to the flow in straight smooth and ribbed passages. Since the matrix model shows this insensitivity to rotational effects for intermediate and high values of Reynolds number, it can be concluded that there is not evident a heat transfer degradation with rotation.

On the other hand, at the lowest Reynolds number $Re_s = 5000$, a significant rotation effect is observed in the second half of the coolant passage ($X/D_{hs} > 30$), with a decrease in average Nusselt number with the increasing of Rotation number Ro_s (Figure 2.55). Other results show that

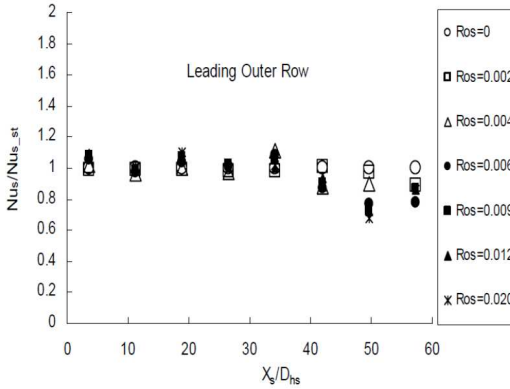


Figure 2.54: Rotation effects on the leading outer row at $Re_s = 20000$ [92]

the heat transfer performance appears to degrade with the rotation especially in the trailing side of the matrix model.

As regards the friction results, Acharya et al. found that the normalized friction factor distributions f_s/f_{s0} are insensitive to the increase of Rotation number, while there is a linear decrease with the increasing of Reynolds number (Figure 2.56).

Finally, by combining heat transfer and friction results, the trend of Thermal Performance Factor TPF with the Reynolds number was determined; TPF values are in the range of $1.2 \div 1.3$ and are comparable to values for $90deg$ ribbed square channel over the same Reynolds and Rotation ranges. However, at higher Reynolds number the f_s/f_{s0} ratio decreases with Re_s , while the Nu_s/Nu_{s0} ratio remains relatively constant; this implies that the TPFs for the matrix geometries becomes higher for $Re_s > 50000$.

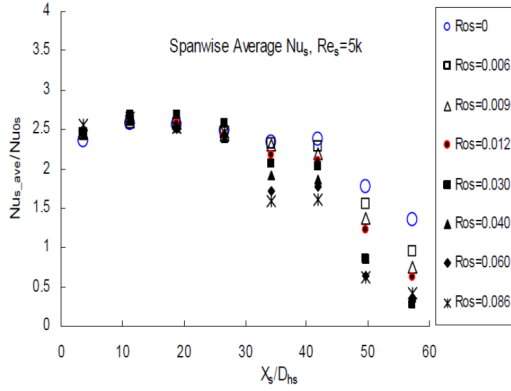


Figure 2.55: Rotation effects at $Re_s = 5000$ [92]

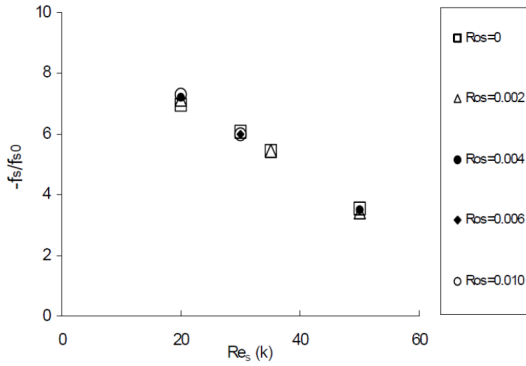


Figure 2.56: Friction factors at different Reynolds and Rotation numbers [92]

2.2.2.6 Oh et al. (2008-2012)

Rotational effects on heat transfer and friction distributions in matrix cooling channels were also investigated by Oh et al. [96] [97].

Tests were carried out on the aluminum test model reported in Figure 2.57a; it has four entry sub-channels and 45deg angled ribs, while the other geometric dimensions are summarized in Table 2.4. These geometric parameters are related to Figure 2.57b.

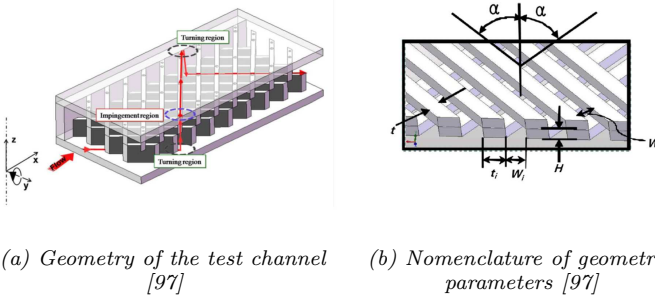


Figure 2.57: Geometry and nomenclature of geometric parameters for the test model used by Oh et al. [97]

Table 2.4: Dimensions of aluminum test model for rotating tests [97]

Parameter	Model	
β	45	deg
H	24	mm
W_i	120	mm
W_i	24	mm
W_c	16.97	mm
t_i	8.0	mm
t	5.57	mm
# Sub-channels	4	-

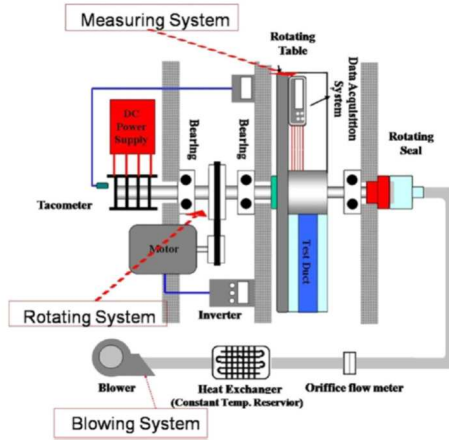


Figure 2.58: Schematic view of the rotating test rig adopted by Oh et al. [97]

This test model was mounted on the rotating test rig in Figure 2.58; more details about this experimental facility are given in Hong et al. [98]. As in the previous work of Acharya et al. [92], the air radially flows into the test model and heat transfer measurements were performed on both the leading surface (i.e. suction side) and trailing surface (i.e. pressure side).

In this case the investigated ranges for Reynolds Re_s and Rotation Ro_s numbers, both based on the sub-channel hydraulic diameter, are: $Re_s = 2600 \div 11000$ and $Ro_s = 0 \div 0.8$.

Unlike all the previous experimental works on matrix cooling systems, the naphthalene sublimation method was employed to obtain the detailed heat/mass transfer coefficients, using the analogy between heat and mass transfer. Details about this experimental procedure and this data reduction process were previously reported by Park et al. [99]. From the local mass transfer coefficient, the Sherwood number was obtained as follows:

$$Sh = \frac{h_m \cdot D_h}{D_{naph}} \quad (2.21)$$

where h_m is the mass transfer coefficient, while D_{naph} is the mass diffusion coefficient of naphthalene vapor in air.

Then the mass transfer results were expressed in terms of Sherwood number ratios Sh/Sh_0 , in order to effectively estimate heat/mass transfer augmentation, where Sh_0 is the Sherwood number for a fully developed turbulent flow in a stationary smooth circular tube derived from McAdams correlation ($Sh_0 = 0.023 \cdot Re^{0.8} \cdot Sc^{0.4}$).

From local values of Sherwood number the linear and average values $\overline{Sh_L}$ and $\overline{Sh_R}$ were calculated by integrating the local Sherwood numbers weighted by area over each sub-channel.

On the other hand, the friction factors were calculated from the overall pressure difference Δp between the inlet and the outlet of the test channel as follows:

$$f = \frac{\Delta p}{\left[4 \cdot \left(\frac{L}{D_h} \right) \cdot \left(\frac{1}{2} \cdot \rho \cdot U^2 \right) \right]} \quad (2.22)$$

These friction factors are normalized by f_0 which represents the friction factor for a fully developed turbulent flow in a stationary smooth circular tube; in this case f_0 is derived from the Petukhov equation ($f_0 = 2 \cdot (2.236 \cdot \ln(Re) - 4.639)^{-2}$) that closely fits the Karman-Nikuradse correlation ($f_0 = 0.046 \cdot Re^{-0.2}$).

As regards the heat or mass transfer results for the stationary cases, the Sh/Sh_0 distributions were similar for the different sub-channels on both the leading and trailing surfaces. As an example, Figures 2.59a and 2.59b reports the contour plots of Sh/Sh_0 and the line-averaged Sh_L/Sh_0 distributions for the trailing surface respectively, while Figures 2.60a and 2.60b reports the same type of results for the leading surface. Both maps and distributions allow to discern the results between turning and impingement regions; the Sh/Sh_0 ratio is higher (up to 4.8) in the impingement region and decreases along the sub-channel as the thermal/mass

boundary layer develops and returns to slightly increase in the turning region.

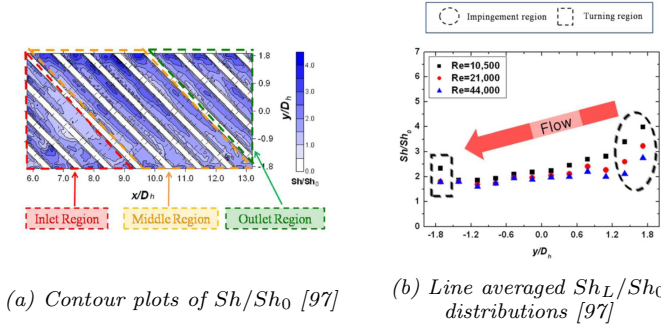


Figure 2.59: Contour plots of Sh/Sh_0 in the stationary case ($Ro = 0$) for the trailing surface and line averaged Sh_L/Sh_0 distributions for the trailing surface [97]

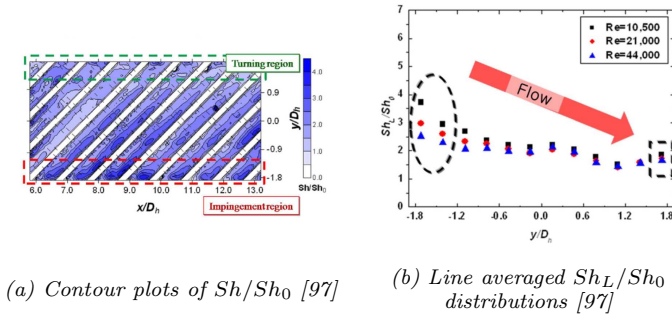


Figure 2.60: Contour plots of Sh/Sh_0 in the stationary case ($Ro = 0$) for the leading surface and line averaged Sh_L/Sh_0 distributions for the leading surface [97]

In the rotating cases the Sh/Sh_0 ratio increases on the leading surface with maximum peaks in the impingement region, while only small changes occur on the trailing surface with the increasing of Rotation number. This was the reverse of what happens in rotating channels with

radial outflow, where the Coriolis effect causes the values to increase on the trailing surface and decrease on the leading surface, as the Rotation number increases. Starting from these results Oh et al. concluded that a matrix cooling system is advantageous when a greater heat load is applied to the leading surfaces of the rotor blades than to the trailing surfaces; in fact in this situation the heat transfer performance for a conventional internal passage decreases significantly on the leading surfaces under rotating conditions.

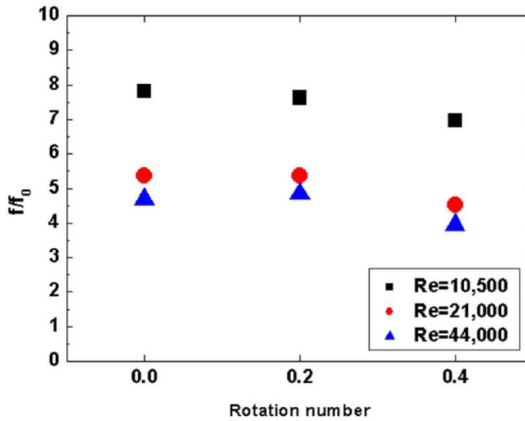
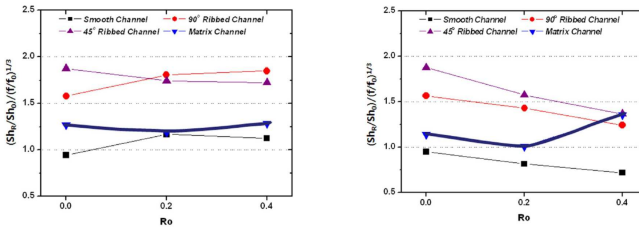


Figure 2.61: Friction factor ratios for various Rotation and Reynolds numbers [97]

As regards the friction factor distributions (Figure 2.61), Oh et al. found similar results to those of Acharya et al. [92]; in fact the f/f_0 ratio decreased with the increasing of Reynolds number but it is quite insensitive to the variation of Rotation number.

Finally, Oh et al. carried out a performance comparison between the investigated matrix geometry and other cooling methods: a smooth channel, a $90deg$ ribbed channel and a $45deg$ ribbed channel. Figures 2.62a and 2.62b show the thermal performance factors with the increasing of



(a) TPF comparison on trailing surface (suction side) [97]

(b) TPF comparison on leading surface (pressure side) [97]

Figure 2.62: Comparison of Thermal Performance Factors TPF for various cooling methods [97]

Rotation number for the different cooling methods on trailing and leading surface respectively.

In the smooth and ribbed channels TPF decreases steadily on the leading surface and increases slightly on the trailing surface with the increasing of Rotation number; on the other hand, the matrix geometry shows a different behaviour and the performance increases on both surfaces for $Ro > 0.2$. In particular, the thermal performance increases rapidly on the leading surface at the highest Rotation numbers.

From these comparisons it should be noted that the overall thermal performance of the matrix geometry is lower than of the ribbed channel but it must be considered that in the present study only the convective heat transfer on the endwall surfaces was included. Considering that the conduction heat transfer of matrix ribs (i.e. fin effect) is much higher than that of a ribbed channel because of the higher heat transfer surface area, the thermal performance of a matrix geometry would be surely improved by including these effects.

2.2.2.7 Saha et al. (2008-2013)

In recent years Saha et al. [100] [6] realized two interesting experimental works on a converging lattice-matrix structure representing a realistic gas turbine blade trailing-edge cooling passage.

In both works heat transfer distributions and pressure drop were evaluated on scaled up models in stationary conditions. In the first work [100] tests were performed varying the Reynolds number from 24000 to 60000, while in the second work [6] the investigated range was from 4000 to 20000; in both cases the Reynolds number is based on the sub-channel hydraulic diameter.

In the first work only one geometry was analyzed, while in the second work two matrix structures with four-entry and two entry sub-channels were studied; in both cases the entry flow is characterized by a $90deg$ flow turn and matrix ribs are placed at an angle of $45deg$ to the flow direction. Unlike the previous works reported in literature, where only matrix geometries with rectangular aspect ratio with radial entry and exit were investigated, the present works are the first to deal with trapezoidal cross section with a $90 deg$ flow turn at the entry. The combination of $90deg$ turn into the matrix geometry and a converging cross section allows to represent a more realistic case.

Since the heat transfer measurements were executed using a transient liquid crystal technique, the test sections (Figure 2.63a) were made using acrylic sheets in order to allow an optical access for the image acquisition, while the different convergent matrix cores (Figure 2.63b) were made of ABS. As shown in this figure one side of the lattice is straight and another side is inclined at an angle $15deg$ to reproduce the channel convergence. Then the matrix geometry with four-inlet sub-channels changes cross section from $AR=2.46:1$ to $AR=11:1$ while the configuration with two-inlet sub-channels changes cross section from $AR=1.12:1$ to $AR=5:1$.

The target surfaces are the front and back walls of the convergent test section that supports the matrix core structure; these surfaces represent the pressure and suction side of the airfoil. A narrow-band thermochromic liquid crystal (TLC 35C1W) is sprayed on the walls and a black paint

is then sprayed over the liquid crystal to enhance the contrast of the acquired images.

For the data analysis the color change of TLCs from red to green is analyzed and the time required for the green color to appear is used; images are post-processed by means of the green band tracking technique used by Vedula et al. [101]. Then the heat transfer coefficient is obtained by assuming 1D transient heat conduction with semi-infinite boundary condition. Under this assumption, when a step change of the mainstream air flow occurs, the solution of the wall temperature can be found by:

$$\frac{T_w - T_0}{T_\infty - T_0} = 1 - \exp\left(\frac{h^2 \alpha t}{k^2}\right) \operatorname{erfc}\left(\frac{h\sqrt{\alpha t}}{k}\right) \quad (2.23)$$

However, since a perfect step change of the mainstream air temperature is not possible to obtain and this temperature is a function of time, the solution of Equation 2.23 has to include the time-variance of this temperature; for this reason Equation 2.23 is modified by applying the Duhamel's superposition theorem and the new solution of wall temperature becomes:

$$T_w - T_0 = \sum_{j=1}^N \left[1 - \exp\left(\frac{h^2 \alpha (t - \tau_j)}{k^2}\right) \operatorname{erfc}\left(\frac{h\sqrt{\alpha (t - \tau_j)}}{k}\right) (\Delta T_\infty(i, j - 1)) \right] \quad (2.24)$$

Saha et al. reported their heat transfer results in terms of both detailed maps and distributions of the heat transfer enhancement ratio Nu/Nu_0 , where Nu_0 is derived from the Dittus-Boelter correlation as in the previous works. Results are reported for both the straight and the inclined side of the test model for different Reynolds numbers. It should be noted that, since the test model is convergent the sub-channel height H changes for different sub-channels as the flow progresses towards the exit; this implies that each sub-channel that originates downstream of the inlet has a different hydraulic diameter. To take into account this fact both Nusselt and Reynolds numbers are calculated with respect to the specific hydraulic diameter of the sub-channel at its entry.

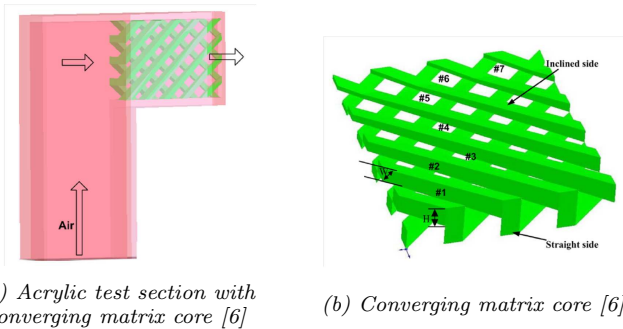


Figure 2.63: Acrylic test section with converging matrix core and convergent structure with dimensions used for calculation of the sub-channel hydraulic diameter at inlet [6]

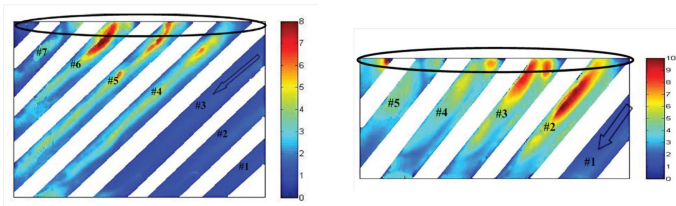


Figure 2.64: Examples of Nu/Nu_0 maps for 4 and 2 inlet channel configurations [6]

Results show that the maximum heat transfer enhancement Nu/Nu_0 with peaks close to 8 is observed in the impingement regions, where the flow turns from one sub-channel to the other. Other localized regions with high Nu/Nu_0 values are present along the different sub-channels and are due to the turbulence created by the cross flow from the other side of the matrix structure. These results are clearly shown by the detailed maps in Figures 2.64a and 2.64b for the 4 inlet channel and 2 inlet channel configuration respectively.

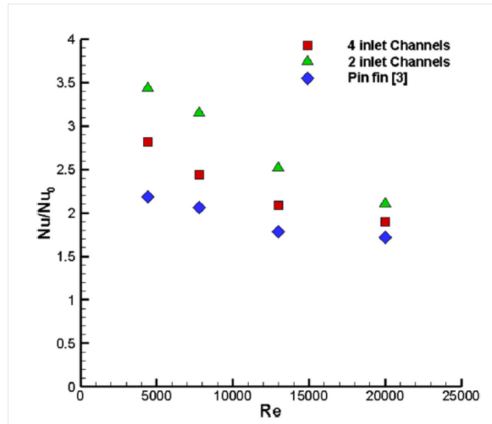


Figure 2.65: Comparison of the average heat transfer enhancement Nu/Nu_0 as a function of Reynolds number between the investigated matrix geometries and a pin fin configuration [6]

Moreover the heat transfer enhancement is reduced with the increase of Reynolds number which is common for internal cooling applications.

In terms of average results, Figure 2.65 shows the comparison of average Nu/Nu_0 ratio of the two matrix structures with the pin-fin configuration used by Metzger et al. [26]. It is shown that the pin-fin geometry produces the lowest value of heat transfer enhancement ($Nu/Nu_0 = 1.7 \div 2.2$); this is followed by the matrix geometry with four-inlet channels ($Nu/Nu_0 = 1.9 \div 2.8$), while the matrix geometry with two-inlet channels has the best performance ($Nu/Nu_0 = 2.1 \div 3.4$) for the whole Reynolds range. These results are in agreement with the findings of Bunker [86], who also found that the matrix configuration with fewer sub-channels performs better in terms of heat transfer enhancement.

As regards friction results, Saha et al. found that the pressure drop increases in the streamwise direction except in the impingement region close to the wall, where a pressure recovery occurs. The turning of flow

from one side of the lattice to the other side, and the interaction with the cross flow produces high pressure drops in the sub-channels.

The overall pressure drop is employed to calculate the friction factor defined as follows:

$$f = \frac{\Delta p / (0.5 \cdot \rho \cdot V_m^2)}{4 \cdot (\Delta x / D_m)} \quad (2.25)$$

These values are normalized by f_0 values from the Karman-Nikuradse correlation ($f_0 = 0.046 \cdot Re^{-0.2}$); then the f/f_0 values together the Nu/Nu_0 values are used to calculate the Thermal Performance Factor TPF as follows:

$$TPF = \frac{Nu/Nu_0}{(f/f_0)^{1/3}} \quad (2.26)$$

TPF values are calculated for both the matrix geometries and are compared with the values for the above mentioned pin fin configuration [26]; from this comparison results that the two-inlet channel matrix geometry has the best performance, but for the highest Reynolds number the pin fin performs better than the matrix structures (Figure 2.66).

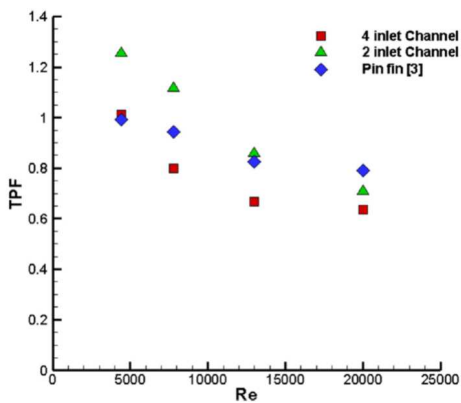


Figure 2.66: TPF comparison between the investigated matrix geometries and a pin fin configuration [6]

Chapter 3

Heat Transfer Measurement Techniques

As already discussed in section 1.2 one of the main objectives of the present experimental work is the measurement of the heat transfer coefficient within scaled up models reproducing matrix cooling geometries for a possible application as internal cooling systems in gas turbine airfoils. For this reason the present chapter reports an overview about the fundamental principles and assumptions of some experimental approaches to measure the local heat transfer coefficient distributions on geometries for internal blade cooling applications.

3.1 Introduction to HTC Measurement

Usually the experimental investigation on the heat transfer coefficient is carried out on both simple and complex internal schemes reproducing heat transfer and flow conditions similar to that in actual gas turbines. Experiments are executed at low temperatures on scaled up test models; data obtained from these experiments are expressed in nondimensional parameters such as: Nusselt and Reynolds numbers, heat transfer coefficient ratios and temperature ratios. Then, these nondimensional parameters may be scaled to engine flow conditions in order to get the heat

transfer performance in real operative conditions.

Before starting to explain the different experimental techniques, it should be noted that the different measurement techniques play a dominant role in the investigation of heat transfer phenomena in internal cooling applications such as: gas turbine cooling, heat exchangers and thermal control of electronic devices. Unlike the heat transfer processes in evaporators and condensers, the cooling fluid for turbine blade cooling is not usually subject to phase changes and hence this process belongs to the category of single-phase forced convection. Other assumptions are considered in order to simplify the heat transfer investigation: cooling fluid may be treated as an ideal gas, the flow velocity in the internal channels corresponds to low Mach number ($M < 0.3$) to avoid large pressure losses due to compressibility effects and hence the fluid may be treated as incompressible. With regard to this latter assumption, some exceptions are possible in trailing edge passages or local impinging jets or local extractions via film cooling holes, where high velocities and pressure losses may occur.

On the other hand geometrical situations to be investigated are complex, the flow is usually turbulent with high three-dimensional velocity and temperature fields and this leads to strong variations in the local heat transfer distributions. In addition to this, in case of rotor blades, Coriolis and centrifugal forces due to temperature difference must be taken into account.

The convective heat transfer coefficient which will be investigated in the present work is defined by means of the so-called "Newton's Law of Cooling", that establishes a linear relationship between the specific heat flux at a surface and an appropriate temperature difference between the surface or wall temperature and a reference fluid temperature. The heat transfer coefficient defines the proportionality in this relationship and is defined as:

$$h_{tc} := \frac{\dot{q}_w}{T_w - T_f} \quad (3.1)$$

where q_w is the area specific wall heat flux from the wall into the fluid

for a cooling situation, for which $T_w > T_f$. Newton also observed that for a given flow and thermal situation the heat transfer coefficient can be considered time-invariant.

The formulation given in Equation 3.1 was used by Fourier in his transient analysis for solid bodies. From this equation it is possible to derive the relationship between heat flux and wall normal solid temperature gradient at the surface, that is also known as "Fourier's Law" and it is expressed as follows:

$$\dot{q}_w = -k_s \left(\frac{\partial T_s}{\partial n} \right)_w \quad (3.2)$$

where k_s is the thermal conductivity and T_s or T_w is the temperature of the solid.

The conduction boundary-value problem for the solid with constant thermal properties is given by:

$$\frac{\partial T_s}{\partial t} = \frac{k_s}{\rho_s c_s} \nabla^2 T_s = \alpha_s \Delta_s T_s = \alpha_s \left(\frac{\partial^2 T_s}{\partial x^2} + \frac{\partial^2 T_s}{\partial y^2} + \frac{\partial^2 T_s}{\partial z^2} \right) \quad (3.3)$$

$$T_s(x, y, z, t = 0) = T_0, \quad -k_s \left(\frac{\partial T_s}{\partial n} \right)_w = htc (T_w - T_f) \quad (3.4)$$

Then, the conduction problem within the solid can be formally decoupled from the fluid convection problem and the local solid-fluid temperature field near the wall is incorporated in the heat transfer coefficient.

The value of the heat transfer coefficient needs then to consider the complexity of the surrounding flow field, the effects of thermal boundary conditions and has to be based on an appropriate fluid reference temperature.

In case of turbulent forced convection the heat transfer coefficient is nearly independent of the temperature boundary condition and is mainly determined by the flow field situation [102].

Moreover, if the temperature differences are not large and thermal proper-

ties of cooling fluid can be considered as constant, then the heat transfer coefficient is independent of the actual wall and fluid temperatures [103]. Under this assumption it is possible to perform laboratory experiments and relate the experimental data to actual engine conditions.

The temperature of solid T_s and fluid T_f have to be equal at the wall and the local heat flux from the solid must be equal at any time to the local heat flux into the fluid:

$$(T_s)_w = (T_f)_w = T_w \quad \text{and} \quad -k_s \left(\frac{\partial T_s}{\partial n} \right)_w = -k_f \left(\frac{\partial T_f}{\partial n} \right)_w \quad (3.5)$$

From Equation 3.5 the following definition of heat transfer coefficient can be derived:

$$h_{tc} = \frac{-k_f \left(\frac{\partial T_f}{\partial n} \right)_w}{(T_w - T_f)} \quad (3.6)$$

where k_f is the thermal conductivity of the fluid.

Then to transfer experimentally determined heat transfer coefficient with respect to the similarity considerations, it needs to be dimensionless represented by the Nusselt number Nu . From Equation 3.6, using a geometrical scaling with a reference length l :

$$\tilde{n} = \frac{n}{l} \quad (3.7)$$

and using a dimensionless form for the fluid temperature field:

$$\Theta = \frac{T_f - T_w}{T_{ref} - T_w} \quad (3.8)$$

the dimensionless temperature gradient normal to the wall is given by the Nusselt number:

$$Nu = \frac{\Theta}{\partial \tilde{n}} \Big|_w = \frac{h \cdot l}{k_f} \quad (3.9)$$

It should be noted that for the typical gas turbine cooling applications an appropriate reference length for the internal cooling ducts is the so-

called hydraulic diameter defined as follows:

$$l = D_h = \frac{4A}{P} \quad (3.10)$$

where A is the through-flow area in each cross-section and P is the wet perimeter at this location. Of course, for complex internal cooling systems, the hydraulic diameter $D_h(x)$ can be different at each streamwise coordinate x . As long as full geometrical similarity is achieved between experiment and application, this local value will scale with any other geometrical length scale selected.

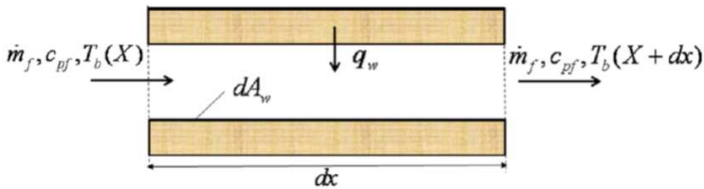


Figure 3.1: Energy balance for a heated element to calculate the bulk fluid temperature along the streamwise direction

Another important issue to allow an accurate transfer of the laboratory measurements to engine situations with respect to similarity considerations it is the reference temperature T_{ref} , that has the same meaning in the experiment and in the design.

Usually for internal cooling applications the fluid bulk temperature $T_b(X)$

for a given streamwise position X can be determined from an overall energy balance (for example using the first law of thermodynamics in a 1-D network analysis) once the heat transfer characteristics are known on all surrounding walls. For example, considering the heated element in Figure 3.1, the energy balance may be written as follows:

$$\dot{m}_f c_{pf} T_b(X + dx) = \dot{m}_f c_{pf} T_b(X) + \int_A q_w dA_w \quad (3.11)$$

Using this method the local heat transfer coefficient is based on the the local fluid reference temperature $T_b(X)$.

Other methods could be applied to determine the fluid bulk temperature; more details about these methods are given by Wolfersdorf et al. [103].

Over the years many measurement techniques have been developed to obtain the local heat or mass transfer information for internal cooling applications. A possible classification of these techniques can be given as:

1. Flow temperature measurements
2. Wall mass transfer measurements
3. Wall heat transfer measurements

3.1.1 Flow Temperature Measurements Techniques

As regards flow temperature measurement techniques, considering the heat transfer coefficient definition given by Equation 3.6, to evaluate the HTC value is necessary to determine the fluid temperature field in the near wall region using fine local thermocouples or optical techniques such as the method of interferometry or the use of Thermochromic Liquid Crystals (TLC). However, for complex geometries as usually found in internal blade cooling applications with highly three-dimensional velocity and fluid temperature fields, these techniques may be difficult to apply.

3.1.2 Mass Transfer Measurements Techniques

Mass transfer techniques use the similarity in the transfer processes between mass and heat to determine heat transfer information. Unlike the previous flow temperature measurements, these techniques can provide local data also for complex internal cooling geometries.

These techniques have also other two important advantages such as: first, they realize idealized boundary conditions (e.g. constant wall concentration relating to isothermal surfaces), second, they are not influenced by heat losses, radiation or undesired conduction processes.

Based on this assumption different methods have been developed for several applications such as: electrochemical methods, absorption methods, swollen polymer technique, ammonia and diazo technique, pressure sensitive paint and naphthalene sublimation method.

The naphthalene sublimation method is a common way to determine local and average mass-transfer coefficients, where these coefficients are determined by measuring the mass of naphthalene sublimed by forced or natural convection. In this kind of experiments a naphthalene surface is cast in the tested geometry and the initial thickness of the naphthalene layer is measured by optical or scanning methods. Then, the surface is subjected to an isothermal flow and after some test time, the change in layer thickness is measured locally with high precision and is related to sublimation due to convective mass transfer.

The associated local mass transfer coefficient h_m is evaluated by the specific naphthalene convective mass flux with respect to the difference in naphthalene vapor densities at the wall and the bulk value in the main stream; this coefficient is defined as:

$$h_m = \frac{\dot{m}''}{\rho_w - \rho_\infty} \quad (3.12)$$

where ρ_w is the local density of naphthalene at the surface and ρ_∞ is the density of naphthalene in the mainstream.

Knowing the local mass transfer coefficient h_m , it is possible to calculate the local mass transfer dimensionless Sherwood number as follows:

$$Sh = h_m \cdot \frac{L}{D_{naph}} \quad (3.13)$$

where L is the reference length for the experiment (i.e. the hydraulic diameter of a duct), while D_{naph} is the diffusion coefficient for the naphthalene.

It should be noted that the naphthalene mass is lost by sublimation due to diffusion or convection in analogy with the heat lost in heat transfer experiments.

The heat-mass transfer analogy states that the Sherwood number Sh is analogous to the Nusselt number Nu ; ratios of Sherwood number for similar conditions can be directly estimated as a ratio of Nusselt numbers for similar flow conditions [2].

The naphthalene sublimation technique allows accurate measurements for complex geometries including rotating conditions and for film cooling tests.

3.1.3 Heat Transfer Measurements Techniques

As regards the different heat transfer techniques a correct classification can be made with respect to the experimental procedure: steady state or transient techniques. A schematic view of this classification is given by Figure 3.2.

All these techniques require wall surface temperature measurements that can be obtained by means of different sensors such as: thermocouples, Thermochromic Liquid Crystals (TLC), Infrared Thermography (IR), and Temperature Sensitive Paints (TSP). A good review about these sensors is given by Wolfersdorf et al. [103].

In the following section will be analyzed the main steady state and transient techniques for the measurement of the heat transfer coefficient.

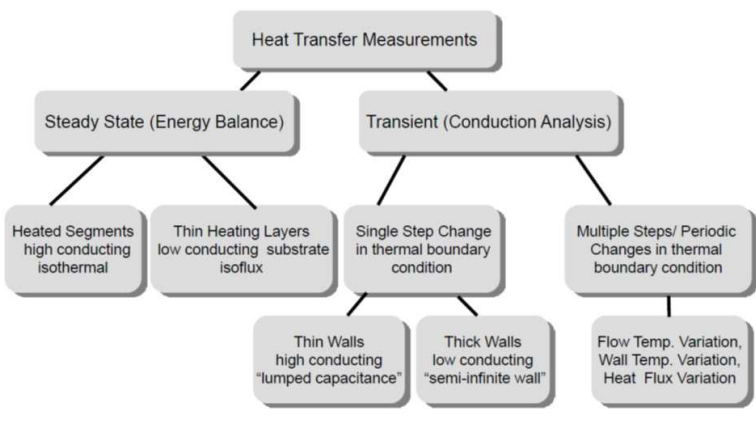


Figure 3.2: Classification of the heat transfer measurement techniques

3.2 Steady State Measurement Techniques

Steady state techniques are based on the setup of a specific heat flux from an electrical power supply. The net heat flux is calculated by estimating the heat losses due to conduction, radiation and outside wall convection. Thereby different thermal boundary conditions can be achieved, for example isothermal walls when using high conducting heated segments or nearly constant heat flux conditions when using a thin heating foil on a low conducting substrate.

3.2.1 Heated High Conducting Elements Technique

This technique consists in using discrete heated high conducting elements, generally segments, that cover the whole investigated area. Then, the thermal power for each element can be independently adjusted to

achieve a constant wall temperature over the element surface area for all elements within the investigated configuration. Temperatures can be measured by embedded thermocouples, for example one for each element; these temperatures can be considered as regionally averaged values of temperature for the entire element because of the high thermal conductivity. According to this approach the local convective heat flux is:

$$\dot{q}_{conv} = htc(x) (T_w(x) - T_{ref}(x)) \quad (3.14)$$

This heat flux can be averaged over a segment with the element length equal to L :

$$\dot{q}_{conv} = \frac{1}{L} \int_0^L q_{conv}(x) dx = \frac{1}{L} \int_0^L htc(x) (T_w(x) - T_{ref}(x)) dx \quad (3.15)$$

Since for high conducting elements (e.g. copper plates) the measured segment temperature will be equal to the average wall temperature and with the segments being relatively small so that the fluid reference temperature can be approximated as constant (averaged) over the segment, the heat flux can be also written as:

$$\dot{q}_{conv} = \frac{1}{L} \int_0^L htc(x) (\overline{T_w} - \overline{T_{ref}}) dx = \frac{1}{L} \int_0^L \overline{htc} (\overline{T_w} - \overline{T_{ref}}) \quad (3.16)$$

This situation is well represented by the scheme in Figure 3.3.

On the other hand the heater power can be written as:

$$P_{el} = \dot{Q}_{conv} - \dot{Q}_{loss} = \overline{q_{el}} A = (\overline{q_{conv}} - \overline{q_{loss}}) A \quad (3.17)$$

Therefore, the heat transfer coefficient results as:

$$\overline{htc} = \frac{\overline{q_{conv}}}{\overline{T_w} - \overline{T_{ref}}} \quad (3.18)$$

Then, since an isothermal wall condition is reached for the segment, the true surface averaged heat transfer coefficient is obtained from the

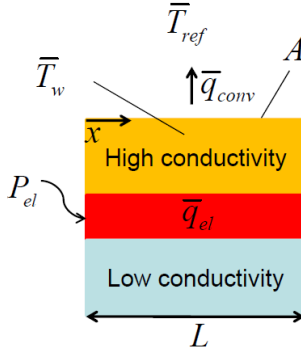


Figure 3.3: Scheme of the heated high conducting elements technique

measurement of the average convective heat flux and the average surface and fluid temperatures. Moreover, because the values of the supplied heat for each segment are known, the variations of the fluid reference temperature in streamwise direction can be obtained from a one-dimensional energy balance by using the following equation:

$$\dot{m}_f c_p \frac{dT_b}{dx} = \int_{P(x)} \dot{q}_w(s) ds \quad \text{with } T_b(0) = T_{inlet} \quad (3.19)$$

This technique includes several advantages such as:

- segments can be shaped to complex geometries including turbulators;
- thermal boundary condition can be well controlled by adjusting the individual segment heater power to obtain isothermal conditions

- a steady state energy balance approach can be applied to evaluate the fluid temperature
- the investigation of temperature ratio effects (wall-to-fluid) can be integrated
- good applicability to rotating test models
- provides temperature differences as in real blade cooling situation (hot wall, cold fluid), in order to simulate the correct buoyancy effects for rotation

3.2.2 Heated Thin Foil Technique

In this technique a uniform heat flux is generated by means of a thin heating foil applied over a low conductive substrate, as depicted in the scheme of Figure 3.4.

According to this scheme the heat transfer coefficient can be obtained as:

$$\overline{h} = \frac{\dot{q}_{conv}}{T_w(x) - T_{ref}(x)} \quad (3.20)$$

Using these heaters an isoflux boundary condition can be reached if the heating layer has a constant cross section and the electrical resistance has no significant temperature dependency.

The local heat transfer distribution is evaluated knowing the local convective heat flux, so taking into account the heat losses with the energy balance.

As regards the measurement of the local surface temperature, it is possible to use local thermocouples or optical methods such as Infrared Thermography or Thermochromic Liquid Crystals (TLC). Depending on the optical properties of the low conducting substrate, the surface temperature might be measured through the substrate or above assuming that the temperature of the thin heating foil is nearly constant over its thickness.

It should be noted that some difficulties arise for complex surfaces (e.g.

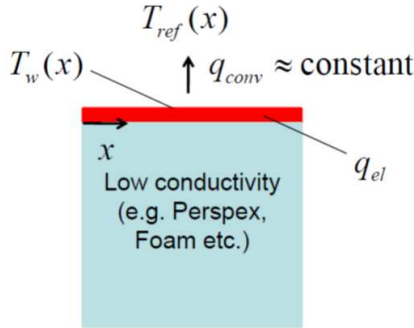


Figure 3.4: Scheme of the heating foil technique

multiple curvatures, or diverging/converging ducts), so that this technique is usually applied to flat or single curvature walls to cope with the consideration of constant local heat release. For more complex configurations it is necessary to apply specific heaters and the local electrical field needs to be analyzed by Finite Element Method numerical simulations. In recent years many studies have been performed by the University of Florence using these techniques (Maiuolo et al. [104], Caciolli et al. [105]); some experiments were also carried out in rotating conditions (Bonanni [62]).

3.3 Transient Measurement Techniques

Since the steady state techniques have some disadvantages in terms of local resolution, instrumentation effort and applicability on complex

surfaces, over the years the transient techniques have been developed especially in combination with temperature sensitive coatings as shown by Ireland et al. [106] [107].

In a transient experiment the heat transfer usually starts keeping the model at a uniform initial temperature and at the start of the test a sudden rise of temperature is imposed to the flow. This can be done using valves that open a closed loop by-pass channel where the air is pre-heated prior to the experiment. However, in recent years Ireland et al. [108] adopted a better method to increase the temperature using an electrical heated fine wire mesh; the time constant for heating the flow using a single fine mesh is relatively low (< 0.1 s) allowing to reach a very defined flow temperature step, while using more connected meshes it is possible to heat relatively large mass flow rates in a short time.

3.3.1 Thin Wall Lumped Capacitance Method

All transient methods use a conduction model to determine the heat transfer from the wall and fluid temperature measurements. One of these is the so-called thin wall lumped capacitance method based on the assumption that, if a solid body is immersed in a fluid with a temperature difference between the solid and the flow, the temperature of the solid is assumed to be spatially uniform at any instant during the transient process.

This assumption implies that the temperature gradients within the solid are negligible, which indicates an infinite thermal conductivity ($k_s \rightarrow \infty$). Even though such a condition is clearly impossible, it can be closely approximated if the resistance to conduction within the solid is much less compared to the resistance to heat transfer between the solid and the surrounding flow (Biot number $Bi < 0.1$ [87]). On this assumption, the overall energy balance relates the rate of heat loss at the surface to the rate of change of the internal energy:

$$\rho_s c_p V \frac{dT_s}{dt} = -htcA_s(T_s - T_{ref}) \quad (3.21)$$

If the solid body is initially at uniform temperature:

$$T_s(t = 0) = T_0 \quad (3.22)$$

this ordinary differential equation can be solved to give the following solution:

$$\frac{T_s - T_i}{T_{ref} - T_i} = 1 - \exp\left(-\frac{htcA_s}{\rho_s c_p V} t\right) \quad (3.23)$$

This solution assumes a constant heat transfer coefficient meaning that htc has to be independent of time as well as independent of the actual temperature difference ($T_s - T_{ref}$) at any time.

If in an experiment the highly conductive solid experiences a temperature step in its surroundings (from T_0 to T_{ref}) under the given assumptions, it is possible to determine the heat transfer coefficient from the measurement of the solid temperature $T_s(t)$ if all the other parameters are known. Therefore, this is representative of the average convective heat transfer on the surface of the body to the surrounding flow.

Typical applications of the lumped capacitance method are the measurements of the averaged heat transfer coefficient on protrusion elements such as ribs, pedestals and pin fins inside cooling channels. These elements are usually made of a high conductive material and are mounted on a well insulated substrate.

This transient heat transfer process is well represented by Figure 3.5. The temperature of the solid body is generally measured by thermocouples located inside the solid, or by means of optical methods such as TLC or IR-Thermography. This method is generally combined with other different approaches to determine the local heat transfer distribution in complex configurations.

An example of this combination is given by Bunker [86], who applied the steady state technique with the thin heating foil to measure the heat transfer between ribs and a transient IR-Thermography for a metallic model representing a latticework or matrix cooling geometry with a high blockage rib arrangements. In this way Bunker was able to evaluate the

3.3.2 Semi-infinite Wall Method

If the test model is made of a low conductive material in order to minimize the lateral conduction effects during a transient experiment and if the wall thickness is large enough, so that the thermal variation at the surface of interest does not influence the remote surface of the model, then the test model under investigation can be assumed to be a one-dimensional “semi-infinite” wall.

Under the assumptions of constant thermal properties, an uniform initial wall temperature T_i and a step variation in the fluid properties at time $t = 0$ to T_{ref} , the differential equation for this problem becomes:

$$\frac{\partial T_s}{\partial t} = \frac{k_s}{\rho_s c_p} \frac{\partial^2 T_s}{\partial y^2} = \alpha_s \frac{\partial^2 T_s}{\partial y^2} \quad 0 \leq y < \infty \quad (3.24)$$

with the following initial and boundary conditions:

$$T_s = T_i \quad \text{at } t = 0 \quad (3.25)$$

$$-k_s \left(\frac{\partial T_s}{\partial y} \right)_w = htc(T_w - T_{ref}) \quad \text{at } y = 0 \quad (3.26)$$

$$T_s = T_0 \quad \text{for } y \rightarrow \infty \quad (3.27)$$

Considering that the heat transfer coefficient is constant with time, this problem can be solved using the following equation:

$$\frac{T_s(y, t) - T_i}{T_{ref} - T_i} = \operatorname{erfc} \left(\frac{y}{2\sqrt{\alpha_s t}} \right) - \exp \left(\frac{\alpha_s y}{k_s} + \frac{htc^2 \alpha_s t}{k_s^2} \right) \operatorname{erfc} \left(\frac{y}{2\sqrt{\alpha_s t}} + \frac{htc\sqrt{\alpha_s t}}{k_s} \right) \quad (3.28)$$

Then, considering the wall temperature ($y = 0$), the Equation 3.28 becomes:

$$\frac{T_w(t) - T_i}{T_{ref} - T_i} = 1 - \exp\left(\frac{htc^2 t}{\rho_s c_p k_s}\right) \operatorname{erfc}\left(\frac{htc\sqrt{t}}{\sqrt{\rho_s c_p k_s}}\right) = 1 - \exp(Bi^2 \tau) \operatorname{erfc}(Bi\sqrt{\tau}) \quad (3.29)$$

where τ is the dimensionless time or Fourier number and it is defined as:

$$\tau = \frac{\alpha_s t}{s^2} \quad (3.30)$$

while the *erfc* is the “complementary error function” and it is defined as follows:

$$\begin{aligned} \operatorname{erfc}(x) &= \frac{2}{\sqrt{\pi}} \int_x^\infty e^{-r^2} dr \\ &= 1 - \frac{2}{\sqrt{\pi}} \left(x - \frac{x^3}{3 \cdot 1!} + \frac{x^5}{5 \cdot 2!} - \frac{x^7}{7 \cdot 3!} + \dots \right) \\ &\simeq \frac{e^{-x^2}}{\sqrt{\pi} x} \left(1 - \frac{1}{2x^2} + \frac{1 \cdot 3}{(2x^2)^2} - \frac{1 \cdot 3 \cdot 5}{(2x^2)^3} + \dots \right) \end{aligned} \quad (3.31)$$

Measuring the wall temperature variation, the initial condition T_i and the fluid temperature T_{ref} during the test, it is possible to evaluate the heat transfer coefficient *htc*. This approach is well applicable using TLC as a surface temperature measurement technique.

An important advantage of this method is the easy application on all channel walls of a cooling configuration, even though several assumptions have been made which need to be analyzed and verified otherwise additional effects need to be included in the data reduction process. One of these include the flow temperature change that might not be a perfect step. For example, if $T_{ref}(t)$ is measured, the actual temperature history might be approximated by a series of small steps and the superposition approach of Duhamel might be used obtaining the following expression:

$$T_w(t) - T_i = \sum_{j=1}^n \left[1 - \exp\left(\frac{htc^2(t - \hat{t}_j)}{\rho_s c_p k_s}\right) \operatorname{erfc}\left(\frac{htc\sqrt{t - \hat{t}_j}}{\sqrt{\rho_s c_p k_s}}\right) \right] \Delta T_{ref(j,j-1)} \quad (3.32)$$

where N is the number of steps, \hat{t}_j are the discrete times and $\Delta T_{ref(j,j-1)}$ is the temperature step between the time steps $(j - 1)$ and j .

However some effects should be considered in order to satisfy the one-dimensional hypothesis of this approach such as: the effect of finite wall thickness, surface curvature and lateral conduction.

The effect of wall thickness was analyzed by Schultz et al. [109] with respect to the application of heat transfer gauges. They used the solution for a semi-infinite wall applying a step change in surface flux, and they showed that the ratios of local heat flux and temperature at depth s to their values at the surface are both less than 1% if the dimensionless measurement time τ_d is:

$$\tau_d = \frac{t\alpha_s}{s^2} < \frac{1}{16} \quad (3.33)$$

This means that for a wall made of plexiglas or PMMA ($\alpha_s \simeq 1.08 \cdot 10^{-7} m^2/s$) and a wall thickness of about 10 mm, the measurement should not exceed 60 seconds for Equation 3.29 to be applicable.

This might not always be possible for complex geometries with long cooling channels due to thinner geometrical features (e.g. webs, divider walls, etc.) and due to the fluid temperature change in streamwise direction and hence with reduced local temperature differences between fluid and wall, so that this effect on the determined heat transfer coefficient needs to be analyzed.

Moreover, the effect of surface curvature on the heat transfer coefficient using Equation 3.29 should be considered; these effects might be important in case of leading edge or serpentine bend regions or when cylindrical or spherical turbulator arrangements (e.g. pins, dimples, etc.) are applied. With regard to this effect Buttsworth et al. [110] derived an approximative solution for curved walls in similarity to Equation 3.29 valid

for $\tau_r = (t\alpha_s)/R^2 \ll 1$ where R is the radius of the surface curvature. More details about this approach are reported by Wolfersdorf et al. [103]. In addition to the previous effects, the lateral conduction should be also considered. Usually the effect of lateral conduction within the wall is neglected assuming that the temperature gradients in lateral direction are much smaller than in vertical direction as provided by the low thermal conductivity of the materials used in the transient tests. Moreover, the short measurement times are often considered to reduce the influence of lateral conduction.

The effects of lateral conduction on heat transfer results obtained in transient tests with temperature surface coatings were analyzed by Vedula et al. [111] using two-dimensional numerical Finite Element computations; they showed that for a change in heat transfer coefficient from $400 \text{ W/m}^2\text{K}$ to $600 \text{ W/m}^2\text{K}$ over a distance of 3.5 mm the maximum error introduced by lateral conduction is about 3.5%.

In case of specific applications (e.g. impingement cooling) the local variations in heat transfer distributions (gradients of heat transfer coefficients) might be larger and their effects should be analyzed using numerical methods.

In recent years other approaches couple directly the data evaluation to three-dimensional numerical models in order to determine the full surface heat transfer distribution by applying 3D inverse procedures. For example, using a three-dimensional unsteady heat conduction solver an iterative scheme for the determination of the heat transfer coefficients has been proposed by Ling et al. [112].

3.4 Critical Aspects on Matrix Cooling Measurements

In the previous sections an accurate evaluation has been carried out about the main advantages and disadvantages of the different experimental measurement techniques used for the determination of the heat transfer coefficient in internal cooling geometries. After this evaluation it has been necessary to choose the most suitable measurement approach to

determine the heat transfer performance of the matrix cooling geometries investigated in the present study.

As reported in Section 2.2 a latticework or matrix cooling geometry is characterized by two opposite layers of high blockage ribs that are in contact with each other resulting in very narrow passages (sub-channels) between the longitudinal ribs. This system of crossing sub-channels together with the continuous switching of the flow from a layer to another determines a high level of turbulence. Moreover, the turbulence is not the only mechanism that contributes to enhance the heat transfer, in fact an important contribution is also given by the high heat transfer surface area and fin effect provided by the same ribs.

For these reasons the experimental technique chosen to investigate the heat transfer in such geometries must be able to evaluate the overall heat transfer performance.

The application of optical measurement techniques, such as Infrared Thermography or Thermo-chromic Liquid Crystals (TLC), allows to evaluate heat transfer only on the endwall surfaces without taking into account the heat transfer due to rib surfaces; however this latter contribution cannot be neglected for this kind of cooling systems. Examples of these optical techniques applied to matrix cooling geometries are reported by Gillespie et al. [89], Bunker [86] and Saha et al.[6].

Also the application of the naphthalene sublimation method, as applied by Oh et al. [96], would allow to investigate the heat transfer only on the endwall surfaces representing pressure and suction side walls of the airfoil.

In addition to this, it should be considered that the high blockage and the presence of very narrow spacings between ribs does not facilitate the application of these optical techniques to evaluate the heat transfer coefficients on the rib surfaces. The only exception among the literary works about matrix cooling is due to Bunker [86], who applied a combination of different techniques to evaluate both local and overall heat transfer coefficients. In fact in this study, first a steady state technique with TLCs was applied to determine heat transfer on the primary or endwall surfaces,

then an infrared thermography technique in conjunction with an inverse conduction analysis was applied to metallic models in order to determine the additional impact of the fin effectiveness provided by the ribs.

In the work reported in this thesis an experimental technique similar to that described in Section 3.2.1 has been chosen. The test models have been divided into different heated segments with embedded thermocouples and regional average heat transfer coefficients have been determined for different streamwise and spanwise positions.

Since one of the objectives of these experiments was to reproduce the Biot number similitude of real applications, the metal chosen for these segments has not a very high thermal conductivity, hence the temperature measurement cannot be considered as the regionally averaged value for the entire element. For this reason it has been necessary to develop a post-processing procedure to evaluate the non uniform temperature field on the surface of matrix ribs; at the same time this procedure has allowed to take into account the fin effectiveness and the additional heat transfer surface area provided by the ribs. In fact, as will be described in Section 4.4.2, this approach provides two possibilities: first, the evaluation of the effective heat transfer coefficient between the fluid and the rib surfaces, second, the evaluation of an equivalent heat transfer coefficient applied to the internal endwalls to determine the overall heat removed from these surfaces.

Even though this approach allows to reach a less detailed measurement of the heat transfer coefficient distributions with respect to the application of an optical technique, it has been possible to quantify the average heat transfer coefficient for different regions of the matrix test cases. However the performance of matrix geometries evaluated in terms of average distributions match the requirements of the industrial partners with the final aim of developing design correlations for the blade cooling.

Chapter 4

Experimental Apparatus and Data Reduction

This chapter reports all the experimental details of the present activity. First of all test rig layouts, test models and measurement devices with corresponding measurement uncertainties will be described. In a second part the description will be focused on the details about the experimental measurement technique and on the development of the data reduction procedure for the evaluation of heat transfer coefficients.

4.1 Test Rig Layout for Static Tests

This section is dedicated to the description of the experimental facility employed to perform tests on several matrix geometries, with the aim to reproduce Reynolds number and Biot number similitude with a real application in static conditions.

The whole experimental survey has been performed at the Department of Industrial Engineering (DIEF) of the University of Florence.

As depicted in Figure 4.1 this test facility consists of an open-loop suction type wind tunnel and it is mainly composed by: a test model, a plenum chamber, a vacuum system, a data acquisition system, a pressure scanner and a DC power supply system.

The air at atmospheric pressure and ambient temperature enters axially into the test rig passing through a shaped inlet section. Air flow rate is supplied to the test section by using four rotary vane vacuum pumps: two with a capacity of $900 \text{ m}^3/\text{h}$ each (PVR pumps) and two with $300 \text{ m}^3/\text{h}$ each (Becker pumps). The mass flow rate is controlled by varying the speed of the pumps and using a throttle valve located between the vacuum pumps and the test section.

The mass flow rate is measured according to the standard EN ISO 5167-1 by means of an orifice located downstream the plenum chamber with a measurement accuracy below 3%.

The flow rate was varied for each test in order to reach the target values of Reynolds number at the inlet of the matrix module and hence at the inlet of the single sub-channel.

The inlet and exit flow temperatures are measured with four T-type thermocouples; two are located at the inlet and two at the outlet section of the test model. The metal temperatures of matrix modules is measured with 20 T-type thermocouples; one thermocouple is embedded into the base of each steel block. Thermocouples are connected with a reference junction to a data acquisition/switch unit (Agilent 34970A) with a measurement accuracy of 0.5 K.

20 Minco Kapton etched foil heaters are applied to the back surface of steel matrix elements to provide a constant heat flux during each test.

A pressure scanner Scanivalve DSA 3217 with temperature compensated piezoresistive relative pressure sensors measure the static pressure in 14 different locations inside the test section with a maximum accuracy of 17 Pa.

Figure 4.2 shows a picture of the test rig ready for a heat transfer test, where it is possible to see the test model instrumented with thermocouples, foil heaters and pressure taps as described above.

The details about the relative uncertainties on the measured quantities are described in section 4.6.

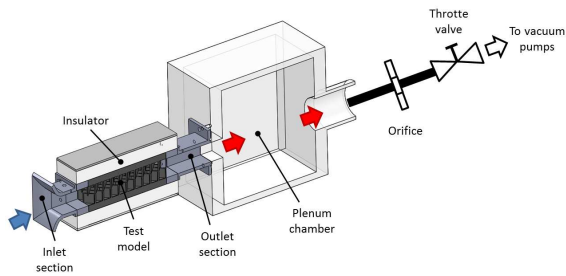


Figure 4.1: Test facility for static tests

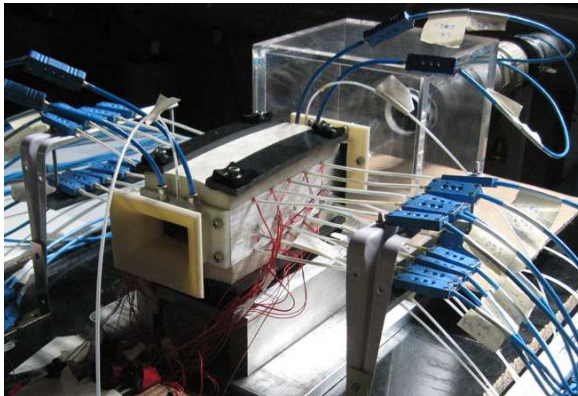


Figure 4.2: Picture of the test facility for static tests instrumented with thermocouples, heaters and pressure taps

4.1.1 Test models

A preliminary work was performed with the aim to select the desired matrix geometries for the following experimental measurements campaigns. During this phase it was necessary to conduct an evaluation of heat transfer and friction performance of many geometries applying the correlations of Nagoga reported in the previous Section 2.2.2.

Performance were analyzed as a function of the main geometric param-

ters such as: number of sub-channels n_{can} , rib thickness t_{rib} , rib height h_{rib} and rib inclination angle β . In this way it was established that the rib inclination angle of $45deg$ with respect to the flow direction is the best solution in terms of heat transfer and friction performance.

The above mentioned values are referred to a single matrix module, but, since a matrix model is composed by two modules (as will be described in next Section 4.1.2), it is necessary to double n_{can} and h_{rib} in order to refer them to the whole cross section.

Once fixed the rib inclination angle $\beta = 45deg$, the next step was to choose the desired values for rib thickness, rib height and number of sub-channels per each matrix module. To limit the number of geometries to be manufactured it was established to change the rib thickness t_{rib} together the number of sub-channels n_{can} ; this results in a significant variation of the flow passage area that is well represented by the following open area ratio R_{vp} :

$$R_{vp} = \frac{W_c}{W_c + t_{rib}} \quad (4.1)$$

Two open ratios representative of extreme geometric cases were selected: $R_{vp} = 84.5\%$ and $R_{vp} = 53.5\%$. The first $R_{vp} = 84.5\%$ is obtained using 4 sub-channels and $t_{rib} = 1.5 \text{ mm}$; it derives from the combination of a minimum number of sub-channels with the minimum rib thickness achievable by means of an investment casting process. On the other hand the second value $R_{vp} = 53.5\%$, obtained using 6 sub-channels and $t_{rib} = 3.0 \text{ mm}$, represents the minimum flow passage area. The comparison between these two configurations has allowed to investigate the combined effects of an increase of rib thickness and number of sub-channels resulting in an extreme reduction of flow passage area.

Since another issue of the present work was the study about the effects of rib height, the two open area configurations were applied for two very different values of rib height: $h_{rib} = 15 \text{ mm}$ and $h_{rib} = 1.5 \text{ mm}$. The first is representative of cooling cavity dimensions in the mid-chord region, while the second represents the typical dimensions of a trailing edge region.

From this study four matrix geometries with a constant cross section were selected for the first experimental campaign in static conditions. In the next phase, starting from the combination of the characteristic dimensions of these four geometries, two convergent geometries suitable for the trailing edge cooling were derived. Each of these two test models maintains the same open area value of the previous geometries ($R_{vp} = 84.5\%$ and 53.5%) from the inlet to the outlet with a converging angle of $\alpha = 5.7 \text{ deg}$ for the single matrix module. This leads to a continuous variation of the rib height h_{rib} from the inlet ($h_{rib,in} = 15 \text{ mm}$) to the outlet ($h_{rib,out} = 1.5 \text{ mm}$). These two models have been employed for the second experimental campaign in static conditions and will be described in the next section (§ 4.1.3).

Finally the same convergent matrix geometries with a different scale factor were designed to be installed on a rotating test rig in order to investigate rotation effects on matrix performance. All the details about these test models and the rotating test will be presented in Section 4.2.

It should be noted that all models for static tests were designed to reproduce Reynolds and Biot number similitude with real conditions. To get as close as possible the Biot number similitude the specific stainless steel AISI 304 with a thermal conductivity equal to 15.1 W/mK was selected. Since test models with variable height but constant width were installed into the test rig, during the phase of design it was necessary to create different inlet/outlet sections corresponding to the specific test model. However the structure of each test model is mainly composed by two halves: an upper module and a lower one, that represents the internal surfaces of pressure (PS) and suction (SS) sides of a gas turbine airfoil. Figure 4.3 illustrates a top section view of the lower module. Each module consists of an aluminum outer frame and a matrix geometry; the latter is formed by 10 stainless steel (AISI 304) elements, 5 in the main flow direction (streamwise) and 2 in the tangential one (spanwise). The adjacent steel elements are separated from each other by insulation spacers of bakelite with a thermal conductivity close to 0.6 W/mK . Moreover an insulation spacer of bakelite is interposed between the aluminum frame

and the steel matrix structure (not shown in Figure 4.3).

The crossing ribs/channels are integrally machined on the steel blocks and the sandwiched insulation spacers.

The two halves are coupled together so as to oppose each other and cross in a lattice structure; on each half the ribs are oriented at an angle of 45 deg to the streamwise direction.

Some screws through the top and bottom frames run through the holes and are tightened to hold the test section together. O-rings are seated in two grooves realized along the frame borders and are compressed during the assembly of the two parts creating a seal at the interface. A row of through holes is present on each of the two lateral walls of the frames; these holes are aligned to those drilled on the different steel blocks so as to allow the insertion of the thermocouples. Another row of through holes is realized on the same lateral walls to allow the location for the pressure taps.

Figure 4.4 shows the details of a group of four steel matrix blocks. Between two adjacent blocks an insulation spacer of bakelite is interposed for both streamwise and spanwise directions. Moreover, to avoid that the insulator affects the flow field, the channels have been carefully remachined to reach a flat surface. A T-type thermocouple is inserted in a blind hole drilled into the base of each steel block. Moreover, each steel matrix block is equipped with a Minco Kapton etched foil heater so as to apply a specific heat flux for each position of the matrix module. Five DC power supplies (MATRIX MPS-3005L-3) with voltage range 0-30V and current range 0-5A are used to individually regulate the heat flux of the heaters; the output of the supplies operate in constant voltage or constant current mode with automatic crossover. Each power supply has two outputs and each output provide the same voltage to a couple of heaters that are connected in parallel. According to this arrangement each streamwise position is identified by two couples of heaters: one for the lower module and one for the upper module.

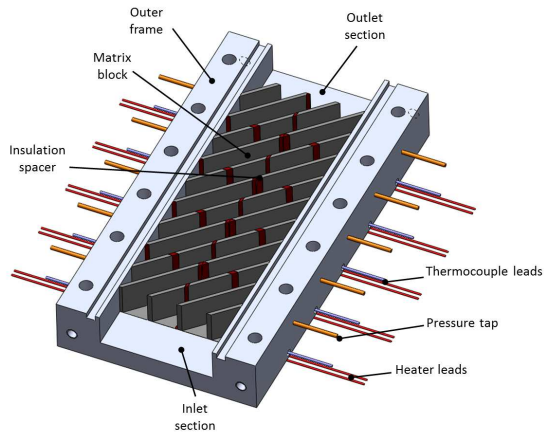


Figure 4.3: Top section view of the lower half of a test model

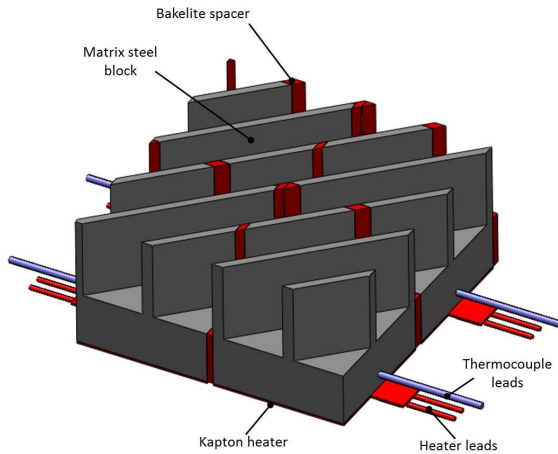


Figure 4.4: Detailed view of four matrix blocks instrumented with thermocouples and foil heaters

4.1.2 Matrix geometries with constant cross section

This paragraph describes the four matrix geometries with constant cross section investigated during the first campaign of static tests. These four geometries are identified by an ID number ranging from 01 to 04 and may be distinguished by the main geometrical parameters reported in Table 4.1; values in this table are referred to the single matrix module, therefore, considering both the halves of the matrix structure, h_{rib} and n_{can} values should be considered as doubled.

To better understand differences among the four geometries the complete set of all geometrical parameters is given in Table 4.2; these parameters are also directly depicted in Figure 4.5. The overall cross section of the test models is the same for *Geom 01, 02* and for *Geom 03, 04* matrix geometries. In the first two cases the dimensions of the cross-section are $W = 52 \text{ mm}$ and $H = 30 \text{ mm}$, while in the other two cases the dimensions are $W = 52 \text{ mm}$ and $H = 3 \text{ mm}$. These dimensions give a hydraulic diameter of $D_h = 38.05 \text{ mm}$ and $D_h = 5.67 \text{ mm}$ respectively. In each case the length of the overall channel of matrix module is $L = 135 \text{ mm}$. It must be pointed out that, as shown in Figure 4.5, h_{rib} is the rib height for a single matrix module, while $H = 2h_{rib}$ represents the overall height of the matrix model and of the overall flow passage area.

As mentioned in section 4.1.1 the four geometries are characterized by two different values of rib height h_{rib} : 15 and 1.5 mm. For each rib height two different configurations have been studied: one having four entry channels and lower rib thickness $t_{rib} = 1.5 \text{ mm}$, one having six entry channels and higher rib thickness $t_{rib} = 3.0 \text{ mm}$. This results in two different open area values: $R_{op} = 84.5\%$ for 01-03 geometries and $R_{op} = 53.5\%$ for 02-04 geometries.

Moving from *Geom 01* to *Geom 04* the values of sub-channel hydraulic diameter $d_{h,s}$ decrease with the increasing of rib thickness t_{rib} and number of sub-channels n_{can} and with the reduction of rib height h_{rib} (Table 4.2).

It must be pointed out that these geometries are representative of extreme cases; in fact *Geom 01, 02* are suitable for an application in the

mid-chord region, while *Geom 03*, *04* are suitable for the trailing edge region of a gas turbine airfoil.

For each of these four geometries heat transfer and pressure drop measurements have been performed varying the Reynolds number $Re_{s,in}$ from 2000 to 12000, where the Reynolds number is calculated considering the hydraulic diameter of the single sub-channel $d_{h,s,in}$ at the inlet section as the reference length according to the following definition:

$$Re_{s,in} = \frac{\dot{m}_{air} \cdot d_{h,s,in}}{A_{can,in} \cdot n_{can} \cdot \mu_{air,in}} \quad (4.2)$$

Table 4.1: Dimensions of matrix geometries with constant cross section

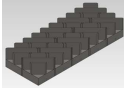
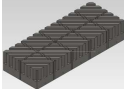
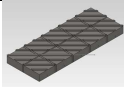
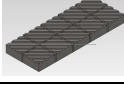
Geometry ID	SF	n_{can}	h_{rib} [mm]	t_{rib} [mm]	β [deg]
01 	5:1	4	15	1.5	45
02 	5:1	6	15	3.0	45
03 	5:1	4	1.5	1.5	45
04 	5:1	6	1.5	3.0	45

Table 4.2: Complete set of geometric dimensions of matrix geometries with constant cross section

Geometry	ID	01	02	03	04
W	[mm]	52	52	52	52
H	[mm]	30	30	3	3
L	[mm]	135	135	135	135
n_{can}	[]	4	6	4	6
t_{rib}	[mm]	1.5	3.0	1.5	3.0
h_{rib}	[mm]	15	15	1.5	1.5
β	[deg]	45	45	45	45
$d_{h,s}$	[mm]	10.59	5.62	2.54	2.09
W_c	[mm]	8.19	3.46	8.19	3.46
$A.R.$	[]	1.83	4.34	5.46	2.31
R_{vp}	[%]	84.5	53.5	84.5	53.5
l	[mm]	73.5	73.5	73.5	73.5

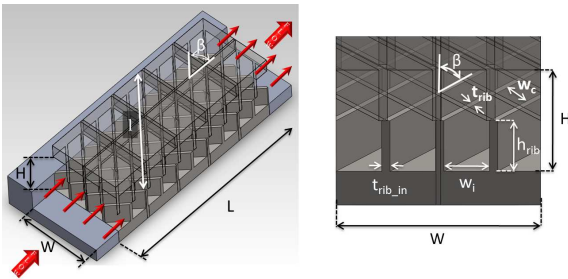


Figure 4.5: Geometric parameters of tested matrix geometries

4.1.3 Matrix geometries with convergent cross section

As mentioned in section 4.1.1 a second campaign of static tests was carried out on two convergent matrix models with the same scale factor of the four geometries with constant cross section.

These are identified by ID numbers 05 and 06; their geometric dimensions are shown in Tables 4.3 and 4.4, while a 3D drawing of a convergent test model is also depicted in Figure 4.6.

Geom 05 has the same geometric dimensions of *Geom 02* in correspondence to the inlet section, and the same dimensions of *Geom 04* at the outlet section. At the same time *Geom 06* has the same geometric dimensions of *Geom 01* and *Geom 03* in correspondence to the inlet and outlet section respectively.

Each module of these convergent geometries, is inclined of $\alpha = 5.7deg$ to replicate the converging channel of a trailing edge cooling system resulting in an overall converging angle of $11.4deg$. This implies a progressive reduction of the rib height from 15 mm at the entry to 1.5 mm at the exit. A similar reduction is obtained for the sub-channel hydraulic diameter $d_{h,s}$; the geometry with four-entry channels (*Geom 06*) changes the sub-channel hydraulic diameter $d_{h,s}$ from 21.19 mm to 5.07 mm, while the geometry with six-entry channels (*Geom 05*) changes $d_{h,s}$ from 11.24 mm to 4.18 mm. This results in a strong reduction of subchannel cross section area A_{can} and aspect ratio $A.R.$ from the inlet to the outlet of the models (1/10 ratio).

In a similar way to the previous static tests, for these two geometries heat transfer and pressure drop measurements have been carried out varying the Reynolds number $Re_{s,in}$ from 2000 to 12000. It should be noted that, since these channels are convergent and cross section, hydraulic diameter and flow velocity changes continuously from the inlet to the outlet, in these cases the Reynolds number was recalculated using the sub-channel hydraulic diameter and flow properties at the middle or average section of the matrix models. Moreover, as will be explained in the following chapters about the results, the choice of the average section represent the best way to correlate together both friction and heat transfer data

coming from both constant and convergent matrix geometries.

In this case Reynolds number $Re_{s,ave}$ is defined as:

$$Re_{s,ave} = \frac{\dot{m}_{air} \cdot d_{h,s,ave}}{A_{can,ave} \cdot n_{can} \cdot \mu_{air,ave}} \quad (4.3)$$

Table 4.3: Dimensions of matrix geometries with convergent cross section

Geometry ID	SF	n_{can}	h_{rib} [mm]	t_{rib} [mm]	β [deg]
05	5:1	6	15 ÷ 1.5	3.0	45
06	5:1	4	15 ÷ 1.5	1.5	45

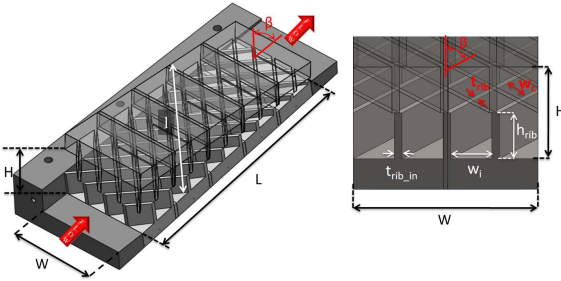


Figure 4.6: Geometric parameters of tested matrix geometries with convergent cross section

Table 4.4: Complete set of geometric dimensions of matrix geometries with convergent cross section

Geometry	ID	05	06
W	[mm]	52	52
H_{in}	[mm]	30	30
H_{out}	[mm]	3	3
L	[mm]	135	135
n_{can}		6	4
t_{rib}	[mm]	3.0	1.5
R_{vp}	[%]	53.5	84.5
$h_{rib,in}$	[mm]	15	15
$h_{rib,out}$	[mm]	1.5	1.5
W_c	[mm]	3.46	8.19
$d_{h,s,in}$	[mm]	5.62	10.59
$d_{h,s,out}$	[mm]	2.09	2.54
$A_{can,in}$		51.87	122.8
$A_{can,out}$		5.19	12.28
$A.R.in$		4.34	1.83
$A.R.out$		0.43	0.18
β	[deg]	45	45
l	[mm]	73.5	73.5

4.2 Test Rig Layout for Rotating Tests

The rotating test rig shown in the Figure 4.7, originally designed and used by Bonanni [62], has been employed to investigate rotation effects on friction and heat transfer performance of two test cases representing the scaled up models of the previous convergent geometries *Geom 05* and *Geom 06* presented in section 4.1.3. Geometric details of these models are reported in the following paragraph 4.2.1.

The rotating test rig consists of an open-loop suction type wind tunnel installed on a rotating chassis. The chassis is connected to a rotary joint and an inverter controlled electric motor (Marelli, IP55 7.5 kW three-phase-asynchronous - inverter Lenze 7.5 kW 400 V IP21) drives the rotary joint and the chassis by means of a transmission belt. On the other end the joint is connected to a system of four rotary vane vacuum pumps: two with a capacity of $900 \text{ m}^3/\text{h}$ each and two with $300 \text{ m}^3/\text{h}$ each. The mass flow rate is set up by varying the speed of the pumps and using a throttle valve located between the vacuum pumps and the joint.

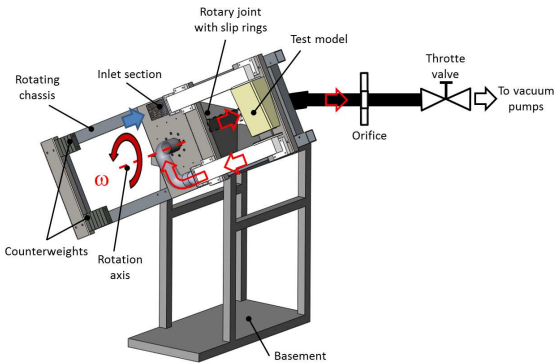


Figure 4.7: Test facility for rotating tests

The rotary joint has three purposes: first, it ensures the mechanical support of the rotating structure, second, it allows the air passage from



Figure 4.8: Details of rotary joint and electric motor [62]

the static to the rotating environment with a rotating seal, third, electric power and signals are transmitted by means of 20 slip rings: 2 designed for high current loads, 2 for low voltage power supply, 8 for TC-IP protocol communication and the remaining are silver made and compensated to connect thermocouples directly to the data switch-acquisition unit.

The test section installed on the rotating chassis is mainly composed by: an inlet section, an inlet duct, the test model and an outlet duct with a connection to the rotary joint. Test models can be mounted on the chassis according to different orientations with respect to the rotation direction; in this way it is possible to investigate the effects of model orientation as well as Coriolis forces on performance. In this activity two different orientations of the matrix channel have been reproduced: $0deg$ and $30deg$ with respect to the rotating plane (Figure 4.9). The $30deg$ configuration reproduces the exit angle of a real gas turbine blade. Figure 4.9 also indicates that the lower matrix module (mod INF) corresponds to the suction side (SS), while the upper module (mod SUP) corresponds to the pressure side (PS).

To ensure the static and dynamic balancing of the rotating test rig a system of more counterweights is installed on the part of the rotating chassis opposite to the position of the test section. Position, mass and

number of counterweights can be varied in order to reach the best balancing according to the different installed test model.

As shown in Figure 4.10, before entering into the test section the air at atmospheric pressure and ambient temperature flows through a polyester fibres filter, that is employed to generate the pressure drop necessary to ensure uniform flow conditions at the test section entry. Then the air passes along a radial inlet duct, flows through a $90deg$ bend and reaches the inlet section of the test model. After the model, the air flow is discharged towards the vacuum pumps passing through an outlet duct and the rotary joint.

The mass flow rate is measured according to the standard EN ISO 5167-1 by means of an orifice located downstream the rotary joint with a measurement accuracy below 3%.

The flow rate and the rotational speed of the test rig are varied for each test in order to reproduce both Reynolds and Rotation number similitude with the real conditions.

The temperatures of the whole test section mounted on the rotating chassis are measured with 15 T-type thermocouples with a measurement accuracy of $0.5K$. In particular 10 thermocouples are used to measure metal temperatures of the matrix modules, while the others measure air temperatures in different points of the test section: one upstream the polyester fibres filter, two in the inlet duct, one at the inlet and one at the outlet of the test model. All these thermocouples are connected to an isothermal thermocouple module (National Instruments NI 9214) mounted within a wireless chassis (National Instruments NI cDAQ-9191). The wireless chassis allows to transfer thermocouples signals to a network router and hence to the acquisition computer.

A pressure scanner Scanivalve DSA 3217 with temperature compensated piezoresistive relative pressure sensors measures the static pressure in 16 different locations from the inlet to the outlet of the whole test section with a maximum accuracy of 17 Pa. This scanner is located on board the rotating chassis at the lowest radius to avoid reading errors due to the centrifugal force. These acquired pressure data are transmitted via

Ethernet using the 8 TCP/IP protocol channels of the rotary joint slip rings.

A low voltage generator Agilent N5763A DC Programmable Power Supply is used to regulate the heat flux of 20 Telemeter etched foil heaters. They are applied to the back surface of the matrix elements to provide a constant heat flux during each test.

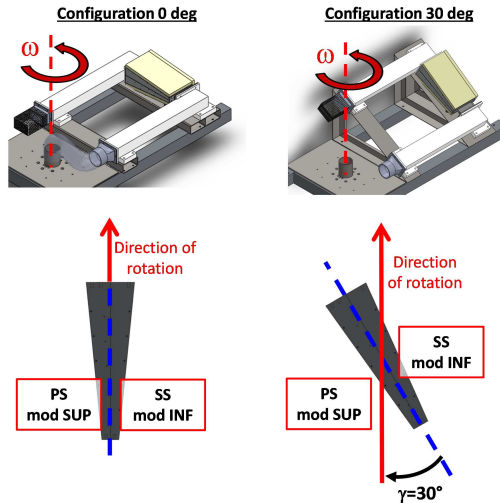


Figure 4.9: Schematic of the two investigated test model orientations: 0deg and 30deg

4.2.1 Matrix geometries for rotating tests

The two same convergent matrix geometries presented in section 4.1.3 were also selected for the experimental tests in rotating conditions. In this case the aim was the reproduction of Reynolds and Rotation number similitude with real applications and the investigation of rotation effects

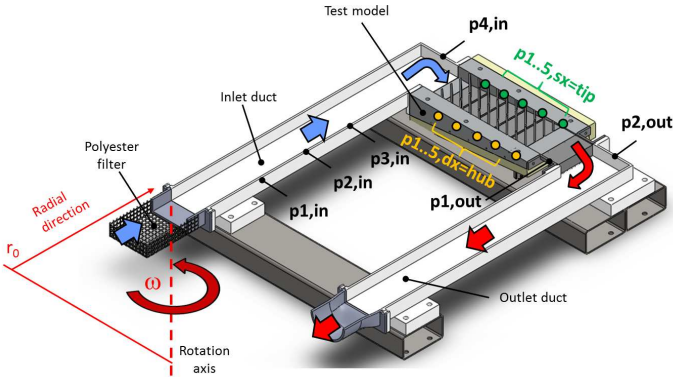


Figure 4.10: Details of the test section installed on the rotating chassis

on heat transfer and friction performance.

To reproduce the desired Rotation numbers at low rotational speeds, the scale factor SF of these test models was increased by two times with respect to the dimensions of the previous static convergent models. On the other hand the increase of geometric dimensions has led to change the material of test models in order to minimize the centrifugal loads; to reach this goal the 5083 aluminum alloy was used instead of the stainless steel AISI 304 of the static models. This different choice of material did not allow to approach the Biot number similitude as done during the static tests.

As above mentioned another aim of this experimental campaign was to evaluate the effects of different model orientations on matrix performance; for this reason rotating tests were replicated for two different model orientations with respect to the rotating plane: $0deg$ and $30deg$ (Figure 4.9). The $30deg$ configuration reproduces the typical exit angle of a real gas turbine blade.

Since these test cases, identified by ID numbers 07 and 08, are the scaled up models of *Geom 05* and *Geom 06* (§ 4.1.3) many common features can be found among them. However an important difference has to be

highlighted and it consists in the different partition of the two metallic modules into blocks. In fact each module of *Geom 05* and *Geom 06* is formed by 10 elements, 5 in the main flow direction (streamwise) and 2 in the tangential one (spanwise), while each module of *Geom 07* and *Geom 08* is formed by only 5 elements in the streamwise direction. This detail is derived from the need to limit the number of thermocouples on board the rotating chassis. Therefore, compared to the static tests, there is no more the distinction between right and left side of each module, but it still remains possible to find differences of performance between pressure and suction side of the matrix channel.

Figure 4.11 illustrates that each matrix block is equipped with a thermocouple and two foil heaters; each aluminum block has a blind hole where a thermocouple is inserted to a depth equal to half the width. Even in this case the adjacent metallic elements are separated from each other by insulation spacers of bakelite with a thermal conductivity close to 0.6 W/mK.

Moreover, as in the previous test models for static experiments, the location of pressure taps has been chosen in order to follow the flow behaviour according to four different sub-channel tracks from the entry to the exit of the model.

As in the previous static tests on convergent geometries, heat transfer and pressure drop measurements were performed for different Reynolds numbers from 2000 to 12000. Reynolds number is calculated as in the previous equation 4.3.

At the same time the Rotation number $Ro_{s,in}$, based on the subchannel hydraulic diameter at the inlet section, was varied from 0 to 0.250 depending on different mass flow and rotational speed conditions. Rotation number $Ro_{s,in}$ is defined as:

$$Ro_{s,in} = \frac{\omega \cdot d_{h,s,in}}{v_{rel,in}} \quad (4.4)$$

where ω is the angular velocity of the test rig expressed in *rad/s* and $v_{rel,in}$ is the bulk velocity of the flow in the sub-channel in correspon-

dence to the inlet section. It should be noted that the Rotation number represents the ratio between the Coriolis force and the bulk flow inertial term.

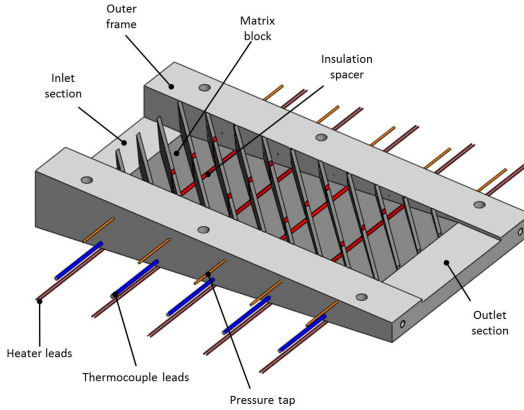


Figure 4.11: Top section view of a test model employed during rotating experiments

Table 4.5: Dimensions of matrix geometries for rotating tests

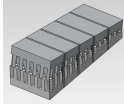
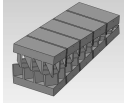
Geometry ID	SF	n_{can}	h_{rib} [mm]	t_{rib} [mm]	β [deg]
 07	10:1	6	$30 \div 3.0$	6.0	45
 08	10:1	4	$30 \div 3.0$	3.0	45

Table 4.6: Complete set of geometric dimensions of matrix geometries for rotating tests

Geometry	ID	07	08
W	[mm]	104	104
H_{in}	[mm]	60	60
H_{out}	[mm]	6	6
L	[mm]	270	270
n_{can}		6	4
t_{rib}	[mm]	6.0	3.0
R_{vp}	[%]	53.5	84.5
$h_{rib,in}$	[mm]	30	30
$h_{rib,out}$	[mm]	3.0	3.0
W_c	[mm]	6.92	16.38
$d_{h,s,in}$	[mm]	11.24	21.19
$d_{h,s,out}$	[mm]	4.18	5.07
$A_{can,in}$		207.6	491.4
$A_{can,out}$		20.76	49.14
$A.R.in$		4.33	1.83
$A.R.out$		0.43	0.18
β	[deg]	45	45
l	[mm]	147	147

4.3 Measuring devices

The static and the rotating test rigs of the present activity are equipped with specific devices for the measurement of pressure, temperature and mass flow rate. Moreover other devices have been adopted to provide a constant heat flux to the metal surface of matrix models during the heat transfer experiments.

This section will give an overview of all these types of instrumentation.

4.3.1 Mass flow rate measurements

The measurement of mass flow rate passing through the model is required in order to set the Reynolds number of each test. In both test rigs the mass flow rate has been measured by means of an orifice plate located at the end of the suction type wind tunnel upstream the vacuum pumps. In each case the mass flow rate has been measured according to the standard UNI-EN ISO 5167-1.

This is one of the most common method to obtain flow rates using the measurement of pressure drop across a restriction; for this reason these devices are also known as differential pressure flow meters. In fact the basic principle of this flow meter is that the flow is accelerated through the restriction resulting in a decrease of static pressure.

As shown in Figure 4.12 in the present case the restriction is represented by an orifice that consists of a thin plate with a centered hole mounted within a duct. Two static pressure taps are located at D and $D/2$ from each side of the orifice, where D is the hydraulic diameter of the duct. In addition to this a temperature measurement is performed to calculate the flow density.

Although this kind of flow meter is characterized by higher pressure losses and lower accuracy than other devices, it guarantees a wide operating range. However there are specific limitations on this range such as the maximum pressure ratio over the orifice that could generate a choked condition. On the other hand the minimum pressure ratio and hence the minimum mass flow rate should be high enough to allow an accurate

measurement. One of the main advantages of this method is that the orifice diameter may be chosen in order to get the maximum accuracy depending on the expected range of the mass flow. As regards the present experiments different diameters, from 12.5 to 18 mm, have been selected for the 2" ducts so as to obtain a measurement accuracy below 3%.

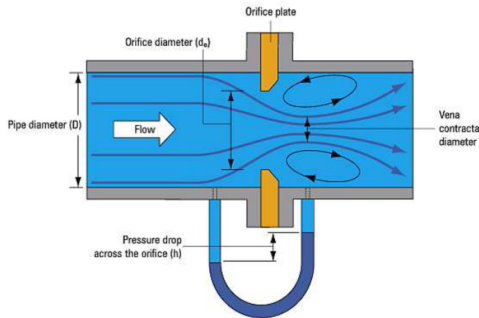


Figure 4.12: Orifice plate for mass flow measurement

4.3.2 Static pressure measurements

As already mentioned in the previous paragraph 4.3.1, the measurement of static pressure is required both downstream and upstream the orifice to calculate the mass flow rate passing through the model. Moreover other pressure measurements are performed at different positions along the test section in order to evaluate both fluid properties and pressure losses through the test models.

In the present test rig static pressure measurements have been carried out by two pressure scanners Scanivalve DSA 3217 (Digital Sensor Ar-

ray). Each pressure scanner incorporates 16 temperature compensated piezoresistive pressure sensors with a pneumatic calibration valve, a 16 bit A/D converter, and a microprocessor with a RAM memory. This latter compensates for temperature changes, performs unit conversion and performs the actuation of an internal calibration valve to set on-line zero. The 16 pressure transducers are manifolded in two groups of 8 sensors; each of them measures the differential pressure between the inlet of its own port and a common reference port. To have multiple pressure ranges for a single scanner, several pneumatic configurations are possible; for example all the 16 sensors can be manifolded to a single reference port, or 2 groups of 8 sensors can be referred to two different reference ports in the dual range configuration. This configuration has been adopted for the DSA scanners used for the present work; in fact 8 channels have a pressure range of 5 psi ($\simeq 35000Pa$) and 8 channels have a range of 15 psi ($\simeq 100000Pa$) both with a 0.05% full scale of accuracy. This means that the first 8 channels have an accuracy of 17 Pa , while the other 8 channels of about 51 Pa .

Since these sensors measure a differential pressure, an absolute pressure measurement is required as a reference value. In this case the reference pressure is the atmospheric pressure given by a mercury barometer within the room.

The two DSA scanners are connected to the acquisition PC by means of a TCP/IP protocol.

4.3.3 Temperature measurements

The temperature measurements performed both in the static and rotating test rigs have mainly involved the flow and the metal elements of each matrix model. In fact, according to the steady state technique described in Section 4.4.1, these temperatures represent the main boundary conditions to calculate the heat transfer coefficients.

Flow temperature is measured in correspondence of the orifices in order to accurately estimate the flow density and hence the mass flow rate. Other flow temperatures are performed at the inlet and outlet sections

of the test model in order to calculate the coolant bulk temperature $T_{b,i}$ or $T_{air,i}$ at any location within the matrix channel using the formulation described by the Equation 4.6. In fact, starting from the air temperature measured at the inlet $T_{air,in}$, the local bulk temperature $T_{air,i}$ can be calculated at the midpoint of each streamwise location of the test model according to the above mentioned formulation based on energy balance equation.

As regards metal temperatures, the local regional wall temperature $T_{w,i}$ is directly measured using a thermocouple installed in the blind hole on each metal block of the test models. The temperature of each block is assumed uniform because each thermocouple is located at a depth where the temperature distortion for fin is negligible. This latter hypothesis has been verified by means of the thermal finite element method (FEM); an example of the results obtained from these FEM simulations is reported in Figure 4.13.

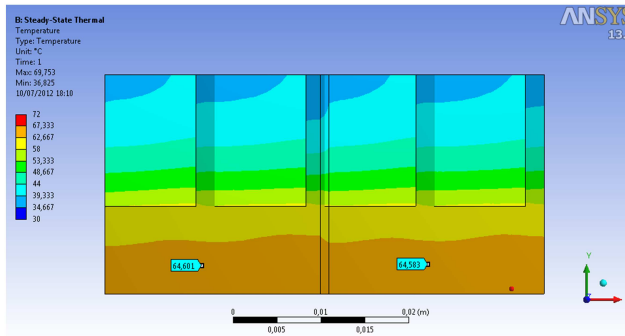


Figure 4.13: Example of a FEM simulation to evaluate the correct depth to locate thermocouples

Both flow and metal temperatures have been measured using sheathed T-type thermocouples (copper-constantan) with a wire diameter of 0.5 mm and an accuracy of 0.5 K certified by the manufacturer (Tersid S.p.A.). All thermocouples are connected with a reference junction to a data acquisition/switch unit (Agilent 34970A); this latter transmits data signals to the acquisition PC by means of a GPIB-USB interface.

Since the voltage generated by thermocouple circuits is a function of the temperature difference between the measuring junction and a reference cold junction, it is important that the reference junction be maintained at a constant and known temperature. For this reason in the present activity the reference cold junction has been accomplished by an electrical circuit located within a thermally insulated hollow cylinder. Cables coming from the several thermocouples are fixed to an electrical terminal located inside the hollow cylinder; other cables fixed to the other end of the terminal are connected to the data acquisition unit. This device allows to reach a constant temperature within the cylinder; the temperature of this reference junction is measured by means of a RTD Pt100 sensor with an accuracy of 0.1 K . Therefore considering the measurement accuracy of T-type thermocouples and RTD sensor, the temperatures of the test rig are measured with a global accuracy of 0.6 K .

The data acquisition/switch unit Agilent 34970A measures and converts 11 different input signals: temperature with thermocouples, RTDs and thermistors, dc and ac voltage, dc and ac current, 2-wire and 4-wire resistance, frequency and period. The unit is equipped with three multiplexer modules of 20 channels each (Agilent 34901A) with a maximum scan rate of 60 channels/second. Each channel is independently configurable.

It should be noted that the Agilent 34970A has not been the only data acquisition unit for temperature signals used in the present work. In fact, since the number of slip rings of the rotary joint dedicated to the temperature signals was not enough to ensure the connections of all the T-type thermocouples installed on the rotating test rig, it has been necessary to adopt a wireless unit in addition to the above mentioned Agilent unit. For this reason these thermocouples have been connected to an isother-

mal module (National Instrument NI 9214) mounted within a wireless chassis (National Instrument NI cDAQ-9191). The wireless chassis allows to transfer the thermocouple signals to a network router and hence to the acquisition PC.

The NI 9214 is a 16-channel thermocouple input module; each channel is multiplexed and sampled by a 24-bit A/D converter. It supports both high-resolution and high-speed timing modes; in the present case the high-resolution mode has been chosen in order to optimize accuracy and rejects noise and power line frequencies.

All the data coming from the above data acquisition units for temperatures and from the pressure scanners have been monitored and recorded by means of a custom-tailored application in-house developed using the LabView software.

4.4 Heat Transfer Coefficient measurement

4.4.1 Heated segments with thermocouples

In the present experimental activity a steady-state technique with heated segments and embedded thermocouples has been employed to determine the regionally averaged heat transfer coefficients for different positions along the test models. It should be noted that a different metal has been used for the heated segments that reproduce the internal surfaces of the cooling cavity (e.g. internal suction and pressure sides of the vane/blade) depending on the different test facility: static or rotating. As regards the static tests, stainless steel elements (AISI 304 with a thermal conductivity equal to 15.1 W/mK) have been used in order to get a Biot number similitude and a thermal gradient on the fins as close as possible to a real application. As regards rotating tests, aluminum elements (5083 aluminum alloy with a thermal conductivity of 117.0 W/mK) have been employed; although this case did not allow to replicate the same Biot number condition of previous static tests, it has been possible to reduce centrifugal loads with the aim of easily reproduce the Rotation number similitude of a real blade.

For both static and rotating tests a constant heat flux condition has been imposed for each position of the test models by the setting of the power input to the etched foil heaters attached to the back surface of the several metal blocks. Power input has been regulated in order to have a temperature difference of at least 30 °C between air flow and metallic wall for each streamwise position.

Then, a wall temperature $T_{w,i}$ has been measured for each position by means of the T-type thermocouple embedded into the base of each matrix block for both steel and aluminum elements (§ 4.1.1). Since the thermal conductivity of the metal block has a strong effect on the temperature distribution along the fin/rib and therefore influences the heat transfer rate, a specific data reduction procedure has been developed to take into account the fin effectiveness and the temperature variation from the base to the tip of matrix fins. It is clear that this variation becomes important in the case of steel blocks because of the lower thermal conductivity, while for the high conducting aluminum elements the measured temperature at the base is quite already a regionally averaged temperature of the whole block.

For both cases the above mentioned data reduction procedure has been applied to obtain heat transfer coefficients starting from the temperature measurements. This procedure is described in the next section (§ 4.4.2).

4.4.2 Data reduction and post-processing procedure

In this study a specific data reduction procedure has been developed in order to determine three heat transfer coefficients HTC's with a different physical meaning: htc_{eqT} , htc_{eqB} and htc_r . The first two coefficients htc_{eqT} and htc_{eqB} are equivalent values that include both heat transfer term due to rib/fin surface and effective term applicable on the rib surfaces. A significant difference has to be highlighted between htc_{eqT} and htc_{eqB} ; the first htc_{eqT} is the equivalent HTC value referred to a flat surface without ribs considering the effective thermal conductivity of the metal matrix blocks (e.g. 15.1 W/mK for static test models and 117.0

W/mK for rotating test models), the second htc_{eqB} is the equivalent HTC value recalculated with the ideal value of thermal conductivity that allows to obtain the Biot number similitude with a real application. This ideal value of thermal conductivity is equal to 10 W/mK and differs little from that of the metal actually used for static tests (e.g. 15.1 W/mK). It should be noted that it wasn't possible to manufacture test models selecting a metal with $k_{met} = 10$ W/mK because this is characteristic of very expensive superalloys.

On the other hand the coefficient htc_r represents the effective average HTC value that derives from the heat transfer between fluid and rib and it is applicable to the rib surfaces. Differences between these HTC values are depicted in Figure 4.14.

The physical meanings of these coefficients are closely related to different purposes within the context of the blade cooling design. In fact the htc_{eqT} and htc_{eqB} values allow to evaluate the overall heat transfer rate from the internal walls of suction and pressure sides of the gas turbine airfoil; this overall heat transfer rate also includes the term due to the additional heat transfer surface area provided by the ribs.

The htc_r values could be used to find out correlations about the influence of the regime flow (Reynolds number) on heat transfer performance (Nusselt number) and could be applied on the rib surfaces of a matrix geometry as boundary conditions in a FEM analysis.

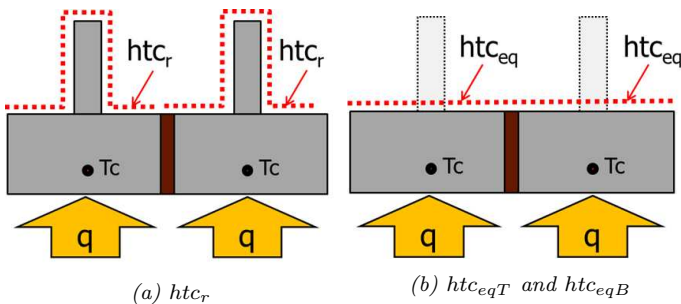


Figure 4.14: Difference between effective and equivalent Heat Transfer Coefficients HTCs

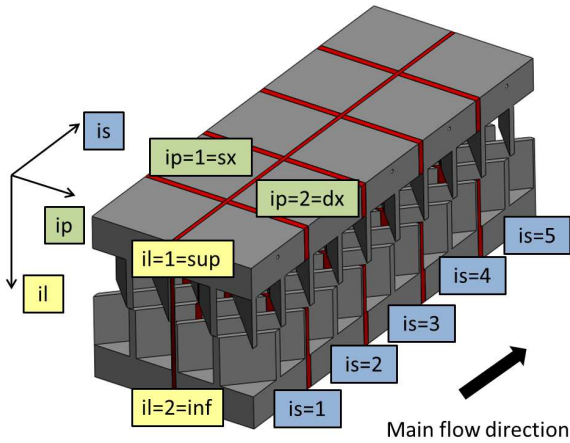


Figure 4.15: Nomenclature of the indices used in the data reduction procedure to identify the position of the blocks

Before reporting the details about the data reduction procedure it is necessary to explain the geometric nomenclature and the geometric quantities used as reference to calculate the main investigated parameters such as: Reynolds number, Nusselt number and friction factor.

In fact, as already described in the previous sections 4.1 and 4.2, each test model is composed by 10 elements per both sides (lower and upper half), 5 in the streamwise or main flow direction and 2 in the spanwise or tangential one. It must be pointed out that test models for rotating tests are similar to the static ones but have only one element in the spanwise direction.

Three indices have been used to identify the position of the specific matrix block within this procedure: il distinguishes the upper or lower module ($il=1=sup$ for the upper, $il=2=inf$ for the lower module), ip points the spanwise position ($ip=1=sx$ for left side, $ip=2=dx$ for right side) while is localizes the streamwise position from 1 to 5 (from inlet to outlet). To identify the variable related to the i -th matrix block, in the next

sections it will be used the generic index i .

Starting from the Newton's law of cooling, htc_{eqT} values are calculated at the base of the rib according to the following relation:

$$htc_{eqT,i} = \frac{Q_{input,i} - Q_{loss,i} - Q_{cond,lat,i}}{A_b \cdot (T_{w,sup,i} - T_{air,i})}; \quad (4.5)$$

where $A_b = W_b^2$ is the base area of the element, $T_{air,i}$ is the average air temperature while $T_{w,sup,i}$ represents the wall temperature at the base of the rib.

The average bulk air temperature $T_{air,i}$ has been estimated for each streamwise location along the test model; that is, starting from the air temperature $T_{air,in}$ measured at the inlet, the $T_{air,i}$ value is calculated at the mid-point of each axial position (i s from 1 to 5) using the following energy balance equation:

$$T_{air,i} = T_{air,in} + \frac{(\sum_{j=1}^{i-1} (Q_{net,j})_{up} + \frac{1}{2}(Q_{net,i})_{up})}{\dot{m}_{air} \cdot c_{p,air}} + \frac{(\sum_{j=1}^{i-1} (Q_{net,j})_{low} + \frac{1}{2}(Q_{net,i})_{low})}{\dot{m}_{air} \cdot c_{p,air}} \quad (4.6)$$

where $Q_{net,i} = Q_{input,i} - Q_{loss,i} - Q_{cond,lat,i}$ is the net heat from the i -th streamwise plate to the cooling air. The bulk air temperature $T_{air,6}$, calculated at the outlet of the test model, is then compared with the measured one $T_{air,out}$ to ensure that a steady state condition has been reached during the experiment and that Q_{loss} have been correctly evaluated.

As regards the heat terms, $Q_{input,i}$ represents the power supplied by each heater, $Q_{loss,i}$ is the heat lost from each matrix block while $Q_{cond,lat,i}$ is the heat transferred from the i -th block to those adjacents; the latter is expressed as:

$$Q_{cond,lat,i} = A_{lat} \cdot \frac{k_{is}}{s_{is}} \cdot (2T_{w,i} - T_{w,i-1} - T_{w,i+1}) \quad (4.7)$$

where $A_{lat} = W_b \cdot h_b$ is the lateral contact area between two adjacent

blocks, while k_{is} and s_{is} are the thermal conductivity and thickness of the insulation spacers made of bakelite ($k_{is} \cong 0.6$ W/mK) between adjacent metal blocks. Details on heat losses $Q_{loss,i}$ determination are given in the next section 4.4.3.

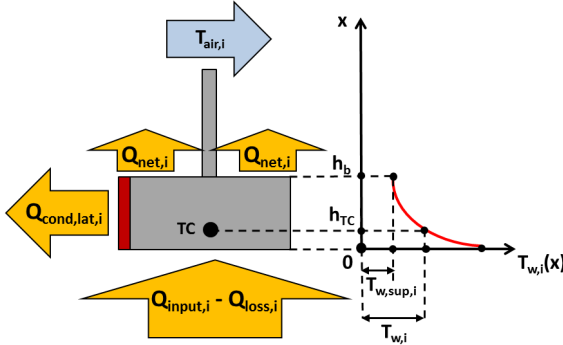


Figure 4.16: Heat fluxes and wall temperature distribution through a single matrix block

The $T_{w,sup,i}$ is evaluated starting from the temperature value $T_{w,i}$, which is the local wall temperature measured by the thermocouple at a given distance h_{TC} from the base of the block, and considering an energy balance of heat fluxes for each matrix block (Figure 4.16). In particular the solution of the second-order differential heat equation provides the $T_{w,i}(x)$ distribution along the thickness of the matrix module:

$$k \cdot \frac{d^2 T}{dx^2} = \frac{Q_{cond,lat,i}}{A_{lat}} \quad (4.8)$$

To solve this equation the two following boundary conditions are considered:

$$T_{w,i}(x = h_{TC}) = T_{w,i} \quad (4.9)$$

$$k \cdot \frac{dT}{dx} \Big|_{x=0} = \frac{Q_{input,i} - Q_{loss,i}}{A_b} \quad (4.10)$$

where the first is specified in terms of the temperature $T_{w,i}$ measured

by the thermocouple at $x = h_{TC}$, while the second corresponds to the net input power supplied at the base of the matrix module $x = 0$. In this way $T_{w,i}(x = h_b) = T_{w,sup,i}$, which is the desired temperature value at the base of the rib, is evaluated.

On the other hand htc_r , which is the applicable value on the rib surfaces, is calculated by applying the fin effectiveness theory [87]. In fact an analogy exists between a matrix rib and a rectangular fin of uniform cross section as that shown in Figure 4.17.

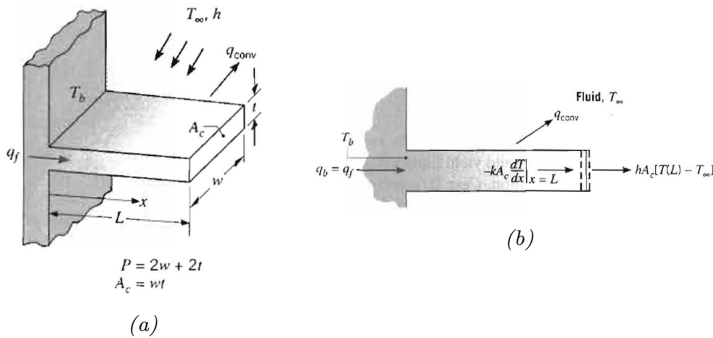


Figure 4.17: Conduction and convection in a rectangular fin of uniform cross section [87]

Thermal conductivity k_{met} and heat transfer coefficient htc_r due to the convection with the fluid generally determine a non uniform temperature distribution along the fin. Each fin is attached to a base surface of temperature $T(x = 0) = T_b$ and extends into a fluid of temperature T_∞ . Considering the rectangular fin in Figure 4.17a, where A_c is the cross-sectional area and P is the perimeter, it is necessary to solve the Fourier's equation in the following form:

$$\frac{d^2T}{dx^2} - \frac{htc_r P}{kA_c} \cdot (T - T_\infty) = 0 \quad (4.11)$$

This equation may be simplified as:

$$\frac{d^2(T(x) - T_\infty)}{dx^2} - m^2 \cdot (T(x) - T_\infty) = 0 \quad (4.12)$$

where m is the so-called fin parameter $(htc_{r,i} \cdot A_c/k_{met} \cdot P)^{0.5}$ [87].

Equation 4.12 is a linear, homogeneous, second-order differential equation with constant coefficients and its general solution may be written as:

$$T(x) - T_\infty = C_1 e^{mx} + C_2 e^{-mx} \quad (4.13)$$

To evaluate the constants C_1 and C_2 of equation 4.13 it is necessary to specify appropriate boundary conditions; one condition is the temperature at the base of the fin ($x=0$):

$$T(x) - T_\infty|_{x=0} = T_b - T_\infty = T_{w,sup,i} - T_\infty \quad (4.14)$$

where T_b is the temperature at the base of the fin and corresponds to the above mentioned $T_{w,sup,i}$ for the present procedure.

The second boundary condition specifies the convection heat transfer from the fin tip ($x = L$); applying an energy balance to a control surface about the tip (Figure 4.17b) it is obtained:

$$-kA_c \frac{dT}{dx}|_{x=L} = htc_r A_c [T(L) - T_\infty] \quad (4.15)$$

In fact, considering the conservation of energy, the rate at which heat is transferred by convection from the tip must equal the rate at which heat is conducted through the base of the fin ($q_f = q_b$).

Then substituting Equation 4.13 into Equations 4.14 and 4.15 the following solutions are obtained respectively:

$$T_b - T_\infty = C_1 + C_2 \quad (4.16)$$

$$htc_r \cdot (C_1 e^{mL} + C_2 e^{-mL}) = k_{met} m \cdot (C_2 e^{-mL} - C_1 e^{mL}) \quad (4.17)$$

Solving for C_1 and C_2 it is possible to obtain the following tempera-

ture distribution through the fin:

$$\frac{T(x) - T_\infty}{T_b - T_\infty} = \frac{\cosh(m(L-x)) + (htc_r/mk_{met})\sinh(m(L-x))}{\cosh(mL) + (htc_r/mk_{met})\sinh(mL)} \quad (4.18)$$

Hence, once known the temperature distribution through the fin, the fin heat transfer rate q_f for the single matrix block may be evaluated as:

$$q_{f,i} = \sqrt{htc_{r,i}Pk_{met}Ac} \cdot \theta_b \cdot \frac{\sinh(mL) + (htc_{r,i}/mk_{met})\cosh(mL)}{\cosh(mL) + (htc_{r,i}/mk_{met})\sinh(mL)} \quad (4.19)$$

where $\theta_b = T_b - T_\infty$.

It should be noted that this temperature distribution (Eq. 4.18) and this fin heat transfer rate (Eq. 4.19) have been found considering the boundary condition of convection heat transfer at the fin tip expressed by Equation 4.15. This latter assumption has been adopted within the data reduction procedure for the determination of the effective heat transfer coefficient $htc_{r,i}$ between matrix fin and cooling fluid. In fact in this case, especially for matrix geometries with smaller rib height, the surface at the tip is not treated as adiabatic because the heat transfer at the rib tip is not negligible compared to the other heat transfer surfaces. Then, since the overall heat exchanged by convection is given by the sum of heat transfer term due to ribbed areas ($q_{f,i}$) and heat transfer term due to non ribbed areas, the following balance equation can be written:

$$q_f + htc_{r,i}W_cL_{rib}(T_{w,sup,i} - T_{air,i}) = htc_{eq,i}A_b(T_{w,sup,i} - T_{air,i}) \quad (4.20)$$

where L_{rib} represents the overall length of rib for each matrix block and W_c is the sub-channel width or the distance between two adjacent ribs (Figure 4.18).

Therefore, knowing $htc_{eqT,i}$ values and using equations 4.19 and 4.20, $htc_{r,i}$ coefficients are determined through an iterative cycle.

As above mentioned, for both $htc_{eqT,i}$ and $htc_{r,i}$ values related to static

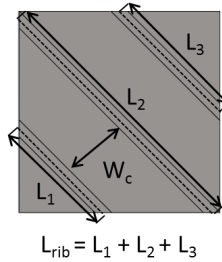


Figure 4.18: Overall length rib and sub-channel width for a single matrix block

tests, the heat transfer coefficients have been calculated in a condition as close as possible to the Biot number similitude with the real application. Finally, for both static and rotating tests, the other equivalent heat transfer coefficients $htc_{eqB,i}$ have been determined applying the same iterative procedure described by the previous equations. In this case $k_{met} = 10 \text{ W/mK}$ was used, that is the thermal conductivity value necessary to reach the ideal Biot number similitude with real case and hence to reproduce the realistic thermal gradient along the fin.

Although this procedure allows to estimate average HTC's for each single block, for each streamwise position and for the whole model, it is necessary to express these values in terms of relevant dimensionless quantities with the final aim to compare heat transfer and friction performance of the different investigated matrix geometries. In fact these are characterized by both different scale factors and different values of the main geometric parameters and a correct comparison between them may be done only using dimensionless quantities. For this reason mass flow rate and heat transfer coefficient have been represented by Reynolds number and Nusselt number respectively as follows:

$$Re_s = \frac{\dot{m}_{air} \cdot d_{h,s}}{A_{can} \cdot n_{can} \cdot \mu_{air}} \quad (4.21)$$

$$Nu_s = \frac{htc \cdot d_{h,s}}{k_{air}} \quad (4.22)$$

where $d_{h,s}$ and A_{can} are the hydraulic diameter and cross-sectional area of the sub-channel, respectively. On the other hand μ_{air} and k_{air} are dynamic viscosity and thermal conductivity of the air and are calculated from pressure and temperature values measured or evaluated at a specific section of the model. In this way starting from $htc_{eqT,i}$, $htc_{eqB,i}$ and $htc_{r,i}$ values the corresponding average Nusselt numbers $Nu_{eqT,s}$, $Nu_{eqB,s}$ and $Nu_{r,s}$ have been calculated.

Reynolds and Nusselt numbers are defined by taking the sub-channel hydraulic diameter as the characteristic length. As regards matrix geometries with constant cross section, Nu_s and Re_s are based on the sub-channel hydraulic diameter $d_{h,s,in}$ at the inlet section, which is constant from the inlet to the outlet (see also Equation 4.2), while the sub-channel hydraulic diameter $d_{h,s,ave}$ at the average or middle section has been adopted for convergent geometries (see also Equation 4.3).

As already defined by Equation 4.4, another relevant dimensionless parameter investigated in the present activity is the Rotation number. This parameter allows to understand in which condition the experimental test rig reproduces the rotational condition of a real blade. In this analysis the Rotation number is based on the sub-channel hydraulic diameter at the inlet section and is indicated as $Ro_{s,in}$.

As regards matrix geometries with convergent cross section the data reduction procedure gives the possibility to calculate the main dimensionless parameters Nu_s and Re_s with respect to hydraulic diameters of inlet, average and outlet sections of each streamwise block and of the whole model (Figure 4.19). In the present work it has been necessary to reduce experimental data of convergent geometries using the sub-channel hydraulic diameter based on both average section of the whole model and average section of each single matrix block. For this reason a specific definition of hydraulic diameter has been implemented in the data reduction procedure to take into account the linear decrease of rib height from the entry to the exit section; in fact the rib height is expressed as a

polynomial function $(a - bx)$, where x is the axial coordinate along the streamwise direction. According to these considerations the hydraulic diameter $d_{h,s,ave,ave}$ referred to the average section of the whole model is defined as:

$$d_{h,s,ave,ave} = \frac{4A_{can}}{P_{can}} = \frac{4 \int_0^L W_c(a - bx) dx}{2 \int_0^L W_c + (a - bx) dx} = \frac{4 \left(\frac{A_{can,IN} + A_{can,OUT}}{2} \right)}{\left(\frac{P_{can,IN} + P_{can,OUT}}{2} \right)} \quad (4.23)$$

where A_{can} and P_{can} are the sub-channel cross section area and sub-channel perimeter at the inlet and outlet sections of the model.

The same definition has been applied to calculate the hydraulic diameter $d_{h,s,ave,i}$ referred to the average section of the single i -th streamwise block as follows:

$$d_{h,s,ave,i} = \frac{4A_{can,i}}{P_{can,i}} = \frac{4 \int_0^{L_i} W_c(a - bx) dx}{2 \int_0^{L_i} W_c + (a - bx) dx} = \frac{4 \left(\frac{A_{can,in,i} + A_{can,out,i}}{2} \right)}{\left(\frac{P_{can,in,i} + P_{can,out,i}}{2} \right)} \quad (4.24)$$

Unlike the previous case, $A_{can,i}$ and $P_{can,i}$ are referred to the inlet and outlet sections of the considered streamwise block.

All the details of this data reduction procedure have also been reported in Carcasci et al. [113].

4.4.3 Heat losses determination

As it is possible to deduce from Equation 4.5 the heat losses $Q_{loss,i}$ play a dominant role in the correct estimation of heat transfer coefficients. That is, an accurate characterization of heat losses implies an accurate determination of HTCs.

For this reason a wide part of this activity has been addressed to the experimental measurement of heat losses for each of the investigated geometries and additional corrections have been applied to evaluate the increase of heat losses during rotating conditions.

Heat losses have been experimentally determined from several static cal-

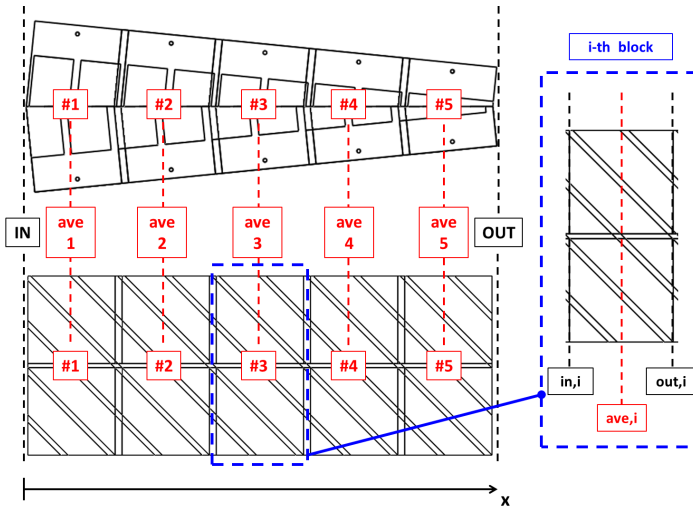


Figure 4.19: Definition of sub-channel hydraulic diameter of the whole matrix model and single i -th matrix block

ibration tests, where the test articles were closed to avoid any air circulation. This configuration is necessary because when the steady state condition is reached it means that the heat supplied by the foil heaters $Q_{input,i}$ is balanced by the heat lost through the thermal insulating shell $Q_{loss,i}$. This heat loss should be equal to the heat lost during the actual measurement of HTCs depending on different test conditions. Since heat loss could change moving from a position to another of the matrix model because of the different metal temperature, it is necessary to obtain several calibration functions that give the heat loss as a function of the different position and different block temperatures $T_{w,i}$ respect to ambient temperature T_{amb} .

Starting from the previous considerations, calibration tests have been repeated for several power inputs $Q_{input,i}$ with the aim to reproduce the whole range of temperature difference $(T_{w,i} - T_{amb})$ expected during heat transfer tests.

Tests have been planned as follows: a first test (reference test) has been performed applying the same power input to each block; then, starting from this condition, an increase of heat flux has been imposed for each position. Tests have also been repeated for different levels of heat flux increase in order to enlarge the investigated $(T_{w,i} - T_{amb})$ range.

Since the duration of each test is higher than 3 hours, it has been necessary to limit the total number of tests; for this reason some assumptions about heat losses have been made: a symmetric behaviour is assumed between the lower and the upper part of each geometry and between the extreme streamwise blocks in positions #1 and #5. This latter hypothesis has been adopted in case of geometries with constant cross section but not in case of convergent geometries. In fact, as regards convergent geometries, each streamwise block has its own thermal behaviour due to the different geometry; in this case different heat fluxes have been imposed for each of the five streamwise locations.

For each calibration test, an energy balance can be written for each block:

$$Q_{input,i} = Q_{loss,i} + \frac{k_{is}}{s_{is}} \cdot (W_b \cdot h_b) \cdot (T_{w,i} - T_{w,i-1}) + \frac{k_{is}}{s_{is}} \cdot (W_b \cdot h_b) \cdot (T_{w,i} - T_{w,i+1}); \quad i = 1, 5 \quad (4.25)$$

As above mentioned the heat loss can be modeled as a function of block temperature $T_{w,i}$ respect to ambient temperature T_{amb} and so it can be expressed as a polynomial function:

$$Q_{input,i} = [a_{loss,i} + b_{loss,i} \cdot (T_{w,i} - T_{amb}) + c_{loss,i} \cdot (T_{w,i} - T_{amb})^2] + \frac{k_{is}}{s_{is}} \cdot (W_b \cdot h_b) \cdot (2T_{w,i} - T_{w,i-1} - T_{w,i+1}) \quad (4.26)$$

If m calibration tests are run and 5 are the streamwise positions then $(m \cdot 5)$ equations can be written where the unknowns are $a_{loss,i}$, $b_{loss,i}$, $c_{loss,i}$ and k_{is} . These coefficients can be determined using linear least

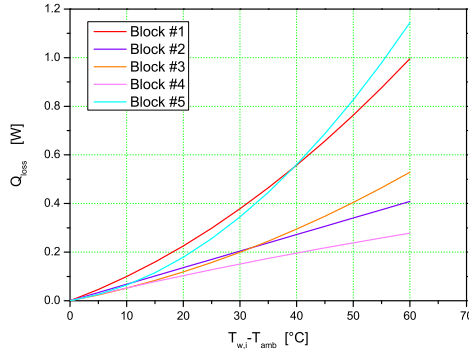


Figure 4.20: Example of Q_{loss} polynomial trends as a function of block temperature $T_{w,i}$ respect to ambient temperature T_{amb}

squares approach. Generally $a_{loss,i} = 0$ because if $(T_{w,i} - T_{amb}) = 0$ then also $Q_{loss,i} = 0$. An example of the polynomial functions experimentally found for each streamwise block (from #1 to #5) is reported in Figure 4.20; in each case Q_{loss} has a rising trend with the increase of temperature difference $(T_{w,i} - T_{amb})$ and, as expected, heat losses are higher for the extreme streamwise blocks located at the inlet and outlet of the model (blocks #1 and #5) because of the higher heat conduction from these blocks to the adjacent metal parts of inlet and outlet sections. Similar trends have been found between the different test articles.

As regards rotating tests with convergent geometries formed by aluminum blocks an additional analysis has been performed to estimate the variation of heat losses in rotating conditions with respect to the static cases. A simplified model, represented by the thermal circuit in Figure 4.21, has been considered; since the thermal conductivity of the aluminum is high the metal temperature $T_{w,i}$, measured by the thermocouple in TC position, is extended to the entire block, and the conduction through thermal insulating shell and external convection with ambient air is also included in the *overall heat transfer coefficient* U_{eq} . First of all, start-

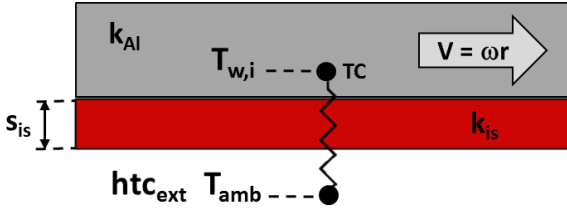


Figure 4.21: Schematic of the thermal circuit used to evaluate heat losses in rotating conditions

ing from the Q_{loss} values measured in static conditions, the outer heat transfer coefficient htc_{ext} between the insulating shell and the ambient has been calculated considering the following heat transfer equation:

$$\begin{cases} Q_{loss} = U_{eq}(A_{lat} + A_{sup})(T_{w,i} - T_{amb}) \\ U_{eq} = \frac{1}{\left(\frac{s_{is}}{k_{is}} + \frac{1}{htc_{ext}}\right)} \end{cases}$$

Then, considering the rotating case, the test model has been reduced to a flat plate, moving in the air with a velocity $v = \omega r$, where ω is the rotational speed of the test rig and r is the average radial distance between test model and rotation axis. According to this configuration htc_{ext} has been recalculated using the heat transfer correlations concerning the forced convection on flat plates with laminar and turbulent flow, even if Reynolds number Re_L for present application is below $5 \cdot 10^5$ (laminar flow). The heat transfer correlations used for this analysis are the following:

$$\begin{cases} Nu_L = \frac{htc_{ext}L}{k_{air}} = 0.664Re_L^{0.5}Pr^{1/3} & Re_L < 5 \cdot 10^5 \quad \text{laminar} \\ Nu_L = \frac{htc_{ext}L}{k_{air}} = 0.036Re_L^{0.8}Pr^{1/3} & Re_L > 5 \cdot 10^5 \quad \text{turbulent} \end{cases}$$

Finally, the above recalculated htc_{ext} values have been employed to calculate the heat loss in the rotating cases. Table 4.7 shows that the average increase of Q_{loss} with respect to the static case is about 10%.

Table 4.7: Comparison of heat losses Q_{loss} between static and rotating experiments

Case	htc_{ext} W/m^2K	ω [rpm]	v [m/s]	$Q_{loss,rot}/Q_{loss,stat}$
Static	10.3	0	0	1
Rotating (laminar)	20.1	100	9.17	1.06
Rotating (turbulent)	43.3	100	9.17	1.09
Rotating (laminar)	26.5	173	15.87	1.07
Rotating (turbulent)	43.3	173	15.87	1.10

4.5 Friction factor measurement

In the present work static pressures were acquired for different positions along each test model to evaluate the overall pressure drop for different Reynolds numbers. These results have been processed in order to obtain: friction factor distributions as a function of Reynolds number, total to static pressure ratios as a function of a non dimensional mass flow rate (i.e. flow functions). At the end of this process some design correlations have been derived with the aim of obtaining the pressure loss and evaluating the coolant consumption in the operating conditions of a real case.

First of all, starting from the overall static pressure drop measured during the tests, the overall friction factor has been calculated for each Reynolds number. However, since the friction factor should be based on total to total pressure values it has been necessary to convert the measured static pressure information to total pressure values.

For this reason an iterative procedure has been adopted to calculate the total pressure on the inlet, average and outlet sections of each matrix model. In each of these sections the following isentropic equation has been applied to calculate the product (ρc) using total temperature T_{tot} and static pressure p values measured in that specific section.

$$\rho c = \frac{p}{\sqrt{R \cdot T_{tot}}} \cdot \sqrt{\gamma} \cdot M \cdot \sqrt{1 + \frac{\gamma - 1}{2} \cdot M^2} \quad (4.27)$$

The product (ρc) , derived from the previous equation by iterating on Mach number M , is then compared with the (ρc) obtained from the measurement of the mass flow rate. At the minimum difference between these (ρc) products corresponds the value of Mach number that allows to derive the desired total pressure value p_{tot} using the following isentropic relationship:

$$\frac{p_{tot}}{p} = \left(1 + \frac{\gamma - 1}{2} \cdot M^2\right)^{\frac{\gamma}{\gamma - 1}} \quad (4.28)$$

Repeating the previous procedure for the inlet and outlet section the overall total pressure drop Δp_{tot} has been calculated; this latter has been employed to determine the overall friction factor according to the following equations:

$$f_{s,in} = \frac{\Delta p_{tot} \cdot d_{h,s,in}}{4 \cdot L_{tot} \cdot 1/2 \cdot \rho \cdot v_{in}^2} \quad (4.29)$$

$$f_{s,ave} = \frac{\Delta p_{tot} \cdot d_{h,s,ave}}{4 \cdot L_{tot} \cdot 1/2 \cdot \rho \cdot v_{ave}^2} \quad (4.30)$$

where v_{in} and v_{ave} are the flow velocity in the sub-channel at the inlet and average section of the model, while L_{tot} is the overall distance of the flow along a track as depicted in Figure 4.22.

It should be noted that for matrix geometries with constant cross section the friction factor has been calculated according to Equation 4.29, while for matrix geometries with convergent cross section the Equation 4.30 has been adopted; in fact for convergent geometries the velocity and hydraulic

diameter at the average or middle section are considered to be the most significant for the calculation of friction factor.

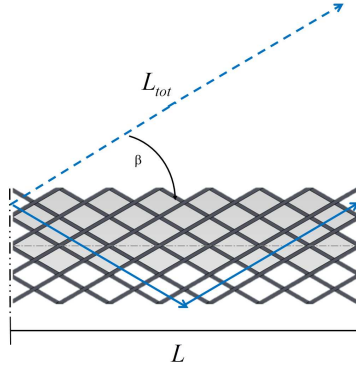


Figure 4.22: Difference between the length of a matrix model L and the effective overall distance of the flow along a track L_{tot}

Moreover, the friction factor values $f_{s,in}$ or $f_{s,ave}$ have been normalized by f_0 values calculated at the same Reynolds number by means of the Karman-Nikuradse correlation:

$$f_0 = 0.046 \cdot Re_s^{-0.2} \quad (4.31)$$

where f_0 is the friction factor of a fully developed turbulent flow in a smooth duct.

From this normalization the f_s/f_0 trends have been obtained in order to get a better comparison between the investigated geometries and other matrix geometries reported in the technical literature.

In addition to this, a total to static pressure ratio β_{TS} has been calculated for each mass flow rate and a trend of this ratio as a function of a non dimensional mass flow rate \dot{m}_{rid} has been derived for each matrix geometry.

The total to static pressure ratio β_{TS} is calculated as follows:

$$\beta_{TS} = \frac{p_{tot,in}}{p_{out}} \quad (4.32)$$

where $p_{tot,in}$ is the total pressure evaluated at the inlet section, while p_{out} is the static pressure measured at the outlet section of the model. On the other hand, the non dimensional mass flow rate is calculated as:

$$\dot{m}_{rid} = \frac{\dot{m}_{can} \cdot \sqrt{R \cdot T_{tot,in}}}{p_{tot,in} \cdot A_{can,out}} \quad (4.33)$$

where \dot{m}_{can} is the mass flow rate for the single sub-channel and $T_{tot,in}$ is the total temperature evaluated at the inlet section.

From Equation 4.33 it should be noted that the non dimensional mass flow rate is based on the sub-channel passage area at the outlet section $A_{can,out}$, because this is the most representative section for the pressure losses in a matrix geometry. In fact, as will be reported in Chapter 5, in case of both constant and convergent matrix geometries, the outlet section is the section that contributes most of all to generate the overall pressure drop.

Moreover, for each matrix geometry, it has been demonstrated that the best fitting for the trend $\beta_{TS} - \dot{m}_{rid}$ is ensured by the following function:

$$\dot{m}_{rid} = (a \cdot \beta + b) \cdot \sqrt{\frac{2 \cdot \gamma}{\gamma - 1} \cdot \left(\beta_{TS}^{-2/\gamma} - \beta_{TS}^{-(\gamma+1)/\gamma} \right)} \quad (4.34)$$

Equation 4.34 derives from the definition of the isentropic mass flow rate in a nozzle.

All the results obtained in terms of pressure loss, friction factor distributions and total to static pressure ratio will be reported in the following Chapter 5.

4.6 Measurement uncertainty

The adoption of a certain measurement technique to investigate a physical phenomenon implies two important principles: first, the measured quantity have a clear relationship to the phenomenon of interest,

second the measurement is performed in a way which will produce the minimum disturbance. The understanding of these two principles allows to exactly define the physical quantity of interest and to correctly place the measurement devices in the environment.

The measurement of a physical quantity is generally performed by means of a measurement chain, that typically consists of the following elements: probe, transducer, manipulation element, recording device, display element and acquisition system (Figure 4.23).

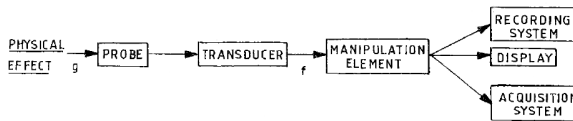


Figure 4.23: Schematic of a generic measurement chain

The *probe* detects the physical effect of the quantity to be measured and converts it into a signal detectable by a transducer. To obtain a reliable signal is necessary that the disturbances due to the presence of the probe in the flowfield are as small as possible (e.g. a hot wire anemometer to measure the flow speed).

The *transducer* is a device that converts the physical effect given by the probe into an electric signal because this is the form of signal that is most easily measured. This signal may be in analog or digital form; this latter is more convenient because it offers the advantage of an easy storage in memory devices and a manipulation with computers. This electrical conversion has other advantages such as: an amplification of the signal, a transmission of the signal at a long distance and a conversion with large frequency band.

The *manipulation element* is a general device dedicated to the acquisition and transmission of the signal with the minimum alteration; it may be an amplifier, a filter or an emitter.

The *recording device*, *display element* and *acquisition system* act to indicate, record and transform the output provided by the manipulation

element into an interpretable form using a computer (e.g. memory of a computer).

Since many different interactions may exist between the elements of the measurement chain and the environment, the measured value is different from the real value; in other words there is difference between what one would like to measure and what one is able to measure. To minimize the effects of these disturbances it is important to compensate them during the measurement process and to accurately design and select the probe and the other elements of the measurement chain.

Moreover, each device, probe or sensor of the measurement chain has its own accuracy that could affect the observed quantity; for this reason it is fundamental to know the accuracy of each measuring device.

All the above mentioned elements have a direct consequence on the so-called *experimental uncertainty*. In fact the measurement of the same quantity using the same equipment but in different facilities will probably give different results. This is mainly due to the differences in instrument calibration, interactions between environment and measurement chain elements and human factors. Even the repetition of an experiment in the same facility will most probably not produce identical results but they are always expected to fall within an interval around a certain measurement point. This interval is the experimental uncertainty and is a measure of the possible error made on a particular experiment [114]. It should be noted that an important difference exists between the concepts of “error” and “uncertainty”. Although it is very common for people to speak of experimental errors, the correct terminology should be “uncertainty” and the two terms should not be confused. In fact the error is associated to a single measurement and is the difference between the “measured” or “corrected” value and the “true” or “real” value. On the other hand the uncertainty is referred to a number of experiments and represents the possible value that the measurement error may have. [115].

According to the technical literature the real experiments are subject to two types of errors:

1. *random errors* or *precision errors* are obtained when repeated trials

of an experiment are done using the same equipment and test facility. This error generally scatters around a mean value according to a Gaussian distribution. The mean value is accurately determined from a sufficient number of data points, while the standard deviation σ measures the amount of variation from this mean value and is an evaluation index of the random error. This type of error can be reduced by improving instrumentation accuracy (Figure 4.24).

2. *systematic errors* or *bias errors* represent the difference between the mean value of the measurements and the actual “true” or “real” value of the measured quantity. Unlike the random error the bias is constant for a repeated trial of an experiment but it can not be estimated from a statistical analysis. It can be difficult to estimate the bias error because the “true” value is generally unknown but an accurate instrument calibration and a comparison with other measurement methods allows to evaluate it (Figure 4.24).

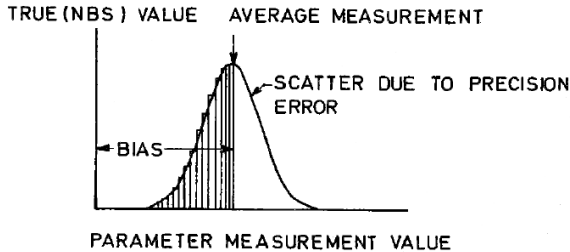


Figure 4.24: Systematic errors vs random errors

On the other hand the uncertainty is determined for a number of experiments and represents the possible value that the error may have within a given confidence level. For example, considering a generic measurement of the heat transfer coefficient HTC, the correct form to express its uncertainty is as follows:

$$HTC = 500 \text{ W/m}^2\text{K} \pm 25 \text{ W/m}^2\text{K} \quad (20 : 1) \quad (4.35)$$

where the measured value is $500 \text{ W/m}^2\text{K}$, the uncertainty value is $\pm 25 \text{ W/m}^2\text{K}$ and the confidence level is $(20 : 1)$; this latter means that 95% (or 19 out of 20) of the measurements will fall within the uncertainty interval $(20 : 1)$. This corresponds to a confidence level of 95% and is commonly used in engineering. It should be noted that the value of uncertainty always depend on the confidence level and an increase of measurement accuracy leads to a smaller uncertainty and a higher confidence level.

The analysis of the experimental uncertainty may be distinguished in two parts:

1. uncertainty in primary or direct measurements
2. uncertainty in a result derived from direct measurements

In the first case the uncertainty is the symmetrical band around a measurement within which the true value should fall (e.g. $300\text{K} \pm 0.5\text{K}$ is the temperature given by a thermocouple with its related uncertainty). The second is the most common case in an experimental activity where the primary measurements must be combined to calculate the desired result; therefore, the uncertainty in the final result is due to the uncertainties in the primary measurements. Thus, it is important to understand how the uncertainties associated to direct measurements can affect the observed quantity.

To calculate the average experimental uncertainty on the observed quantities the following method reported by Holman [115] and proposed by Kline and McClintock [116] is usually adopted.

Let's call R the observed quantity of an experiment that is a given function of n independent variables $x_1, x_2, x_3 \dots x_n$, which in turn are characterized by their uncertainties with the same confidence level of 95%. Thus, the overall uncertainty in the indirect quantity R can be expressed as:

$$R = R(x_1, x_2, x_3 \dots x_n) \quad (4.36)$$

Let's call ΔR the uncertainty in the result and $\Delta x_1, \Delta x_2, \Delta x_3 \dots \Delta x_n$ the uncertainties in the independent variables, then the uncertainty in the result is given by:

$$\Delta R = \sqrt{\left(\frac{\partial R}{\partial x_1} \Delta x_1\right)^2 + \left(\frac{\partial R}{\partial x_2} \Delta x_2\right)^2 + \dots + \left(\frac{\partial R}{\partial x_n} \Delta x_n\right)^2} \quad (4.37)$$

Therefore, the application of this method allows to establish that the final observed quantity R is measured with an uncertainty of $\pm \Delta R$ and a confidence level of 95%.

Finally, since the uncertainty propagation in the result ΔR predicted by Eq. 4.37 depends on the squares of the several uncertainties $\Delta x_1 \dots \Delta x_n$ it is possible that the uncertainty of one variable is significantly larger than the uncertainties in the other variables; this means that it is the largest uncertainty that predominates and the others could be neglected [115].

In the present work the above reported method was applied to evaluate the experimental uncertainty on the following final quantities: mass flow rate, Reynolds number, friction factor and heat transfer coefficient.

As regards the mass flow rate, this was measured using an orifice plate equipped with two static pressure taps and a thermocouple according to the standard UNI-EN ISO 5167-1 (§ 4.3.1). The overall uncertainty in mass flow rate is mainly given by the combination of the uncertainties in the primary measurements such as pressures and temperatures. These uncertainties were derived by the data sheets of the measuring devices. For example the static pressures at the orifice were measured with an accuracy of 51 Pa, 17 Pa and 6.9 Pa for sensor pressure range of 15, 5 and 1 psi respectively. Pressure range has been changed depending on the expected mass flow rate in order to guarantee the best measurement accuracy for each test. Temperature at the orifice was measured using a T-type thermocouple with an accuracy of $\pm 0.5K$, while the accuracy of

the duct diameter is given by the accuracy of the caliper. Starting from these considerations, it was found that the maximum uncertainty falls into the range $1.2 \div 4\%$ (Table 4.8).

Once known the mass flow rate uncertainty, fluid properties and some geometric dimensions, it was possible to estimate that the maximum uncertainty in Reynolds number is 5% (Table 4.9).

As regards the average friction factor f its uncertainty is mainly affected by the uncertainty on the estimation of the flow velocity through a sub-channel of the matrix model. It was evaluated that the maximum uncertainty on friction factor is $\pm 10\%$ (Table 4.10).

Finally the uncertainty on heat transfer coefficient HTC was evaluated taking into account the combination of the accuracies coming from all the devices used for both static and rotating steady tests. Even the uncertainty on heat losses determination was included in this procedure through the evaluation of the uncertainty on the heat loss coefficients a_i that characterize the polynomial functions derived from heat losses calibration tests. This uncertainty is estimated around 10% (§ 4.4.3).

Even the uncertainty on heat input Q_{input} gives an important contribution to the final uncertainty on HTCs. It should be noted that this uncertainty is higher ($\pm 7\%$) for rotating tests with respect to static ones ($\pm 3\%$); this is mainly due to the lower accuracy of current measurement for the DC power supply adopted during these tests.

For this reason the maximum uncertainties on HTCs for static and rotating tests are about $\pm 6\%$ (Table 4.11) and $\pm 10\%$ respectively (Table 4.12).

Table 4.8: Uncertainty analysis on mass flow rate

	Variable	Exp. Technique	Uncertainty	Units
d	Orifice diameter	Caliper	$\pm 0.5\%$	[-]
D	Duct diameter	Caliper	$\pm 0.5\%$	[-]
T	Temperature	T-type thermocouple	± 0.5	[K]
p	Pressure	Pressure taps DSA 3217 15 psi	± 51	[Pa]
p	Pressure	Pressure taps DSA 3217 5 psi	± 17	[Pa]
p	Pressure	Pressure taps DSA 3217 1 psi	± 6.9	[Pa]
\dot{m}	Mass flow rate	Orifice	$\pm 4\%$	[-]

Table 4.9: Uncertainty analysis on Reynolds number

	Variable	Exp. Technique	Uncertainty	Units
\dot{m}	Mass flow rate	Orifice	$\pm 4\%$	[-]
d_h	Hydraulic diameter	-	$\pm 2\%$	[-]
A	Area	-	$\pm 3\%$	[-]
μ	Dynamic air viscosity	-	$\pm 0.1\%$	[-]
Re	Reynolds number	-	$\pm 5\%$	[-]

Table 4.10: Uncertainty analysis on Friction Factor

	Variable	Exp. Technique	Uncertainty	Units
d_h	Hydraulic diameter	-	$\pm 2\%$	[-]
p	Pressure	Pressure taps DSA 3217 15 psi	± 51	[Pa]
p	Pressure	Pressure taps DSA 3217 5 psi	± 17	[Pa]
L_{tot}	Overall flow distance	-	$\pm 0.05\%$	[-]
ρ	Air density	-	$\pm 0.15\%$	[-]
v	Flow velocity	-	$\pm 5\%$	[-]
f	Friction factor	-	$\pm 10\%$	[-]

Table 4.11: Uncertainty analysis on Heat Transfer Coefficient HTC for Static Tests

	Variable	Exp. Technique	Uncertainty	Units
Q_{input}	Heat input	0-30V,0-5A DC power supplies	$\pm 3\%$	[-]
a_i	Heat loss coefficients	Steady state calibration tests	$\pm 10\%$	[-]
T	Temperature	T-type thermocouple	± 0.5	[K]
A	Area	-	$\pm 0.3\%$	[-]
HTC	Heat Transfer Coefficient	-	$\pm 6\%$	[-]

Table 4.12: Uncertainty analysis on Heat Transfer Coefficient HTC for Rotating Tests

	Variable	Exp. Technique	Uncertainty	Units
Q_{input}	Heat input	12.5V, 120A DC power supply	$\pm 7\%$	[-]
a_i	Heat loss coefficients	Steady state calibration tests	$\pm 10\%$	[-]
T	Temperature	T-type thermocouple	± 0.5	[K]
A	Area	-	$\pm 0.3\%$	[-]
HTC	Heat Transfer Coefficient	-	$\pm 10\%$	[-]

Chapter 5

Experimental Results: Friction and Pressure Losses

In this chapter will be reported all the experimental data about friction factors and pressure losses of the eight investigated matrix geometries.

It is well known that the study of pressure losses within internal cooling passages represents an important step of blade cooling design as well as the heat transfer. In fact both pressure losses and heat transfer have to be considered in a synergistic combination in order to reach the best cooling efficiency without affecting the cooling performance.

As it is well known from heat transfer correlations available in literature, the heat transfer enhances with the increase of coolant mass flow rate. Since this latter is a function of the coolant supply pressure and internal cooling geometry, an optimized design of these internal passages is necessary to minimize the coolant flow blockage and hence the overall pressure drop. A low pressure drop is advantageous because it guarantees a lower penalty on the global performance and provides a wider coolant operating range to match the design and off-design operating conditions of the gas turbine.

In the present chapter the results for each investigated geometry will be

reported in the following way. First of all, the results are given as pressure ratio distributions along the streamwise direction for different Reynolds numbers; these trends allow to quantify the increase of pressure loss with the increasing of the streamwise distance from the inlet and with the increasing of the Reynolds number.

Then, from the evaluation of the overall total pressure drop from the inlet to the outlet of each model, the friction factor trends as a function of Reynolds number will be presented.

In addition to this, other results will be given as the overall total to static pressure ratio trends as a function of a non dimensional mass flow rate; these flow functions will also allow to evaluate performance of the tested geometries in the context of the operating conditions of a real application.

5.1 Friction results of static tests for matrix geometries with constant cross section

Static pressures were acquired along four different sub-channels tracks from the inlet to the outlet of each test model; Figure 5.1 shows the pressure taps locations for *Geom 01*, while Figures 5.2 depicts the pressure tracks for the other three matrix geometries with constant cross section. In each case all the pressure taps are realized on both side walls, where the flow has to turn and switch from one layer/module to another one. Since in this case (*Geom 01*) these taps are located in the lower matrix module a difference should be highlighted between the left taps and the right taps. In fact pressure taps on the right side ($p_{1,dx} \dots p_{5,dx}$) are directly invested by the flow that hits the side walls before turning, while pressure taps on the left side ($p_{1,sx} \dots p_{5,sx}$) measure the pressure after that the flow has turned.

This different behaviour is clearly visible in the graph of Figure 5.3; in fact, from the comparison between the pressure trend of track #1 (i.e. blu line) and track #2 (i.e. red line) results that higher pressure values are recorded by pressure taps on the right side for each streamwise position.

The same behaviour has been also found for higher Reynolds numbers. However these differences between pressures on right side and left side are not so high; the maximum difference is about 200 Pa at the highest Reynolds number $Re_{s,in} = 8726$.

Similar trends for pressure values on the right side and pressure values on the left side have been also found for the other geometries.

Then, since the pressure measurements are very similar along the four tracks, only pressure values of track #1 are shown in the following comparison, that shows the pressure drop in terms of pressure ratios from the ambient pressure p_{amb} with the increasing of Reynolds number $Re_{s,in}$ (Figure 5.4).

As expected, the pressure drop rises with the increasing of streamwise distance from the inlet, especially in the second half of the geometry from the position $x/L = 0.5$ corresponding to the third pressure tap indicated as $p_{3,sx}$.

Moreover pressure drop increases with the increasing of Reynolds number; for example, considering the pressure value at the outlet p_{out} with respect to ambient pressure $p_{amb} = 100000$ Pa, the overall pressure drop through the model is about 100 Pa at the minimum Reynolds number $Re_{s,in} = 2480$, while is about 1300 Pa at the maximum Reynolds number $Re_{s,in} = 8726$.

As mentioned in section 4.1.2, two of these geometries (*Geom 01*, *02*) are characterized by a high rib height ($h_{rib} = 15$ mm) suitable for an application in the mid-chord region of the airfoil, while the other two (*Geom 03*, *04*) have a low rib height ($h_{rib} = 1.5$ mm) comparable with the thickness of the airfoil in the trailing edge region.

For this reason a first good comparison about pressure losses can be made between *Geom 01* and *Geom 02* (Figures 5.5), and between *Geom 03* and *Geom 04* (Figures 5.6).

In the first comparison (Figures 5.5) it is clear how a reduction of hydraulic diameter from 10.59 to 5.62 mm due to an increase of rib thickness from 1.5 to 3.0 mm for *Geom 02* determines a significant increase of pressure drop. In fact at the same Reynolds number nearly 6300 (i.e

$Re_{s,in} = 6350$ for *Geom 01* and $Re_{s,in} = 6386$ for *Geom 02*) the overall pressure drop is about 650 Pa for *Geom 01* and 4000 Pa for *Geom 02* starting from an ambient pressure $p_{amb} = 100000$.

In the second comparison (Figures 5.6) a similar situation occurs moving from *Geom 03* to *Geom 04*, but these trends are characterized by much higher pressure losses because of the very narrow flow passage areas. In this case the reduction of hydraulic diameter from 2.54 to 2.09 mm due to an increase of rib thickness from 1.5 to 3.0 mm for *Geom 04* determines an increase of the overall pressure drop from 50000 Pa to 80000 Pa (considering $p_{amb} = 100000$) at the highest Reynolds number (i.e $Re_{s,in} = 10280$ for *Geom 03* and $Re_{s,in} = 10176$ for *Geom 04*).

By the comparison of Figures 5.5 with Figures 5.6 results clear that the behaviour of geometries *Geom 03* and *Geom 04* is extremely far from the previous *Geom 01* and *Geom 02*; these different results are due not only to the extremely different passage areas but also to the different flow velocities along the sub-channels.

Starting from the overall total pressure drop Δp_{tot} evaluated for each test model and following the definition given by Equation 4.29, the overall friction factor $f_{s,in}$ distributions have been determined as a function of the Reynolds number $Re_{s,in}$ for the four investigated geometries (*Geom 01, 02, 03, 04*).

These distributions are reported in Figure 5.7 together with a comparison with the Karman-Nikuradse correlation (Equation 4.31) for smooth ducts. There are significant differences between the trends of geometries with the higher rib height (*Geom 01, Geom 02*) and geometries with the lower rib height (*Geom 03, Geom 04*). First of all, values of friction factors are quite lower for *Geom 03* and *Geom 04* because of the higher flow velocities into the sub-channels. This latter consideration is justified by the definition of friction factor $f_{s,in}$ according to Equation 4.29.

Moreover, the trends for *Geom 01* and *Geom 02* become asymptotic at higher Reynolds numbers, while the trends for *Geom 03* and *Geom 04* slightly increase; this is mainly due to the very high velocities and hence the very high Mach number, which is close to one at the outlet section.

On the other hand Figure 5.8 shows the comparison between the same friction factor distributions and the Nagoga correlation valid for the basic section of matrix geometries (Equation 2.13). In this latter case, since the Nagoga correlation is based on the Reynolds number Re_l referred to the length of the channel l (Equation 2.8) instead of the sub-channel hydraulic diameter, it has been necessary to convert the Reynolds range for present geometries multiplying Re_s values by $l/d_{h,s}$ to guarantee a correct comparison with the correlation.

From this comparison there are significant differences between the experimental trends and Nagoga correlation and only at higher Re_l these differences seem to become smaller. It is not easy to understand the reasons of these discrepancies; in fact most of parameters for the four geometries (i.e. β , $l/d_{h,s}$, Re and L/W) fall into the same ranges valid for the correlation (Table 2.1). However the different form of sub-channel cross-section and the type of side wall (concave or flat) for the matrix geometries investigated by Nagoga could be the causes of these deviations. In addition to this, the flow functions for the four investigated geometries have been determined as trends of the total to static pressure ratio β_{TS} as a function of a non dimensional mass flow rate \dot{m}_{rid} . These two parameters have been calculated according to Equations 4.32 and 4.33 respectively. Figures 5.9, 5.10, 5.11 and 5.12 report these trends $\beta_{TS} - \dot{m}_{rid}$ together with the function which guarantees the best fitting for each experimental distribution.

Then, Figure 5.13 reports all the flow functions of the four geometries with constant cross section. It is clear that all these trends are quite well fitted by a single curve, even if this curve does not correctly represent the phenomenon at the highest total to static pressure ratios β_{TS} ; in fact an asymptotic trend should be expected for these values, while this curve maintain a growing trend. Further considerations on this fact will be given in the next sections.

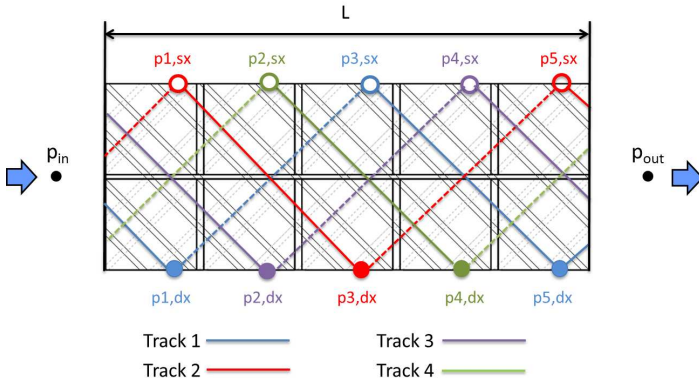


Figure 5.1: Geom 01 - pressure taps location along different sub-channel tracks

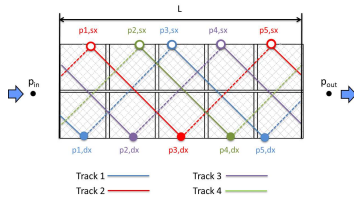
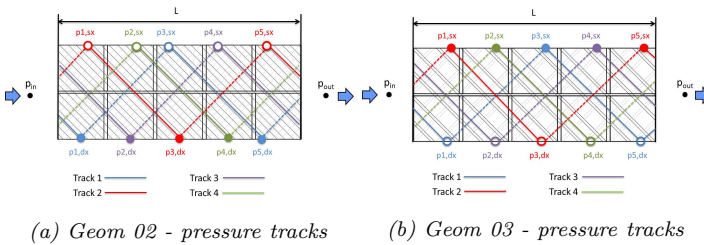


Figure 5.2: Geom 02, Geom 03, Geom 04 - pressure taps location along different sub-channel tracks

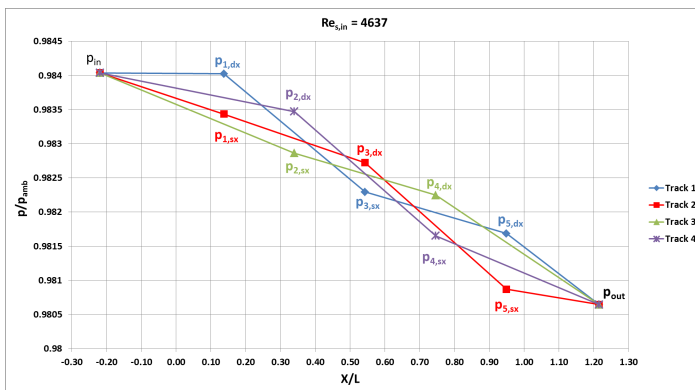


Figure 5.3: Geom 01 - pressure ratio distributions along different sub-channel tracks

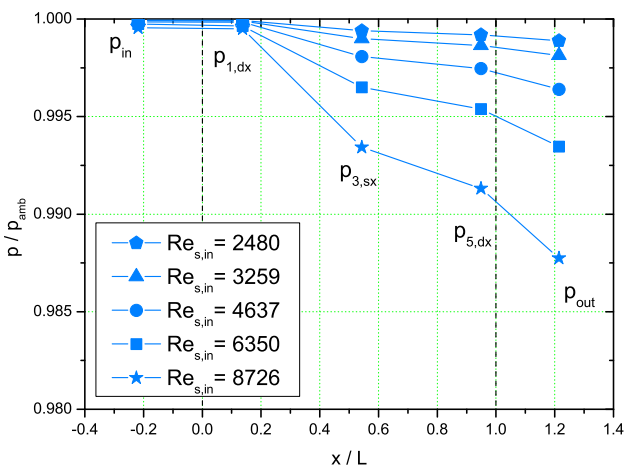
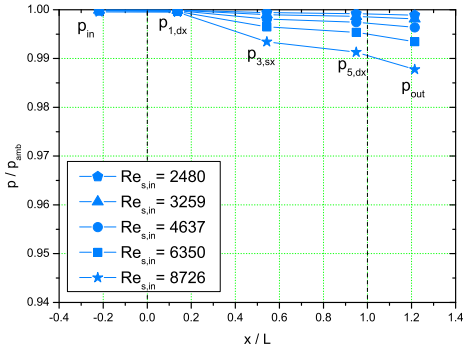
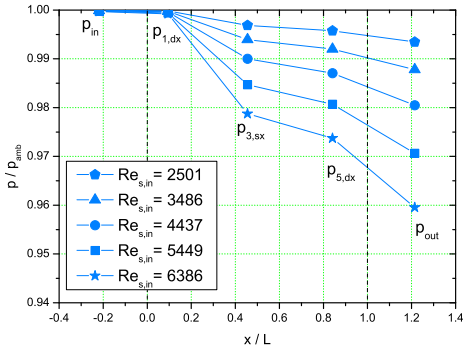


Figure 5.4: Geom 01 - pressure ratio distributions along track #1

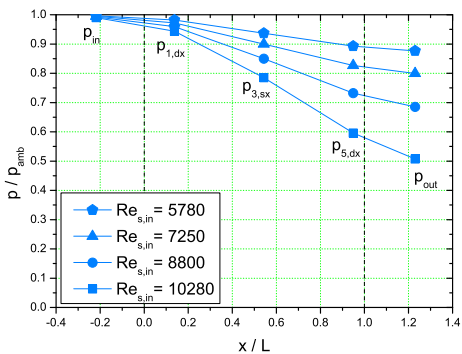


(a) Geom 01 - track #1

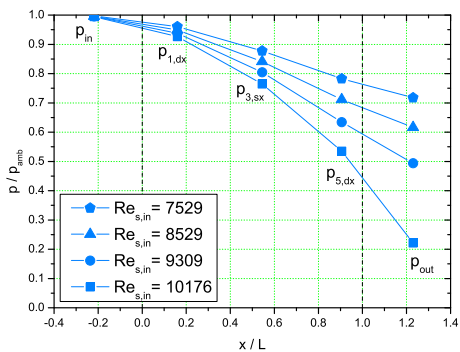


(b) Geom 02 - track #1

Figure 5.5: Geom 01 vs Geom 02 - Comparison of pressure ratio distributions along track #1



(a) Geom 03 - track #1



(b) Geom 04 - track #1

Figure 5.6: Geom 03 vs Geom 04 - Comparison of pressure ratio distributions along track #1

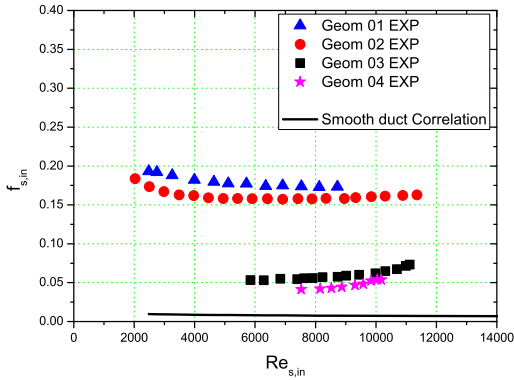


Figure 5.7: Comparison between friction factor distributions for Geom 01,02,03,04 and Karman-Nikuradse correlation for smooth ducts (Equation 4.31)

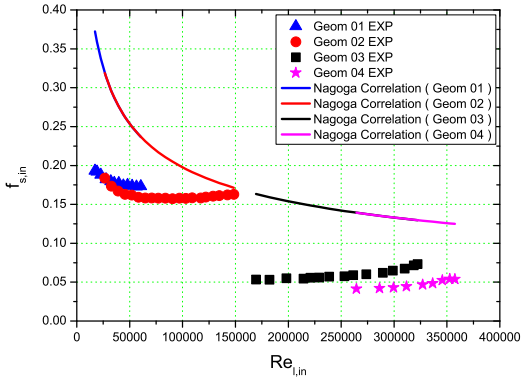


Figure 5.8: Comparison between friction factor distributions for Geom 01,02,03,04 and Nagoga correlation for matrix geometries (Equation 2.13)

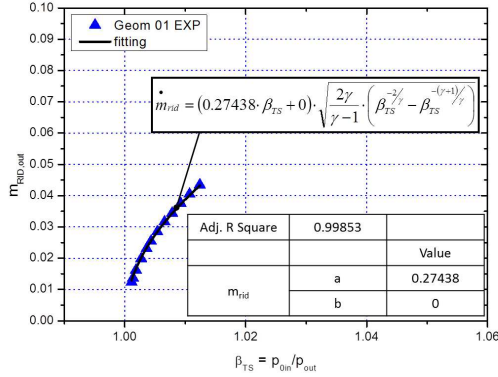


Figure 5.9: Geom 01 - Non dimensional mass flow as a function of total to static pressure ratio

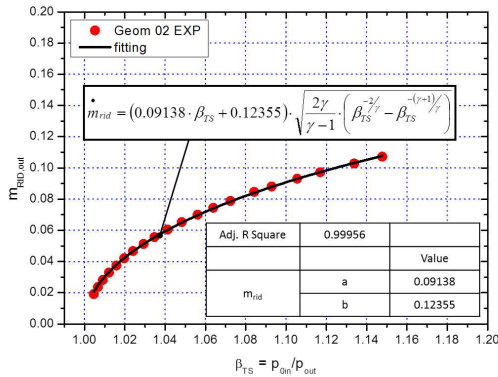


Figure 5.10: Geom 02 - Non dimensional mass flow as a function of total to static pressure ratio

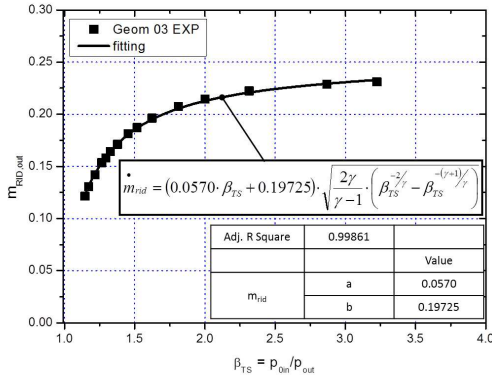


Figure 5.11: Geom 03 - Non dimensional mass flow as a function of total to static pressure ratio

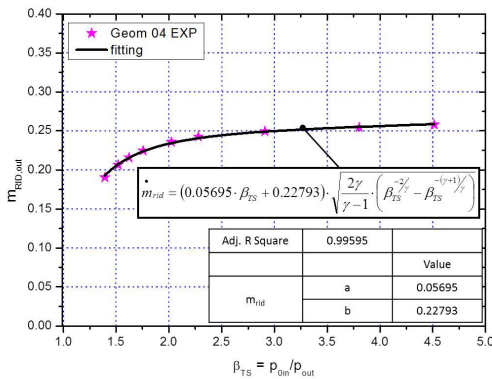


Figure 5.12: Geom 04 - Non dimensional mass flow as a function of total to static pressure ratio

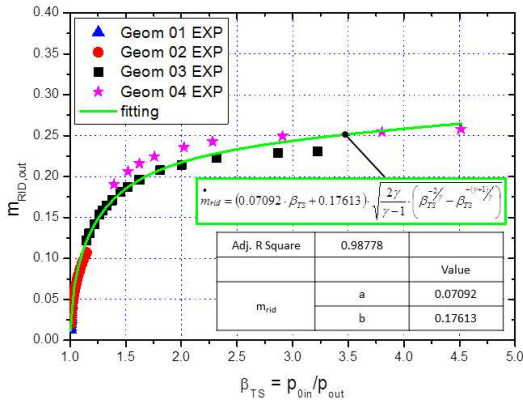


Figure 5.13: Comparison of non dimensional mass flow as a function of total to static pressure ratio for Geom 01,02,03,04

5.2 Friction results of static tests for matrix geometries with convergent cross section

As already done for the test models with constant cross section, also for the convergent models (*Geom 05* and *Geom 06*) static pressures have been acquired along four different sub-channels tracks. Figures 5.14a and 5.14b show the pressure tracks for these two geometries.

Pressure ratio distributions with respect to ambient pressure have been derived for different Reynolds numbers. An example of these distributions for the convergent geometry with four-entry channels *Geom 06* is reported in Figure 5.15, but similar results have been obtained for the convergent geometry with six-entry channels *Geom 05*.

As in the previous results for geometries with constant cross section (Figure 5.3) the pressure taps on the right side have recorded higher pressure values than those located on the opposite side wall, even though these differences are less noticeable for the present convergent cases because the graph scale has been chosen in order to represent the whole pressure variation from the inlet to the outlet of these test models.

Then, Figures 5.16a and 5.16b report a comparison between the pressure ratio distributions along track #1 with the increasing of Reynolds number $Re_{s,in}$ or $Re_{s,ave}$; unlike the previous cases, for the convergent geometries the value of Reynolds number based on the sub-channel hydraulic diameter at the middle section $Re_{s,ave}$ becomes significant in view of a possible correlation valid for both constant and convergent matrix geometries. For this reason the graph legends for these geometries include both $Re_{s,in}$ and $Re_{s,ave}$ numbers.

By the comparison of Figure 5.16a and Figure 5.16b results that in both cases pressure loss gradually increases along the convergent channel with the streamwise distance x/L , but the highest pressure drop occurs in the final part of the models, where the sub-channel height is extremely reduced and the flow velocity is higher. Moreover, the six-entry channel geometry (*Geom 05*) produces much higher pressure losses than the four-entry channel geometry (*Geom 06*); for example, considering an am-

bient pressure value $p_{amb} = 100000$ Pa, the overall pressure drop is about 16700 Pa for *Geom 05* at $Re_{s,in} = 3878$ and about 4150 Pa for *Geom 06* at $Re_{s,in} = 4309$ and hence at nearly the same Reynolds number.

However, Figure 5.16a for *Geom 05* with six sub-channels also highlights that the overall pressure drop have a rapid increase for higher Reynolds numbers, while the same does not occurs for geometry with four sub-channels (*Geom 06*).

From this comparison it can be concluded that the pressure penalty for the convergent geometry with six sub-channels becomes extremely significant even when little higher mass flow rates of coolant are required during the operating condition.

As explained in Section 4.1.3, the convergent geometries have common geometric features with the corresponding constant geometries and all these geometries can be distinguished in two groups: matrix modules of *Geom 06*, *Geom 01* and *Geom 03* have 4 sub-channels at the entry with a lower rib thickness $t_{rib} = 1.5$ mm, while matrix modules of *Geom 05*, *Geom 02* and *Geom 04* have 6 sub-channels at the entry with a higher rib thickness $t_{rib} = 3.0$ mm.

Starting from these considerations an interesting comparison can be made between these two groups of matrix geometries in order to put in evidence the behaviour of the convergent geometries with respect to the corresponding geometries with constant cross section. Figures 5.17 reports this comparison for the group of geometries with 4 sub-channels, while Figures 5.18 show this comparison for the group of geometries with 6 sub-channels. In each case it should be noted how the pressure losses for the convergent geometries fall into an intermediate range between the corresponding geometries with minimum and maximum cross section or rib height. Moreover, it can be noticed that the pressure drop for a convergent channel increases more gradually than the corresponding geometry with minimum cross section (*Geom 05* vs *Geom 04* or *Geom 06* vs *Geom 03*). From this information it can be concluded that the gradual increase of pressure losses for these convergent geometries could represent a good advantage in view of an application in a trailing edge

region of a real gas turbine airfoil.

Then the overall pressure drop Δp_{tot} has been used to determine the friction factor distributions $f_{s,ave}$ (Equation 4.30) as a function of $Re_{s,ave}$; unlike the previous constant geometries, in these cases friction factor and Reynolds number definitions are based on the hydraulic diameter and flow properties at the middle or average section of the matrix model. These friction factor distributions for these two convergent geometries (*Geom 05* and *Geom 06*) are reported in Figure 5.19 together with values from Karman-Nikuradse correlation and in Figure 5.20 together with values recalculated from Nagoga correlation. It can be noticed that in both these graphs the friction factor trend for *Geom 05* is very steep with the increase of Reynolds number and values become negative at the highest $Re_{s,ave}$; this may be due to some errors in the manufacturing of the test model and pressure taps. For this reason values for *Geom 05* have been considered with particular attention; in some cases it has been necessary to consider values of the similar scaled up test model *Geom 07* employed for the rotating experimental tests (Section 5.3).

Even for these cases the overall total to static pressure ratio β_{TS} as a function of a non dimensional mass flow \dot{m}_{rid} has been derived; the trends are reported in Figures 5.21 and 5.22 for *Geom 05* and *Geom 06* respectively together with the function which guarantees the best fitting for both cases.

In addition to this, both trends have been collected in an unique graph and have been fitted by a single curve (Figure 5.23); however, unlike the fitting for the four constant geometries (Figure 5.13), in this case a unique fitting curve is not enough accurate for both cases and some deviations are evident at the higher β_{TS} . Further considerations about this fitting will be reported in Chapter 7.

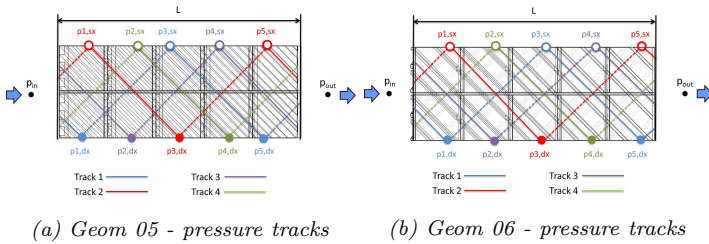


Figure 5.14: Geom 05, Geom 06 - pressure taps location along different sub-channel tracks

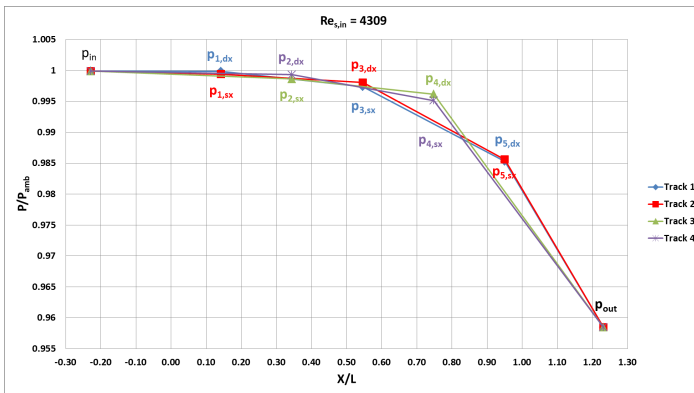
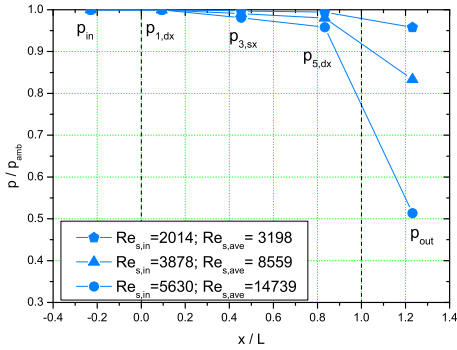
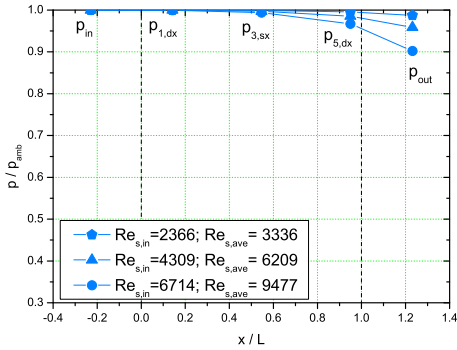


Figure 5.15: Geom 06 - pressure ratio distributions along different sub-channel tracks

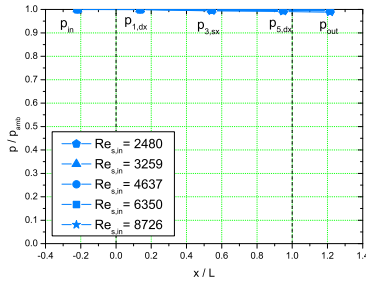


(a) Geom 05 - track #1

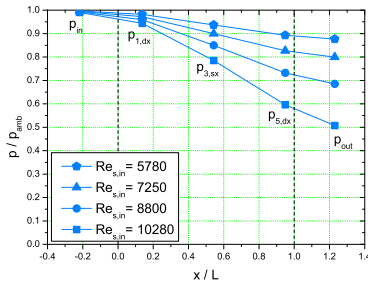


(b) Geom 06 - track #1

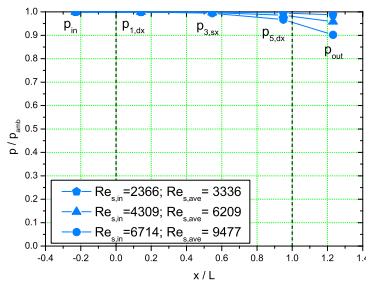
Figure 5.16: Geom 05 vs Geom 06 - Comparison of pressure ratio distributions along track #1



(a) Geom 01 - track #1

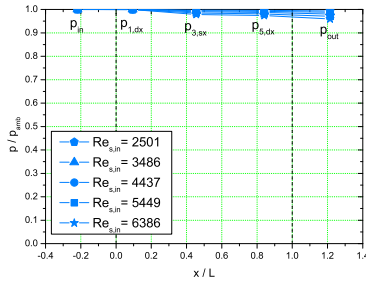


(b) Geom 03 - track #1

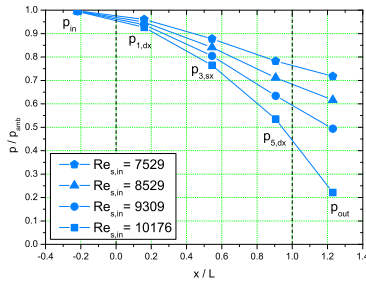


(c) Geom 06 - track #1

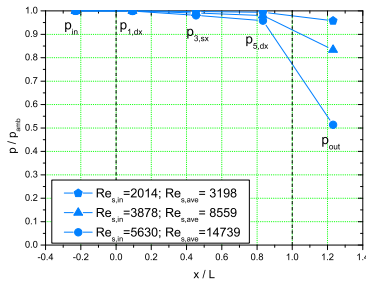
Figure 5.17: Geom 01 vs Geom 03 vs Geom 06 - Comparison of pressure ratio distributions along track #1



(a) Geom 02 - track #1



(b) Geom 04 - track #1



(c) Geom 05 - track #1

Figure 5.18: Geom 02 vs Geom 04 vs Geom 05 - Comparison of pressure ratio distributions along track #1

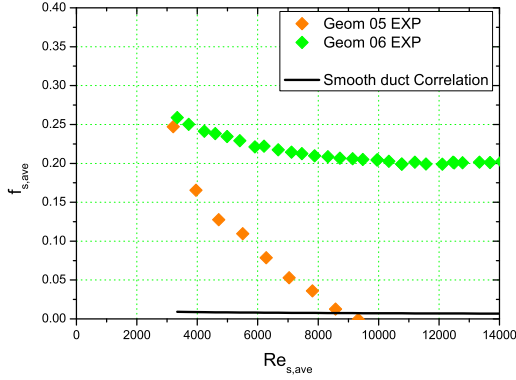


Figure 5.19: Comparison between friction factor distributions for Geom 05,06 and Karman-Nikuradse correlation for smooth ducts (Equation 4.31)

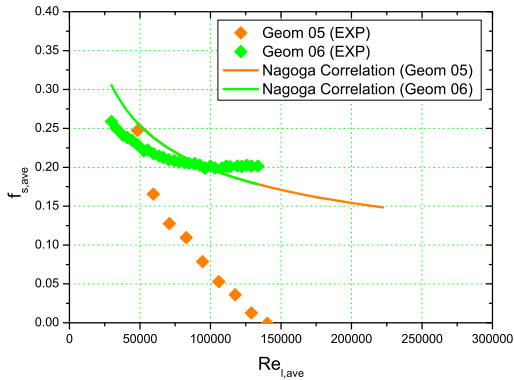


Figure 5.20: Comparison between friction factor distributions for Geom 05,06 and Nagoga correlation for matrix geometries (Equation 2.13)

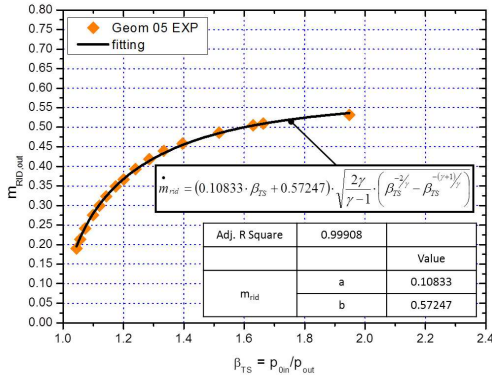


Figure 5.21: Geom 05 - Non dimensional mass flow as a function of total to static pressure ratio

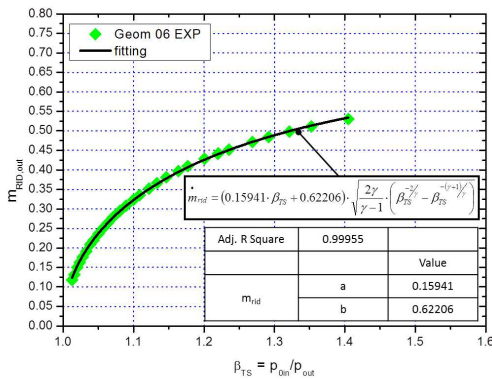


Figure 5.22: Geom 06 - Non dimensional mass flow as a function of total to static pressure ratio

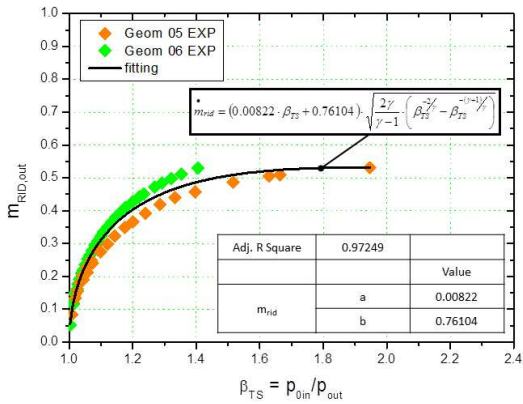


Figure 5.23: Comparison of non dimensional mass flow as a function of total to static pressure ratio for Geom 05,06

5.3 Friction results of rotating tests

As mentioned in Section 4.2.1, the two test articles employed for rotating tests, identified as *Geom 07* and *Geom 08*, are the scaled up models of *Geom 05* and *Geom 06* with 6 and 4 entry sub-channels respectively. Therefore, in a similar manner to the previous test models, the static pressures have been acquired along the four sub-channel tracks as depicted by the schemes in Figures 5.24a and 5.24b.

Before starting to present pressure results for these rotating tests, it should be noted that it has been necessary to correct the acquired pressure values in order to take into account the centrifugal effect on pressure taps located at the different radial positions. In fact, as mentioned in Section 4.2, the pressure scanner is located at the lowest radius while the several pressure taps are located at different radii (Figure 4.10).

For this reason a pressure gradient due to the centrifugal effect is generated within the several connection pipes that connect pressure taps with the scanner. Considering the schematic of pressure connection pipe in Figure 5.25, the centrifugal pressure gradient within this pipe between two radial positions r_i and r_{i-1} may be expressed as:

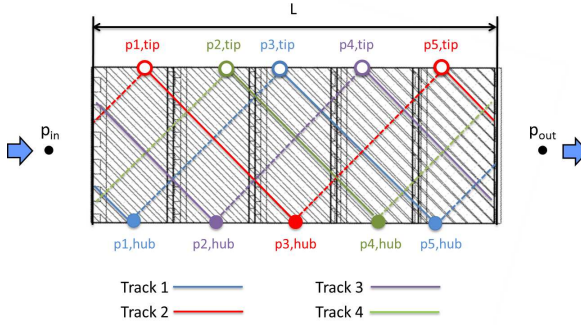
$$\Delta p = -\frac{1}{2}\rho\omega^2 (r_i - r_{i-1})^2 \quad (5.1)$$

According to Equation 5.1, the measured pressure value p_{meas} for each pressure tap has been corrected each time taking into account the specific radial position r_i and rotational speed ω as follows:

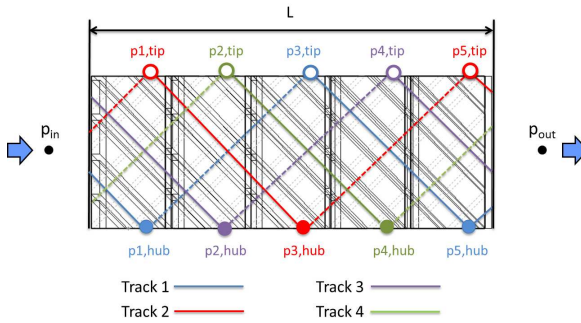
$$p_{corr} = p_{meas} + \frac{1}{2}\rho\omega^2 r_i^2 \quad (5.2)$$

Static pressures along the test models have been acquired both in static and in rotating conditions.

As regards static tests, Figures 5.26a and 5.26b show the pressure ratio distributions along track #1 for *Geom 07* and *Geom 08* with 6 and 4 entry sub-channels respectively. These distributions are reported as a function of the streamwise distance along the model for different Reynolds numbers. These results are similar to the above reported pressure ratio



(a) Geom 07 - pressure tracks



(b) Geom 08 - pressure tracks

Figure 5.24: Geom 07, Geom 08 - pressure taps location along different sub-channel tracks

distributions for the similar geometries *Geom 05* and *Geom 06*; even in this case the pressure loss increases gradually along the streamwise direction and the highest pressure drop is located in the final part of the convergent channel.

As regards rotating tests, Figure 5.27 reports the pressure ratio distributions for *Geom 08* at the same Reynolds number but for different

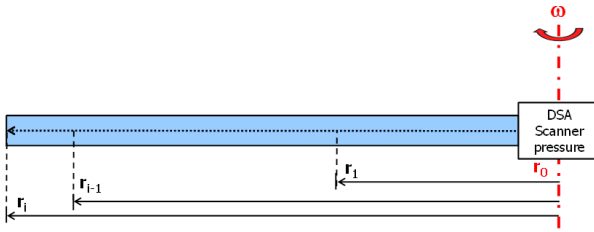


Figure 5.25: Schematic of the pressure connection pipe between the pressure scanner and the pressure taps

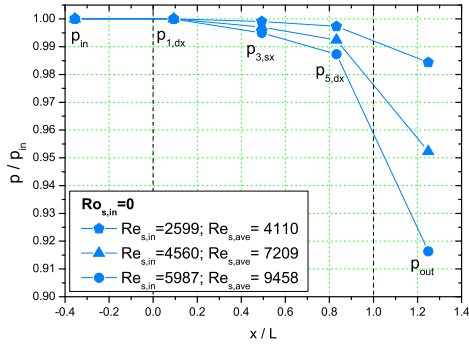
Rotation numbers ($Ro_{s,in} = 0 \div 0.093$); it is clear that the pressure distribution along the model is insensitive to the increase of rotational speed. Similar results about rotation effects have been found for *Geom 07*.

Then, it should be noted that for the rotating pressure distributions (i.e. Figure 5.27) the pressure values are normalized by the pressure measured at the inlet of the model $p_{4,in}$ instead of the ambient pressure value p_{amb} . From the evaluation of pressure drop the friction factor distributions $f_{s,ave}$ (Equation 4.30) as a function of $Re_{s,ave}$ have been derived in a similar way to the previous convergent geometries *Geom 05* and *Geom 06*. Figure 5.28 shows the comparison between these friction factor distributions and the Karman-Nikuradse correlation for smooth ducts, while Figure 5.29 reports the comparison with the Nagoga correlation. From these graphs it is clear that friction factors are higher for the geometry with 4 sub-channels and higher flow passage area *Geom 08*, even if it

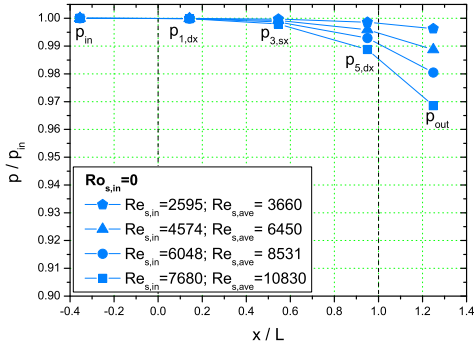
would be expected higher friction factors for geometries with more sub-channels and hence narrow flow passages (*Geom 07*). This aspect, that is also confirmed by the results on constant geometries (Figure 5.7) is mainly due to the much higher flow velocity into the sub-channels for geometries with narrow passages and is well described by the friction factor definition (Equation 4.30).

In addition to this, the friction factor trend for the 6 entry channels matrix geometry (*Geom 07*) follows a trend similar to that of the 4 entry channels geometry (*Geom 08*); in fact both of these have a slight decrease with the increasing of Reynolds number and seem to assume an asymptotic behaviour at the highest $Re_{s,ave}$. The trend for *Geom 07* confirms the errors found for *Geom 05*; in fact, as depicted in Figures 5.19 and 5.20, a very different trend has been found for *Geom 05* but this is not in agreement with all the other trends and this is surely due to manufacturing errors.

Finally, Figures 5.30 and 5.31 report the overall total to static pressure ratio β_{TS} as a function of the non dimensional mass flow rate \dot{m}_{rid} based on the sub-channel passage area at the outlet section (Equation 4.33). In the graph of Figure 5.30 values of *Geom 05* are reported together with values of *Geom 07*, while in Figure 5.31 values of *Geom 06* are reported together with values of *Geom 08*; in both graphs a very good agreement is found between the geometry with scale factor 5 : 1 and the corresponding scaled up geometry with scale factor 10 : 1. This is well confirmed by the two fitting curves: in fact only one curve is enough to fit the trends of each group of geometries.



(a) Geom 07 - track #1



(b) Geom 08 - track #1

Figure 5.26: Geom 07 vs Geom 08 - Comparison of pressure ratio distributions along track #1

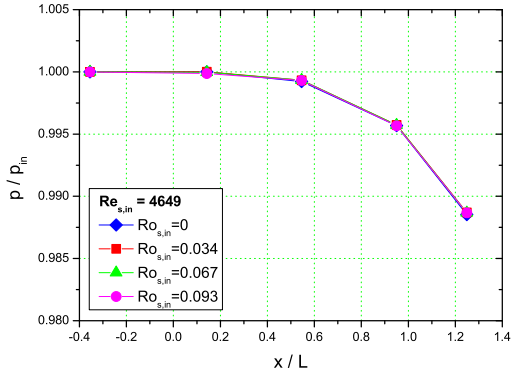


Figure 5.27: *Geom 08* - pressure ratio distributions along track #1 for different Rotation numbers

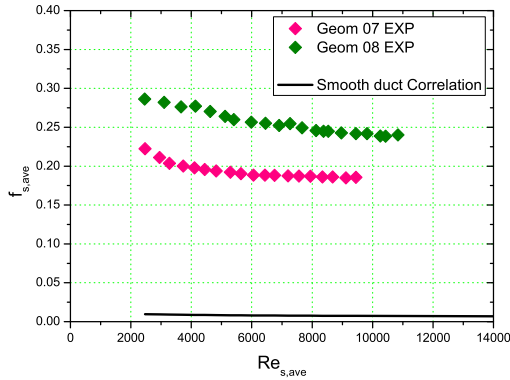


Figure 5.28: Comparison between friction factor distributions for *Geom 07,08* and Karman-Nikuradse correlation for smooth ducts (Equation 4.31)

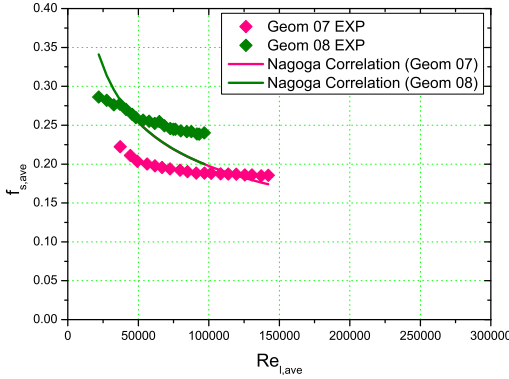


Figure 5.29: Comparison between friction factor distributions for Geom 07,08 and Nagoga correlation for matrix geometries (Equation 2.13)

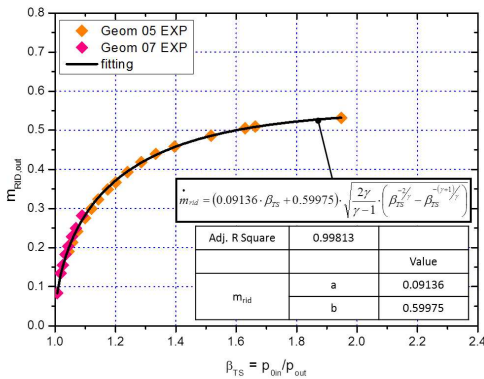


Figure 5.30: Geom 07 + Geom 05 - Non dimensional mass flow as a function of total to static pressure ratio

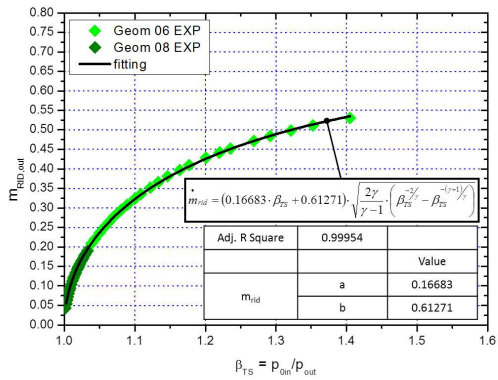


Figure 5.31: Geom 08 + Geom 06 - Non dimensional mass flow as a function of total to static pressure ratio

5.4 Comparison of friction results and critical evaluation

This section at the end of this chapter on pressure losses and friction factor results is necessary to give a summary about the above reported results of all the investigated matrix geometries.

First of all, the pressure trends along the four different sub-channel tracks for each test model have allowed to put in evidence differences between pressure values on the right side and those on the left side (example in Figure 5.3). It has been found that these differences are due to the flow that directly hits the pressure taps on the right side. However, in each flow condition, these differences are not so significant and it is correct to consider the pressure trend only on a single track from the entry to the exit of the matrix model.

Then, a comparison between the different matrix geometries has been made in terms of pressure ratio distributions p/p_{amb} or p/p_{in} as a function of the streamwise distance x/L . From these comparisons several results have been found:

- Increase of pressure losses due to an increase of rib thickness and number of sub-channels for geometries with the same rib height (Figures 5.5 and 5.6)
- Increase of pressure losses moving from geometries with higher rib height to geometries with lower rib height (*Geom 01,02* vs *Geom 03,04*)
- Effect of the converging angle on pressure losses and comparison with the corresponding constant geometries with the same rib thickness and number of sub-channels (Figures 5.17 and 5.18).
- The gradual increase of pressure losses for the convergent geometries (*Geom 05,06* vs *Geom 07,08*), even for the convergent geometries with narrower passages (*Geom 05,07*), represents a good starting point for a potential application in the trailing edge region of a gas turbine airfoil.

After this, a comparison in terms of friction factor distributions as a function of the Reynolds number has been performed for each investigated case; results show that friction factor is low for geometries with narrower sub-channels (i.e. geometries with 6 entry sub-channels and higher rib thickness) but, as already reported, this is mainly due to the higher flow velocities through the sub-channels. In addition to this, geometries with the minimum rib height (*Geom 03,04*) are characterized by high Mach numbers (i.e. close to one) at the outlet section.

As a summary, Figure 5.32 collects the friction factor distributions for all the investigated geometries (from *Geom 01* to *Geom 08*); in this case, for both constant and convergent geometries, friction factor and Reynolds values are based on flow properties and geometric parameters at the middle or average section of the test models. This graph shows that all the trends become insensitive to the increase of Reynolds number and show the characteristic horizontal asymptote with the exception of geometries with the smallest flow passage areas (*Geom 03,04*). In fact, in these cases the trends slightly increase with the increasing of Reynolds number because of the high Mach numbers and hence of the relevant compressibility effects near the outlet section.

To allow a better comparison between the investigated geometries and experimental results reported in literature, the friction factor distributions have been normalized by f_0 values calculated at the same Reynolds numbers by means of the correlation of Karman-Nikuradse for turbulent flows in smooth ducts (Equation 4.31). The normalized friction factor distributions $f_{s,ave}/f_0$ are summarized in Figure 5.33.

At the end, Figure 5.34 collects the flow functions $\beta_{TS} - \dot{m}_{rid}$ of the all investigated geometries; it is clear that these distributions seem to assume two trends: one for constant geometries and one for convergent geometries. In this latter case larger deviations exist at the higher total to static pressure ratios β_{TS} .

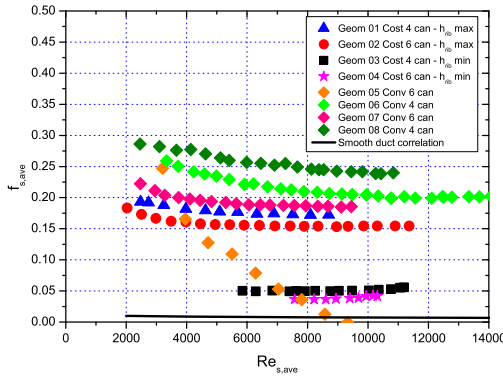


Figure 5.32: Friction factor distributions for different Reynolds numbers - Comparison between all investigated geometries

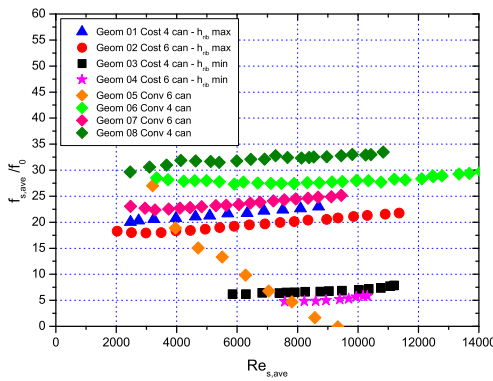


Figure 5.33: Normalized friction factor (f/f_0) distributions for different Reynolds numbers - Comparison between all investigated geometries

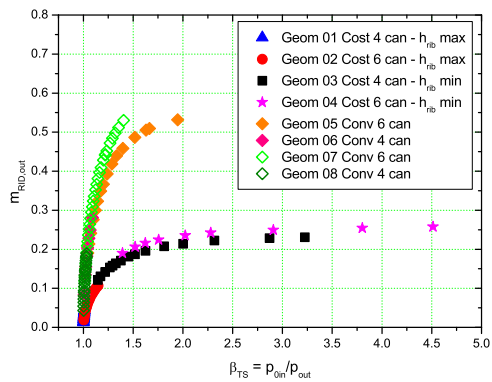


Figure 5.34: Nondimensional mass flow as a function of total to static pressure ratio - Comparison between all investigated geometries

Chapter 6

Experimental Results: Heat Transfer

The present chapter reports all the experimental data about the heat transfer performance of the eight investigated matrix geometries.

For each geometry the results are presented in the following way.

First of all, the effective heat transfer coefficient distributions with the increasing of streamwise position are given for each single row of matrix blocks that form the test models; these distributions are given for the minimum and maximum Reynolds number and comparisons are made between the different geometries.

Then, the same distributions are reported as the effective Nusselt numbers averaged on two couple of rows with the increasing of Reynolds number in order to highlight significant effects due to the coolant flow path.

In the next step, the effective and equivalent heat transfer coefficients and Nusselt numbers distributions as a function of the mass flow rate and Reynolds number will be presented; the effective heat transfer trends allow to evaluate the performance in terms of heat transfer between the coolant flow and the rib surfaces, while the equivalent trends quantify the overall heat removed from the endwall surfaces.

In the second part of the chapter the above mentioned trends are also reported for the rotating results. The rotation effects are evaluated by means of the overall rotation-to-stationary ratio between the Nusselt number in rotating condition and that found by the corresponding static case at the same Reynolds number. These values are reported as a function of the Rotation number for the different Reynolds numbers.

In addition to this, more detailed distributions of the same ratio are given as a function of the streamwise position for the rows of the matrix blocks corresponding to the pressure and suction side of the model. Further trends are then reported to compare the rotating results for the two different model orientations: *0deg* and *30deg* with respect to the rotating plane.

Finally, the last part of this chapter is focused on the comparison between the investigated geometries in terms of heat transfer enhancement and Thermal Performance Factor; comparisons have been also performed between the experimental and literary cases.

6.1 Heat transfer results of static tests for matrix geometries with constant cross section

As described in Section 4.4.2 the average heat transfer coefficients (HTCs) have been determined for each matrix block both along streamwise and spanwise direction. In fact each test model is considered to be divided into four different rows of matrix blocks: two rows for the upper module (SUP) and two rows for the lower module (INF); then, for each matrix module, there is a left row (SX) and a right row (DX). Each row is composed by 5 streamwise positions or blocks.

Heat transfer coefficient distributions have been determined for each of these four rows. Figures 6.1a and 6.1b report typical distributions of the effective heat transfer coefficients htc_r between fluid and rib surfaces for *Geom 01*; a comparison is made between the distributions for the minimum and maximum Reynolds numbers. From this comparison it is possible to quantify the increase of the htc_r value with the increasing of

Reynolds number for each position of the matrix model.

These distributions have been normalized by htc_{ref} that represents the htc_r value averaged on the first four blocks (streamwise position #1) for *Geom 01* at the minimum Reynolds number.

Figures 6.2, 6.3 and 6.4 report the same comparisons for geometries *Geom 02*, *Geom 03* and *Geom 04* respectively.

All these trends have some common features; first of all the HTC value is lower at the first streamwise position (block #1), then is quite constant in the middle part between block #2 and #4 and it is higher in the last position close the outlet section (block #5).

Another important common feature among the distributions for the several matrix geometries is that, for each case, the HTCs on the right row of the upper module (mod SUP - row DX) and on the left row of the lower module (mod INF - row SX) are higher with respect to the other two rows. The higher HTC values on these rows are related to the coolant flow path within the matrix structure; in fact the two above mentioned rows represent the regions where the flow impinges immediately after a turning region. In the turning region a strong vortical flow is formed together with the destruction of the thermal and fluid boundary layers; once the fluid has reached the opposite sub-channel it locally impinges creating a new thin boundary layer, accelerating again with a local increase of heat transfer coefficients. This result is in good agreement with the experimental work of Bunker [86] described in the previous Section 2.2.2 (Figure 2.44a).

To better highlight the higher heat transfer in these impingement regions, the htc_r values have been averaged on the two couple of rows: an average htc_r value has been obtained from the average values on the right row of upper module and left row of the lower module (mod SUP - row DX and mod INF - row SX), while an average htc_r value has been obtained for the other two rows (mod SUP - row SX and mod INF - row DX). In this way two average Nusselt numbers $Nu_{r,s,in}$ have been obtained for each investigated Reynolds number, and hence two trends of $Nu_{r,s,in}$ with the increasing of $Re_{s,in}$. It should be noted that Nusselt number

$Nu_{r,s,in}$ is calculated according to Equation 4.22 and for matrix geometries with constant cross section it is related to the inlet section as well as the Reynolds number $Re_{s,in}$.

These results are reported in Figures 6.5 and 6.6; the first present a comparison between *Geom 01* and *Geom 02*, the second report the same comparison between *Geom 03* and *Geom 04*. These distributions of $Nu_{r,s,in}$ have been normalized by Nu_{ref} , that is the value of $Nu_{r,s,in}$ averaged on all matrix blocks at the minimum Reynolds number for *Geom 01*. From these distributions it can be noticed that the increase of heat transfer on the impingement regions is not so high for matrix geometries with the lower rib height (*Geom 03* and *Geom 04*), but it becomes significant for geometries with higher rib height (*Geom 01* and *Geom 02*). In these latter cases the heat transfer increase on these impingement regions ranges from $8 \div 10\%$ for *Geom 01* to $18 \div 25\%$ for *Geom 02*.

From Figure 6.6 it should be noted that only two mass flow conditions or Reynolds numbers have been investigated for *Geom 04*; this limitation was due on one side to the minimum measurable mass flow rate, while on the other side to the very high pressure losses achieved for this kind of matrix structure with very narrow sub-channels.

As mentioned in Section 4.4.2, in addition to htc_r , other two types of heat transfer coefficients htc_{eqT} , htc_{eqB} have been determined; these are equivalent coefficients that include both heat transfer term due to rib surface and effective term applicable on the rib surfaces and are referred to the flat surface without ribs. The first htc_{eqT} is evaluated considering the thermal conductivity of the test models, while the second htc_{eqB} is recalculated considering the thermal conductivity that allows to obtain the Biot number similitude with the real application.

Figures 6.7a and 6.7b report the comparison between the four matrix geometries with constant section about the average values of equivalent heat transfer coefficients htc_{eqT} , htc_{eqB} as a function of total mass flow rate \dot{m}_{air} and Reynolds number $Re_{s,in}$ respectively; Figures 6.8a and 6.8b depict the same comparisons in terms of average values of effective heat transfer coefficients htc_r .

In all these cases the heat transfer coefficients are averaged on all matrix blocks.

From Figures 6.7a and 6.8a it can be observed how the slope of the HTC trend rises moving from *Geom 01* to *Geom 04*; this means that geometries with lower rib height and narrower passages guarantee higher HTCs at low mass flow rates because of the higher flow velocities along the sub-channels and of the higher turbulence level.

However to get a correct comparison about the overall heat transfer performance of these extremely different matrix geometries, it has been necessary to determine the average Nusselt number trends as a function of Reynolds number. Figures 6.9a and 6.9b show the average distributions of the equivalent and effective Nusselt numbers for the four investigated geometries. From Figure 6.9a it is clear that Nusselt values are higher for models with the higher heat transfer surface area given by longitudinal ribs. For example, at the same rib height, the six entry channels geometry *Geom 02* has a higher heat transfer performance with respect to the four entry channels *Geom 01*. The same effect is not present between the other two geometries with the minimum rib height, but the data for *Geom 04* are not enough to offer a good comparison.

Then, always referring to Figure 6.9a, it can be concluded that a strong reduction of rib height h_{rib} (from 15 to 1.5 mm) have a strong effect on the heat transfer performance; in fact, moving from *Geom 01* to *Geom 03* or from *Geom 02* to *Geom 04*, the ratio $Nu_{r,s,in}/Nu_{ref}$ is reduced to the half.

Even in this case the value Nu_{ref} used to normalize the Nusselt number distributions is the average effective Nusselt value $Nu_{r,s,in}$ at the minimum Reynolds number for *Geom 01*.

In these distributions each Nusselt value derive from the average on all matrix blocks and is referred to the inlet section of the matrix models.

Finally, Figures 6.10a, 6.10b, 6.11a and 6.11b present the distributions of the $Nu_{r,s,in}/Nu_{ref}$ ratio as a function of the streamwise position for different Reynolds numbers; it can be observed that the heat transfer is very uniform from the inlet to the outlet of each matrix model.

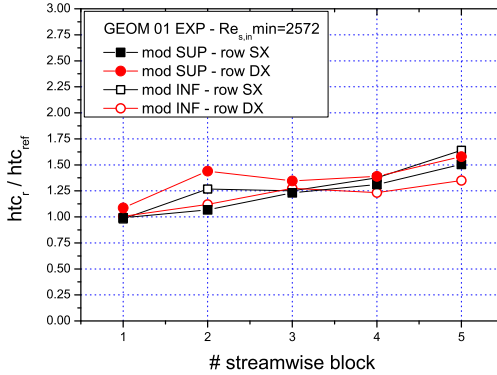
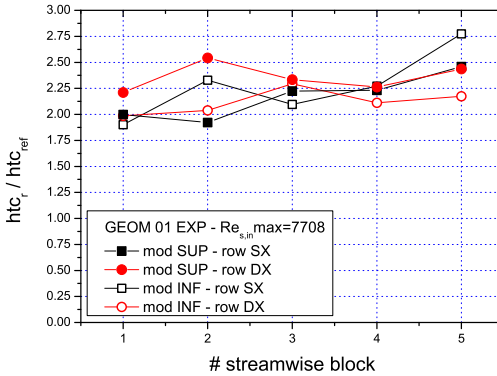
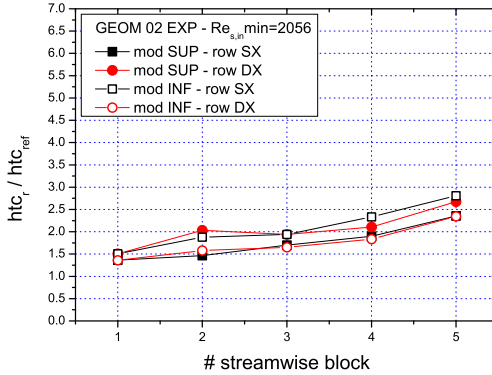
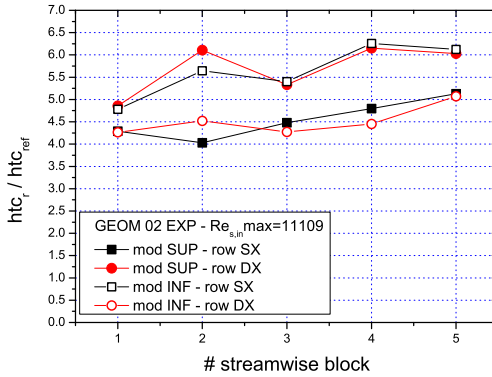
(a) *Geom01 - $Re_{s,in} min=2572$* (b) *Geom01 - $Re_{s,in} max=7708$*

Figure 6.1: *Geom 01 - Distributions of the normalized effective heat transfer coefficient htc_r/htc_{ref} for the different rows of matrix blocks*



(a) *Geom02* - $Re_{s,in} min=2056$



(b) *Geom02* - $Re_{s,in} max=11109$

Figure 6.2: *Geom 02* - Distributions of the normalized effective heat transfer coefficient htc_r/htc_{ref} for the different rows of matrix blocks

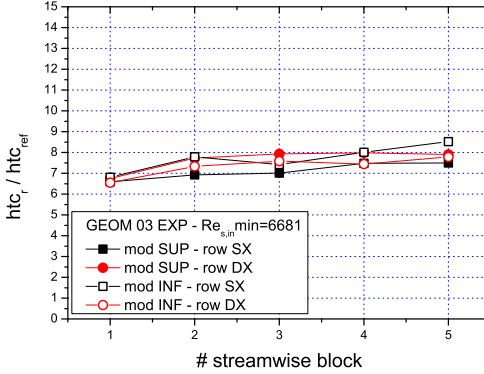
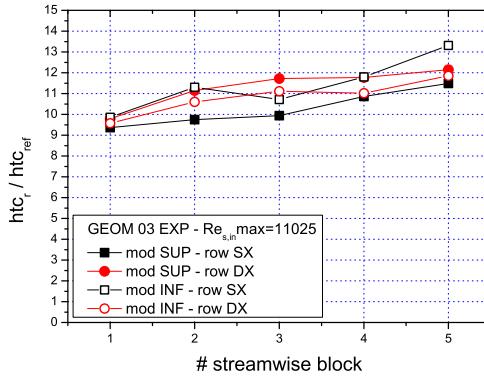
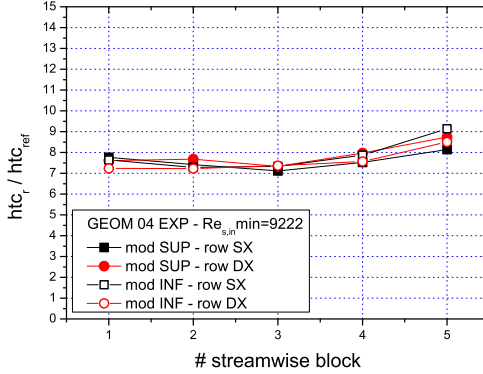
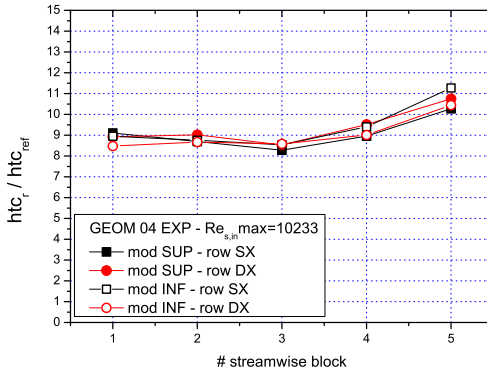
(a) *Geom03 - $Re_{s,in} min = 6681$* (b) *Geom03 - $Re_{s,in} max = 11025$*

Figure 6.3: *Geom 03 - Distributions of the normalized effective heat transfer coefficient htc_r / htc_{ref} for the different rows of matrix blocks*

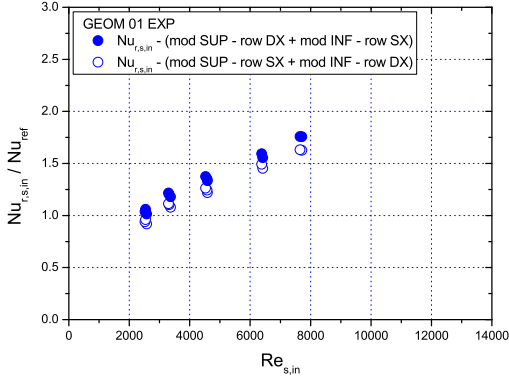


(a) *Geom04* - $Re_{s,in} min=9222$

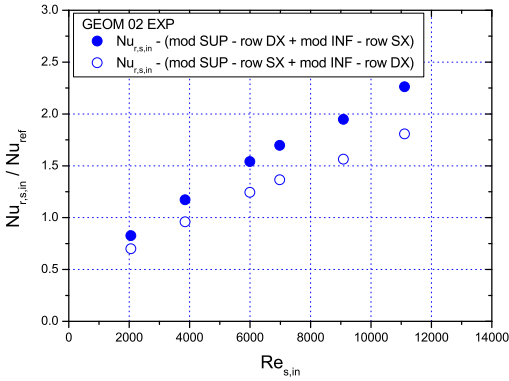


(b) *Geom04* - $Re_{s,in} max=10233$

Figure 6.4: *Geom04* - Distributions of the normalized effective heat transfer coefficient htc_r/htc_{ref} for the different rows of matrix blocks

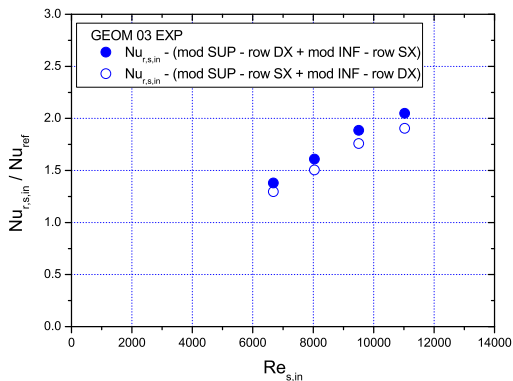


(a) Geom01

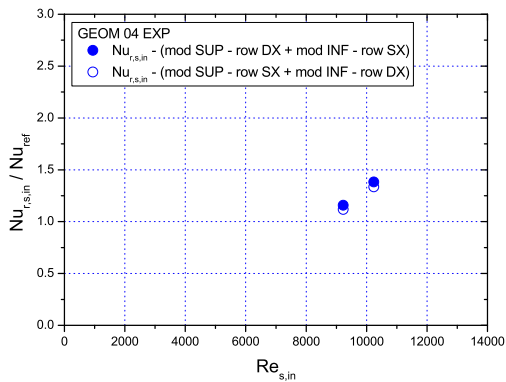


(b) Geom02

Figure 6.5: Geom 01 vs Geom 02 - Distributions of the normalized effective Nusselt number $Nu_{r,s,in}/Nu_{ref}$ for the two couple of rows

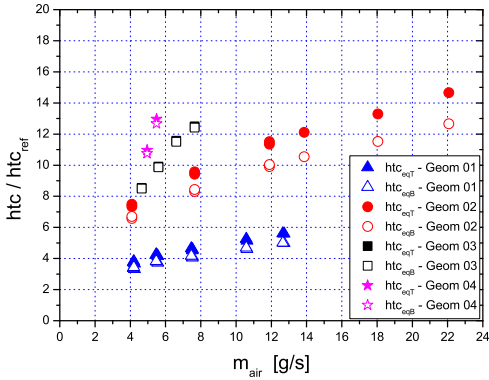


(a) Geom03

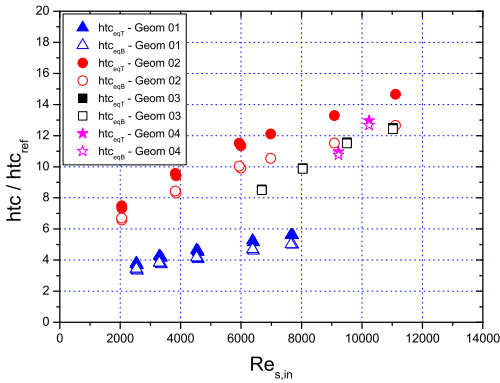


(b) Geom04

Figure 6.6: Geom 03 vs Geom 04 - Distributions of the normalized effective Nusselt number $Nu_{r,s,in}/Nu_{ref}$ for the two couple of rows

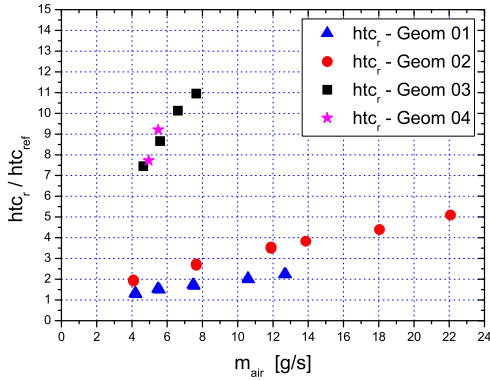


(a) htc_{eqT}/htc_{ref} , htc_{eqB}/htc_{ref} vs. \dot{m}_{air}

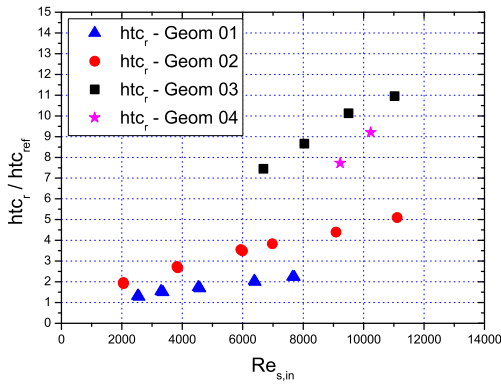


(b) htc_{eqT}/htc_{ref} , htc_{eqB}/htc_{ref} vs. $Re_{s,in}$

Figure 6.7: Distributions of the normalized equivalent heat transfer coefficients htc_{eqT}/htc_{ref} and htc_{eqB}/htc_{ref} as a function of mass flow rate \dot{m}_{air} and Reynolds number $Re_{s,in}$

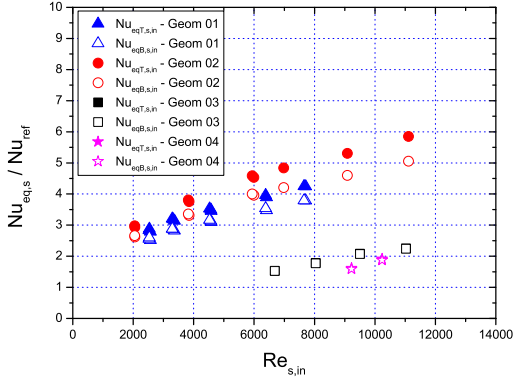


(a) htc_r / htc_{ref} vs. \dot{m}_{air}

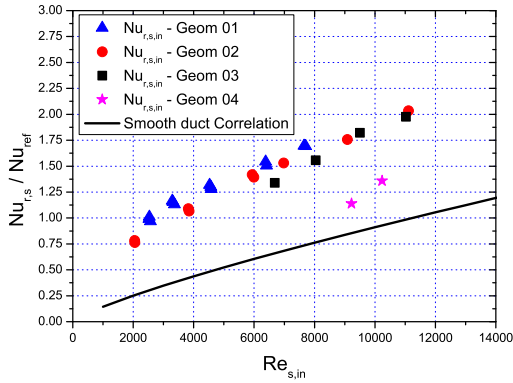


(b) htc_r / htc_{ref} vs. $Re_{s,in}$

Figure 6.8: Distributions of the normalized effective heat transfer coefficients htc_r / htc_{ref} as a function of mass flow rate \dot{m}_{air} and Reynolds number $Re_{s,in}$

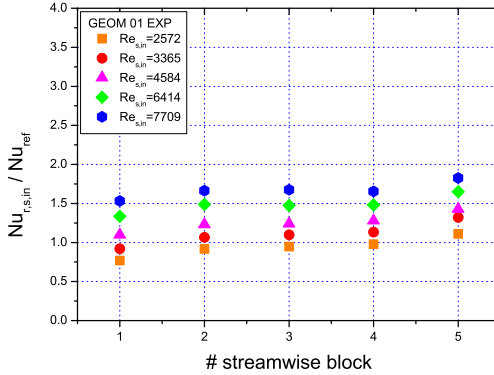


(a) Nu_{eqT}/Nu_{ref} , Nu_{eqB}/Nu_{ref} vs. $Re_{s,in}$

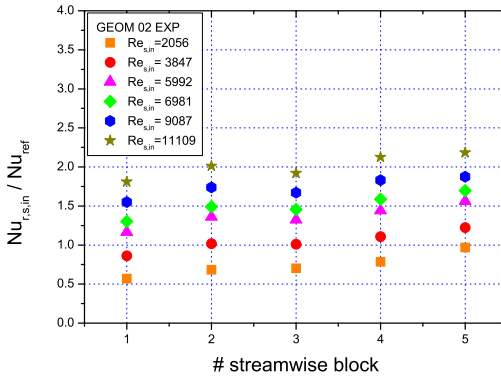


(b) Nu_r/Nu_{ref} vs. $Re_{s,in}$

Figure 6.9: Distributions of the normalized equivalent and effective average Nusselt number as a function of Reynolds number $Re_{s,in}$

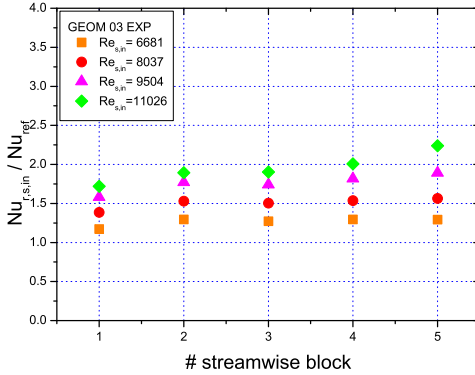


(a) Geom 01 - Nu_r/Nu_{ref} vs. streamwise block

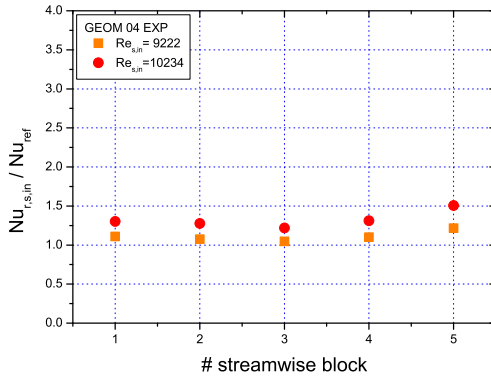


(b) Geom 02 - Nu_r/Nu_{ref} vs. streamwise block

Figure 6.10: Geom 01 vs Geom 02 - Distributions of the normalized effective Nusselt number $Nu_{r,s,in}/Nu_{ref}$ for different streamwise positions and Reynolds numbers



(a) Geom 03 - Nu_r/Nu_{ref} vs. streamwise block



(b) Geom 04 - Nu_r/Nu_{ref} vs. streamwise block

Figure 6.11: Geom 03 vs Geom 04 - Distributions of the normalized effective Nusselt number $Nu_{r,s,in}/Nu_{ref}$ for different streamwise positions and Reynolds numbers

6.2 Heat transfer results of static tests for matrix geometries with convergent cross section

Figures 6.12 and 6.13 report the effective normalized heat transfer coefficient distributions htc_r/htc_{ref} along the four different rows of matrix blocks for the two investigated convergent matrix geometries (*Geom 05* and *Geom 06*).

Like the previous results for constant geometries, as shown in Figures 6.1, 6.2, 6.3 and 6.4, these distributions have been normalized by htc_{ref} that represents the htc_r value averaged on the first four blocks (streamwise position #1) for *Geom 01* at the minimum Reynolds number.

However, unlike the distributions for matrix geometries with constant cross section, the htc_r/htc_{ref} trends for convergent geometries have a steep increase moving from the inlet to the outlet of the models (from #1 to #5). In fact, as shown by Figures 6.12a and 6.13a, the heat transfer coefficient on the last #5 position is about $2 \div 4$ times than that on the first #1 at the minimum Reynolds numbers. However, the increase of htc_r is much higher at the maximum Reynolds number; in this case the htc_r/htc_{ref} on the last position may increase $4 \div 6$ times over the values on the first streamwise position (Figures 6.12b and 6.13b).

By a comparison of these results with the previous for constant matrix geometries it is clear how the heat transfer performance trends of a convergent geometry is intermediate between the two corresponding constant models with the same number of entry sub-channels and rib thickness. This is well demonstrated by Figures 6.14 by means of the comparison between the 4 entry sub-channels convergent geometry (*Geom 06*) and the constant geometries *Geom 01* and *Geom 03* with maximum and minimum rib height respectively.

Also for these convergent models an increased heat transfer performance has been found in the impingement regions (mod SUP - row DX and mod INF - row SX); however this effect is much higher with respect the previous cases of constant geometries. In fact, as shown in Figures 6.15a and 6.15b the average Nusselt number ratio $Nu_{r,s,ave}/Nu_{ref}$ on the im-

pingement rows is about $35 \div 45\%$ and $45 \div 48\%$ higher than values on the other regions for *Geom 05* and *Geom 06* respectively. Moreover, it should be noted that both Nusselt $Nu_{r,s,ave}$ and Reynolds $Re_{s,ave}$ numbers are based on the sub-channel hydraulic diameter at the middle section of the matrix model.

Figures 6.16a and 6.16b report the average values of equivalent heat transfer coefficients htc_{eqT} , htc_{eqB} as a function of total mass flow rate \dot{m}_{air} and Reynolds number $Re_{s,ave}$ respectively. In these cases each HTC value derives from the average on all matrix blocks.

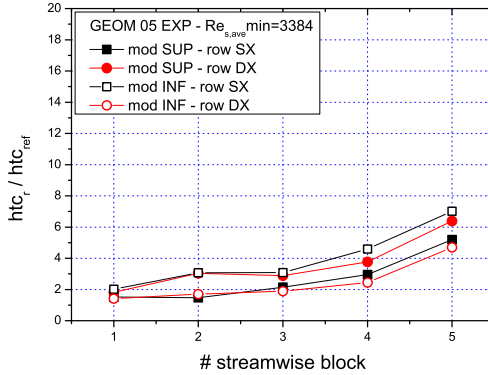
On the other hand Figures 6.17a and 6.17b report the same comparison in terms of the effective heat transfer coefficient htc_r .

From these results it is clear that, keeping constant the converging angle, the matrix model with narrower sub-channels (*Geom 05*) allow to reach higher heat transfer coefficients; in fact, as already found for constant geometries, the six entry channels geometry guarantee a higher level of turbulence even at low mass flow rates.

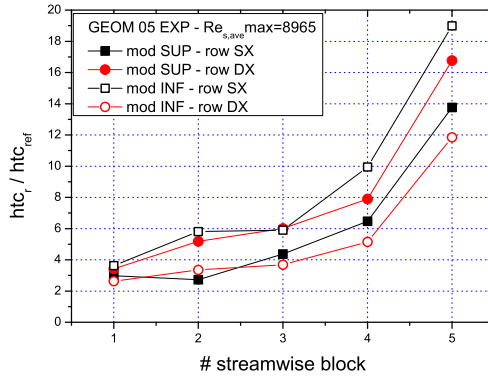
The heat transfer performance of these two convergent geometries has been also compared in terms of normalized distributions of Nusselt numbers as a function of Reynolds number. The distributions of the equivalent Nusselt number $Nu_{eq,s,ave}$ (Figure 6.18a) put in evidence higher values for the convergent geometry with six entry channels (*Geom 05*) because of the higher rib surface (higher fin effect). On the other hand, in terms of effective Nusselt number $Nu_{r,s,ave}$, values for *Geom 05* are little lower than *Geom 06* for the same Reynolds numbers but follow a trend with a higher slope; this result confirms a higher turbulence level for the geometry with more sub-channels and a higher rib thickness.

Finally, as regards the streamwise distribution of $Nu_{r,s,in}/Nu_{ref}$ ratio, it is possible to observe a quite uniform heat transfer till block #4 for *Geom 06* (6.19b) that is similar to that obtained for constant geometries; on the other hand the trend for *Geom 05* increases continuously from the inlet to the outlet (6.19a). However, in both cases an increase of slope is present between block #4 and #5, where the flow reaches the smallest passage area and experiences a strong acceleration. As expected

this acceleration has a higher effect on the heat transfer performance for the matrix model with the narrower sub-channels *Geom 05*.

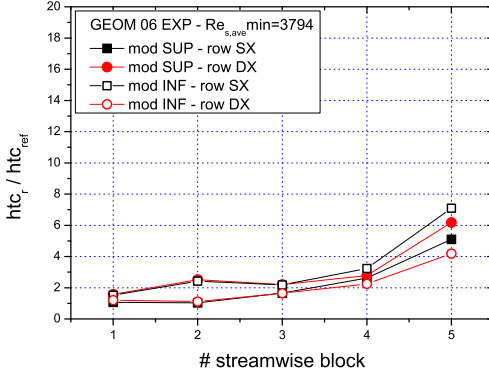


(a) *Geom05* - $Re_{s,ave} min=3384$

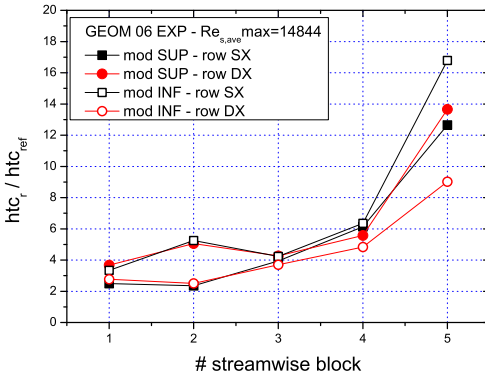


(b) *Geom05* - $Re_{s,ave} max=8965$

Figure 6.12: *Geom 05* - Distributions of the normalized effective heat transfer coefficient htc_r / htc_{ref} for the different rows of matrix blocks

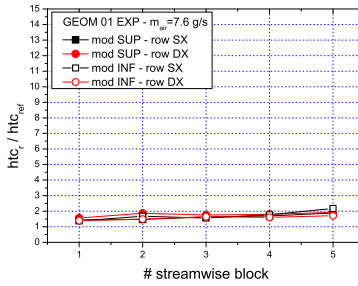


(a) *Geom06* - $Re_{s,ave} min=3794$

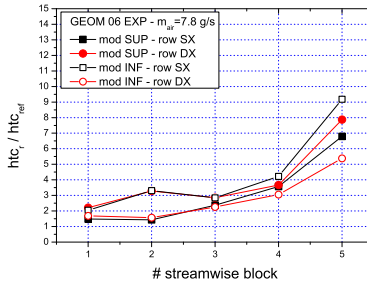


(b) *Geom06* - $Re_{s,ave} max=14844$

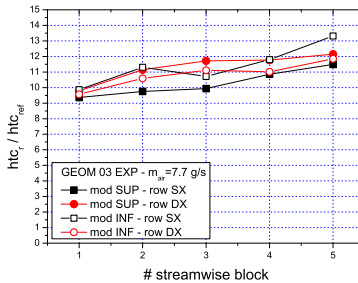
Figure 6.13: *Geom 06* - Distributions of the normalized effective heat transfer coefficient htc_r/htc_{ref} for the different rows of matrix blocks



(a) Geom 01

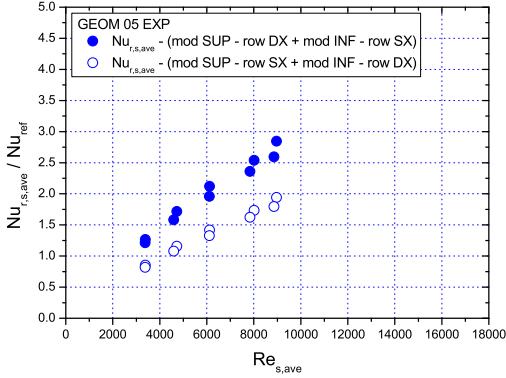


(b) Geom 06

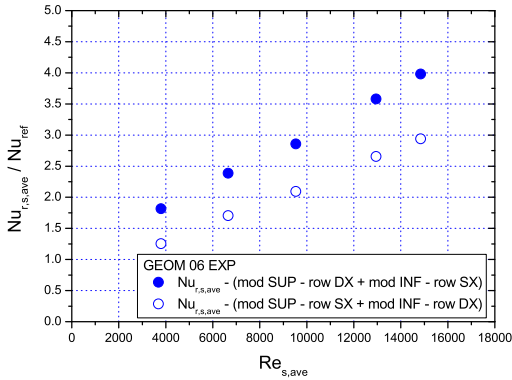


(c) Geom 03

Figure 6.14: Geom 01 vs Geom 03 vs Geom 06 - Comparison between distributions of the normalized effective heat transfer coefficient htc_r/htc_{ref} for the different rows of matrix blocks at the same mass flow rate

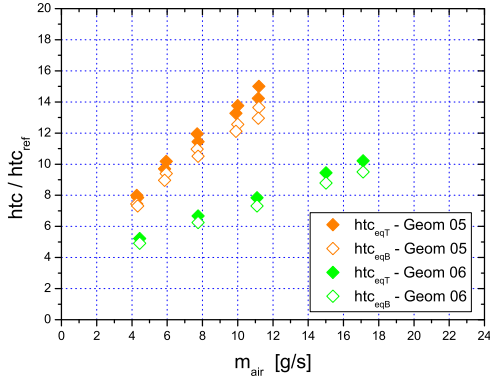


(a) Geom05

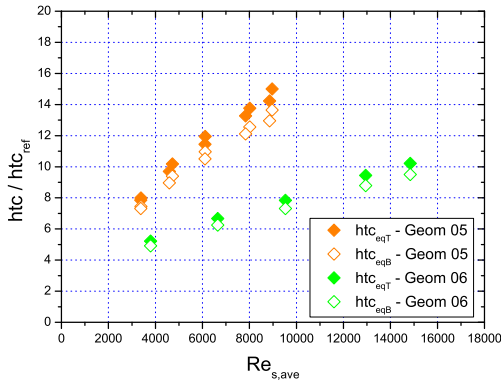


(b) Geom06

Figure 6.15: Geom 05 vs Geom 06 - Distributions of the normalized effective Nusselt number $Nu_{r,s,ave}/Nu_{ref}$ for the two couple of rows



(a) htc_{eqT}/htc_{ref} , htc_{eqB}/htc_{ref} vs. \dot{m}_{air}



(b) htc_{eqT}/htc_{ref} , htc_{eqB}/htc_{ref} vs. $Re_{s,ave}$

Figure 6.16: Geom 05 vs Geom 06 - Distributions of the normalized equivalent heat transfer coefficients htc_{eqT}/htc_{ref} and htc_{eqB}/htc_{ref} as a function of mass flow rate \dot{m}_{air} and Reynolds number $Re_{s,ave}$

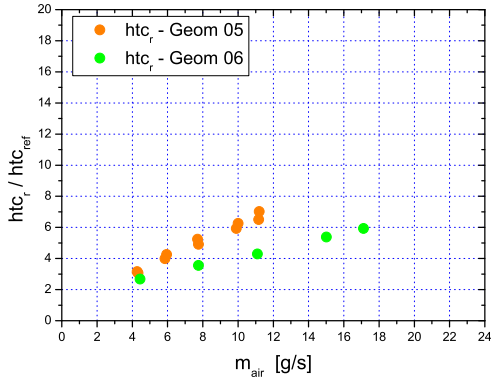
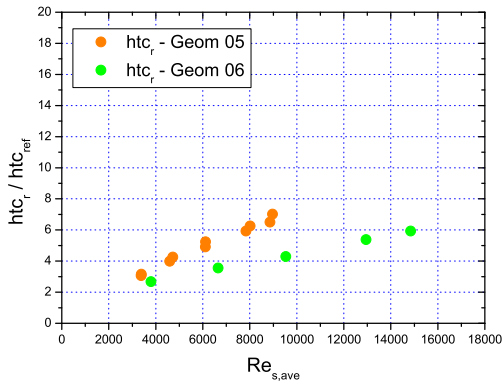
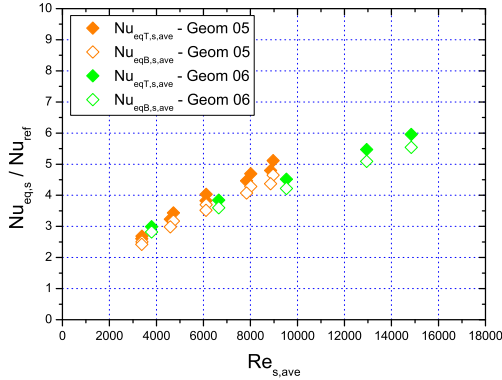
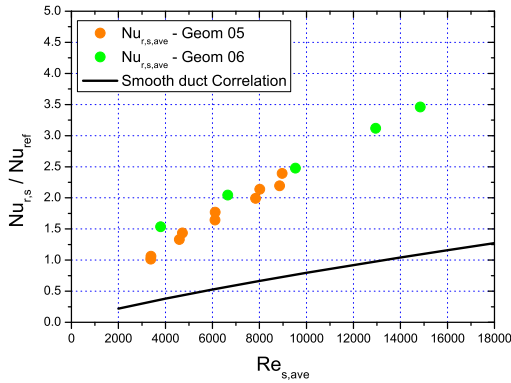
(a) htc_r / htc_{ref} vs. \dot{m}_{air} (b) htc_r / htc_{ref} vs. $Re_{s,ave}$

Figure 6.17: Geom 05 vs Geom 06 - Distributions of the normalized effective heat transfer coefficients htc_r / htc_{ref} as a function of mass flow rate \dot{m}_{air} and Reynolds number $Re_{s,ave}$

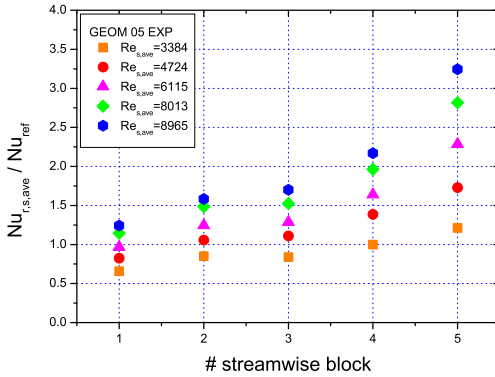


(a) Nu_{eqT} / Nu_{ref} , Nu_{eqB} / Nu_{ref} vs. $Re_{s,ave}$

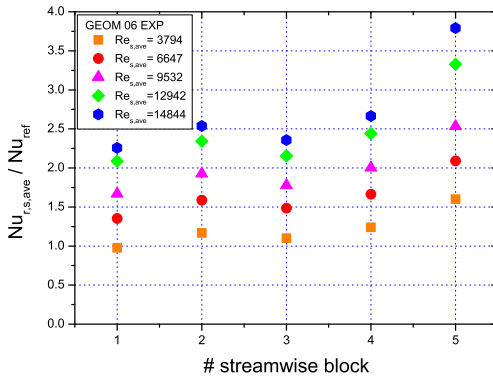


(b) Nu_r / Nu_{ref} vs. $Re_{s,ave}$

Figure 6.18: Geom 05 vs Geom 06 - Distributions of the normalized equivalent and effective average Nusselt number as a function of Reynolds number $Re_{s,ave}$



(a) Geom 05 - Nu_r/Nu_{ref} vs. streamwise block



(b) Geom 06 - Nu_r/Nu_{ref} vs. streamwise block

Figure 6.19: Geom 05 vs Geom 06 - Distributions of the normalized effective Nusselt number $Nu_{r,s,ave}/Nu_{ref}$ for different streamwise positions and Reynolds numbers

6.3 Heat transfer results of rotating tests

As described in Section 4.2.1 the rotating tests have been performed on the two scaled up models (scale factor SF=10) of the same convergent geometries investigated by means of static tests (SF=5) in Reynolds and Biot number similitude with real cases (§ 6.2). The matrix models employed for this activity are *Geom 07* and *Geom 08*, that are the scaled up models of *Geom 05* and *Geom 06* with six and four entry channels respectively.

Since these models were made of an aluminum alloy to limit the centrifugal loads, it has not been possible to reproduce the Biot number similitude as done in previous static tests.

The main aim of this experimental campaign has been focused to reproduce the Reynolds and Rotation number similitude with real applications. The results presented in the first part of this section have been derived from the *0deg* configuration (Figure 4.9), where the test model is aligned with the rotating plane.

Figures 6.20a and 6.20b report the test ranges about Reynolds and Rotation number investigated for *Geom 07* and *Geom 08* respectively. In both cases the sub-channel Reynolds number ranges from 2000 to 10000, while the sub-channel Rotation number varies from 0 to 0.1 for *Geom 07* and from 0 to 0.25 for *Geom 08*. These ranges are in line with actual operating conditions for industrial gas turbines and the similitude with real cases has been obtained operating the rotating test rig at the maximum rotational speed (173 rpm).

It should be noted that the models employed for these tests are formed by 5 streamwise blocks for each module; then, each of these streamwise blocks is not divided into two spanwise elements (DX and SX) as instead done for previous static test articles with scale factor SF=5. For this reason only one thermocouple and hence only one temperature is measured for each streamwise position along both pressure (PS) and suction side (SS). Therefore, even if the presence of only one thermocouple per block does not allow to reach a detailed measurement, it has been possi-

ble to obtain the average heat transfer performance on the two sides of the models.

Figures 6.21 and 6.22 report the htc_r/htc_{ref} distributions for *Geom 07* and *Geom 08* at the minimum and maximum Reynolds numbers. Each graph includes the trends as a function of the streamwise block for the three operating conditions of test rig: 0, 100 and 173 rpm.

In these cases the reference value htc_{ref} used to normalize the distributions is the htc_r value averaged on the first two streamwise blocks (streamwise position #1) for *Geom 08* at the minimum Reynolds number.

Like the previous results for convergent geometries *Geom 05* and *Geom 06* reported in Figures 6.12 and 6.13, also the distributions for *Geom 07* and *Geom 08* increase with the increasing of the streamwise distance from the inlet reaching the highest values on the last streamwise position (block #5). As expected, this increase is higher for geometry with six entry sub-channels for each Reynolds number.

In addition to this, these graphs also give important information about the effects of Coriolis force on heat transfer coefficient distributions for each streamwise position and each flow condition. By a comparison of Figure 6.21a with Figure 6.21b and of Figure 6.22a with Figure 6.22b, it is clear that the Coriolis force due to the rotation have a stronger effect on the heat transfer coefficient distribution at the low Reynolds number, while this effect is practically negligible at the maximum Reynolds number; in this latter case the distributions for the three operating conditions follow exactly the same trend (Figures 6.21b and 6.22b). From these comparisons it can be concluded that the Coriolis force is able to affect the flow field and the heat transfer performance when the bulk flow inertial force is weak; this situation occurs at low mass flow rates and hence at low flow velocities.

The effects of rotation on heat transfer performance have been also evaluated on the average equivalent and effective heat transfer coefficient distributions. Figures 6.23 present the normalized average distributions of the three heat transfer coefficients as a function of Reynolds num-

ber for both geometries; for each kind of heat transfer coefficient the trends are reported for the three operating conditions (0, 100 and 173 rpm). These trends confirms the higher effects of rotation at the lower Reynolds numbers; for example, at the minimum $Re_{s,ave}$ the HTC's at 173 rpm are about 20 ÷ 30% higher than corresponding values at 0 rpm. These differences are about the same for the three ratios htc_{eqT}/htc_{ref} , htc_{eqB}/htc_{ref} and htc_r/htc_{ref} . On the other hand, with the increasing of Reynolds number, these differences become about 2 ÷ 5% and can be considered negligible.

The same levels of heat transfer enhancement due to the rotation are confirmed by the normalized average distributions of the different Nusselt numbers as reported in Figures 6.24. Even in this case the distributions are reported for the three rotational speed of the test rig.

As regards Nusselt number distributions the reference value Nu_{ref} is the effective $Nu_{r,s}$ value averaged on the first two streamwise blocks (streamwise position #1) for *Geom 08* at the minimum Reynolds number.

A more detailed view about the effects of rotation on Nusselt number is given by the streamwise distributions reported for both pressure (PS) and suction side (SS); Figures 6.25 and 6.26 show the effective Nusselt number trends for *Geom 07* and *Geom 08*. In both cases a comparison is reported between the minimum and maximum Reynolds number. It should be noted that these distributions are expressed in terms of rotation-to-stationary ratios $Nu_{r,s}/Nu_{stat}$, where Nu_{stat} are the corresponding average Nusselt values for the static cases at the considered Reynolds number.

At the minimum Reynolds number ($Re_{s,ave}$ close to 3000 for both geometries) the heat transfer enhancement due to rotation is about 20% till block #4 and increases substantially towards the end of the convergent channel; in fact, as regards block #5, $Nu_{r,s}/Nu_{stat}$ is about 40% for six entry channels *Geom 07* (Figure 6.25a) and about 33% for the four entry channels *Geom 08* (Figure 6.26a). On the other hand, as already shown by previous heat transfer distributions, the heat transfer enhancement is very small at the maximum Reynolds number: only 2.5%

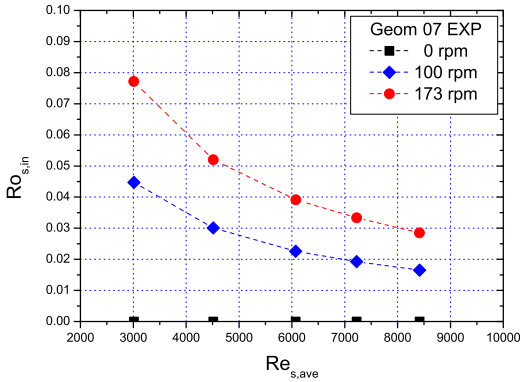
for *Geom 07* and 5% for *Geom 08*. From all these results it is possible to observe that no differences exist between pressure and suction side of the model; this means that the Coriolis force acts in the same way on the two halves of the matrix model.

To summarize the overall heat transfer enhancement due to rotation, Figure 6.27 reports the distributions of the rotation-to-stationary ratio $Nu_{r,s}/Nu_{stat}$ as a function of the Rotation number $Ro_{s,in}$ for different Reynolds numbers $Re_{s,ave}$, where $Nu_{r,s}$ is the value obtained from the average on all matrix blocks and $Ro_{s,in}$ is defined according to Equation 4.4. The corresponding values of the overall heat transfer enhancement are also reported by Table 6.1. It has been found that for each mass flow condition the rotation enhances the heat transfer rate with respect to the static cases up to a maximum of about 23% for the four entry channels *Geom 08* and about 30% for the six entry channels *Geom 07* at the minimum Reynolds number and maximum Rotation numbers $Ro_{s,in} = 0.25$ and 0.077 respectively. Although the ranges of Rotation numbers are different for the two geometries, the rotation enhancement is progressively increased with the decreasing of Reynolds numbers because of the greater influence of Coriolis force due to rotation.

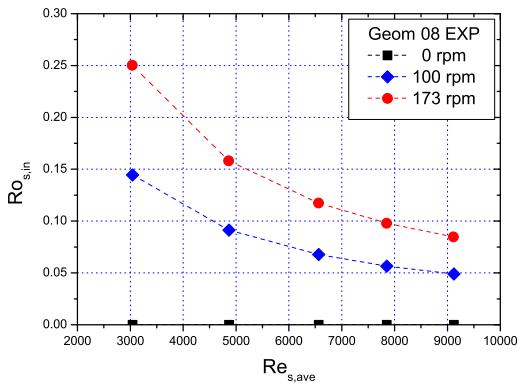
Since the above reported results for the *0deg* configuration can not be representative of a realistic trailing edge orientation, rotating tests have been also replicated with the test model inclined of *30deg* with respect to the rotating plane in order to simulate a typical exit angle of a real gas turbine blade (Figure 4.9).

The comparison in terms of streamwise Nusselt number between *0deg* and *30deg* configurations at the same Reynolds and Rotation numbers are shown by the distributions in Figures 6.28 and 6.29 for the two matrix models. In each case the comparison is made for the minimum and maximum Reynolds number. Each of these graphs include the trends for the static case and for both rotating cases (*0deg* and *30deg*) at the same rotational speeds. These results confirm that the major effects are present at the minimum $Re_{s,ave}$ for both the matrix channel orientations. In addition to this, it is clear that the different channel orientation does

not affect the heat transfer performance; in fact the $Nu_{r,s}/Nu_{stat}$ distributions for $30deg$ follow the same trends of those at $0deg$. Therefore it can be concluded that Coriolis force has the same effects for the investigated range of channel orientation with respect to the rotating plane.



(a) Test matrix - Geom07



(b) Test matrix - Geom08

Figure 6.20: Test matrices for rotating tests on Geom 07 and Geom 08

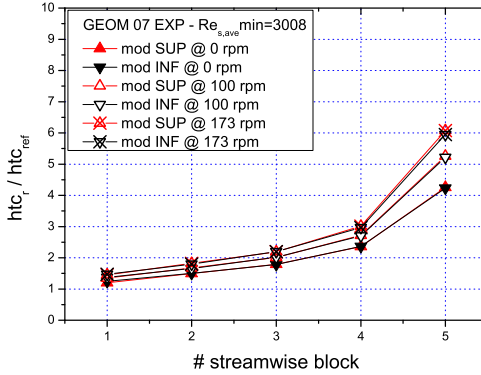
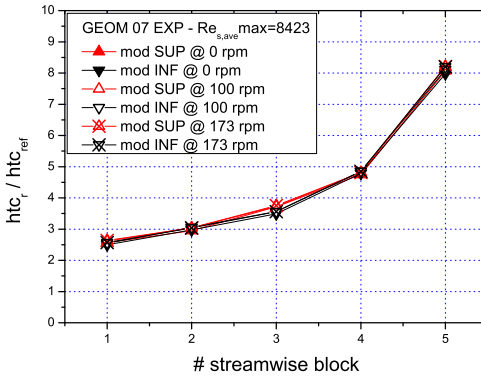
(a) *Geom07* - $Re_{s,ave} min=3008$ (b) *Geom07* - $Re_{s,ave} max=8423$

Figure 6.21: *Geom 07* - Distributions of the normalized effective heat transfer coefficient htc_r/htc_{ref} for the different rows of matrix blocks at different rotating conditions

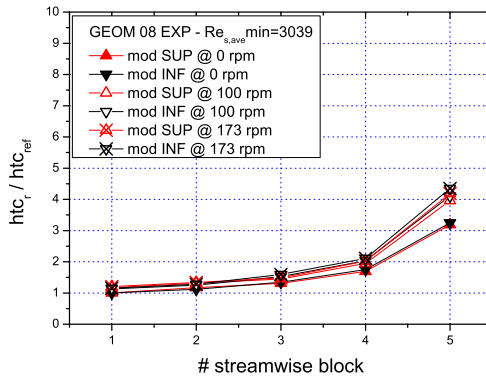
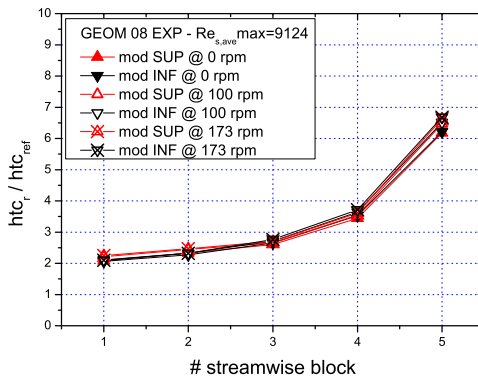
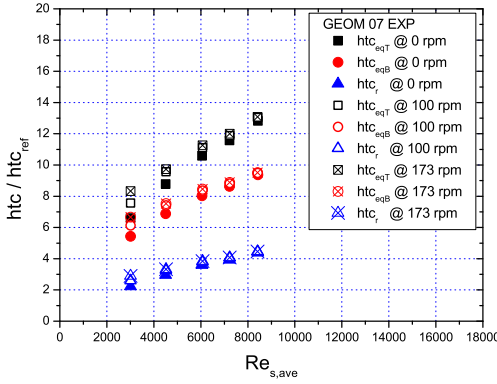
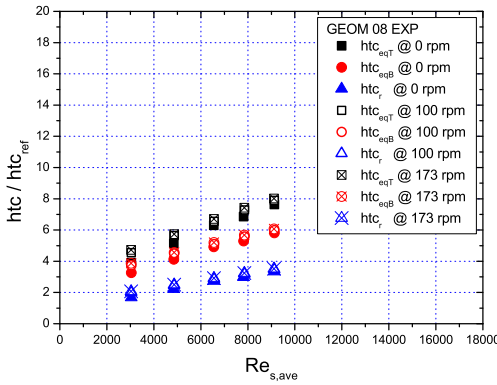
(a) *Geom08* - $Re_{s,ave} min=3039$ (b) *Geom08* - $Re_{s,ave} max=9124$

Figure 6.22: *Geom 08* - Distributions of the normalized effective heat transfer coefficient htc_r / htc_{ref} for the different rows of matrix blocks at different rotating conditions

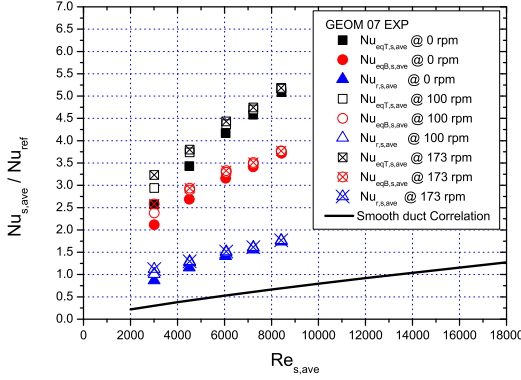


(a) Geom 07 - htc_{eqT}/htc_{ref} , htc_{eqB}/htc_{ref} , htc_r/htc_{ref}

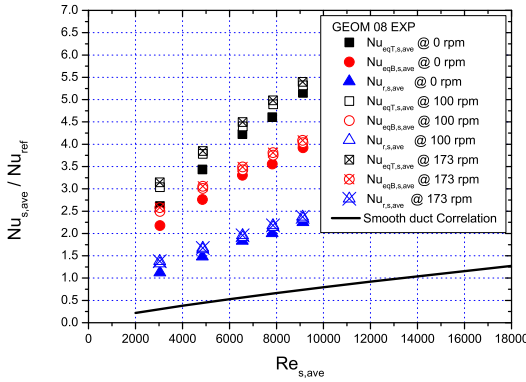


(b) Geom 08 - htc_{eqT}/htc_{ref} , htc_{eqB}/htc_{ref} , htc_r/htc_{ref}

Figure 6.23: Geom 07 vs Geom 08 - Distributions of the normalized equivalent and effective heat transfer coefficients htc_{eqT}/htc_{ref} , htc_{eqB}/htc_{ref} and htc_r/htc_{ref} as a function of Reynolds numbers at different rotating conditions

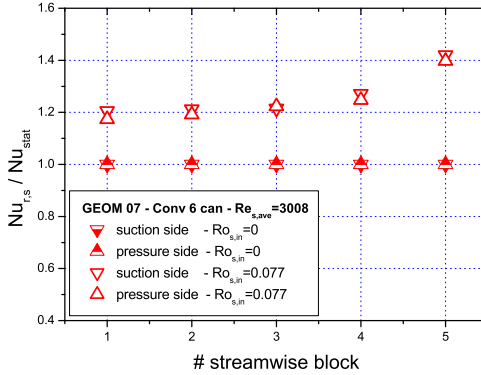


(a) Geom 07 - Nu_{eqT}/Nu_{ref} , Nu_{eqB}/Nu_{ref} , Nu_r/Nu_{ref}

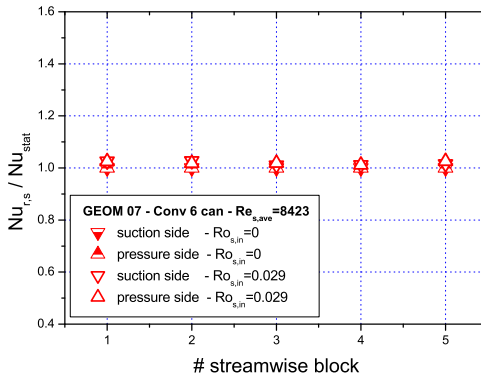


(b) Geom 08 - Nu_{eqT}/Nu_{ref} , Nu_{eqB}/Nu_{ref} , Nu_r/Nu_{ref}

Figure 6.24: Geom 07 vs Geom 08 - Distributions of the normalized equivalent and effective Nusselt numbers Nu_{eqT}/Nu_{ref} , Nu_{eqB}/Nu_{ref} , Nu_r/Nu_{ref} as a function of Reynolds numbers at different rotating conditions



(a) *Geom 07* - $Re_{s,ave} min = 3008$



(b) *Geom 07* - $Re_{s,ave} max = 8423$

Figure 6.25: *Geom 07* - Streamwise distributions of the normalized effective Nusselt number Nu_r/Nu_{ref} for pressure and suction sides of the matrix model at different rotating conditions

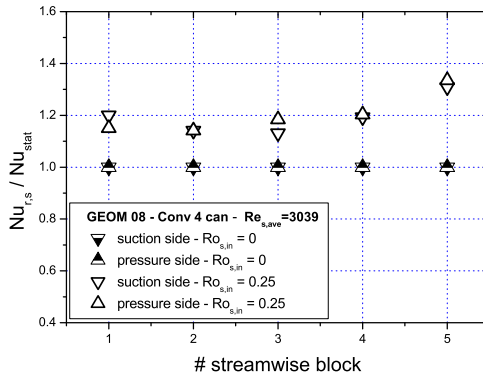
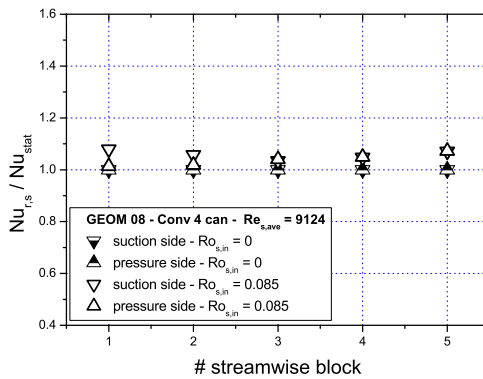
(a) *Geom 08 - $Re_{s,ave} min=3039$* (b) *Geom 08 - $Re_{s,ave} max=9124$*

Figure 6.26: *Geom 08 - Streamwise distributions of the normalized effective Nusselt number Nu_r / Nu_{stat} for pressure and suction sides of the matrix model at different rotating conditions*

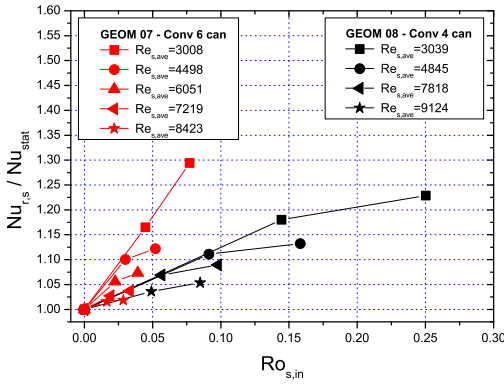
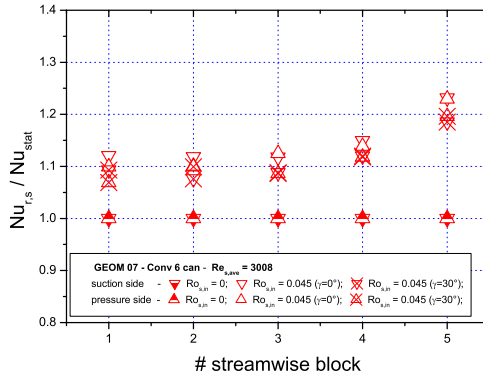


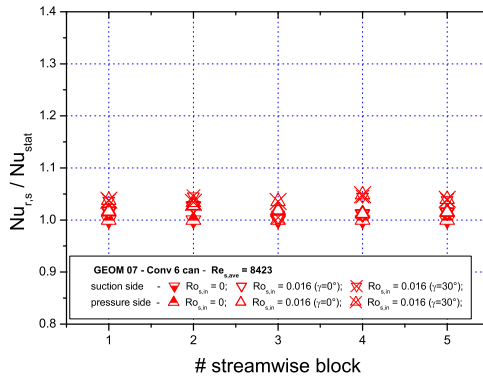
Figure 6.27: Geom 07 vs Geom 08 - overall rotation effects at different Reynolds numbers: distributions of the rotation-to-stationary ratio Nusselt number $Nu_{r,s}/Nu_{stat}$

Table 6.1: Geom 07 vs Geom 08 - Overall heat transfer enhancement due to rotation

Geom 07 (6 can)			Geom 08 (4 can)		
$Re_{s,ave}$	$Ro_{s,in}$	$+\Delta Nu$	$Re_{s,ave}$	$Ro_{s,in}$	$+\Delta Nu$
$Re_{s,ave} = 3008$	$Ro_{s,in} = 0.077$	29.4%	$Re_{s,ave} = 3039$	$Ro_{s,in} = 0.250$	22.9%
$Re_{s,ave} = 4498$	$Ro_{s,in} = 0.052$	12.2%	$Re_{s,ave} = 4845$	$Ro_{s,in} = 0.158$	13.2%
$Re_{s,ave} = 7219$	$Ro_{s,in} = 0.033$	3.7%	$Re_{s,ave} = 7818$	$Ro_{s,in} = 0.098$	8.9%
$Re_{s,ave} = 8423$	$Ro_{s,in} = 0.021$	1.8%	$Re_{s,ave} = 9124$	$Ro_{s,in} = 0.085$	5.4%

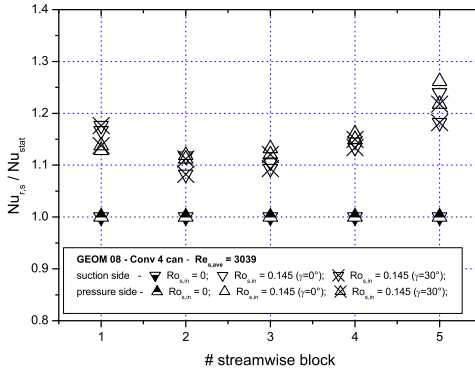


(a) *Geom 07 - 0deg vs 30deg - $Re_{s,ave}min=3008$*

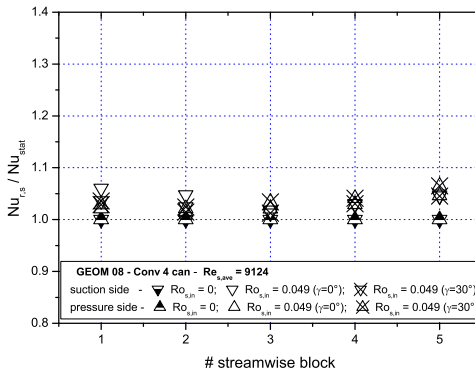


(b) *Geom 07 - 0deg vs 30deg - $Re_{s,ave}max=8423$*

Figure 6.28: *Geom 07 - Distributions of the normalized effective heat transfer coefficient $Nu_{r,s} / Nu_{stat}$ for the different rows of matrix blocks at different rotating conditions*



(a) *Geom 08 - 0deg vs 30deg - $Re_{s,ave} min = 3039$*



(b) *Geom 08 - 0deg vs 30deg - $Re_{s,ave} max = 9124$*

Figure 6.29: *Geom 07 - Distributions of the normalized effective heat transfer coefficient $Nu_{r,s} / Nu_{stat}$ for the different rows of matrix blocks at different rotating conditions*

6.4 Comparison of Heat Transfer Results and Critical Evaluation

At the end of this chapter, the present section reports a summary and a comparison between the six different matrix geometries investigated during the three experimental campaigns of measurements: the four constant geometries with maximum and minimum rib height and the two convergent geometries.

It should be noted that in the following graphs Reynolds and Nusselt numbers have been referred to the geometric parameters and flow properties at the middle section of the models in order to get a correct comparison between constant and convergent matrix geometries.

First of all, Figure 6.30 provides a comparison in terms of the average distributions of the normalized equivalent Nusselt number Nu_{eqB} . These trends are significantly higher for the constant geometries with the maximum rib height (*Geom 01* and *Geom 02*) with respect to the corresponding convergent geometries (*Geom 06* and *Geom 05*).

Moreover, keeping constant the cross section, values are higher for the six entry channels geometries: *Geom 02* has higher values than *Geom 01* and *Geom 05* has higher values than *Geom 06*.

In fact, as already proved during this chapter, the equivalent Nusselt number is higher for the models with larger heat transfer surface area because it takes into account the fin effect due to the presence of ribs.

On the other hand, Figure 6.31 provides the comparison in terms of the average distributions of the effective Nusselt number Nu_r . Since these Nusselt values derive from the heat transfer coefficients between fluid and rib surface, this graph puts in evidence the high turbulent behaviour for the convergent geometries. In fact, the heat transfer performance for *Geom 05* and *Geom 06* grows with a higher rate with the increasing of Reynolds number $Re_{s,ave}$.

To get a comparison of the heat transfer performance between the investigated geometries and other previous works on matrix geometries the graphs of Figures 6.32 have been realized. Both of them present the heat

transfer enhancement evaluated by means of the $Nu_{r,s,in}/Nu_0$ ratio as a function of Reynolds number, where $Nu_{r,s,in}$ derives from the average of Nusselt values on all matrix blocks at the desired Reynolds number and Nu_0 represents the corresponding Nusselt number in a smooth duct at the same flow condition. Nu_0 values are calculated by means of the Dittus-Boelter correlation ($Nu_0 = 0.023 \cdot Re^{0.8} \cdot Pr^{0.4}$).

Figure 6.32a shows the comparison between the six geometries investigated in the current activities and other three cases taken from the work of Saha et al. [6] (§ 2.2.2); about this work the results of 2 and 4 inlet channels derive from two convergent matrix structures, while those for the pin fin configuration derives from Metzger et al. [26]. From this it is clear that all the $Nu_{r,s,in}/Nu_0$ experimental trends are in good agreement with the other literary matrix cases with the exception of *Geom 04*. Then, a common feature found in both literary and present experimental cases is that the matrix geometries with a lower number of sub-channels has higher heat transfer enhancement values; for example, $Nu_{r,s,in}/Nu_0$ values for the four entry channels geometries *Geom 01* and *Geom 06* are higher than the values for the six entry channels geometries *Geom 02* and *Geom 05*.

These results also highlight that the heat transfer enhancement decreases slightly with an increasing of Reynolds number. Moreover, the performance of each matrix case is higher than the pin fin configuration.

Always concerning the heat transfer enhancement Figure 6.32b reports the comparison between the same experimental trends and other literature data taken from the publication of Acharya et al. [92] (§ 2.2.2), which investigated a constant matrix geometry with $45deg$ angled ribs and 6 sub-channels. Also in this case a good agreement is found especially at higher Reynolds values, while there are some discrepancies at the lower values.

Finally, since the evaluation of the overall performance of a cooling system must take into account not only the heat transfer performance but also the behaviour in terms of friction factor and pressure losses, at the end of this section a comparison has been also carried out in terms of

Thermal Performance Factor TPF defined according to equation 2.26. For this reason TPF values have been calculated combining the previous Nu/Nu_0 results together with the f/f_0 trends shown in Figure 5.33. In fact the Thermal Performance Factor is generally used to choose the optimum cooling geometry among several solutions in terms of both heat transfer enhancement and pressure loss.

Figure 6.33a reports the TPF trends for the six investigated geometries, while Figure 6.33b show the TPF comparison between the investigated convergent geometries, the same convergent geometries from the work of Saha et al. [6] and the same pin fin configuration from the work of Metzger et al. [26]. This latter comparison is very important in view of an application of a matrix geometry in a trailing edge system. TPF values for the two investigated geometries are in the range of $0.9 \div 1.2$ for the whole Reynolds range and the trends are in a very good agreement with the other literary results. Like the previous results on heat transfer enhancement, the performance is higher for geometries with a lower number of sub-channels (2 inlet channels geometry and *Geom 06* with 4 entry channels); in these cases the TPF values are higher than the pin fin system especially at the lower Reynolds numbers.

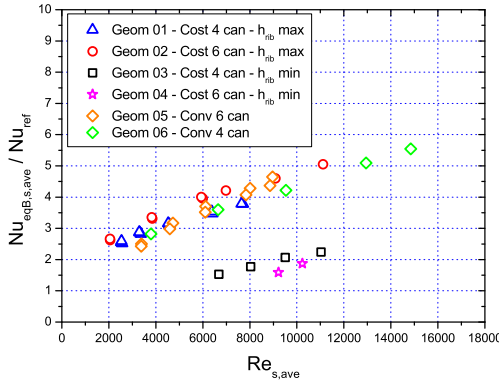


Figure 6.30: Normalized equivalent Nusselt number distributions for different Reynolds numbers - Comparison between all investigated geometries

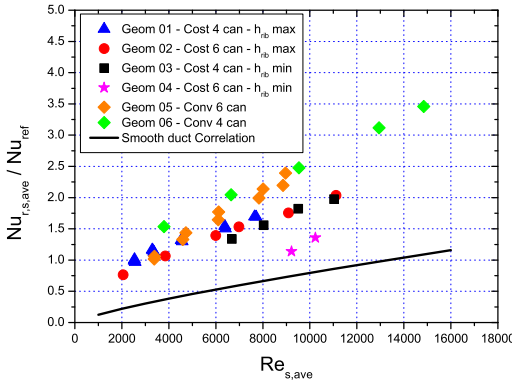
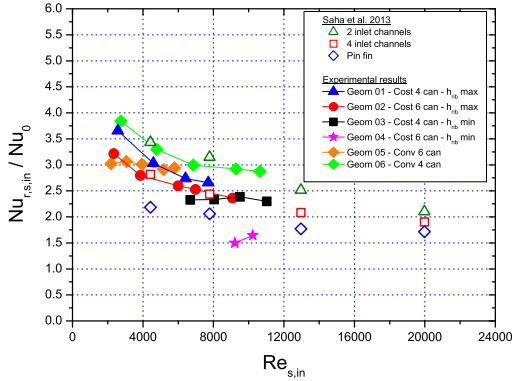
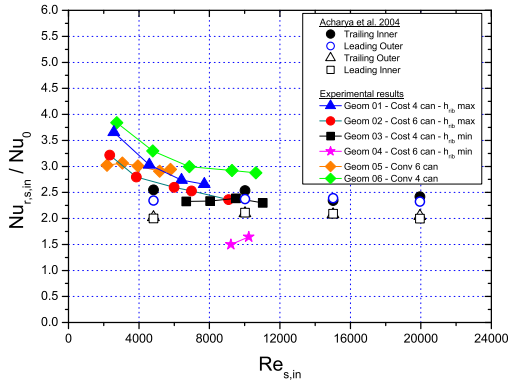


Figure 6.31: Normalized effective Nusselt number distributions for different Reynolds numbers - Comparison between all investigated geometries

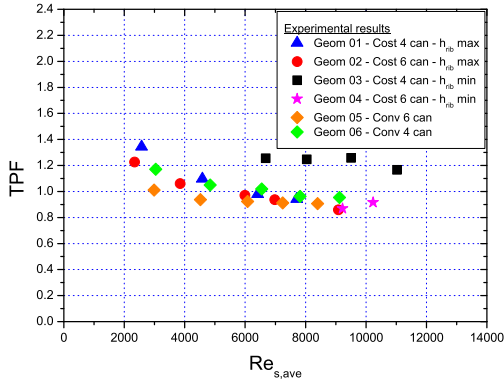


(a) Experiments vs Saha et al. [6]

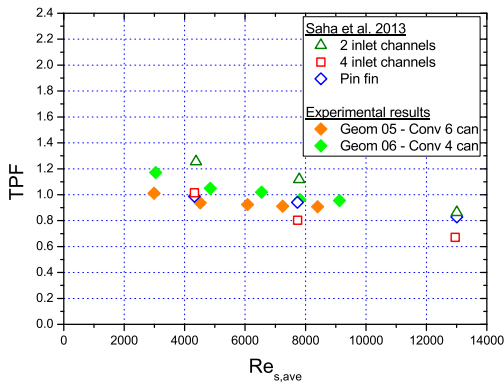


(b) Experiments vs Acharya et al. [92]

Figure 6.32: Heat transfer enhancement $Nu_{r,s}/Nu_0$ vs Reynolds number - Comparison between experimental and literature data



(a) TPF comparison for all the investigated geometries



(b) TPF comparison with Saha et al. [6]

Figure 6.33: Thermal Performance Factor TPF vs Reynolds number - Comparison between experimental and literature data

Chapter 7

Experimental Correlations for Blade Cooling Design

The last part of the present work has been devoted to the research of heat transfer and friction correlations with the aim of a future implementation in an in-house code commonly used for the design of internal cooling systems for gas turbine airfoils.

For this reason Section 7.1 summarizes the research of heat transfer correlations in terms of equivalent and effective Nusselt number, while Section 7.2 reports the correlations of pressure losses in two forms: friction factor as a function of Reynolds number and total to static pressure ratio as a function of a non dimensional mass flow rate.

In the last Section 7.3 of this chapter the experimental correlations for matrix geometries have been applied to evaluate heat transfer and pressure loss performance in the design point of the coolant conditions for a real blade. Then, a final comparison has been determined between the performance obtained applying a matrix structure and the performance for the current cooling solution of the considered real blade.

7.1 Heat Transfer Correlations

Starting from the heat transfer data acquired for the six investigated geometries (constant and convergent), it has been established to determine correlations between Nusselt number, Reynolds number and some specific dimensionless geometric parameters.

First of all, as regards the heat transfer correlations in terms of effective Nusselt number Nu_r , it has been decided to consider the average Nusselt values for each streamwise position (from block #1 to block #5) in order to include an information about the axial position along the matrix channel in the correlation. For this reason the input data have been taken as average Nusselt number distributions for each streamwise block as a function of the corresponding Reynolds number. For example each average Nusselt number $Nu_{r,s,ave,i}$ for the specific $i - th$ streamwise block derives from the average of Nusselt numbers on the matrix blocks for the considered streamwise position; at the same time the Reynolds number $Re_{s,ave,i}$ is calculated starting from the geometric dimensions and flow properties at the considered streamwise block. Therefore, $Nu_{r,s,ave,i}$ and $Re_{s,ave,i}$ are calculated as:

$$Nu_{r,s,ave,i} = \frac{htc_{r,i} \cdot d_{h,s,ave,i}}{k_{air,ave,i}} \quad (7.1)$$

$$Re_{s,ave,i} = \frac{\dot{m}_{air} \cdot d_{h,s,ave,i}}{A_{can,ave,i} \cdot n_{can} \cdot \mu_{air,ave,i}} \quad (7.2)$$

where the hydraulic diameter $d_{h,s,ave,i}$ referred to the average section of the single $i - th$ streamwise block is calculated following the Equation 4.24.

According to these definitions Figure 7.1b shows an example of average $Nu_{r,s,ave} - Re_{s,ave,i}$ distributions for *Geom 01*; in Figure 7.1a different colors have been used to indicate the values depending on the different streamwise position. As already reported by previous results, Nusselt values are: quite constant in the intermediate blocks of the model, slightly lower in the first block (#1) and slightly higher in the last block (#5).

In addition to this, it is possible to observe that the variation of Reynolds number for each group of Nusselt values is not significant because the geometric dimensions are constant along the streamwise direction and the variations of the flow properties (i.e. air density and viscosity) along this direction are very small. On the other hand the variation of Reynolds number along a convergent matrix model is very significant. To give an idea about this, Table 7.3 reports the increase of Reynolds number from block #1 to block #5 at the minimum and maximum mass flow rate for *Geom 05*; the corresponding $Nu_{r,s,ave} - Re_{s,ave,i}$ distributions are shown by Figure 7.2.

Then, to get a correlation valid for both constant and convergent matrix geometries, it has been necessary to select a set of dimensionless geometric parameters that were representative of the main features of a matrix structure. To reach this purpose the following set of parameters has been chosen:

- $\left(\frac{t_{rib}}{d_{h,s}}\right)_{ave}$ - rib thickness to sub-channel hydraulic diameter ratio
- $\left(\frac{h_{rib}}{d_{h,s}}\right)_{ave}$ - rib height to sub-channel hydraulic diameter ratio
- α - converging angle of a matrix module

The $t_{rib}/d_{h,s}$ takes into account the effect of both rib thickness and number of sub-channels and is representative of the open area available for the flow passage. Then, the $h_{rib}/d_{h,s}$ is representative of the channel cross section along the streamwise direction and gives an information about the axial position along the matrix model, while α represents the converging angle of the cross section. These ratios are referred to the average or middle section of the whole model (Figure 7.3).

Among a large number of tested correlations using the above described parameters, Equation 7.3 is the one that best fits the experimental data of the six investigated geometries:

$$Nu_{r,s,ave,i} = a \cdot Re_{s,ave,i}^b \cdot \left(\frac{t_{rib}}{d_{h,s}}\right)_{ave}^{(c+e \cdot \alpha)} \cdot \left(\frac{h_{rib}}{d_{h,s}}\right)_{ave}^{(d+f \cdot \alpha)} \quad (7.3)$$

Table 7.1: Exponents and coefficients of the heat transfer correlation

<i>a</i>	<i>b</i>	<i>c</i>	<i>d</i>	<i>e</i>	<i>f</i>
0.110	0.683	-0.166	0.126	-0.002	0.041

Values of exponents and coefficients of the correlation are shown in Table 7.1 and have been found by minimizing the standard deviation between Nusselt values coming from both experimental and correlation data. As shown by the expression of the standard deviation (Equation 7.4) discrepancies between experimental and calculated Nusselt values are less than 6.

$$dev.st. = \sqrt{\frac{\sum_{i=1}^n ((Nu_{r,s,ave,i})_{exp} - ((Nu_{r,s,ave,i})_{corr}))^2}{n}} = 5.920 \quad (7.4)$$

To show how the correlation fits well the experimental data, the graph in Figure 7.4 reports the experimental average Nusselt numbers against the Nusselt numbers calculated by the above shown correlation (Equation 7.3). It is clear that a good fitting is obtained for each streamwise block with the exception of some values for the last position (block #5). To better identify the geometries with the higher relative deviations from the correlation, Figure 7.5 shows the comparison between the experimental trends for all the geometries and the identified correlation with the relative uncertainty bands about $\pm 10\%$. It should be noted that on both axes values are shown in logarithmic scale; on the vertical axis the Nusselt values $Nu_{r,s,ave,i}$ are divided by the quantity K expressed as follows:

$$K = \left(\frac{t_{rib}}{d_{h,s}} \right)_{ave}^{(c+e \cdot \alpha)} \cdot \left(\frac{h_{rib}}{d_{h,s}} \right)_{ave}^{(d+f \cdot \alpha)} \quad (7.5)$$

From this comparison it is clear that most of the data falls within the correlation bands; as already shown by Figure 7.4 deviations higher than $\pm 10\%$ are due to block #5 for the six entry channels geometries *Geom 02* and *Geom 04*.

At the end of this part about the correlation on the effective Nusselt number, it is important to report the ranges of parameters for which the correlation is valid; these ranges are shown in Table 7.2.

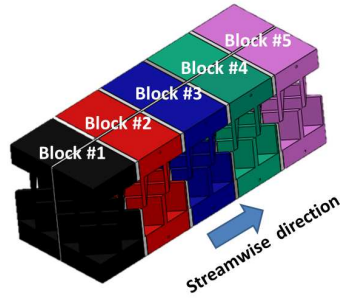
Table 7.2: Ranges for heat transfer correlation

Parameter	Range
$Re_{s,ave}$	2500 ÷ 22000
$t_{rib}/d_{h,s}$	0.14 ÷ 1.43
$h_{rib}/d_{h,s}$	0.59 ÷ 2.67
α	0 ÷ 5.7deg

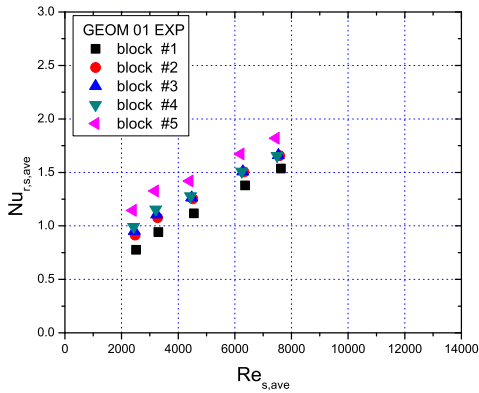
In addition to the above reported heat transfer correlations about the effective Nusselt number Nu_r , other correlations have been found for each of the investigated geometries in terms of equivalent average Nusselt number Nu_{eqB} evaluated in Biot number similitude with a real case typical of industrial gas turbines.

In this case the correlations are simply reported as $Nu_{eqB} = a \cdot Re_{s,ave}^b$, where Nu_{eqB} results from the average of Nusselt values on all matrix blocks. These correlations are reported in the graph of Figure 7.6 and in Table 7.4.

These relationships have been applied in Section 7.3 to determine the overall heat transfer from the internal endwall surface of a real blade assuming to use one of the studied matrix configurations in place of the current solution.



(a) Schematic of the 5 streamwise blocks



(b) Average effective Nusselt number distributions for each streamwise block

Figure 7.1: Examples of schematic division for a matrix model in 5 streamwise positions and corresponding averaged effective Nusselt number distribution for each streamwise block

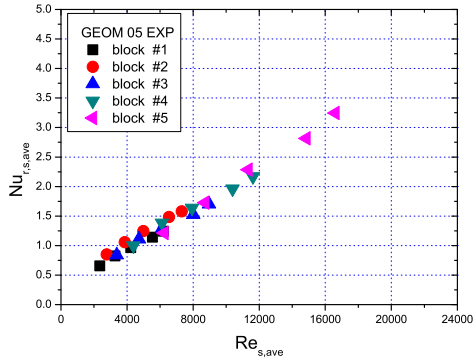


Figure 7.2: Example of the averaged effective Nusselt number distribution for each streamwise block for a convergent model (Geom 05)

Table 7.3: Geom 05 - Example of Reynolds number variation for different streamwise blocks

Geom 05 (6 can)	$m_{air} = 4.3 \text{ g/s}$	$m_{air} = 11.0 \text{ g/s}$
block #1	$Re_{s,ave} = 2343$	$Re_{s,ave} = 6194$
block #2	$Re_{s,ave} = 2763$	$Re_{s,ave} = 7316$
block #3	$Re_{s,ave} = 3382$	$Re_{s,ave} = 8964$
block #4	$Re_{s,ave} = 4380$	$Re_{s,ave} = 11620$
block #5	$Re_{s,ave} = 6256$	$Re_{s,ave} = 16609$

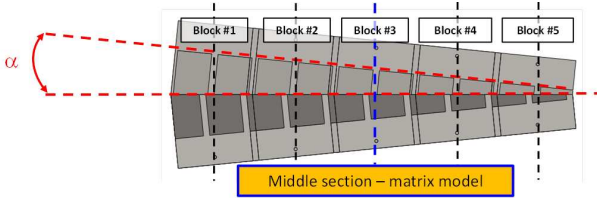


Figure 7.3: Schematic of the reference middle section for the geometric parameters used in the correlations

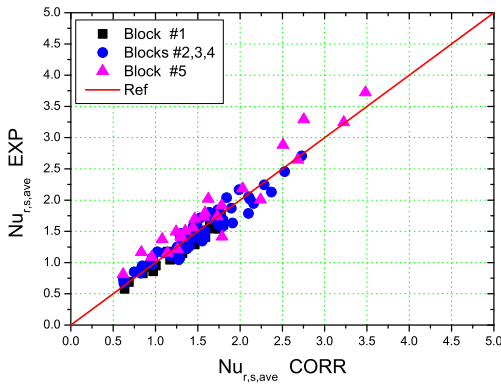


Figure 7.4: Comparison between experimental and calculated effective Nusselt number by correlation

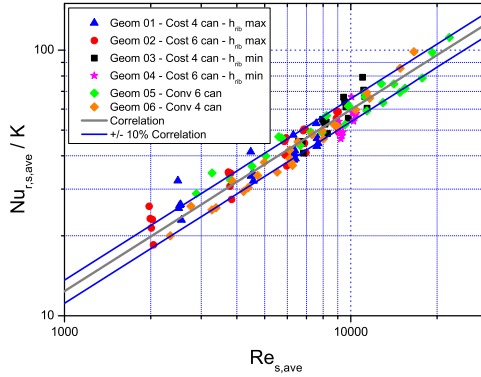


Figure 7.5: Comparison between effective Nusselt experimental trends and relative correlation

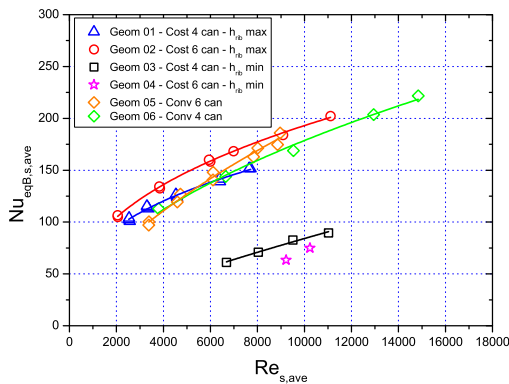


Figure 7.6: Equivalent Nusselt number correlations for the investigated geometries

Table 7.4: Exponents and coefficients of equivalent Nusselt number correlations

Geometry	Correlation
Geom 01 - cost 4 can - h_{rib} max	$Nu_{eqB} = 5.989 \cdot Re_{s,ave}^{0.360}$
Geom 02 - cost 6 can - h_{rib} max	$Nu_{eqB} = 5.397 \cdot Re_{s,ave}^{0.388}$
Geom 03 - cost 4 can - h_{rib} min	$Nu_{eqB} = 0.070 \cdot Re_{s,ave}^{0.771}$
Geom 04 - cost 6 can - h_{rib} min	—————
Geom 05 - conv 6 can	$Nu_{eqB} = 0.711 \cdot Re_{s,ave}^{0.609}$
Geom 06 - conv 4 can	$Nu_{eqB} = 1.641 \cdot Re_{s,ave}^{0.509}$

7.2 Friction Correlations

In a similar manner to the previous case for the heat transfer, two types of correlation have been determined to evaluate friction or pressure losses: one has been derived from the friction factor trends as a function of Reynolds number, one from a non dimensional mass flow rate as a function of the total to static pressure ratio.

As regards the friction factor correlation, all data have been considered with the exception of those for *Geom 05*. In fact, as already explained in Section 5.2, the friction factor trend for this case totally disagrees with the physical phenomenon of the friction in a channel; this is probably due to some errors in manufacturing of test model or pressure taps along the channel.

The input data for this correlation have been taken as:

- overall friction factor $f_{s,ave}$ based on the sub-channel hydraulic diameter at the average section of the model and calculated by means of Equation 4.30;
- Reynolds number $Re_{s,ave}$ referred to the average section of the model;

These data have been correlated with the same dimensionless geometric parameters adopted for the above reported heat transfer correlation; even in this case the best fitting is ensured by the same mathematical form already used to correlate heat transfer data (Equation 7.3). Therefore, it has been determined the friction factor correlation given by Equation 7.6 with the coefficients and exponents reported in Table 7.5:

$$f_{s,ave} = a \cdot Re_{s,ave}^b \cdot \left(\frac{t_{rib}}{d_{h,s}} \right)_{ave}^{(c+e \cdot \alpha)} \cdot \left(\frac{h_{rib}}{d_{h,s}} \right)_{ave}^{(d+f \cdot \alpha)} \quad (7.6)$$

Values reported in the previous Table 7.5 have been found by minimizing the following expression of standard deviation:

$$dev.st. = \sqrt{\frac{\sum_{i=1}^n ((f_{s,ave})_{exp} - ((f_{s,ave})_{corr}))^2}{n}} = 0.0112 \quad (7.7)$$

Table 7.5: Exponents and coefficients of the friction factor correlation

a	b	c	d	e	f
0.263	-0.166	-0.403	0.688	-0.067	0.126

The good fitting of this correlation is shown by Figures 7.7 and 7.8. It is clear that all experimental data are in a very good agreement with the correlation and only few points fall outside the uncertainty bands of correlations; the higher deviations from these bands occur at the highest Reynolds number for the four entry channel geometry with the minimum rib height *Geom 03*.

Always referring to Figure 7.8 values on the vertical axis are normalized by the same quantity K (Equation 7.5), while Reynolds values on the horizontal axis are shown in logarithmic scale.

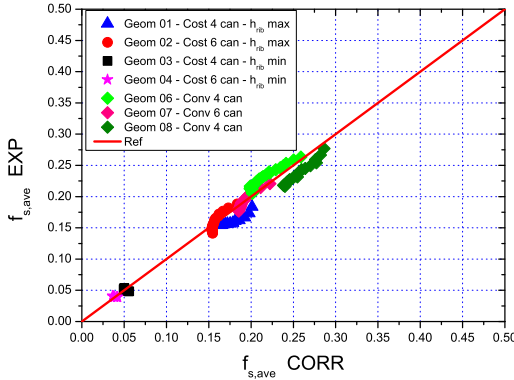


Figure 7.7: Comparison between experimental and calculated friction factor values by correlation

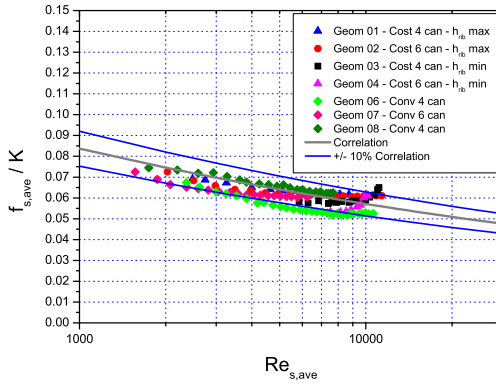


Figure 7.8: Comparison between experimental trends of friction factor and relative correlation

According to the same procedure it has been also found the other form of pressure loss correlation in terms of a non dimensional mass flow rate \dot{m}_{rid} as a function of the total to static pressure ratio β_{TS} , where \dot{m}_{rid} is based on the sub-channel passage area at the outlet section (Equation 4.33) while β_{TS} is the ratio between the total pressure at the inlet and the static pressure at the outlet of the model (Equation 4.32) .

The following correlation has been determined with the exponent and coefficient values reported in Table 7.6:

$$\dot{m}_{rid} = (a \cdot \beta + b) \cdot \left(\frac{t_{rib}}{d_{h,s}} \right)_{ave}^{(c+e \cdot \alpha)} \cdot \left(\frac{h_{rib}}{d_{h,s}} \right)_{ave}^{(d+f \cdot \alpha)} \cdot \sqrt{\frac{2 \cdot \gamma}{\gamma - 1} \cdot \left(\beta_{TS}^{-2/\gamma} - \beta_{TS}^{-(\gamma+1)/\gamma} \right)} \quad (7.8)$$

Using the values shown in Table 7.6 the standard deviation evaluated on the non dimensional mass flow rate \dot{m}_{rid} is only 0.005. The higher accuracy of this correlation is proved by the comparison between experimental and correlation data in Figure 7.9.

Table 7.6: Exponents and coefficients of the \dot{m}_{rid} vs. β_{TS} correlation

a	b	c	d	e	f
0.049	0.217	0.123	-0.102	0.042	-0.406

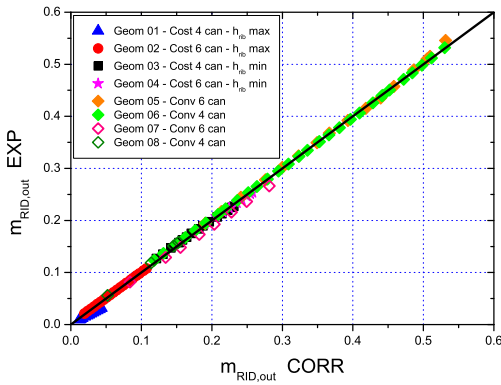


Figure 7.9: Comparison between experimental and calculated non dimensional mass flow values by correlation

7.3 Application of Correlations to a Real Case

In this last section of the thesis a real case of a gas turbine blade has been considered and the performance of the current internal cooling solution have been compared with those achievable by means of the investigated matrix geometries using the above reported experimental correlations.

The case chosen for this comparison refers to the trailing edge system of an industrial gas turbine blade for oil and gas applications. The current cooling technology adopted in the considered trailing edge is a ribbed serpentine; no more information are given about this system since these data are sensitive for industrial applications.

Since this comparison is made with a current system for a trailing edge, only the two investigated convergent matrix geometries have been considered because are more suitable for this kind of application.

The conditions of the coolant supply in this trailing edge system, given by the industrial partner of this collaboration GE Oil & Gas, are reported in Table 7.7; these conditions are related to the design point of the considered gas turbine.

It should be noted that the coolant supply conditions are referred to the inlet section at the root of the blade; $m_{cool,tot}$ represents the total coolant mass flow rate that enters the trailing edge cavity. It is assumed that the height of the considered blade is such that 7 matrix modules can be installed along the spanwise direction. These 7 modules are considered to be in parallel with each other; for this reason it may be assumed that the total coolant mass flow $m_{cool,tot}$ is equally splitted into the several matrix modules. Under this assumption the present comparison has been made considering one of these modules supplied by a coolant mass flow rate equal to $m_{cool,mod} = 2.735$ g/s instead of 19.144 g/s.

As regards the heat transfer performance, the equivalent Nusselt number correlations reported in Table 7.4 have been applied to determine the equivalent heat transfer coefficient HTC_{aveeq} . As shown by Figure 7.10 this HTC value is applied to the internal endwall surface of the blade and

allows to globally determine the overall heat removed from this surface. To evaluate this heat transfer coefficient, the geometric dimensions of the considered matrix modules have been divided by the scale factor $SF=5$, while the flow properties (i.e. air thermal conductivity, density and viscosity) have been recalculated at the inlet temperature $T_{cool,in}$ and pressure conditions $p_{cool,in}$ of the coolant.

Table 7.7: Coolant supply conditions of the real case at the design point

$m_{cool,tot}$	19.144 g/s
$m_{cool,mod}$	2.735 g/s
$T_{cool,in}$	700 K
$p_{cool,in}$	11.825 bar
$\Delta p_{cool,tot}$	4 bar

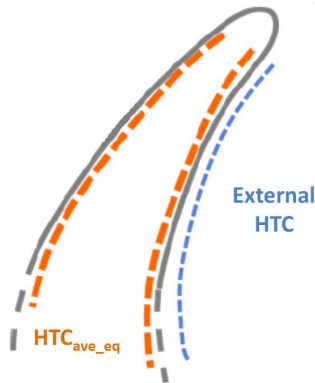


Figure 7.10: Schematic representation of the $HTC_{ave_{eq}}$ applied to the internal endwall surface of the airfoil

As regards the pressure loss, correlations reported in Figures 5.30 and

5.31 for the six and four entry channels convergent geometries have been applied to determine the total to static pressure ratio β_{TS} by calculating the non dimensional mass flow rate at the design operating conditions. Then, knowing the β_{TS} and the coolant pressure at the inlet $p_{cool,in}$, it has been possible to obtain the overall pressure $\Delta p_{cool,tot}$ through the considered matrix modules.

Once calculated the heat transfer and pressure loss performance in the design point of the coolant conditions, some assumptions have been made to extrapolate these performance in off-design conditions. For each geometry two extreme cases have been considered; these cases correspond to a minimum and a maximum of coolant consumption during operating conditions. These off-design points have been obtained calculating the non dimensional mass flow \dot{m}_{rid} from the minimum and the maximum mass flow rate measured during the experimental tests for these two matrix geometries.

Tables 7.8 and 7.9 summarize the overall pressure drops $\Delta p_{cool,tot}$ and the equivalent heat transfer coefficients $HTC_{ave_{eq}}$ calculated at the design and off-design conditions for the 4 entry channels and 6 entry channels matrix geometry. These values are reported in the graph of Figure 7.11 and are compared with the current performance of ribbed serpentes coming from the GE Oil & Gas experience.

From this comparison it is clear that both the matrix geometries guarantee higher heat transfer performance than the current values. As regards the 4 entry channels geometry the heat transfer enhancement in the design point is about $1.2 \div 2.4$ with an overall pressure drop of only 0.76 bar, while the 6 entry channels geometry has a very high heat transfer enhancement, from 2 to 4 times over the current solution, with an overall pressure drop of about 3 bar against $\Delta p_{cool,tot}=4$ bar.

In addition to this, it is also clear that the matrix cases can provide the same performance of current solutions at lower mass flow rates and hence with a lower coolant consumption.

In conclusion, the promising results obtained from this experimental research clearly show that both the investigated matrix geometries for the

trailing edge application are able to replace current cooling schemes and lead to important advantages such as: an increase of the heat transfer performance together with a reduction of coolant consumption and bleed air pressure from the compressor. This surely contributes to improve the overall performance of the gas turbine maintaining the lifetime and reliability operation requirements.

Table 7.8: Heat transfer and pressure loss performance of the convergent matrix geometry with 4 entry channels evaluated in design and off-design points of a real case

Geom Conv 4 can			
Parameter	Off Des - Min	Design	Off Des - Max
$m_{cool,mod}$ [g/s]	1.242	2.735	6.930
β_{TS} []	1.016	1.068	1.405
$\Delta p_{cool,tot}$ [bar]	0.172	0.757	4.467
$HTC_{ave_{eq}}$ [W/m^2K]	3164	4700	7458

Table 7.9: Heat transfer and pressure loss performance of the convergent matrix geometry with 6 entry channels evaluated in design and off-design points of a real case

Geom Conv 6 can			
Parameter	Off Des - Min	Design	Off Des - Max
$m_{cool,mod}$ [g/s]	0.943	2.735	4.904
β_{TS} []	1.044	1.333	1.947
$\Delta p_{cool,tot}$ [bar]	0.392	2.952	8.405
$HTC_{ave_{eq}}$ [W/m^2K]	4236	8131	11403

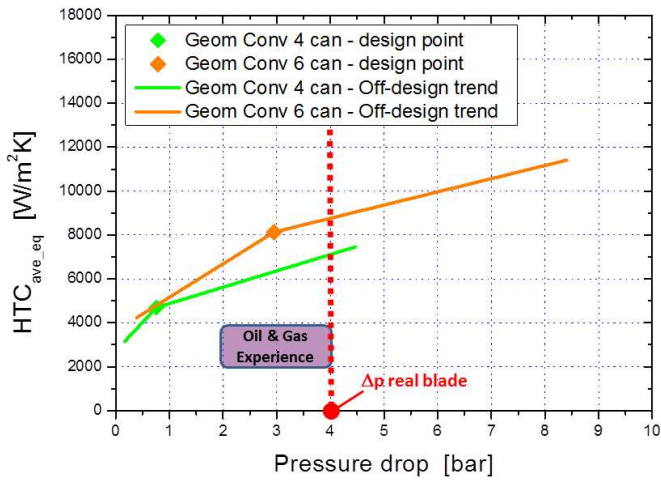


Figure 7.11: Performance comparison between the experimental matrix geometries and current serpentine solutions from GE Oil & Gas experience

Conclusions

An intensive experimental survey has been performed to investigate heat transfer and friction performance of different matrix cooling geometries in view of a possible application as internal cooling systems of both nozzles and vanes of industrial gas turbines. This activity has been carried out within a collaboration between the Department of Industrial Engineering of the University of Florence and GE Oil & Gas.

Three main experimental activities have been carried out on scaled up test models characterized by internal geometries manufacturable by means of the existing investment casting processes.

The first experimental activity has been performed on four matrix geometries characterized by a constant cross section from the inlet to the outlet and by two different rib heights representing two extreme cases: in fact two are suitable for an application in the mid chord region and the other two for the trailing edge region. For each rib height two configurations characterized by a different open area through the sub-channels have been investigated: one having four sub-channels with a lower rib thickness and one having six sub-channels with a higher rib thickness. The experimental tests on these geometries have provided the effects of a variation of the main geometric parameters on the heat transfer and friction performance.

The second experimental activity has been performed on two convergent matrix geometries resulting from the combination of the previous test articles with constant cross section; these tests have allowed to understand the effects of a progressive variation of the passage area (i.e. convergence

angle) on the performance of two realistic trailing edges.

In the first and in the second experimental activities tests have been carried out under static conditions reproducing the Reynolds and Biot number similitude with a real case provided by the industrial partner.

In the third and last experimental activity the two convergent geometries have been investigated under rotating conditions reproducing both Reynolds and Rotation number similitude with the real application. The effects of rotation have been found for two different orientations of the test model with respect to the rotating plane: 0deg and 30deg. This latter configuration replicates the exit angle of a real gas turbine blade.

To evaluate friction performance the pressure drops have been derived by measuring pressures in different points along the test model and the overall total pressure loss from the inlet to the outlet has been considered to determine the average friction factor for each flow condition.

As regards heat transfer tests, the regionally averaged heat transfer coefficients have been measured by means of a steady state technique based on heated segments and embedded thermocouples, where a constant heat flux has been provided for each streamwise and spanwise position of the test models. Then a specific post-processing procedure has been adopted to evaluate the non uniform temperature distribution along the matrix ribs/fins starting from the measurement of the wall temperature at a given distance from the base of the matrix blocks. This procedure, based on the solution of the differential heat equation and on the fin effectiveness theory, has allowed to determine two types of average heat transfer coefficients with a different physical meaning: the effective coefficients htc_r between the rib surfaces and the fluid, and the equivalent coefficients htc_{eqT} applicable on the internal endwalls of the airfoil to determine the overall heat removed from these surfaces. The equivalent heat transfer coefficients have been also recalculated with the ideal value of thermal conductivity that allows to obtain the Biot number similitude with a real application (htc_{eqB}).

As regards friction results the pressure drop distributions as a function

of the streamwise distance have been found for each Reynolds number condition and comparisons have been made between the investigated geometries.

The increase of pressure losses has been found and quantified for: an increase of rib thickness together with the increase of sub-channels number and a reduction of rib height for geometries with constant cross section. For convergent matrix geometries a progressive increase of pressure losses with the streamwise distance has been found and compared with the distributions of the corresponding constant matrix geometries.

Then from the evaluation of the overall pressure drop from the inlet to the outlet of each test model, the average friction factor $f_{s,ave}$ distributions have been found as a function of the Reynolds number $Re_{s,ave}$. All the trends are insensitive to the increase of Reynolds number and show the characteristic horizontal asymptote with the exception of constant geometries with the smallest passage area; in fact in these latter cases the trends slightly increase with the increasing of Reynolds number because of the high Mach numbers at the outlet sections.

Further comparisons between the different investigated geometries have been performed in terms of normalized friction factors distributions $f_{s,ave}/f_0$, where f_0 values have been derived by the correlation of Karman-Nikuradse for turbulent flows in smooth ducts.

Friction data have been also evaluated in terms of total to static pressure ratio as a function of a non dimensional mass flow rate; these trends represent the flow functions of the different geometries and allow to estimate the coolant consumption with the varying of the above mentioned pressure ratio. It should be noted that these non dimensional results are also be approximately valid for matrix geometries similar to those investigated and may be also applied to find the performance of such geometries under realistic engine conditions.

As regards the heat transfer results the distributions of the average heat transfer coefficients and Nusselt numbers have been found as a function of both Reynolds number and streamwise position. First of all, an important common feature has been found among the distributions for the

different matrix geometries: higher HTC's have been found on the right row of the upper module and on the left row of the lower module because of the flow impingement after the turn regions. In fact, as also proved by previous works, the turning regions are characterized by a strong vortical flow with the destruction of the thermal and fluid boundary layers; after the turn a new thin boundary layer is formed and the flow accelerates again resulting in a local increase of heat transfer coefficients.

This effect is more significant for the convergent geometries especially in the last streamwise blocks where the passage areas are smaller and the flow velocities higher.

The heat transfer results expressed in terms of equivalent Nusselt number $Nu_{eqT,s}$ distributions have allowed to quantify the fin effect due to the presence of ribs for each geometry; as expected, higher values have been obtained for geometries with the maximum rib height and number of sub-channels and hence with the maximum heat transfer surface area. Because of this higher fin effect these geometries would allow to remove more heat from the endwall surfaces of the airfoils.

On the other hand, the effective Nusselt number $Nu_{r,s}$ distributions have allowed to put in evidence the high turbulent behaviour for the convergent geometries and for the constant geometries with the minimum rib height; in fact, with respect to the other cases, these geometries show a higher dependence on Reynolds number.

From the effective Nusselt number distributions the heat transfer enhancement values $Nu_{r,s}/Nu_0$ have been derived over the investigated Reynolds number range, where the corresponding Nu_0 values have been calculated by the Dittus-Boelter correlation for turbulent flows in smooth ducts. These trends show a higher heat transfer enhancement at lower Reynolds numbers; moreover, even though the $Nu_{r,s}/Nu_0$ ratio slightly decreases with the increasing of Reynolds number, the performance of each matrix case is higher than a pin fin configuration reported in literature. These results also show that the heat transfer enhancement is higher for matrix geometries with a lower number of sub-channels. In addition to this, all the trends for the investigated geometries are in good agreement with

the experimental data coming from literary works on similar matrix geometries.

To compare the overall performance of the investigated geometries in terms of both friction and heat transfer, the Thermal Performance Factor TPF has been calculated for each Reynolds number starting from the $Nu_{r,s,ave}/Nu_0$ and $f_{s,ave}/f_0$ ratios. Results for the two investigated matrix geometries are in good agreement with literature data and are slightly higher than those for a pin fin configuration at the lower Reynolds numbers.

With regard to the rotating results on the two convergent matrix geometries, a significant heat transfer enhancement due to the rotation has been found at the lowest Reynolds numbers. In fact the overall rotation-to-stationary ratio $Nu_{r,s}/Nu_{stat}$ is about $20 \div 30\%$ at the minimum Reynolds number $Re_{s,ave} \simeq 3000$ and only $2 \div 5\%$ at the maximum $Re_{s,ave} \simeq 8000 \div 9000$. This is mainly due to the stronger effect of the Coriolis force on the flow field with a weaker flow inertial force at the low mass flow rates. The same values of heat transfer enhancement have been found for $0deg$ and $30deg$ configurations; this means that the Coriolis effect does not change over the investigated range of channel orientation with respect to the rotating plane.

In the final part of the present work some heat transfer and friction correlations have been obtained starting from the experimental data of matrix geometries with constant and convergent cross section.

The heat transfer correlation gives the average Nusselt number for the specific $i - th$ streamwise block as a function of Reynolds number and some dimensionless geometric parameters representative of a matrix structure such as: rib thickness to sub-channel hydraulic diameter ratio $t_{rib}/d_{h,s}$, rib height to sub-channel hydraulic diameter ratio $h_{rib}/d_{h,s}$, α converging angle of a matrix module.

As regards the friction correlations, the best fitting to experimental data has been ensured by the same mathematical expression used for the heat transfer correlation; in this case the overall friction factor $f_{s,ave}$ has been

put in relation with Reynolds number and the same dimensionless geometric parameters.

Finally, a relation of the same mathematical form has been found between the total to static pressure ratio β_{TS} and the non dimensional mass flow rate \dot{m}_{rid} .

These correlations have been applied to a real case in order to compare the current performance of a serpentine ribbed duct in a trailing edge with those achievable by means of the two investigated convergent matrix geometries. The comparison has been performed considering the coolant supply conditions at the design point in terms of coolant mass flow rate, inlet pressure and inlet temperature, but some assumptions have been made to extrapolate these performance also in off-design conditions.

The results obtained from this comparison are very promising, in fact both the considered matrix geometries guarantee higher heat transfer coefficients for the whole range; moreover, both solutions provide the same performance of current technology at lower mass flow rates and hence with a lower coolant consumption.

These results represent a good starting point in view of a future application of matrix cooling systems within blades and nozzles of industrial gas turbines. However, before the implementation of these geometries in the current blade designs, it will be necessary to evaluate the opportunity to realize them by means of the recent additive manufacturing technologies with cost savings in respect to the conventional investment casting processes.

Bibliography

- [1] Giampaolo, A. *Gas Turbine Handbook: Principles and Practices*. CRC Press, Taylor & Francis, 2006.
- [2] Han, J. C., Dutta, S., and Ekkad, S. *Gas Turbine Heat Transfer and Cooling Technology*. Taylor & Francis, 2000.
- [3] plc. Rolls-Royce. *The Jet Engine*. fifth edition, 1996.
- [4] Schlichting, H. *Boundary-Layer Theory*. McGraw-Hill, 1979.
- [5] Bunker, R.S. Gas turbine heat transfer: Ten remaining hot gas path challenges. *ASME J. Turbomach.*, 129, 2007.
- [6] Saha, K., Acharya, S., and Nakamata, C. Heat transfer enhancement and thermal performance of lattice structures for internal cooling of airfoil trailing edges. *Journal of Thermal Science and Engineering Applications*, 5, 2013.
- [7] Sundberg, J. The heat transfer correlations for gas turbine cooling. *Linköping University, Linköping, Sweden*, (pp. 38-63), 2006.
- [8] Bonini, A. *A Decoupled Conjugate Heat Transfer Procedure Involving Flow Network Approach: Application to GT Blade Cooling*. PhD thesis, University of Florence, Florence, 2011.
- [9] Metzger, D.E., Florschuetz, L.W., Takeuchi, D.I., Behee, R.D., and Berry, R.A. Heat transfer characteristics for inline and staggered

- arrays of circular jets with crossflow of spent air. *ASME J Heat Trans*, (101), 1979.
- [10] Florschuetz, L.W., Berry, R.A., and Metzger, D.E. Periodic streamwise variations of heat transfer coefficients for inline and staggered arrays of circular jets with crossflow of spent air. *ASME J Heat Trans*, (102), 1980.
- [11] Koopman, R.N. and Sparrow, E.M. Local and average transfer coefficients due to an impinging row of jets. *International Journal of Heat and Mass Transfer*, 92:73–82, 1976.
- [12] Florschuetz, L.W. and Su, C.C. Effects of crossflow temperature on heat transfer within an array of impinging jets. *ASME J Heat Trans*, (109), 1987.
- [13] Kercher, D.M. and Tabakoff, W. Heat transfer by a square array of round air jets impinging perpendicular to a flat surface including the effect of spent air. *ASME Journal of Engineering for Power*, 92:73–82, 1970.
- [14] Florschuetz, L.W., Truman, C.R., and Metzger, D.E. Streamwise flow and heat transfer distributions for jet array impingement with crossflow. *ASME J Heat Trans*, (103), 1981.
- [15] Bailey, J.C. and Bunker, R.S. Local heat transfer and flow distributions for impinging jet arrays of dense and sparse extent. *ASME Turbo Expo*, (Paper GT-2002-30473), 2002.
- [16] Ekkad, S.V., Huang, Y., and Han, J.C. Impingement heat transfer on a target plate with film holes. *AIAA Journal of Thermophysics and Heat Transfer*, 13(4):522–528, 1999.
- [17] L.W. Florschuetz, D.E. Metzger and Su, C.C. Heat transfer characteristics for jet array impingement with initial crossflow. *ASME J Heat Trans*, (106), 1984.

-
- [18] Chupp, R.E., Helms, H.E., McFadden, P.W., and Brown, T.R. Evaluation of internal heat transfer coefficients for impingement cooled turbine airfoils. *AIAA Journal of Aircraft*, 6:203–208, 1969.
- [19] Bunker, R.S and Metzger, D.E. Local heat transfer in internally cooled turbine airfoil leading edge regions. part i: Impingement cooling without film coolant extraction. *ASME J. Turbomach.*, 112: 451–458, 1990.
- [20] Metzger, D.E. and Bunker, R.S. Local heat transfer in internally cooled turbine airfoil leading edge regions. part ii: Impingement cooling with film coolant extraction. *ASME J. Turbomach.*, 112: 459–466, 1990.
- [21] Taslim, M.E. and Bethka, D. Experimental and numerical impingement heat transfer in an airfoil leading-edge cooling channel with crossflow. *ASME Turbo Expo*, (Paper GT-2007-28212), 2007.
- [22] Maiuolo, F., Andrei, L., Carcasci, C., Soghe, R. Da, Facchini, B., Tarchi, L., and Zecchi, S. Heat transfer measurements in a leading edge geometry with racetrack holes and film cooling extraction. *ASME Turbo Expo*, (Paper GT-2012-69581), 2012.
- [23] Maiuolo, F., Facchini, B., Tarchi, L., and Ohlendorf, N. Experimental investigation on the heat transfer of a leading edge cooling system: Effects of jet-to-jet spacing and showerhead extraction. *ASME Turbo Expo*, (Paper GT-2013-94759), 2013.
- [24] Metzger, D. E., Berry, R. A., and Bronson, J. P. Developing heat transfer in rectangular ducts with staggered arrays of short pin fins. *ASME J. Heat Transfer*, 104:700–706, 1982.
- [25] VanFossen, G. J. Heat transfer coefficients for staggered arrays of short pin fins. *ASME Journal of Engineering for Power*, 104: 268–2745, 1982.

- [26] Metzger, D. E., Fan, C. S., and Haley, S. W. Effects of pin shape and array orientation on heat transfer and pressure loss in pin fin arrays. *ASME J. Eng. Gas Turbine Power*, 106:252–257, 1984.
- [27] Chyu, M.K. Heat transfer and pressure drop for short pin-fin arrays with pin-endwall fillet. *ASME J Heat Trans*, (112), 1990.
- [28] Chyu, M. K., Hsing, Y. C., and Natarajan, V. Convective heat transfer of cubic fin arrays in a narrow channel. *ASME J. Turbomach.*, 120:362–367, 1998.
- [29] Shepard, W. B., Metzger, D. E., and Haley, S. W. Row resolved heat transfer variations in pin-fin arrays including effects of non-uniform arrays and flow convergence. *ASME Turbo Expo*, (Paper GT1986-132), 1986.
- [30] Chyu, M.K., Natarajan, V., and Metzger, D.E. Heat/mass transfer from pin-fin arrays with perpendicular flow entry. *ASME HTD*, 226, 1992.
- [31] Kumaran, T.K., Han, J.C., , and Lau, S.C. Augmented heat transfer in a pin fin channel with short or long ejection holes. *International Journal of Heat and Mass Transfer*, 34:2617–2628, 1991.
- [32] Hwang, J.J. and Lu, C.C. Lateral flow effect of endwall heat transfer and pressure drop in a pin-fin trapezoidal duct of various pin shapes. *ASME Turbo Expo*, (Paper GT2000-0232), 2000.
- [33] Afanas'yev, V.N., Veselkin, V.Yu., Leont'ev, A.I., Skibin, A.P., and Chudnovskiy, Ya.P. Thermohydraulics of flow over isolated depressions (pits, grooves) in a smooth wall. *Heat Transfer Research*, 25: 22–56, 1993.
- [34] Isaev, S.A., Leont'ev, A.I., and Baranov, P.A. Identification of self-organized vortexlike structures in numerically simulated turbulent flow of a viscous incompressible liquid streaming around a well on a plane. *Technical Physics Letters*, 26:15–18, 2000.

- [35] Mahmood, G.I., Hill, M.L., Nelson, D.L., Ligrani, P.M., Moon, H.K., and Glezer, B. Local heat transfer and flow structure on and above a dimpled surface in a channel. *ASME J. Turbomach.*, 123:115–123, 2001.
- [36] Moon, S.W. and Lau, S.C. Turbulent heat transfer measurements on a wall with concave and cylindrical dimples in a square channel. *ASME Turbo Expo*, (Paper GT2002-30208), 2002.
- [37] Bunker, R.S. and Donnellan, K.F. Heat transfer and friction factors for flows inside circular tubes with concavity surfaces. *ASME Turbo Expo*, (Paper 2003-38053), 2003.
- [38] Syred, N., Khalatov, A., Kozlov, A., Shchukin, A., and Agachev, R. Effect of surface curvature on heat transfer and hydrodynamics within a single hemispherical dimple. *ASME Turbo Expo*, (Paper 2000-GT-236), 2000.
- [39] Gupta, S., Chaube, A., and Verma, P. Review on heat transfer augmentation techniques: Application in gas turbine blade internal cooling. *Journal of Engineering Science and Technology Review*, 5: 52–57, 2012.
- [40] Yang, S.F., Han, J.C., Azad, S., and Lee, C.P. Heat transfer in rotating serpentine coolant passage with ribbed walls at low mach numbers. *ASME Turbo Expo*, (Paper GT2013-94288), 2013.
- [41] Bonanni, L., Soghe, R. Da, Facchini, B., Micio, M., Pievaroli, M., Tarchi, L., Abba, L., and Maritano, M. Heat transfer and friction in circular ducts with shaped ribs. *10th European Turbomachinery Conference*, (ETC129-2013), 2013.
- [42] Han, J.C. Heat transfer and friction characteristics in rectangular channels with rib turbulators. *ASME J Heat Trans*, (110), 1988.
- [43] Han, J.C., Glicksman, L.R., and Rohsenow, W.M. An investigation of heat transfer and friction for rib-roughened surfaces. *International Journal of Heat and Mass Transfer*, 21:1143–1156, 1978.

- [44] Han, J.C. and Park, J.S. Developing heat transfer in rectangular channels with rib turbulators. *International Journal of Heat and Mass Transfer*, 31:183–195, 1988.
- [45] Han, J.C., Ou, S., Park, J.S., and Lei, C.K. Augmented heat transfer in rectangular channels of narrow aspect ratios with rib turbulators. *International Journal of Heat and Mass Transfer*, 32:1619–1630, 1989.
- [46] Han, J.C., Zhang, Y.M., and Lee, C.P. Augmented heat transfer in square channels with parallel, crossed, and v-shaped angled ribs. *Journal of Heat Transfer, Transactions ASME*, 113, 1991.
- [47] Cho, H.H., Wu, S.J., and Kwon, H.J. Local heat/mass transfer measurements in a rectangular duct with discrete ribs. *ASME J. Turbomach.*, 122:579–586, 2000.
- [48] Han, J.C., Huang, J.J., and Lee, C.P. Augmented heat transfer in square channels with wedge-shaped and delta-shaped turbulence promoters. *ASME J. Turbomach.*, 1:37–52, 1993.
- [49] Bailey, J.C. and Bunker, R.S. Heat transfer and friction in channels with very high blockage 45° staggered turbulators. *ASME Turbo Expo*, (GT-2003-38611), 2003.
- [50] Shen, J.R., Wang, Z., Ireland, P.T., Jones, T.V., and Byerley, A.R. Heat transfer enhancement within a turbine blade cooling passage using ribs and combinations of ribs with film cooling holes. *ASME J. Turbomach.*, 188:428–433, 1996.
- [51] Thurman, D. and Poinsette, P. Experimental heat transfer and bulk air temperature measurements for a multipass internal cooling model with ribs and bleed. *ASME Turbo Expo*, (2000-GT-233), 2000.
- [52] Chyu, M. K., Hsing, Y. C., Shih, T. I. P., and Natarajan, V. Heat transfer contributions of pins and endwall in pin-fin arrays: Effects

- of thermal boundary condition modeling. *ASME J. Turbomach.*, 121:257–263, 1999.
- [53] Hwang, J.J. and Lui, C. C. Detailed heat transfer characteristic comparison in straight and 90-deg turned trapezoidal ducts with pin-fin arrays. *International Journal of Heat and Mass Transfer*, 42:4005–4016, 1999.
- [54] Hwang, J.J. and Lui, C. C. Measurement of endwall heat transfer and pressure drop in a pin-fin wedge duct. *International Journal of Heat and Mass Transfer*, 45:877–889, 2002.
- [55] Facchini, B., Carcasci, C., and Innocenti, L. Heat transfer and pressure drop evaluation in thin wedge-shaped trailing edge. *ASME Turbo Expo*, (Paper GT2003-38197), 2003.
- [56] Facchini, B., Innocenti, L., and Tarchi, L. Pedestal and endwall contribution in heat transfer in thin wedge shaped trailing edge. *ASME Turbo Expo*, (Paper GT2004-53152), 2004.
- [57] Bianchini, C., Facchini, B., Simonetti, F., and Tarchi, L. Numerical and experimental investigation of turning flow effects on innovative pin fin arrangements for trailing edge cooling configurations. *ASME Turbo Expo*, (Paper GT2010-23536), 2010.
- [58] Bianchini, C., Bonanni, L., Carcasci, C., Facchini, B., and Tarchi, L. Experimental survey on heat transfer in an internal channel of a trailing edge cooling system. 65° *Associazione Termotecnica Italiana National Conference*, (Paper 12_085), 2010.
- [59] Bonanni, L., Carcasci, C., Facchini, B., and Tarchi, L. Experimental survey on heat transfer in a trailing edge cooling system: Effects of rotation in internal cooling ducts. *ASME Turbo Expo*, (Paper GT2012-69638), 2012.
- [60] Liu, Y. H., Huh, M., Wright, L. M., and Han, J. C. Heat transfer in trailing edge wedge shaped cooling channels with slot ejection

- under high rotation numbers. *ASME Turbo Expo*, (Paper GT2008-50343), 2008.
- [61] Lee, C. P. Turbine blade trailing edge cooling openings and slots. (U.S. Patent 6,174,135B1), 16 Jan. 2001.
- [62] Bonanni, L. *Investigation on a Trailing Edge Cooling System*. PhD thesis, University of Florence, Florence, 2011.
- [63] Naik, S. and Schnieder, M. Gas turbine airfoil with shaped trailing edge coolant ejection holes. (U.S. Patent 8,770,920 B2), 8 Jul. 2014.
- [64] Anderson, H.I. Introduction on the effects of turbulence. *Von Karman Lecture Series*, 2010.
- [65] Han, J.C., Zhang, Y.M., and Kalkuehler, K. Uneven wall temperature effect on local heat transfer in a rotating two-pass square channel with smooth walls. *ASME J Heat Trans*, (114), 1993.
- [66] Parsons, J.A., Han, J.C., and Zhang, Y.M. Wall heating effect on local heat transfer in a rotating two-pass square channel with 90-degree rib turbulators. *International Journal of Heat and Mass Transfer*, 37:1411–1420, 1994.
- [67] Zhang, Y.M., Han, J.C., Parsons, J.A., and Lee, C.P. Surface heating effect on local heat transfer in a rotating two-pass square channel with 60-degree angled rib turbulators. *ASME J. Turbomach.*, 117:272–278, 1995.
- [68] Acharya, S., Eliades, V., and Nikitopoulos, D.E. Heat transfer enhancements in rotating two-pass coolant channels with profiled ribs: Part 1 average results. *ASME Turbo Expo*, (2000-GT-0227), 2000.
- [69] Wagner, J.H., Johnson, B.V., Graziani, R.A., and Yeh, F.C. Heat transfer in rotating serpentine passages with trips normal to the flow. *ASME J. Turbomach.*, 114:847–857, 1992.

- [70] Park, C.W., Lau, S.C., and Kukreja, R.T. Heat mass transfer in a rotating two-pass square channel with transverse ribs. *AIAA Journal of Thermophysics and Heat Transfer*, 12(1):80–86, 1998.
- [71] Johnson, B.V., Wagner, J.H., Steuber, G.D., and Yeh, F.C. Heat transfer in rotating serpentine passages with selected model orientations for smooth or skewed trip walls. *ASME J. Turbomach.*, 116: 738–744, 1994.
- [72] Dutta, S., Andrews, M.J., and Han, J.C. Prediction of turbulent flow and heat transfer in rotating square and rectangular smooth channels. *ASME Turbo Expo*, (96-GT-234), 1996.
- [73] Fu, W.L., Wright, L.M., and Han, J.C. Buoyancy effects on heat transfer in five different aspect-ratio rectangular channels with smooth walls and 45-degree ribbed walls. *ASME Turbo Expo*, (GT2005-68493), 2005.
- [74] Epstein, A.H., Kerrebrock, J.L., Koo, J.J., and Preiser, U.Z. Rotational effects on impingement cooling. *GTL Report*, (184), 1985.
- [75] Mattern, C.H. and Hennecke, D.K. The influence of rotation on impingement cooling. *ASME Turbo Expo*, (96-GT-161), 1996.
- [76] Glezer, B., Moon, H.K., Kerrebrock, J., J.Bons, and Guenette, G. Heat transfer in a rotating radial channel with swirling internal flow. *ASME Turbo Expo*, (98-GT-214), 1998.
- [77] Parsons, J.A., Han, J.C., and Lee, C.P. Rotation effect on jet impingement heat transfer in smooth rectangular channels with four heated walls and radially outward crossflow. *ASME J. Turbomach.*, 120:79–85, 1998.
- [78] Akella, K.V. and Han, J.C. Impingement cooling in rotating two-pass rectangular channels. *AIAA Journal of Thermophysics and Heat Transfer*, 12(4):582–588, 1998.

- [79] Zhou, F. and Acharya, S. Mass/heat transfer in dimpled two-pass coolant passages with rotation. *Heat Transfer in Gas Turbine Systems ed. R. J. Goldstein, Ann. N. Y. Acad. Sci.*, (934):424–431, 2001.
- [80] Griffith, T.S., Al-Hadhrani, L., and Han, J.C. Heat transfer in rotating rectangular cooling channels ($ar = 4$) with dimples. *ASME J. Turbomach.*, 125:555–563, 2003.
- [81] Willett, F.T. and Bergles, A.E. Heat transfer in rotating narrow rectangular ducts with heated sides oriented at 60-degree to the r-z plane. *ASME Turbo Expo*, (2000-GT-224), 2000.
- [82] Willett, F.T. and Bergles, A.E. Heat transfer in rotating narrow rectangular pin-fin ducts. *Experimental Thermal and Fluid Science*, 25:573–582, 2002.
- [83] Wright, L.M., Lee, E., and Han, J.C. Effect of rotation on heat transfer in narrow rectangular cooling channels ($ar = 8:1$ and $4:1$) with pin-fins. *ASME Turbo Expo*, (GT 2003-38340), 2003.
- [84] Chang, S.W., Liu, T.M, Chiou, S.F., and Chang, S.F. High rotation number heat transfer of rotating trapezoidal duct with 45-deg staggered ribs and bleeds from apical side wall. *Journal of Heat Transfer*, 130, 2008.
- [85] Rallabandi, A.P., Liu, Y.H., and Han, J.C. Heat transfer in trailing edge wedge-shaped pin-fin channels with slot ejection under high rotation numbers. *Journal of Thermal Science and Engineering Applications*, 3, 2011.
- [86] Bunker, R.S. Latticework (vortex) cooling effectiveness part 1: stationary channel experiments. *ASME Turbo Expo*, (Paper GT2004-54127), 2004.
- [87] Incropera, F. P. and DeWitt, D. P. *Foundamentals of Heat and Mass Transfer*. John Wiley & Sons, fourth edition, 1996.

- [88] Goreloff, V., Goychengerg, M., and Malkoff, V. The investigation of heat transfer in cooled blades of gas turbines. *AIAA*, (Paper NO. 90-2144), 1990.
- [89] Gillespie, D.R.H., Ireland, P.T., and Dailey, G.M. Detailed flow and heat transfer coefficient measurements in a model of an internal cooling geometry employing orthogonal intersecting channels. *ASME Turbo Expo*, (Paper 2000-GT-653), 2000.
- [90] Nagoga, G.P. Effective methods of cooling of blades of high temperature gas turbines. *Publishing House of Moscow Aerospace Institute*, (p. 100), 1996.
- [91] D.H.R., Gillespie. *Intricate internal cooling systems for gas turbine blading*. PhD thesis, University of Oxford, 1996.
- [92] Acharya, S., Zhou, F., Lagrone, J., Mahmood, G., and Bunker, R.S. Latticework (vortex) cooling effectiveness part 2: rotating channel experiments. *ASME Turbo Expo*, (Paper GT2004-53983), 2004.
- [93] Farina, D.J., Hacker, J.M., Moffat, R.J., and Eaton, J.K. Illuminant invariant calibration of thermochromic liquid crystals. *Experimental Thermal and Fluid Science*, 9:1–9, 1994.
- [94] Nirmalan, N.V., Bunker, R.S., and Hedlund, C.R. The measurement of full-surface internal heat transfer coefficients for turbine airfoils using a non-destructive thermal inertia technique. *ASME J. Turbomach.*, 125, 2002.
- [95] Zhou, F., Lagrone, J., and Acharya, S. Internal cooling in 4:1 ar passages at high rotation numbers. *ASME Turbo Expo*, (Paper GT2004-53501), 2004.
- [96] Oh, I.T., Kim, K.M., Lee, D.H., Park, J.S., and Cho, H.H. Local heat/mass transfer and friction loss measurement in a rotating matrix cooling channel. *ASME Turbo Expo*, (Paper GT2009-59873), 2009.

- [97] Oh, I.T., Kim, K.M., Lee, D.H., Park, J.S., and Cho, H.H. Local heat/mass transfer and friction loss measurement in a rotating matrix cooling channel. *ASME J Heat Trans*, (134), 2012.
- [98] Hong, S.K., Lee, D.H., and Cho, H.H. Heat mass transfer measurement on concave surface in rotating jet impingement. *J Mech Sci Technol*, 22:1952–1958, 2008.
- [99] Park, J.S., Kim, K.M., Lee, D.H., Cho, H.H., and Chyu, M.K. Heat transfer in rotating channel with inclined pin-fins. *ASME J. Turbomach.*, 133, 2011.
- [100] Saha, K., Guo, S., Acharya, S., and Nakamata, C. Heat transfer and pressure measurements in a lattice-cooled trailing edge of a turbine airfoil. *ASME Turbo Expo*, (Paper GT2008-51324), 2008.
- [101] Vedula, R.J. and Metzger, D.E. A method for the simultaneous determination of local effectiveness and heat transfer distributions in three temperature convection situations. *ASME Turbo Expo*, (Paper 91-GT-345), 1991.
- [102] Kays, W.M., Crawford, M.E., and Weigand, B. *Convective Heat and Mass Transfer*, 4th ed. McGraw-Hill, 2005.
- [103] Wolfersdorf, J. and Weigand, B. Internal cooling in turbomachinery. in turbine blade internal cooling-selected experimental approaches. *Von Karman Lecture Series*, (05), 2010.
- [104] Facchini, B., Maiuolo, F., Tarchi, L., and Coutandin, D. Combined effect of slot injection, effusion array and dilution hole on the heat transfer coefficient of a real combustor liner - part 1 experimental analysis. *ASME Turbo Expo*, (GT2010-22936), 2010.
- [105] Caciolli, G., Andreini, A., Facchini, B., Tarchi, L., Coutandin, D., Pesciulli, A., and Taddei, S. Density ratio effects on the cooling performances of a combustor liner cooled by a combined slot effusion system. *ASME Turbo Expo*, (GT2012-68263), 2012.

- [106] Ireland, P.T., Wang, Z., and Jones, T.V. Liquid crystal heat transfer measurements. *Von Karman Lecture Series*, (05), 1993.
- [107] Ireland, P.T. and Jones., T.V. Liquid crystal measurements of heat transfer and surface shear stress. *Measurement Science Technology*, 11:969–986, 2000.
- [108] Ireland, P.T., Gillespie, D., Neely, A.J., and Robertson, A.J. Turbulent heat transfer measurements using liquid crystals. *International Journal of Heat and Fluid Flow*, 20:355–367, 1999.
- [109] Schultz, D.L. and Jones, T.V. Heat transfer measurements in short duration hypersonic facilities. *NATO Advisor Group Aeronautical RD AGARDograph*, 165, 1973.
- [110] Buttsworth, D.L. and Jones, T.V. Radial conduction effects in transient heat transfer experiments. *Aeronautical Journal*, 101:209–212, 1997.
- [111] Vedula, R.J., Metzger, D.E, and Bickford, W.B. Effects of lateral and anisotropic conduction of local convection heat transfer characteristics with transient tests and surface coatings. *Collected Papers in Heat Transfer, ASME, HTD*, 104:21–28, 1998.
- [112] Ling, J.P.C.W., Ireland, P.T., and Turner, L. A technique for processing transient heat transfer, liquid crystal experiments in the presence of lateral conduction. *ASME J. Turbomach.*, 126:247–258, 2004.
- [113] Carcasci, C., Facchini, B., Pievaroli, M., Tarchi, L., Innocenti, L., and Ceccherini, A. Heat transfer and pressure loss measurements of matrix cooling geometries for gas turbine airfoils. *ASME J. Turbomach.*, 136, 2014.
- [114] Arts, T. Introduction to measurement techniques. *Von Karman Lecture Series*, (3rd revised edition), 2012.

- [115] Holman, J. P. *Experimental Methods for Engineers*. McGraw-Hill International Edition, 2001.
- [116] Kline, S. J. and McClintock, F. A. Describing uncertainties in single sample experiments. *Mechanical Engineering*, 75:3–8, Jan 1953.